

**GEOFORSCHUNGSZENTRUM POTSDAM**  
STIFTUNG DES ÖFFENTLICHEN RECHTS

---

# Scientific Technical Report

ISSN 1610-0956

# **Anatomy of an ancient subduction channel in the depth range of its seismogenic coupling zone - insights from field studies in the Swiss Alps and Southern Chile**

Raik Bachmann



1. Gutachter: Prof. Dr. O. Oncken  
GeoForschungsZentrum Potsdam, Freie Universität Berlin
2. Gutachter: Prof. Dr. C. M. Krawczyk  
GGA-Institut Hannover, Technische Universität Berlin
- Datum der Disputation: 09.01.2008

# **Anatomy of an ancient subduction channel in the depth range of its seismogenic coupling zone - insights from field studies in the Swiss Alps and Southern Chile**

Raik Bachmann

Dissertation zur Erlangung des akademischen Grades  
Doktor der Naturwissenschaften (Dr. rer. nat.)  
in der Wissenschaftsdisziplin Geologie

vorgelegt im Fachgebiet  
Geowissenschaften der Freien Universität Berlin

Potsdam, November 2007

begutachtet durch:

Prof. Dr. O. Oncken  
Prof. Dr. C. M. Krawczyk

2007



## **Eidesstattliche Erklärung**

Hiermit versichere ich, dass ich die vorliegende Dissertation ohne unzulässige Hilfe Dritter und ohne Benutzung anderer als der angegebenen Literatur angefertigt habe; die aus fremden Quellen direkt oder indirekt übernommenen Gedanken sind als solche kenntlich gemacht.

Potsdam, November 2007



*„Etwas lernen und mit der Zeit darin immer geübter werden,  
ist das nicht auch eine Freude? Wenn dann von fern her  
Gleichgesinnte kommen und zu Freunden werden,  
ist das nicht auch eine Freude?  
Von anderen aber nicht erkannt  
und doch nicht verbittert werden,  
ist man dann nicht erst recht ein Edler?“*

*Konfuzius*



## Contents

Summary

Zusammenfassung

1. Introduction	1
1.1. Overview	1
1.2. Objectives and motivation	2
1.3. Working areas	2
1.3.1. Alps	2
1.3.2. Chile	7
2. Methods	13
2.1. Overview	13
2.2. Analyses of structural data	13
2.3. PT estimates	13
2.4. Image analyses	15
2.5. Profile reconstruction using 2DMove	15
2.6. Provenance analyses	15
2.7. Sr isotope signature	17
2.8. Geochronology	17
2.8.1. Rb/Sr dating	17
2.8.1.1. The Rb/Sr isotope system	17
2.8.1.2. Sample preparation and analyzing procedure	19
2.8.2. Ar/Ar dating	19
2.8.2.1. The Ar isotope system	19
2.8.2.2. Sample preparation and analyzing procedure	21
3. Anatomy of recently active convergent plate interface zones - structures and processes within a subduction channel	23
3.1. General remarks	23
3.2. Concepts of plate interface processes	23
3.3. Material input and fluid release	25
3.4. Earthquake distribution	27

---

3.5. Geophysical signatures	29
4. Anatomy of a fossil subduction channel - a quantitative view on changing structures along the plate interface	35
4.1. Introduction	35
4.2. Concepts of plate interface processes	37
4.2.1. The subduction channel	37
4.2.2. Mechanical concepts for coseismic and interseismic deformation	39
4.3. Geological setting	40
4.3.1. Alpine evolution	40
4.3.2. Geology of the working area	41
4.3.3. Age constraints and metamorphism	41
4.4. Methods	42
4.5. Observations and results	44
4.5.1. Structural data	44
4.5.2. Geothermobarometry and temperature estimates	46
4.6. Restoration of the fossil plate interface	46
4.7. Spatial variation of characteristics along the fossil plate interface	48
4.7.1. General information	48
4.7.2. Deformation	51
4.7.3. Clasts	53
4.7.4. Pseudotachylytes	53
4.7.5. Mineralized veins	56
4.8. Discussion	58
4.8.1. Post-accretion changes	58
4.8.2. Long-term kinematics - tectonic erosion vs. accretion	59
4.8.3. Short-term kinematics - unstable slip vs. stable sliding	61
4.8.4. Fluid flow and constraints for long- and short-term deformation	63
4.9. Conclusion	65

---

5. Temporal constraints for unstable slip - $^{40}\text{Ar}/^{39}\text{Ar}$ geochronology applied to pseudotachylytes	67
5.1. Introduction	67
5.2. Geological, metamorphical and structural framework of the working area	68
5.3 Pseudotachylytes - General information	70
5.4. Published age data	73
5.5. Methods	73
5.6. Sampling and petrography	75
5.7. Results	77
5.8. Discussion	81
5.9. Conclusion	83
6. Abandonment of the South Penninic-Austroalpine paleosubduction interface zone, Central Alps: constraints from Rb/Sr geochronology	85
6.1. Introduction	85
6.2. Geological framework	86
6.2.1. Alpine evolution	86
6.2.2. Geology of the working area	88
6.2.3. Structural aspects of the fossil plate interface zone	90
6.3. Published age data	91
6.4. Analytical procedure of Rb/Sr geochronology and Sr isotope signature	93
6.5. Petrography and sampling	94
6.6. Results	98
6.6.1. Rb/Sr data	98
6.6.2. Sr isotope signature	100
6.7. Discussion	101
6.7.1. Rb/Sr ages	101
6.7.2. Sr isotopes	105
6.7.3. Exhumation of the South Penninic-Austroalpine plate interface zone	106
6.7.4. Gosau group - additional evidence for abandonment of the Alpine subduction zone	108

6.7.5. Isotopic dating - a hint for mass transfer mode	109
6.8. Conclusion	113
7. Final discussion and conclusions	115
References	125
Appendix A – Microprobe bulk analyses of pseudotachylyte groundmass	135
Appendix B – $^{40}\text{Ar}/^{39}\text{Ar}$ analytical data	141
Appendix C – Sample locations	149
Acknowledgement	155
CV	159

Chapters 4 and 6 are going to be submitted in the following international scientific journals:

**Chapter 4:**

**“Anatomy of a fossil subduction channel – a quantitative view on changing structures along the plate interface”**

R. Bachmann, O. Oncken, W. Seifert, V. Georgieva

to be submitted to *Journal of Structural Geology*

**Chapter 6:**

**“Abandonment of the South Penninic-Austroalpine paleosubduction interface zone, Central Alps: constraints from Rb/Sr geochronology”**

R. Bachmann, J. Glodny, W. Seifert, O. Oncken

to be submitted to *International Journal of Earth Science*

Chapter 5 is going to be prepared for submission to an adequate scientific paper in the following way:

**Chapter 5:**

**“Temporal constraints for unstable slip –  $^{40}\text{Ar}/^{39}\text{Ar}$  geochronology applied to pseudotachylytes”**

R. Bachmann, M. Sudo, V. Georgieva, O. Oncken



## Summary

Modern concepts on processes of seismically active parts of converging plate interfaces are derived from lab experiments, theoretical inferences, and geophysical observations, which have either poor resolution, or are strongly dependent on insufficiently constrained assumptions. Therefore, we studied a continuous exposure of an ancient subduction channel in the depth range of its former seismogenic zone in the Central Alps of Europe. This subduction channel developed due to Late Cretaceous - Early Tertiary subduction and accretion of the South Penninic lower plate underneath the Adriatic upper plate (Austroalpine domain). Additionally, we include information from Southern Chile, where material, which formerly underwent deformation within a subduction channel, was exhumed to the surface by large scale basal accretion. There, we concentrated on the formation of mineralized vein systems. However, we mainly focused on the exhumed plate interface zone in the European Alps. During subduction of the South Penninic ocean, material from both the continental upper plate and the oceanic lower plate was progressively involved into the subduction factory and transported downwards, forming either the shaly and serpentinitic matrix of the subduction mélangé, or competent clasts. Rb/Sr deformation ages for mylonitized rocks of the South Penninic mélangé and for deformed Austroalpine basement shed light on the pre-Alpine and Alpine deformation history along the suture, as well as on the mode of syn-subduction interplate mass transfer. According to our Rb/Sr deformation ages and our structural data, the latest increment of subduction-related deformation occurred at ~50 Ma, and is characterized by a roughly top-W direction of tectonic transport. Identical Rb/Sr ages for pervasively deformed Austroalpine and South Penninic rocks point to tectonic erosion of the upper plate

during subduction. This is also evidenced by the presence of upper plate clasts in the subduction mélangé, and from the syn-subduction evolution of Gosau forearc basins pointing to tectonic erosion as prevailing mass transfer mode during the time of subduction. Lack of a metamorphic contrast between the South Penninic mélangé and the Austroalpine upper plate favors exhumation of the suture zone due to a combination of tectonic underplating and surface erosion. The end of sedimentation in the forearc Gosau basins is contemporaneous with basal accretion of the South Penninic mélangé and the Middle Penninic units at ~50 Ma. Therefore, we hypothesize a causal link of both processes, with the change from tectonic erosion to basal accretion caused by underplating of subducted material, which is responsible for a regional uplift leading to inversion of the forearc basins. The end of subduction-related deformation is most likely caused by locking of the South Penninic paleosubduction interface due to underplating of the Middle Penninic micro-continent, so that the active subduction interface is relocated into the new Middle Penninic footwall.

Pseudotachylytes along a restricted segment of the upper plate base – delineated by ca. 200°C updip and ca. 300°C downdip - define the limits of the unstable slip region within the fossil seismogenic coupling zone. Our  $^{40}\text{Ar}/^{39}\text{Ar}$  ages constrain the generation of pseudotachylytes during a time span between 60 Ma to 80 Ma. The heterogeneous texture of the ultra fine grained pseudotachylyte groundmass is composed of a mixture of amphibole, feldspar and biotite, as well as of incorporated rock fragments and single minerals of comparable size. Due to the temporal similarity between subduction and pseudotachylyte formation, and the fact that the pseudotachylytes occur subparallel to the main thrust where Austroalpine rocks were overthrust onto

South Penninic rocks, we interpret the generation of pseudotachylytes to be related to unstable slip processes occurring along the plate interface zone during subduction.

The zone of unstable slip coincides with a domain of intense formation of foliation-parallel mineralized veins with partly blocky minerals in the subduction *mélange*. We suggest that the mineralized veins reflect seismic failure in the *mélange* due to their similarity in spatial distribution and textures compared to pseudotachylytes. Mineralized veins, and brittle fractures continue into the conditionally stable region below, maybe indicating a domain of slow earthquakes and non-volcanic tremors as recently discovered for this depth range along many active convergent margins. The conditionally stable zone above the unstable slip area is devoid of mineralized veins, but displays ample evidence of fluid-assisted processes like the deeper zone: solution-precipitation creep and dehydration reactions in the *mélange* matrix, hydration and sealing of the base of the upper plate. Seismic rupture is possibly expressed by ubiquitous localized deformation zones.

Fluids are most likely provided by dehydration during subduction of sedimentary material from different sources. This is indicated by elevated Sr isotope signatures of marine (meta-) carbonates from the South Penninic *mélange*, which are caused by the interaction of syn-subduction fluids with old continental crust.

In summary, the exposed plate interface has experienced flow and fracturing over an extended period of time reflecting a multistage evolution, but resembles active convergent plate margins in terms of e.g. sediment input, earthquake distribution, fluid circulation, and possible slow slip events and associated tremors.

## Zusammenfassung

Moderne Konzepte über Prozesse in seismisch aktiven Bereichen konvergenter Plattenränder stammen vorwiegend aus Laborexperimenten, theoretischen Überlegungen und geophysikalischen Messungen. Diese haben entweder eine geringe räumliche und/ oder zeitliche Auflösung, oder sind in hohem Maße von nur ungenügend gefestigten Randbedingungen abhängig. Aus diesem Grund stellen wir Beobachtungen aus einem fossilen Subduktionskanal in den Schweizer Alpen vor, der im Tiefenbereich seiner ehemaligen seismogenen Koppelzone komplett zugänglich ist. Dieser Subduktionskanal entstand im Laufe von Subduktion und Akkretion der Südpenninischen ozeanischen Platte unter die Adriatische Oberplatte (Austroalpine Einheiten), welche in der späten Kreide bis zum frühen Tertiär stattfand. Zusätzlich verwenden wir Feldbefunde aus Südchile, wo Gesteine aus der ehemaligen Plattengrenzfläche durch großskalige basale Akkretion an die Erdoberfläche gebracht worden. Dort untersuchten wir vor allem die Ausbildung von mineralisierten Rissen. Allerdings fokussieren wir in der hier vorliegenden Arbeit weitestgehend auf die exhumierte Plattengrenzfläche in den Schweizer Alpen.

Während der Subduktion des Südpenninischen Ozeans wurde Material von der kontinentalen Oberplatte sowie von der ozeanischen Platte fortwährend entlang der Plattengrenzfläche in Richtung Erdmantel transportiert. Dabei bildete das Material einerseits die tonige oder serpentinierte Matrix der Subduktionsmélange, oder kompetentere Klasten. Rb/Sr Deformationsalter mylonitisierter Gesteine aus der Subduktionsmélange sowie der Austroalpinen Oberplatte geben Hinweise auf die prä-Alpine und Alpine Deformationsgeschichte entlang der

Suturzone, sowie auf den subduktionsbezogenen Massentransfer im Interplattenbereich. Unser Rb/Sr-Alter in Kombination mit gemessenen Strukturdaten deuten das Ende der subduktionsbezogenen Deformation im Arbeitsgebiet um ca. 50 Ma mit einem westgerichteten Transport der Hangendeinheiten an. Tektonische Erosion an der Basis der Oberplatte ist durch nahezu identische Deformationsalter für Südpenninische und Austroalpine Gesteine entlang der Suturzone belegt. Dies ist auch durch das Auftreten von Klasten bestehend aus Oberplattenmaterial in der Subduktionsmélange und der subduktionsbezogenen Entwicklung der Gosau forearc Becken bestätigt, für die tektonische Erosion als Hauptgrund ihrer Entstehung von verschiedenen Autoren postuliert wird.

Der fehlende Metamorphosekontrast zwischen der Südpenninischen Subduktionsmélange und der Austroalpinen Oberplatte im Arbeitsgebiet ist erklärbar durch eine Kombination aus Oberflächenerosion und tektonischer Unterplattung (basale Akkretion) als Mechanismen der Exhumierung. Das Abklingen der Sedimentation in den Gosau forearc Becken tritt zeitgleich zur basalen Akkretion der Subduktionsmélange und Mittelpenninischer Einheiten an die Basis der Austroalpinen Oberplatte um ca. 50 Ma auf. Daher postulieren wir einen kausalen Zusammenhang zwischen beiden Ereignissen, wobei der Wechsel von einem erosiven zu einem akkretiven Plattenrand für den regionalen Hebungspuls, der zur Inversion der forearc Becken führte, verantwortlich ist. Publierte paläogeographische Rekonstruktionen erklären das Ende der subduktionsbezogenen Deformation am ehesten mit dem Stilllegen der Südpenninischen Subduktionszone, bedingt durch die Unterplattung Mittelpenninischer Einheiten, wobei dadurch die Deformation von der

Südpenninischen Subduktionsmélange ins Liegende verlagert wird.

Das Vorkommen von Pseudotachyliten in einem eng begrenzten Bereich entlang der Basis der Oberplatte – zwischen ca. 200°C und 300°C – definiert die obere und untere Grenze der Region instabilen Gleitens in der seismogenen Koppelzone. Unsere  $^{40}\text{Ar}/^{39}\text{Ar}$  Alter grenzen die Bildung der Pseudotachylite im Arbeitsgebiet auf eine Zeit zwischen 80 Ma und 60 Ma ein. Die heterogene ultra-feinkörnige Grundmasse der Pseudotachylite setzt sich aus einer Mischung aus Amphibol, Feldspat und Biotit zusammen. Neben diesen rekristallisierten Phasen findet man auch Fragmente und Einzelminerale aus dem Nebengestein in vergleichbarer Korngröße. Auf Grund der Gleichzeitigkeit von Subduktion und Pseudotachylitbildung, sowie der Lage der Pseudotachylite subparallel zur Hauptüberschiebung, interpretieren wir, dass die Pseudotachylite auf Erdbeben in der seismogenen Koppelzone während der Subduktion des Südpenninischen Ozeans zurückzuführen sind.

Der Bereich instabilen Gleitens (d.h. der Entstehung von Erdbeben) fällt mit einem Bereich intensiver Bildung foliationsparalleler mineralisierter Risse mit zum Teil bockiger Textur in der Subduktionsmélange zusammen. Das Vorkommen dieser Risse im selben Tiefenbereich wie Pseudotachylite, aber ausschließlich auf die Subduktionsmélange bezogen, interpretieren wir als Anzeichen für Seismizität in der Subduktionsmélange. Mineralisierte Risse und spröde Brüche findet man ebenfalls entlang der Plattengrenzfläche im Bereich unterhalb der Region instabilen Gleitens. Dort sind sie möglicherweise Anzeiger für sogenannte „langsame“ Erdbeben und damit verbundener „tremors“, wie sie derzeit an verschiedenen aktiven Subduktionszonen in vergleichbaren Tiefenbereichen entdeckt werden. Die

Zone oberhalb des Bereiches instabilen Gleitens entlang der Plattengrenzfläche zeigt keine mineralisierten Risse, aber auch hier gibt es zahlreiche Hinweise auf Fluidzirkulationen: Lösungs-Fällungskriechen und Entwässerungsreaktionen in der Subduktionsmélange, Hydratation und damit einhergehende Abdichtung durch Mineralneuwachstum in der Oberplatte. Auch hier ist Seismizität möglicherweise durch das Auftreten von spröden Bruchflächen gegeben.

Fluide, die im Subduktionskanal zirkulieren, sind vor allem durch Entwässerungsreaktionen des subduzierten Materials freigesetzt worden. Darauf deuten erhöhte Sr-Isotopensignaturen mariner (Meta-) Karbonate aus der Südpenninischen Subduktionsmélange hin, die durch die Interaktion mit kontinentalem Krustenmaterial alteriert wurden.

Zusammenfassend lässt sich sagen, dass das fossile Platteninterface zwar Überprägungen durch spätere Prozesse erfahren hat und damit eine vielschichtige Geschichte besitzt, es aber immer noch vergleichbare Strukturen und Hinweise auf Prozesse aufzeigt, die auch an rezent aktiven konvergenten Plattenrändern vorkommen. Dies beinhaltet vor allem den Sedimenteintrag, die Verteilung von Erdbeben, die Fluidzirkulation und möglicherweise auch „langsame“ Erdbeben und damit verbundene „tremors“.

## 1. Introduction

### 1.1. Overview

This introductory chapter aims to present the motivations and objectives for the here presented thesis, and to give a guide post through the different chapters. In addition, both natural laboratories are shortly introduced.

The here presented project is a PhD thesis supported by the German National Merit Foundation, together with the GeoResearchCentre Potsdam (GFZ).

*Chapter 2 (“Methods”)* gives an overview over the methods used in this study, which encompasses the analyses of structural data, estimation of PT conditions, image analyses for clast scaling, microscopic scale investigations using petrographical and binocular microscopes and SEM, structural restoration of a cross section, provenance analyses, analyses of Sr isotope signatures, and Rb/Sr as well as Ar/Ar geochronology.

*Chapter 3 (“Anatomy of recently active plate interfaces”)* gives an overview about the “state-of-the-art” knowledge of structures and processes obtained from recently active convergent plate margins. This includes hypotheses about the subduction channel, a database of geophysical investigations, and the distribution of interface earthquakes in the depth range of the seismogenic coupling zone.

*Chapter 4 (“Anatomy of a fossil subduction channel – a quantitative view on changing structures along the plate interface”)* concentrates on the analysis of the fossil subduction mélange and its upper plate in the European Alps. Therein, a coarse overview about the Alpine evolution and the geology of the working area are given. In addition, basic concepts

of subduction channels and of coseismic and interseismic deformation are reviewed. The temporal framework of deformation within the study area is mentioned on the base of published data. This chapter provides information about the distribution of different key features along the ancient plate interface, which was restored into its former subduction geometry on the base of published and own geothermobarometric data. Finally, we discussed our field data in terms of post-accretion changes, long-term kinematics, short-term kinematics, and fluid flow.

*Chapter 5 (“Temporal constraints for unstable slip –  $^{40}\text{Ar}/^{39}\text{Ar}$  geochronology applied to pseudotachylytes”)* concentrates on Ar/Ar age dating of pseudotachylytes sampled at the northwestern rim of the Engadine window immediately above the base of the upper plate. Pseudotachylytes are unambiguous evidence for fossil seismicity. Despite of analytical limitations and constraints by recrystallization of the pseudotachylyte groundmass since the time of melt generation,  $^{40}\text{Ar}/^{39}\text{Ar}$  geochronology provides an approximation about the time frame of occurrence of unstable slip.

*Chapter 6 (“Abandonment of the South Penninic-Austroalpine paleosubduction interface zone, Central Alps: constraints from Rb/Sr geochronology”)* deals with Rb/Sr isotopic data in order to constrain the termination of subduction related deformation in the study area. In addition, Sr isotope signatures of marine (meta-) carbonates are used to define the influence and nature of fluids circulating through the subduction mélange. We used our isotopic data as hints for the mass transfer mode along the fossil plate interface zone. Tectonic erosion as the prevailing mass transfer mode is referred to the geological evolution of the Gosau group depocenters, which represents slope basins formed onto the upper plate during the time of subduction. Finally, isotopic dating yielded

information about the pre-Alpine history of the study area as well.

*Chapter 7* (“**Final discussion and conclusions**”) summarizes the results of the different subchapters and aims to integrate them into a model of structures and processes along the seismogenic zone of convergent plate interfaces with special emphasis on the spatiotemporal subduction history of the European Alps.

Additionally, microprobe analyses,  $^{40}\text{Ar}/^{39}\text{Ar}$  analytical data, and sample locations are given in the “**Appendix A, B and C**”.

## *1.2 Objectives and motivation*

Convergent plate margins generate most of the world’s seismicity, and nearly all of the earthquakes with magnitudes  $>8$ . They initiate within the seismogenic coupling zone, which marks the transient, seismically active part of the subduction channel developed between the two converging plates. Despite the enormous social, economic and scientific importance associated with seismogenic zones of convergent plate interfaces (e.g. destructive earthquakes, tsunamis), processes occurring in the intervening subduction channels are poorly understood. To date, the plate interface of convergent plate boundaries (i.e. subduction channels) cannot be directly accessed by drilling nor through surface observations, but has been intensely studied with geophysical methods, numerical modeling, and sandbox simulations. These, however, either have only poor resolution, or are strongly dependent on a number of poorly constrained assumptions. In consequence, direct investigations of exhumed ancient convergent plate boundaries are requested to achieve insights into deformation processes, which occurred along the plate interface despite multiple overprinting during exhumation. No continuous

exposure exhibiting the complete seismogenic part of a subduction channel has been analyzed as yet. However, outcrops of rocks, which suffered subduction and subsequent exhumation, exist e.g. in the European Alps or Southern Chile.

The here presented study contributes to the understanding of convergent plate boundaries in the depth range of their former seismogenic zone aiming at testing inferences and hypotheses of the various kinematic and mechanical concepts presented for the seismogenic zone. Therefore, we use the complete exposure of this part of a former plate interface in the European Alps, one of the best-studied mountain belts that has resulted from successive subduction, accretion and collision, where we analyzed a *mélange* zone tracing the plate interface zone of the fossil convergent plate margin. Additionally, we included information from Southern Chile, where material, which formerly underwent deformation along the plate interface, was exhumed to the surface by large scale basal accretion at a certain depth to the base of the upper plate. This part of the study provided additive hints for structures and processes occurring along the plate interface zone of convergent plate margins (i.e. within the subduction channel), at least for a restricted PT domain.

## *1.3 Working areas*

### *1.3.1 Alps*

A detailed discussion about the working area in the European Alps, comprising their geological, structural, metamorphical and geochronological framework, as well as the general Alpine evolution as far as interesting for our purpose, can be found in Chapters 4, 5 and 6. Here, we only present a brief overview about the location of the

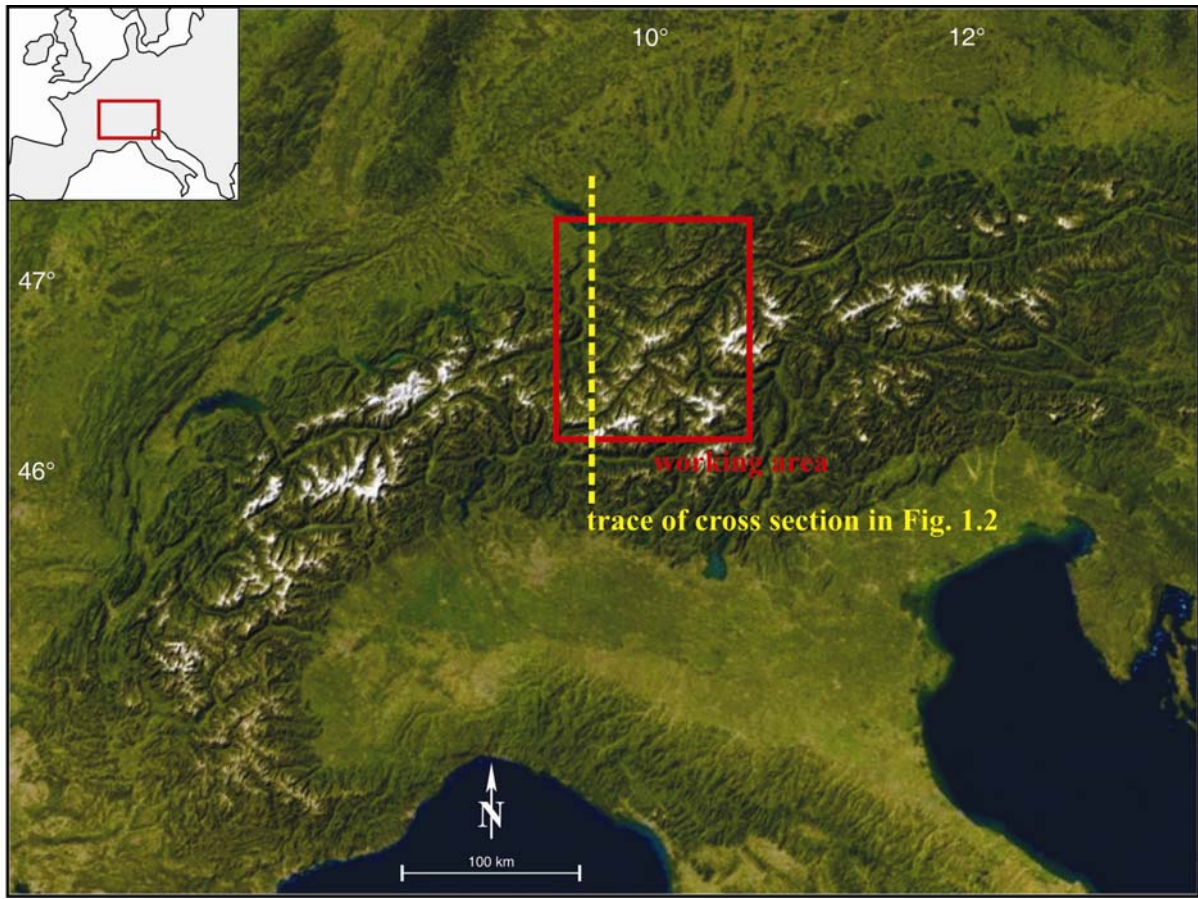


Figure 1.1: Satellite image of the European Alps. The shown section is comparable to the geological maps presented in Chapters 4 and 6. Red rectangle outlines the working area, yellow line represents the trace of the cross section of Figure 1.2. Source: [www.worldwind.arc.nasa.gov](http://www.worldwind.arc.nasa.gov).

study area, the main geological units, and their evolution in time and space.

The working area for the main part of this study is located in the central part of the European Alps along the transition from the Western to the Eastern Alps (Fig. 1.1). It extends from the Swiss-Austrian border in the north to the Swiss-Italian border in the south.

The European Alps are the result of continent-continent collision between the European plate and the Adriatic plate following the subduction and accretion of intervening oceanic domains (Penninic units) during the Mesozoic and Tertiary times. Most models differentiate two orogenic cycles during Alpine evolution: A Cretaceous orogenic cycle (referred to as Eoalpine, e.g. Wagreich 1995) is defined

by an east to southeast dipping subduction zone related with the closure of the Meliata ocean leaving signatures of subduction-related deformation within the Austroalpine nappes (Adriatic plate, e.g. Schmid et al. 2004). Stacking within the Austroalpine is associated with top-W, locally top-SW and top-NW thrusting (Froitzheim et al. 1994, Handy 1996). The direction of convergence changed to north – south during the Tertiary orogenic cycle (referred to as Mesoalpine to Neoalpine, e.g. Wagreich 1995) with top-N thrusting and closure of the Alpine Tethys in-between the European and Adriatic plate (Froitzheim et al. 1994, Handy 1996, Schmid et al. 2004). According to Froitzheim et al. (1994) the transition between top-W thrusting and top-N thrusting is marked by a Late Cretaceous extensional phase with top-SE directed

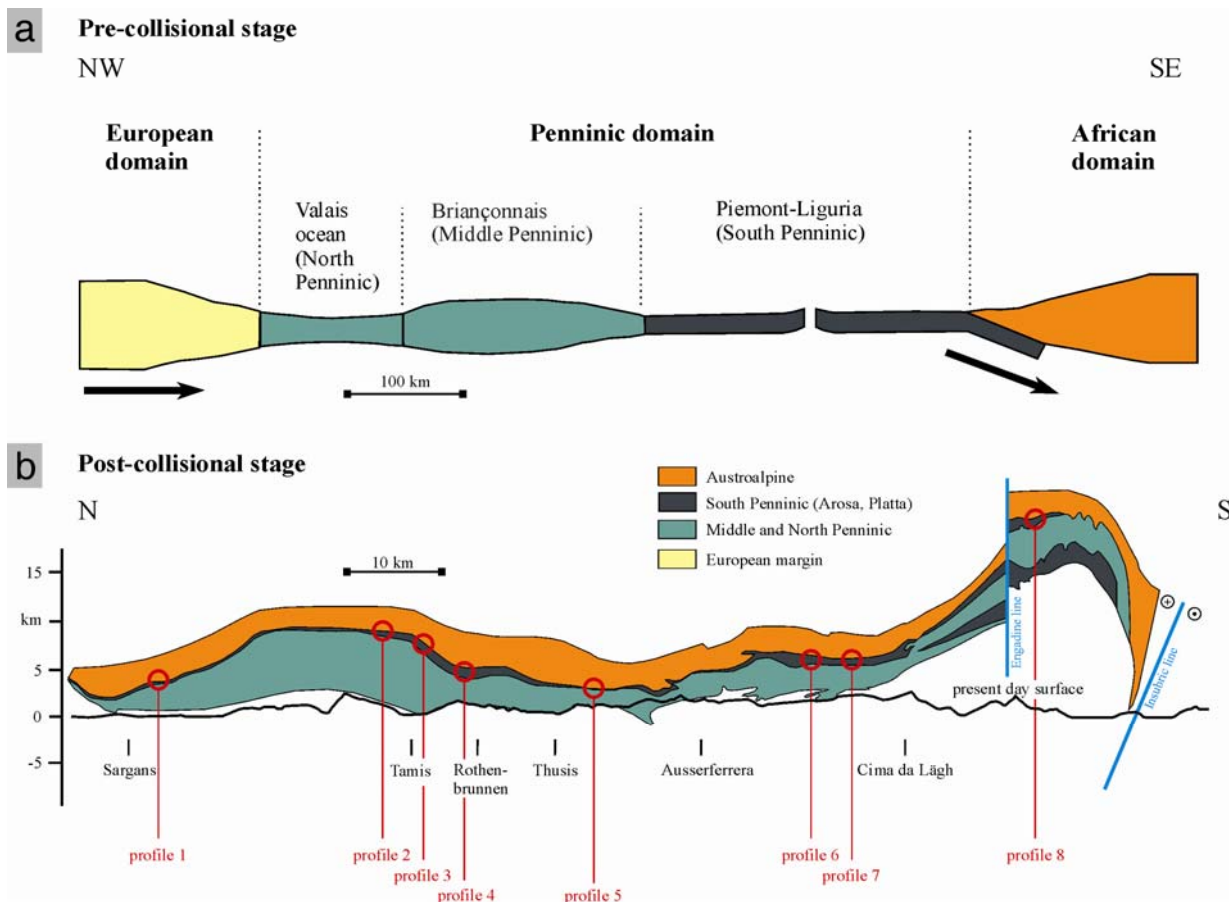


Figure 1.2: a) Schematic profile from NW towards SE illustrates the relationship between the different tectonic units. Note the subdivision of the Penninic domain into the North Penninic ocean, the Middle Penninic micro-continent, and the South Penninic ocean. The South Penninic ocean was subducted beneath parts of the African plate during Mesozoic and Tertiary times. b) N-S section of the present day situation of the tilted and exhumed South Penninic-Austroalpine plate interface zone, based on Schmid et al. (1996). The positions of the analyzed profiles are also indicated (in addition, see Chapter 4). Trace of cross section is shown in Figure 1.1.

normal faulting, which partly reactivated deformation features of the former deformational stages. This clear separation between the Cretaceous and the Tertiary orogenic cycles is only well observable in the Austroalpine nappes of the Eastern Alps (e.g. Schmid et al. 2004). However, subduction and accretion of oceanic units in the Western Alps represent a continuous process from the Late Cretaceous to the Paleogene, transforming a passive continental margin into an active one (e.g. Schmid et al. 2004).

In various paleogeographic models, the intervening oceanic Penninic units are subdivided into two oceanic basins related

to the Alpine Tethys, and a micro-continent separating the oceanic sub-basins (Fig. 1.2a). The oceanic basins are termed North Penninic Valais basin and South Penninic ocean (Arosa zone and Platta nappe as local names in the study area), whereas the micro-continent is the Middle Penninic domain, respectively the Briançonnais continental swell (e.g. Florineth and Froitzheim 1994). These units were successively subducted and accreted to the Adriatic plate until the final collision of the Adriatic plate with the European plate.

The main geological units within the study area are represented by remnants of the

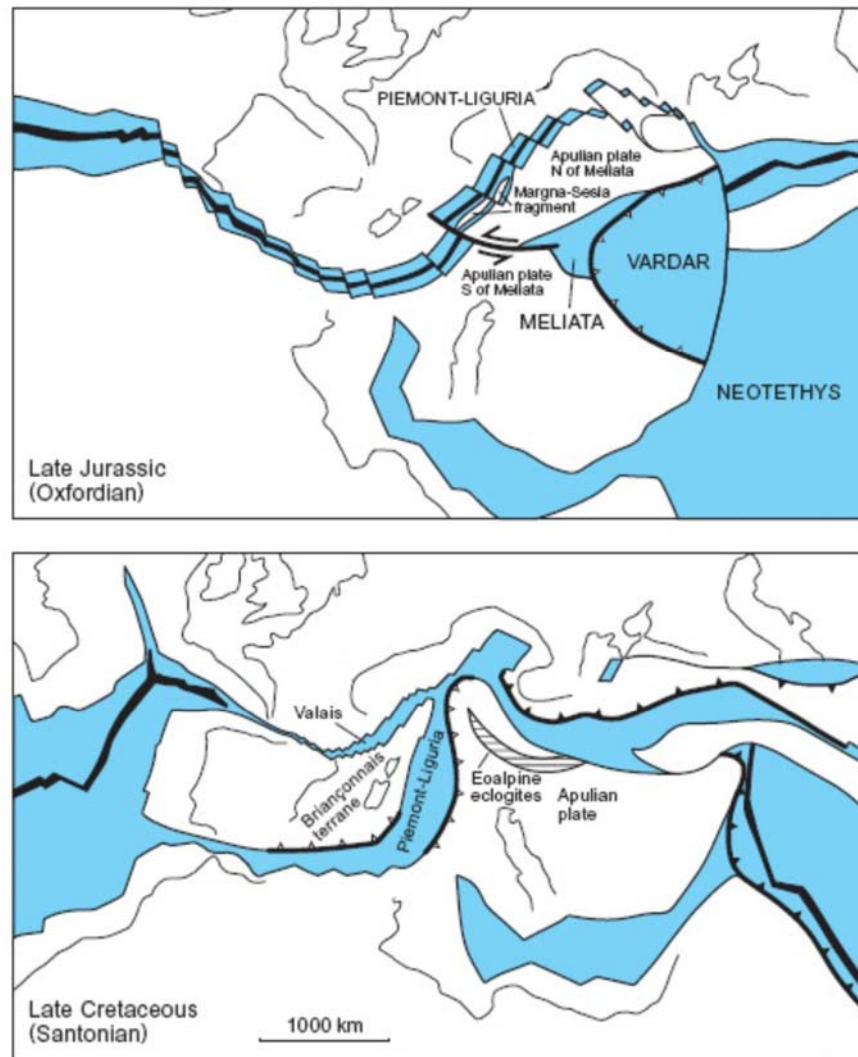


Figure 1.3: Paleogeographic map indicating the evolution of the European Alps in the Late Jurassic (upper part), and the Late Cretaceous (lower part). Modified after Schmid et al. 2004. See text for details.

South Penninic domain forming parts of the lower plate, and the Austroalpine domain as part of the Adriatic upper plate (Figs. 1.2a, b). The South Penninic domain represents a tectonic subduction mélange, which is composed of intensely deformed oceanic and continental material (Deutsch 1983, Ring et al. 1988, and references therein). It comprises Jurassic ophiolites, radiolarian chert, pelagic limestone, shale and sandstone (Ring et al. 1988). Competent blocks of Austroalpine and Penninic affinity are embedded in the incompetent shaly or serpentized matrix (Ring et al. 1990). The apparent thickness of the South Penninic domain varies from a few tens of meters up to more than

2500 m, either reflecting their original thickness or a reduction by subsequent thinning processes. The Austroalpine upper plate consists of a suite of gneissic to amphibolitic, mainly upper crustal rocks, which experienced pre-Alpine (mainly Permo-Carboniferous) and Early (Eo-) Alpine deformation (e.g. Florineth and Froitzheim 1994, Manatschal et al. 2003, Ring et al. 1988). Metamorphic conditions of South Penninic rocks in the working area are in the range from lower greenschist facies to middle greenschist facies. The Austroalpine domain was metamorphosed to lower greenschist facies conditions during Alpine deformation (e.g. Handy and Oberhänsli 2004).

Time constraints on the evolution of the South Penninic-Austroalpine plate interface zone are sparse; a few existing data are given below. Ocean spreading, and thus opening of the South Penninic ocean, is dated to have been occurred at least since the Early to Middle Jurassic (Fig. 1.3) ( $186 \pm 2$  Ma Ar/Ar bt, Ratschbacher et al. 2004, 165 Ma Ar/Ar phl, Gebauer 1999). Subduction of the Penninic domain underneath the Austroalpine should have been initiated during the Cretaceous (Fig. 1.3) (Wagreich 2001). This author reported the change from a passive continental margin into an active margin during the Aptian/Albian, respectively  $\sim 110$  Ma ago. Latest sedimentation within the Arosa zone (South Penninic) and the Platta nappe (South Penninic) are documented to have occurred within the Early Coniacian (Late Cretaceous, Ring 1989), or the Aptian to Albian (late Early Cretaceous; Ring 1989), respectively. Biostratigraphic ages for the flysch deposits comprising the footwall of the South Penninic mélange (derived from Middle and North Penninic units, and from the distal European margin) range between Early Cretaceous to Early/Middle Eocene (Trautwein et al. 2001). In addition, Stampfli et al. (2002) reported distal flysch deposition until 43 Ma. Furthermore, isotopic ages point to 90 Ma - 60 Ma for a pressure-dominated metamorphism of the Lower Austroalpine units, and 60 Ma to 35 Ma for the South Penninic and European units, respectively (Handy and Oberhänsli 2004, and references therein). Schmid et al. (2004) reported HP metamorphism of South Penninic rocks during the Tertiary, at least for the Western Alps. Handy and Oberhänsli (2004, and references therein) reported thrusting and accreting under HP-greenschist facies conditions during a time span between 88 Ma and 76 Ma for the Austroalpine domain in the southern part of our study area. Additionally, Markley et al. (1995) used Ar/Ar geochronology on synkinematic white mica from Middle Penninic (Briançonnais domain) rocks.

They obtained ages at around 38 Ma. Together, these data show the migration of subduction and therewith related deformation towards the foreland (respectively towards NW), which finally culminated in the collision with the European margin. The northwestward younging of flysch deposition is consistent with this migration (e.g. Handy and Oberhänsli 2004, and references therein).

The boundary between the South Penninic mélange in the footwall and the Austroalpine plate in the hanging wall represents the major large scale thrust zone in the working area, where Austroalpine rocks were thrust onto the South Penninic mélange. In a modern geodynamic context, this zone represents a fossil convergent plate interface with an associated subduction channel, along which subduction of the South Penninic ocean underneath the Austroalpine upper plate occurred. Large-scale tilting during exhumation of the fossil plate interface provides access to various paleodepths and metamorphic conditions. We analysed transects crossing the former plate interface (Fig. 1.2b) in order to identify downdip variation of key features along the former plate interface. Each transect covers a profile from the basal parts of the Austroalpine upper plate into rocks of the South Penninic subduction mélange, and in some cases even to the upper parts of the Middle Penninic domain, which was accreted to the base of the South Penninic domain.

The exposed ancient plate interface has experienced flow and fracturing over an extended period of time, including minor overprint during collision and exhumation. Although this bears resemblance to active convergent plate margins that have been active over 10s of Myrs, our results invariably contain the effects of a multistage evolution.

It has to be pointed out that we consider only remnants of the South Penninic domain as parts of the here studied fossil subduction channel. All other domains including the Middle Penninic domain and the North Penninic domain do not belong to the here analyzed subduction channel, as they were subducted beneath and accreted to a hanging wall later in the Alpine evolution. Therefore, for subduction and accretion of these domains newly formed deformation zones developed. Deformation was transferred further into the footwall, respectively into the foreland. Consequently, deformation and metamorphism for the Middle Penninic and North Penninic domains are younger in comparison to the deformation along the

South Penninic-Austroalpine boundary zone. Finally, due to the occurrence of oceanic material (pelagic cherts, metabasalts) as clasts embedded within a matrix, together forming a tectonic *mélange*, we treat the South Penninic domain as a subduction *mélange*, and consequently the material of the *mélange* as the material, which formerly composed the fossil subduction channel at the time of abandonment of this plate interface zone.

### 1.3.2. Southern Chile

Several active and passive seismic measurement campaigns cover the active convergent plate margin in South-Central

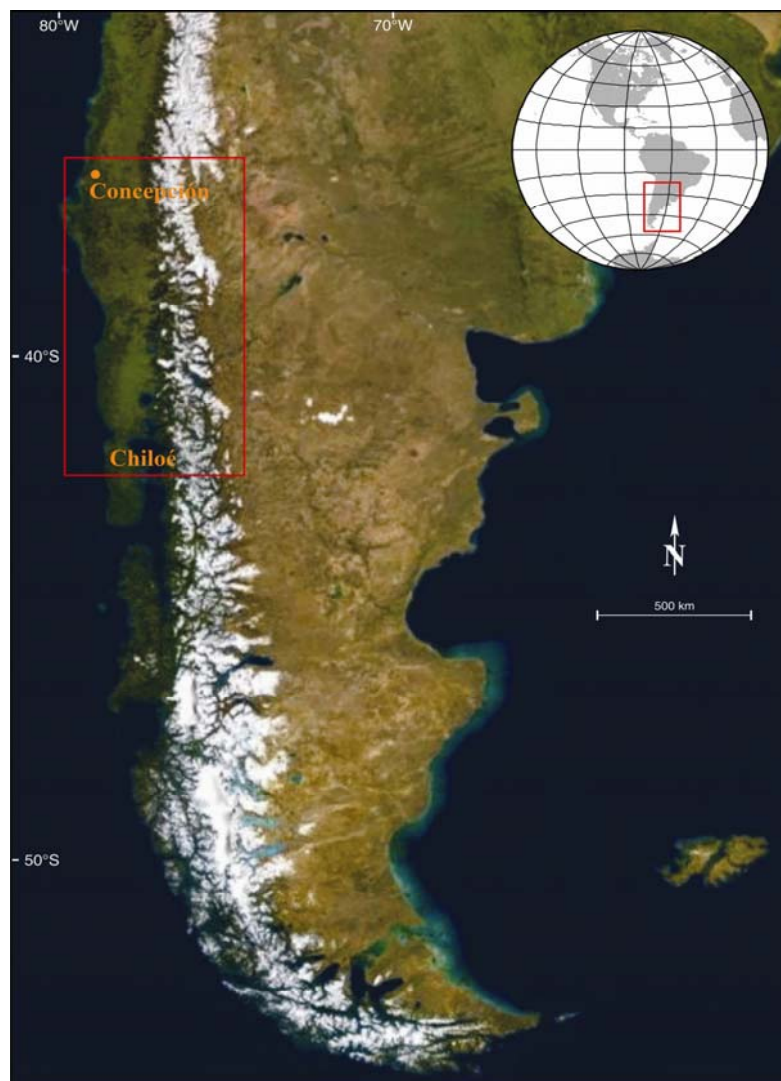


Figure 1.4: Satellite image of the southern part of South America. The study area (see also Fig. 1.5) is located along the coast between 37°S and 42°S (red rectangle). Source: [www.worldwind.arc.nasa.gov](http://www.worldwind.arc.nasa.gov).

DOI: 10.2312/GFZ.b103-08012

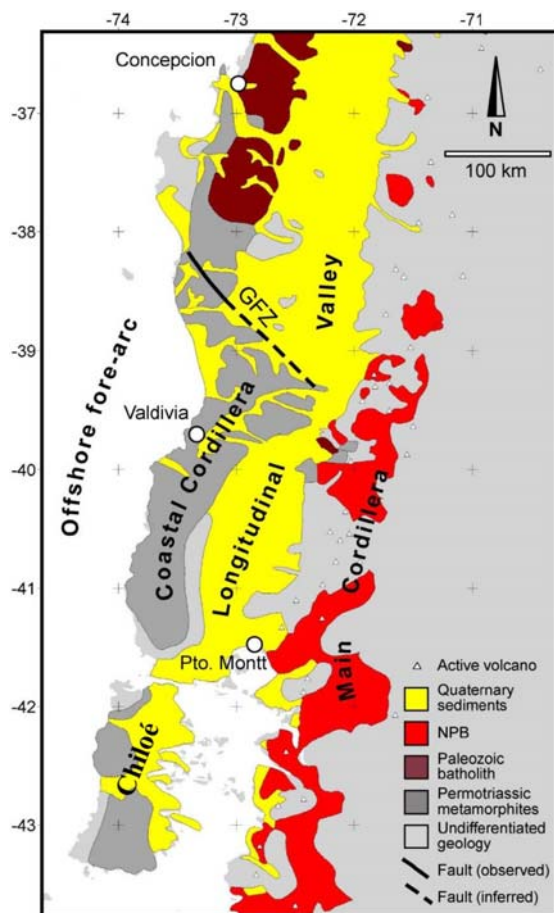


Figure 1.5: Morphotectonic units of the Southern Andes with simplified geology. GFZ = Gastre Fault Zone. The study area is located along the coastline between Concepción in the north and the island of Chiloé in the south (see also Fig. 1.4). Modified after Rosenau (2004).

Chile aiming to image structures along the plate interface (e.g. ANCORP [Oncken et al. 2003], SPOC [Krawczyk and the SPOC team 2003], TIPTEQ [Haberland et al. 2006]). In addition, we analysed outcropping rocks, which formerly underwent deformation within the subduction channel, and were brought to the present day surface by basal accretion (e.g. Glodny et al. 2005). Therefore, this particular study area favors the comparison between data about structures and processes along the plate interface (i.e. the subduction channel) gained from both recently and formerly active convergent plate margins, and we used it as our second naturally laboratory. A brief overview about the geological and structural

framework of this working area is given below.

The working area for this part of the study is located in the Southern Andes, between  $\sim 37^\circ\text{S}$  and  $\sim 42^\circ\text{S}$  (Fig. 1.4). It extends from Concepción in the north to the island of Chiloé in the south (Figs. 1.4, 1.5). During a field campaign in 2005 we analyzed outcrops along the coast in order to compare structures within the exposed PT range with structures formed within a similar PT range studied on outcrops in the European Alps. Additionally, we used existing data from previous field studies in the same area (e.g. Rosenau 2004, Glodny et al. 2005, Melnick 2007).

The Andes formed along the active convergent plate margin of South America, and result from subduction of the Nazca and Antarctic oceanic plates underneath the South American continental upper plate. Subduction lasts at least since  $\sim 200$  Ma. At present, the Nazca plate subducts with a dip angle of  $25^\circ$  to  $30^\circ$  beneath the South American plate (e.g. Barazangi and Isacks 1976). The subduction velocity is 66 mm/a, the subduction direction is oblique to the continental edge with an azimuth of  $78^\circ$  (Angermann et al. 1999). Due to oblique subduction, dextral strike-slip faults developed landwards, striking almost parallel to the trench (e.g. Liquiñe-Ofqui Fault Zone). To the south, the Antarctic oceanic plate subducts almost orthogonal to the trench with 20 mm/a (DeMets et al. 1994). Active subduction related deformation is mainly localized along the plate interface, and is accommodated by megathrust earthquakes (Rosenau 2004, and references therein).

According to e.g. Eppinger and Rosenfeld (1996), Forsythe (1982), Linares et al. (1988), Parada et al. (1997), and Rosenau (2004, and references therein), the continental margin of the Southern Andes shows a roughly margin-parallel segmentation into different morphotectonic

## Reflection seismic section (38°15'S)

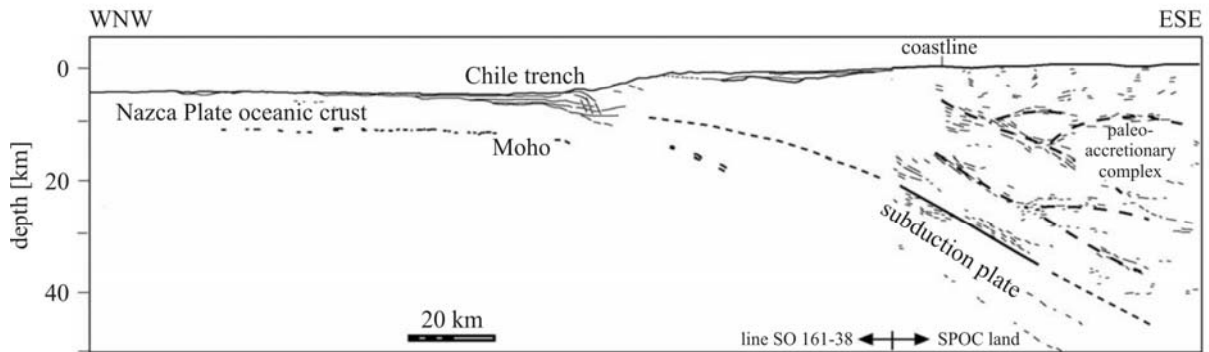
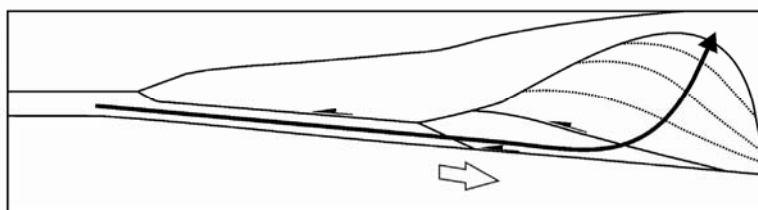


Figure 1.6: Schematic cross section through the South Central Chilean forearc at 38°15'S showing the combined reflection seismic sections from SO 161-38 and SPOC land. Note the large scale paleo-accretionary wedge with antiformal structures. Based on Krawczyk and the SPOC team (2003). Modified after Glodny et al. (2005).

units (Fig. 1.5). These are from east to west: the intra-arc (Main Cordillera), the inner forearc (Longitudinal Valley), the outer forearc (Coastal Cordillera), and the offshore forearc (e.g. Arauco peninsula). Our study area comprises the outer forearc, which is composed of a Paleozoic accretionary wedge. These rocks that formerly underwent deformation along the plate interface (i.e. within the subduction channel) were exhumed to the present-day

Eastern Series and a Western Series (e.g. Glodny et al. 2005, and references therein). The Eastern Series is characterized by low P/T metamorphism and consists of metagreywackes and metapelites. In contrast, the Western Series is dominated by rocks, which suffered a high P/T metamorphism. Typical lithologies are metasediment-metabasite intercalations, which are formed by meta-turbidites, metabasites, ribbon cherts, serpentinites

## a Schematic view of basal accretion



## b Sandbox model with basal accretion

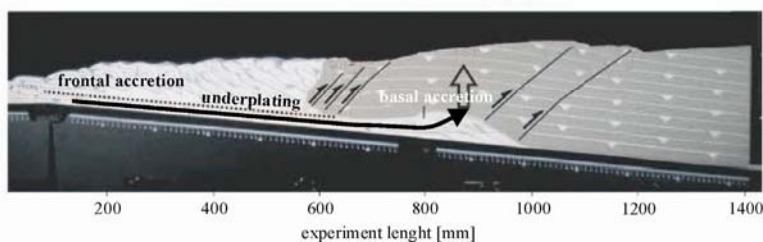


Figure 1.7: (a) Principle drawing of underplating of material to the base of the upper plate favouring exhumation, (b) Sandbox model indicating processes of frontal and basal accretion (modified after Glodny et al. 2005, Lohrmann et al. 2006).

and sulphide bodies (Glodny et al. 2005). These rocks represent the fossil sedimentary input into the subduction channel and remnants of the formerly subducted oceanic plate. Metamorphic signatures point to the transition from greenschist to blueschist facies (Glodny et al. 2005), which is indicative for subduction related metamorphism. Estimated PT conditions for outcrops of the Western Series in the study area done by Glodny et al. (2005) point to 420°C and 8-9 kbar. Therefore, this study area provides additional information about the plate interface zone in this particular PT range.

The predominant structure within the Western series is a shallow dipping, often subhorizontal foliation. Glodny et al. (2005) stated that these structures were

formed during the transfer of material from the subduction channel to the base of the upper plate. Additionally, according to Martin et al. (1999), this foliation is possibly associated with low-angle recumbent nappes (see also Glodny et al. 2005). The thereby formed foliated complex is shown within reflection seismic data (e.g. Krawczyk and the SPOC team 2003), and interpreted to occur down to the plate interface (Fig. 1.6). According to e.g. Glodny et al. (2005), this complex is formed by basal accretion of material formerly transported to depth within the subduction channel. Moreover, processes of basal accretion are predicted from numerical and analogue modeling (e.g. Glodny et al. 2005, Lohrmann 2002, Lohrmann et al. 2006) (Fig. 1.7).

We observed mineralized veins, which run

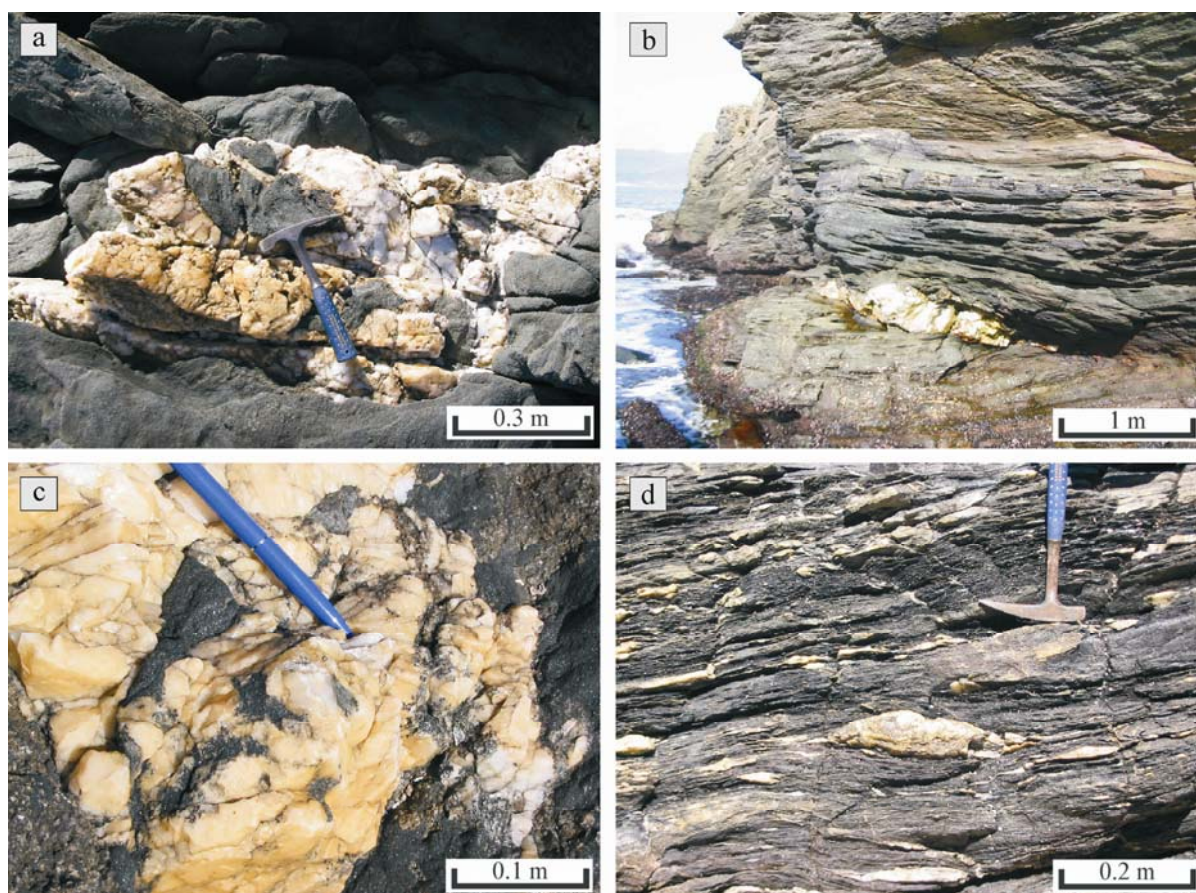


Figure 1.8: Outcrop images of mineralized veins, which run parallel or sub-parallel to the overall foliation. a) Coarse grained blocky textured mineralized vein, b) Large scale mineralized vein running sub-parallel to the tight foliation. Note the boudinaged structure of the vein, c) close-up of minerals with blocky texture comprising the vein filling, and c) smaller scale mineralized veins parallel to the foliation.

sub-parallel to the overall foliation, in both metasediments and metabasic rocks of the Coastal Cordillera within outcrops along the southern part of the Chilean coast (Figs., 1.4, 1.5, 1.8). In some cases the veins fill dilational jogs. Vein filling has a blocky texture of large minerals mostly formed by quartz and calcite, indicative for growth from a free fluid phase into a wide open cavity (Yardley, 1984; Nüchter and Stöckhert, 2007). In addition to quartz and calcite, the veins carry partly minor barroisitic amphibole, epidote, dolomite, chlorite, biotite, apatite, and white mica (Glodny et al. 2005). The incorporation of wall rock fragments within the mineralized veins with no or minor contact to the wall rock supports rapid crystallization. We propose that these veins denote prograde fluid expulsion during subduction of sedimentary material (Glodny et al. 2005). In some cases, the mineralized veins are boudinaged, which points to extensional deformation most likely during the removal of the material out of the subduction channel.

The exposed material exhumed from the plate interface has only experienced minor overprint within the brittle regime during exhumation. Therefore, it is almost undisturbed, and still contains information about structures and processes, which have occurred along the plate interface zone making this working area a suitable laboratory for the purpose of the entire study.

This second natural laboratory provided us additional hints for fluid release and formation of foliation-parallel mineralized veins deeper along the plate interface zone when compared with the Alpine example. According to Glodny et al. (2005), formation of these mineralized veins occurred at ~ 8 to 9 kbar along the Chilean subduction zone. Additionally, we prepared geochemical, fluid inclusion and isotope studies for the vein samples. Due to a shortage of time, these analyses cannot

be included within this PhD thesis, and the insights from this working area remain limited to the foliation-parallel mineralized veins.



## 2. Methods

### 2.1. Overview

For this project we used different methods, which are shortly introduced in this chapter: analyses of structural data, estimation of PT conditions, image analyses for clast scaling, structural restoration of cross section, provenance analyses, analyses of Sr isotope signatures, and Rb/Sr as well as Ar/Ar geochronology. The results of the different methods can be found within the subsequent chapters. In addition, the sample preparation procedures for Rb/Sr, Ar/Ar and Sr isotope analyses are also mentioned within Chapters 4, 5 and 6, because they are part of submitted publications. Microscopic investigations are not mentioned explicitly, because they are the basics for most of the above mentioned methods.

### 2.2. Analyses of structural data

Structural data were collected during field campaigns in summer 2004, 2005 and 2006 in the Western Alps (Eastern Switzerland and Western Austria). Foliation, lineation, shear bands, fold axes, mineralized veins and pseudotachylytes were measured, their distribution and density, geometric proportions, as well as relative age relationships were determined in the field. We investigated shear sense indicators like drag folds and the orientation of shear bands to assess the direction of tectonic transport for the hanging wall.

### 2.3. PT estimates

Geothermobarometry is used to calculate metamorphic temperature and pressure conditions. Therefore, the metamorphic paragenesis has to be in a chemical

equilibrium in order to fulfill the following equation:

$$\Delta G = 0 \quad [1]$$

where G is the Gibbs free energy. If the change of the Gibbs free energy equals 0, no reaction occurs and the system is in an equilibrium state.

Most geothermobarometers are based on element exchange during mineral reactions (univariate, continuously or cation exchange), but there are also other methods based on e.g. net transfer reactions or solvus thermometry. It is not the aim of this study to explain the different geothermobarometers, but the interested reader is referred to Spear (1995) for overview information. The use of different methods for PT estimates was constrained by the limited paragenesis associated with Alpine deformation and metamorphism in the study area (diagenetic to lowest greenschist facies conditions in the northern part, roughly upper greenschist facies conditions towards the south), because geothermobarometry is more difficult with paragenesis formed at low PT conditions.

The thermodynamic basics for geothermobarometry are expressed in equation [2],

$$\left( \frac{\partial P}{\partial T} \right)_{\ln(K_{eq})} = \frac{\Delta S - R \ln(K_{eq})}{\Delta V} \quad [2]$$

where P means pressure, T temperature, S entropy, V volume, R is the gas constant and Keq the equilibrium constant. This equation describes the position of possible reaction curves within the PT field (Fig. 2.1).

Two additional equations are necessary to understand the thermodynamic constraints of geothermobarometry:

$$\Delta V_R = \Delta V_{Pr} - \Delta V_{Ed} \quad [3]$$

$$\Delta S_R = \Delta S_{Pr} - \Delta S_{Ed} \quad [4]$$

Herein, V represents volume, S entropy, R refers to reaction, Pr to products and Ed to educts. These equations describe the change of the volume and the entropy for a particular reaction. With the help of Figure 2.1 and equations [2], [3] and [4] it is possible to perform an estimation of metamorphic PT conditions.

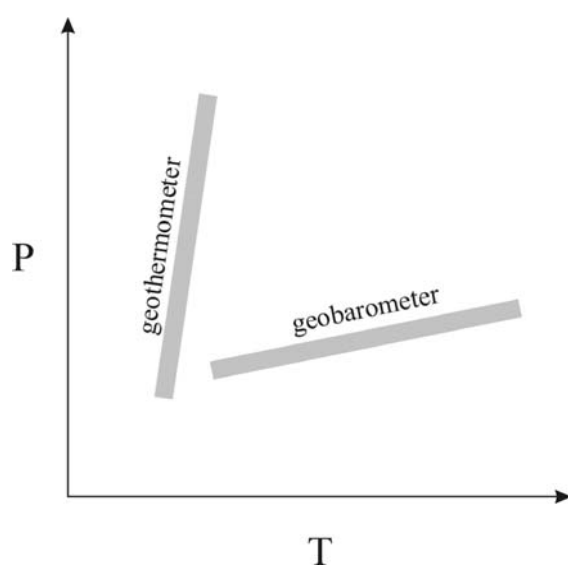


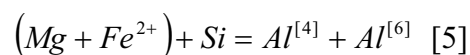
Figure 2.1: Position of reaction curves based on equation [2]. Steep slope represents a reaction useful as geothermometer, flat slope a reaction which can be used as a geobarometer.

As mentioned above, the reacting phases have to be in mineral-chemical equilibrium, which, however, is often not clear. Additionally, it is assumed that the metamorphic mineral paragenesis was formed under the highest temperature conditions the rock has ever experienced. However, these two important facts cannot be proven well and therefore they form the greatest source of error. Other effects influencing geothermobarometry are Mg and Fe exchange reactions on the retrograde PT-path, which often result in too low metamorphic temperatures. Another error may be introduced by false

estimates of the  $Fe^{2+}/Fe^{3+}$ -ratios in silicate minerals or oxides. Although charge balance constraints may provide good evidence for this ratio (e.g. in case of garnet analyses), they often fail in case of amphibole or mica analyses. Finally, there are systematic errors of the geobarometers and geothermometers due to the error of the experimental conditions or thermodynamic database. Despite all these constraints and sources of errors, geothermobarometry allows a rather precise determination of metamorphic temperature and pressure conditions.

Due to the mineralogical composition and the microstructures of the different samples observed in thin sections it is possible to assess their metamorphic grade and – in part – also temperature and pressure conditions the rocks suffered. The deformational behavior of certain minerals (calcite, quartz, feldspar; e.g. recrystallization due to bulging, subgrain rotation) and the magnitude of ductile or brittle-ductile deformation observable in the field can yield primary information about deformation temperatures.

We estimated pressure conditions of samples from both the Austroalpine nappe stack and the South Penninic mélange. We used the Si-content of phengite based on the Tschermak's substitution (equation [5]) with the graphical solution provided by Massonne and Szpurka (1997) (Fig. 2.2).



Phengite represents an intermediate member in the solid solution range between nearly ideal muscovite and Al-celadonite (e.g. Massonne and Szpurka 1997). Due to the absence of critical mineral assemblages for which this geobarometer was calibrated (K-feldspar + phlogopite + quartz, quartz + garnet + kyanite, talc + kyanite + quartz), this method only yields minimum pressure

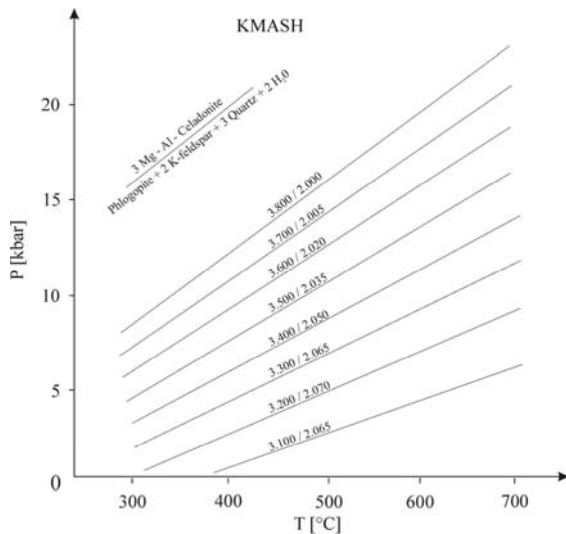


Figure 2.2: Diagram to assess the pressure conditions based on the Si content p.f.u. of phengite based on and redrawn after Massonne and Szpurka (1997). Numbers on isopleths correspond to: Si content / octahedral occupancy.

conditions. Mineral analyses were performed using a CAMECA SX100 electron microprobe operating in the wavelength-dispersive mode. Major and minor elements were determined at 15 kV acceleration voltage and a beam current of 20 nA with counting times of 20 s for major elements, and 30 s for minor elements. The beam diameter used for the mineral analyses was 5  $\mu\text{m}$  for all mineral except for plagioclase, where we used 10  $\mu\text{m}$  in order to suppress sodium diffusion. The standard sets of the Smithsonian Institute (cf. Jarosewich et al. 1980) and of MAC<sup>TM</sup> were used for reference.

#### 2.4. Image analyses

Field images and geological maps were processed with the image-processing software Scion Image (Scion Corporation). We scaled every image using a given amount of pixel per length unit. Thresholds were applied for different gray scales in order to convert the images into black and white bitmaps. Afterwards, the software automatically outlined, counted and measured the individual clasts, to analyze

their major and minor axes, and the clast area.

#### 2.5. Profile reconstruction using 2DMove

In order to relocate plate interface features to their former position we projected the investigated profiles into a composite synthetic section perpendicular to the strike of the former subduction zone. This restoration is based on the N-S section provided by Schmid et al. (1996), redrawn after the NFP-20-East seismic traverse covering the main geological and tectonical units in the working area (see Chapter 4). We used the software 2DMove (Midland Valley) for restoration. After loading the basic cross section into the software, we digitized important horizons and faults. For simplification we used only the top and the base of the South Penninic mélangé as horizons to be restored. The first restoration step was the backward movement of the vertical offset along the Engadine line using the deformation algorithm “fault parallel flow”. In a second step “line length unfolding” was applied to the folded South Penninic mélangé, which resulted in two flat lying horizons (Fig. 2.3).

#### 2.6. Provenance Analyses

Provenance analyses provide information about the origin of the source rocks and tectonic background of the metasedimentary material. Based on the ratio of stable to unstable detrital components in siliciclastic rocks (see text below) (Dickinson 1970), which was obtained by point-counting in thin sections, the provenance of the studied sediments is presented in a variety of discrimination diagrams (ternary systems, Chapter 7). Counting was performed on lithoclasts of 600 – 1000  $\mu\text{m}$  in size, in fine layers of a calcarenitic matrix.

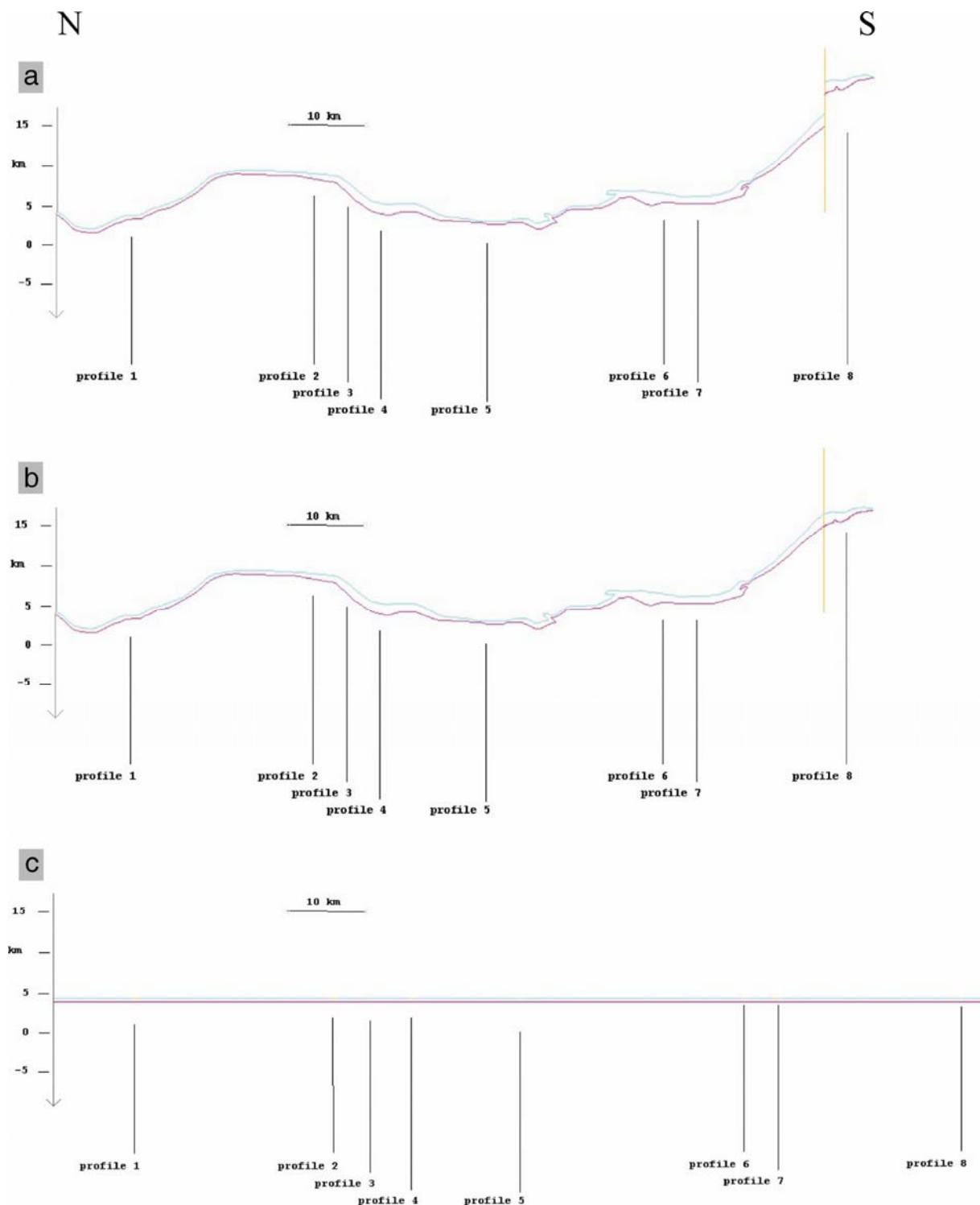


Figure 2.3: Reconstructed profiles using the Midland Valley software 2DMove. Blue line corresponds to the top of the South Penninic mélangé, red line to its base. a) digitized starting cross section, b) removal of vertical offset along the Engadine line (yellow) using “fault parallel flow”, c) final result of applying the “line length unfold” algorithm to remove later deformation along the South Penninic-Austroalpine plate interface zone. This resulted in two flat lying horizons.

The components used here are defined as follows: Single quartz grains (QM) and polycrystalline quartz aggregates (QP) form the stable components, whereas single feldspar grains (F), feldspar aggregates and quartz-feldspar aggregates, also associated with mica and other minerals (QF) form part of the unstable components. These further comprise all rock fragments (L) derived from volcanic (Lv), metamorphic (Lm), and sedimentary rocks (Ls). Since for a more distinct discrimination the genetic aspect of rock provenance is of higher impact, microtextural features have always taken into account. Cherts, which are polycrystalline quartz aggregates as well, may also belong to the Ls component or represent fragments of recrystallized acid volcanic glass matrix. Similar, Lvt comprises the total number of potential magmatic rock components, i.e., QM, F, QF, and Lv. On the other hand, a QF component may also belong to Ls or Lm depending on its micro texture. As far as possible, Lv was subdivided into fragments of acid (Lva) and intermediate (? to basic) (Lvi) composition.

## 2.7. Sr isotope signatures

We studied the Rb/Sr isotope signature of marine (meta-) carbonatic samples to get information about both their age relationships and possible interaction with either crustal or mantle derived fluids. The samples are believed to have formed in a seawater environment, and thus should record the syn-precipitatorial  $^{87}\text{Sr}/^{86}\text{Sr}$  ratio of seawater, given that no later, post-depositional fluid-rock interaction occurred. The Sr-isotopic ratio of seawater is known to vary with time (e.g. Wickman 1948, Gast 1955) (Fig. 2.4), so that Sr isotopic compositions of seawater precipitates may directly be converted to absolute age information (strontium isotope stratigraphy, Look-Up Table

Version 4: 08/ 03, Howarth and McArthur 1997, McArthur et al. 2001). Several preconditions have to be met in this context, namely that no detrital components contaminated the seawater precipitates, that the Sr isotopic signature is not altered by in-situ decay of Rb, and that no secondary exchange of Sr with external fluids ever occurred. In our analytical protocol we dissolved the carbonate samples with dilute HCl and monitored Rb contents and Rb/Sr ratios of the samples. Determinations of Rb and Sr isotope ratios were carried out by thermal ionization mass spectrometry (TIMS) on a VG Sector 54 multicollector instrument (GFZ Potsdam). Sr was analyzed in dynamic mode.

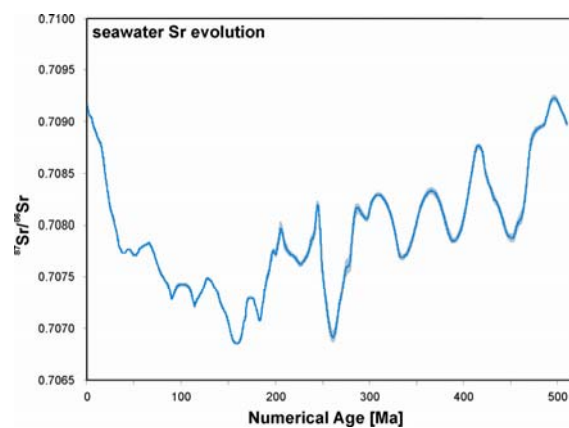


Figure 2.4: Diagram showing the Sr seawater evolution curve (McArthur et al. 2001).

## 2.8. Geochronology

### 2.8.1. Rb/Sr dating

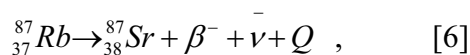
#### 2.8.1.1. The Rb/Sr isotope system

We used the Rb/Sr isotope system to shed light on the temporal constraints for the deformation along the South Penninic-Austroalpine plate interface zone. The first age determination using this method has been done by Hahn et al. in 1943. Later on, this method became into wide use due to

the accessibility of modern mass spectrometers.

Rubidium belongs to the group-1 alkali metals, and has two naturally occurring isotopes,  $^{85}\text{Rb}$  and  $^{87}\text{Rb}$ . Its ionic radius is 1.46 Å, which is quiet similar to that of potassium (1.33 Å). This allows the substitution of potassium by rubidium in all K-bearing minerals, such as mica or K-feldspar. Strontium belongs to the group-2 earth alkaline. Its ionic radius (1.13 Å) is comparable to the ionic radius of calcium (0.99 Å) allowing for the substitution of Ca by Sr in minerals like calcite, plagioclase, and apatite. Sr has four naturally occurring isotopes:  $^{88}\text{Sr}$ ,  $^{87}\text{Sr}$ ,  $^{86}\text{Sr}$  and  $^{84}\text{Sr}$ . Radiogenic  $^{87}\text{Sr}$  is formed by the decay of  $^{87}\text{Rb}$  (see text below). Due to the large geochemical difference of Rb and Sr, both elements behave rather unequal.

The Rb/Sr system is based on the decay of  $^{87}\text{Rb}$  into  $^{87}\text{Sr}$  including the irradiation of a  $\beta^-$  particle, which is expressed by the following equation:



where  $\beta^-$  represents the beta particle,  $\bar{\nu}$  an antineutrino and  $Q$  the decay energy. The decay energy  $Q$  is quiet low (0.275 MeV), which causes problems in the determination of the specific decay rate for this isotope (Faure 1986). The international used decay constant  $\lambda$  is  $1.42 \times 10^{-11} \text{ a}^{-1}$ .

The principle decay equation is expressed by:

$$D = N(e^{\lambda t} - 1), \quad [7]$$

where  $D$  represents the number of daughter nuclides,  $N$  the number of radioactive mother nuclides,  $\lambda$  is the decay constant, and  $t$  means time. For the Rb/Sr system equation [7] is modified as:

$${}^{87}\text{Sr} = {}^{87}\text{Sr}_i + {}^{87}\text{Rb}(e^{\lambda t} - 1) \quad [8]$$

Due to the fact that at  $t = 0$  the amount of  $^{87}\text{Sr}$  within the mineral has not to be 0 (because it is a naturally occurring isotope), it has to be included in equation [8] as  ${}^{87}\text{Sr}_i$ , where “i” means initial. By using mass spectrometry, not the number of atoms for one isotope is measured, but a proportion of isotopes. Therefore, one uses a stable isotope that is not produced by a decay process. For the Rb/Sr system one uses  $^{86}\text{Sr}$  due to its rather similar abundance as  $^{87}\text{Sr}$ , resulting in neither too large nor to small ratios. Therefore, the basic equation for the purpose of age determination using the Rb/Sr isotope system results in:

$$\frac{{}^{87}\text{Sr}}{{}^{86}\text{Sr}} = \left( \frac{{}^{87}\text{Sr}}{{}^{86}\text{Sr}} \right)_i + \frac{{}^{87}\text{Rb}}{{}^{86}\text{Sr}}(e^{\lambda t} - 1) \quad [9]$$

The  $^{87}\text{Sr}$  to  $^{86}\text{Sr}$  ratio can be directly measured with the mass spectrometer,  $^{87}\text{Rb}$  to  $^{86}\text{Sr}$  with the help of the isotope dilution method. The initial  $^{87}\text{Sr}$  to  $^{86}\text{Sr}$  ratio, as well as the term  $(e^{\lambda t} - 1)$  remains unknown. Therefore, one needs at least two analyses from one sample (i.e. cogenetic minerals, different physical fractions of one mineral) to solve this equation with two unknowns. Measuring several cogenetic minerals from one samples result in different data points within a x-y-diagram, where  $x$  represents the ratio of  $^{87}\text{Rb}$  to  $^{86}\text{Sr}$  and  $y$  means the ratio of  $^{87}\text{Sr}$  to  $^{86}\text{Sr}$ . With the slope of the regression line, the age of the sample can than be calculated. When all sample points fall onto the regression line, this line represent an isochron, and the diagram is called isochron diagram. Otherwise, the regression line represents an errorchron. Beside the calculation of the regression line, the MSWD value (mean standard weighted deviation) is also calculated, which expresses the quality of the data in relation to their position relative to the regression line. The result of solving

equation [9] represents a geological meaningful age only when the mineral system has remained a closed system with respect to Rb and Sr.

### 2.8.1.2. Sample preparation and analyzing procedure

The Rb/Sr isotope system of white mica is assumed to be thermally stable up to temperatures  $>500^{\circ}\text{C}$  to  $550^{\circ}\text{C}$ , but may be fully reset by dynamic recrystallization even at lower temperature (Inger and Cliff 1994, Freeman et al. 1997, Villa 1998). According to Müller et al. (1999) isotopic reequilibration between white mica and coexisting phases during mylonitization may occur at temperatures as low as  $350^{\circ}\text{C}$ . Careful correlations between microtextures and isotopic signatures, both by conventional mineral separation techniques (Müller et al. 1999, Glodny et al. submitted) and Rb/Sr microsampling (Müller et al. 2000, Cliff and Meffan-Main 2003) has shown that complete synkinematic recrystallization in mylonites is usually accompanied by isotopic reequilibration. Therefore, Rb/Sr isotopic data from penetratively deformed rocks can be used to date the different stages of mylonitic deformation, as long as deformation occurred below the temperature range for diffusional resetting. To detect possible Sr isotope inhomogeneities resulting from long-term incomplete dynamic recrystallization, from diffusional Sr redistribution, and/or from alteration processes, white mica was analysed in several, physically different (in terms of magnetic properties and/or grain size) fractions whenever possible. According to Müller et al. (1999) this approach ensures control on possible presence of unequilibrated, pre-deformational white mica relics. Care was taken to exclude material altered by weathering or late fluid-rock interaction. White mica sieve and magnetic fractions

were ground in ethanol in an agate mortar, and then sieved in ethanol to obtain pure, inclusion-free separates. All mineral concentrates were checked, and finally purified by hand-picking under a binocular microscope. Rb and Sr concentrations were determined by isotope dilution using mixed  $^{87}\text{Rb}/^{84}\text{Sr}$  spikes. Determinations of Rb and Sr isotope ratios were carried out by thermal ionization mass spectrometry (TIMS) on a VG Sector 54 multicollector instrument (GFZ Potsdam). Sr was analyzed in dynamic mode. The value obtained for  $^{87}\text{Sr}/^{86}\text{Sr}$  of NBS standard SRM 987 was  $0.710268 \pm 0.000015$  ( $n = 19$ ). The observed Rb isotopic ratios were corrected for 0.25% per a.m.u. mass fractionation. Total procedural blanks were consistently below 0.15 ng for both Rb and Sr. Because of generally low, and highly variable blank values, no blank correction was applied. Isochron parameters were calculated using the Isoplot/Ex program of Ludwig (1999). Standard errors, as derived from replicate analyses of spiked white mica samples, of  $\pm 0.005\%$  for  $^{87}\text{Sr}/^{86}\text{Sr}$ , and of  $\pm 1.5\%$  for Rb/Sr were applied in isochron age calculations.

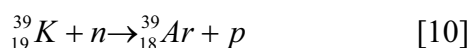
## 2.8.2. Ar/Ar dating

### 2.8.2.1. The Ar isotope system

Age dating using the Ar/Ar isotope system is a version of the K/Ar method, which was introduced by Merrihue and Turner in 1966 due to limitations in the K/Ar system caused by the very different chemical affinities of potassium and argon. Potassium is one of the major constituent of many rock-forming minerals making the K/Ar and the Ar/Ar methods widely applicable. Potassium has three naturally occurring isotopes:  $^{39}\text{K}$ ,  $^{40}\text{K}$  and  $^{41}\text{K}$ . Argon, a noble gas, has also three naturally occurring isotopes ( $^{36}\text{Ar}$ ,  $^{38}\text{Ar}$ ,  $^{40}\text{Ar}$ ).  $^{40}\text{K}$  decays to  $^{40}\text{Ca}$  and  $^{40}\text{Ar}$  via  $\beta^{-}$  decay,  $\beta^{+}$  decay and electron capture. Most

atmospheric Ar derives from this decay reaction.

More important for the use of the Ar/Ar method is the decay of  $^{39}\text{K}$  into  $^{39}\text{Ar}$ , which is forced in a nuclear reactor by irradiation with fast neutrons:



Within this equation  $n$  represents neutron capture and  $p$  proton emission. The potassium content of a sample is constrained by its amount of argon. Otherwise,  $^{39}\text{Ar}$  is a radioactive element, which decays back into  $^{39}\text{K}$  with a half life time of 269 a. Due to this half life time the amount of  $^{39}\text{Ar}$  is assumed as constant over the time of Ar/Ar analyses.

The production of  $^{39}\text{Ar}$  from  $^{39}\text{K}$  during irradiation is expressed by:

$$^{39}\text{Ar} = ^{39}\text{K} \Delta t \int_{\min e}^{\max e} \varphi_e \sigma_e de \quad [11]$$

where  $t$  means time,  $\varphi_e$  stands for the flux density of neutrons with energy  $e$ , and  $\sigma_e$  is the capture cross section of  $^{39}\text{K}$  for neutrons of energy  $e$ .

The principle decay equation [7] adjusted for this method results in:

$$^{40}\text{Ar}_{\text{total}} = ^{40}\text{Ar}_i + \frac{\lambda_{\text{EC}}}{\lambda_{\text{total}}} ^{40}\text{K} (e^{\lambda_{\text{total}} t} - 1) \quad [12]$$

where  $^{40}\text{Ar}_i$  means the initial amount of  $^{40}\text{Ar}$  at  $t = 0$ , and  $\lambda_{\text{EC}}$  stands for the electron capture decay constant.

Combining equation [11] with equation [12] results in:

$$\frac{^{40}\text{Ar}^*}{^{39}\text{Ar}} = \left( \frac{\lambda_{\text{EC}}}{\lambda_{\text{total}}} \frac{^{40}\text{K}}{^{39}\text{K} \Delta t \int \varphi_e \sigma_e de} \right) (e^{\lambda_{\text{total}} t} - 1) \quad [13]$$

where  $^{40}\text{Ar}^*$  represents the radiogenic argon.

During the course of irradiation within the reactor, a standard of known age is irradiated in addition to the sample. The term in large parentheses in equation [13] remains the same for both the sample and the standard, and is used as a single quantity. Its reciprocal is called  $J$  is evaluated as a constant (Mitchell 1968). The age is calculated by rearranging equation [13] into:

$$t = \frac{1}{\lambda} \ln \left[ J \left( \frac{^{40}\text{Ar}^*}{^{39}\text{Ar}} \right) + 1 \right] \quad [14]$$

In addition, irradiation corrections have to be applied, because Ar isotopes are also generated from calcium and other potassium isotopes than  $^{39}\text{K}$  by neutron reactions.

For Ar/Ar geochronology the method of stepwise heating is widely used. Argon is expelled from the sample in different temperature steps, and simultaneously measured in a mass spectrometer. Ar isotopes are calculated for each step, being the same for all steps in an ideal case. Due to excess argon (captured Ar from other sources) or argon loss (less bonded Ar in the outer rims of analyzed grains) this is often not the case. In these circumstances, the analysed sample is expected to reach a plateau, after rise and fall of the calculated ages. This plateau is assumed to represent a geological meaningful age. For our purpose of Ar/Ar geochronology on pseudotachylytes we used the method of laser ablation as recommended by Müller et al. (2002) (see text below).

### 2.8.2.2. Sample preparation and analyzing procedure

We used the Ar/Ar method to date brittle deformation and associated formation of pseudotachylytes. In an initial phase, we macroscopically selected pseudotachylytes, which appear to be undeformed and less altered. Petrographic microscopy was used to study the chosen samples in more detail in terms of amount and petrography of clasts embedded within the fine grained pseudotachylyte matrix. Afterwards, 300 µm thick slices of pseudotachylytes were produced and highly polished on both sides. Then, these slices were cut into small pieces of roughly 5 x 5 mm, and were checked using a binocular microscope to avoid embedded clasts, which would represent an error source for excess argon. Care was taken to exclude material altered by weathering or fluid-rock interaction. Samples were washed in de-ionized water to remove fine powder on the surface of grains (health risk after irradiation). After washing, grains were dried in an oven at roughly 100°C.

For irradiation, samples were individually wrapped in Al foil and then packed into holes within a 99.999 % pure Al disk. Samples were irradiated for four days in a reactor at the GKSS Geesthacht. After the irradiated samples returned from the reactor, the Al foils were opened and the samples were recollected for subsequent argon isotope analyses. The grains were loaded into holes within a Cu disk. This disk was finally introduced into a vacuum line at the Ar laboratory of the University of Potsdam. We used an automated laser extraction and gas cleanup system operating with both a Merchantek LUV266X quadrupled laser emitting UV at 266 nm and a Merchantek floating MIR10IR (CO<sub>2</sub>) (20W Nd-YAG) laser. These laser systems allow both in-situ ablation of small spots on the samples and bulk step-heating. After extraction of Ar

gas from the sample by step heating (several steps until total fusion), the gas was purified in the ultra high vacuum analytical line. Ar gas was introduced into a Micromass 5400 Static Vacuum Mass Spectrometer. Then, the isotopic ratios were obtained. Finally, obtained data were used to produce isochron and plateau plots, and ages were calculated using the Isoplot/Ex program of Ludwig (1999). Analytical errors were applied within the calculation using weighted errors. The validity of isochron plots was checked with the MSWD values (see Chapter 2.8.1.1.). Data of the different analyses are summarized in the appendix.



### **3. Anatomy of recently active convergent plate interface zones – structures and processes within a subduction channel**

#### *3.1. General remarks*

Here, we present concepts of plate interface structures and processes which are obtained by geophysical methods, numerical modeling and sandbox simulations, in order to compare them with the studied structures and processes of fossil convergent plate margins.

#### *3.2. Concepts of plate interface processes*

Cloos and Shreve (1988 a, b) have introduced the subduction channel concept denoting a zone between the upper and the lower plate of convergent plate margins (Fig. 3.1). This zone may typically be up to a few kilometers wide, and probably extends to a depth of more than 100 km (Gerya and Stöckhert 2002). During convergent plate motion material transport is performed within the subduction channel by conveying incoming sediments from the oceanic plate and slivers of oceanic and/or continental material down into the mantle, and by forced return-flow of low-viscosity material back to shallow crustal levels or even to the surface (Ábalos et al. 2003, Gerya et al. 2002). The material within the subduction channel exhibits a velocity gradient towards both plates (Fig. 3.1) (Gerya and Stöckhert 2002) – the material within the subduction channel has neither overcome the velocity of the overriding plate nor has it reached the velocity of the incoming plate. Material is partly scraped off and may either be accreted to the front of the accretionary wedge (frontal accretion) or to the base of the hanging wall (basal accretion) leading to duplex formation and antiformal stacking (e.g. von Huene and Scholl 1991). Material may also be removed from the tip (frontal tectonic

erosion) or the base (basal tectonic erosion) of the upper plate by tectonic erosion (e.g. Clift and Vannucchi 2004). Both accretion and tectonic erosion cause a shift of the currently active subduction thrust. Therefore, Beaumont et al. (1999) refined the existing model of Cloos and Shreve (1988a, b) by defining the area above the subduction channel and below the hanging wall as a subduction conduit, in which material is slowly accumulated by tectonic underplating or removed by tectonic erosion. Consequently, we assume a fluctuating thickness of the subduction channel in space and time, and the active subduction megathrust is not a stationary feature, but composed of transiently active interfaces within and at the boundaries of the subduction channel.

Subduction channels developing at erosive margins should be composed of deformed slope sediments, continental basement and cover-rocks in addition to the pelagic and hemipelagic sediments of accretive subduction channels. Strain localization in subduction channels may preserve original sedimentary and magmatic textures in blocks of all sizes. These blocks are bounded by a network of active shear zones or sheared matrix (Ábalos et al. 2003) that promote the downward transport of incoming material. The deformational record of a subduction channel is persistently renewed due to continuous processes such as sediment subduction and tectonic erosion. Only when material finally left the active parts of the subduction channel and became accreted to the base of the hanging wall, the deformational record can be preserved. Deformation of the material leaving the subduction channel during accretion to the base of the upper plate is caused by permanent strain accumulation due to the velocity gradient between material flow within the channel and the upper plate.

Long-term deformation within a subduction channel is assumed to be

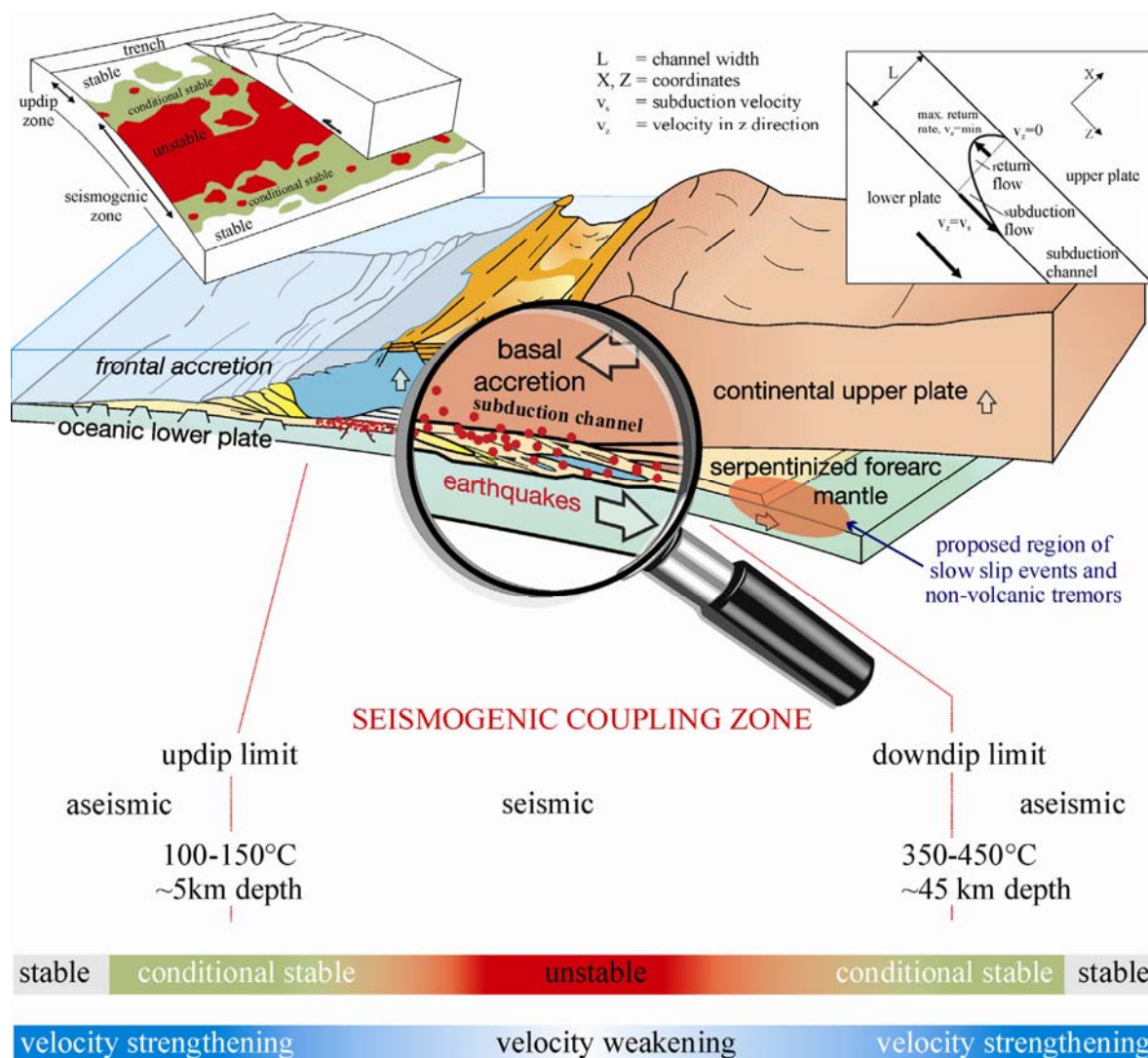


Figure 3.1: Schematic profile of a convergent plate margin with its subduction channel and the seismogenic coupling zone. The subduction channel may be defined by gradients in the flow velocity of the deforming material with respect to the upper and the lower plate (right inset, modified after Gerya and Stöckhert 2002). The updip limit of seismogenic coupling (about 5 km) is probably caused by the dehydration of stable sliding smectite to unstable sliding illite or chlorite (Hyndman et al. 1997). The downdip limit, i.e. the maximum depth of thrust earthquakes and aftershocks (Peacock and Hyndman 1999), is located at approx. 45 km, and may be caused by the increasing dominance of ductile behavior (Nedimović et al. 2003, Oleskevich et al. 1999) or the serpentinization of the forearc mantle leading to a talc rich layer, which lubricates the plate interface (Hyndman et al. 1997, Peacock and Hyndman 1999). Model of frictional conditions (left inset) modified and extended downdip following Bilek and Lay (2002) delineating stable areas, conditionally stable and unstable regions. These areas are variable in space and time. Seismic slip (i.e. velocity weakening behavior) cannot occur in stable areas, which are characterized by a velocity strengthening behavior of the involved material. Earthquakes only nucleate within unstable regions, but they can also propagate into the conditionally stable field (see text for detail).

mainly characterized by stable sliding. However, at a shorter time scale, unstable slip occurs in the upper part of the subduction channel within a limited depth range along the plate interface, i.e. a depth of 5 km to 45 km (Fig. 3.1, so-called

seismogenic coupling zone, e.g. Ruff and Kanamori 1983, Tichelaar and Ruff 1993), causing major interplate earthquakes. The exact location of earthquake nucleation and the succeeding distribution of slip are mainly constrained by asperities or the

variation of the material state, which control the strength of the otherwise weak subduction channel (Pacheco et al. 1993, Ruff 1999).

According to conceptual models, the updip limit of the seismogenic coupling zone is probably caused by the dehydration of stable sliding smectite to unstable sliding illite or chlorite, or due to the interaction of the subduction channel with a rigid backstop (upper plate basement [Hyndman et al. 1997]). However, Saffer and Marone (2003) reported a velocity-strengthening behavior of illite in laboratory experiments, which contradicts to its proposed seismic behavior. Therefore, they suggest other temperature- and depth-dependent processes, such as cementation, consolidation and slip localization to be important for changing the frictional behavior of subduction zone material (see also e.g. Sobolev et al. 2006). Additionally, the alignment of clay minerals due to shearing is a key factor controlling the strength and frictional behavior of clay-rich gouges (Saffer and Marone 2003). The proposed processes take place over a broad range of pressure and temperature conditions. Therefore, Wang and Hu (2006) state that the updip limit of seismogenic behavior must be a transitional feature.

The downdip limit, i.e. the maximum depth of thrust earthquakes and aftershocks (Peacock and Hyndman 1999), is located at approx. 45 km (Fig. 3.1), and may be caused by increasing ductile behavior of the deformed material (Nedimović et al. 2003, Oleskevich et al. 1999). Another discussed process is the serpentinization of the forearc mantle leading to a talc rich layer along the contact of both plates, which lubricates the plate interface (Hyndman et al. 1997, Peacock and Hyndman 1999). Fluids necessary for this proposed serpentinization are thought to be provided by prograde metamorphism of the subducted slab (oceanic plate and

metamorphosed remnants of its sedimentary cover).

Scholz (1998) described different stability regimes along the plate interface (Fig. 3.1): stable, unstable, and conditional stable. The stable regime exhibits velocity strengthening behavior, the unstable regime velocity weakening. Conditional stability defines a region, which exhibits a stable regime under quasistatic conditions. Such areas are thought to be variable in space and time (Schwartz and Rokosky 2007, and references therein). According to Bilek and Lay (1998, 1999) seismic slip cannot occur in the stable zone, because elastic strain is relaxed by aseismic creep. Earthquakes only nucleate within unstable regions, but they can also propagate into conditionally stable areas (Scholz 1998, Moore and Saffer 2001). The distribution of stable, unstable and conditional stable regions may be heterogeneous both downdip and along strike the plate interface producing islands of locked asperities embedded in weaker sedimentary material due to the heterogeneous distribution of subducted material, and the continuously occurring processes along the plate interface (e.g. cementation, dehydration) (Fig. 3.1).

### *3.3. Material input and fluid release*

The material transported into subduction zones consists of clay minerals, carbonates and trench-filling sand (Hashimoto et al. 2006). Therefore, not only the transition from smectite to illite should play an important role in controlling the interface properties, but also the deformational behavior of sandstone blocks or layers should be taken into account. Downward transported sediments strongly influence the physical properties of the plate interface, because they are less rigid than the rest of the subducting plate. Diverse sediment input will lead to spatiotemporal modifications of the physical properties

along the plate interface (i.e. frictional regimes). Bilek and Lay (1998, 1999) assumed that subducted sediments increase in rigidity and frictional resistance due to compaction, and are therefore responsible for unstable slip, and for the decrease of source durations in earthquake rupturing. Scholz (1998) reported a velocity strengthening behavior for less consolidated sediments, possibly promoting areas of stable sliding. Compaction and phase transitions within both sediments and the subducting slab lead to dewatering and dehydration, providing fluids to the plate interface system. This water release increases the pore pressure, and therefore reduces effective stress and effective friction. This in turn increases the probability of fracture formation. Further down the plate interface loss of fluids increases the strength of the sediments. The replacement of clay minerals by zeolite or quartz enforces velocity weakening due to the velocity weakening behavior of low-porosity rocks and framework silicates (Moore and Saffer 2001), thus increasing the probability of earthquakes. Whether this change is abrupt or gradual is mostly defined by the general permeability along the plate interface.

Fluids play an important role within the subduction system. They influence metamorphic reactions, and they are thought to be responsible for the generation of seismicity due to their influence on the effective normal stresses acting on a fault plane. When the fluid pressure is close to the lithostatic pressure, the probability of earthquake occurrence increases. Then, the rupture decreases the fluid pressure to hydrostatic levels due to dilatancy and higher fault connectivity. In this stage the probability of further earthquakes is decreased (Renard et al. 2000). According to Husen and Kissling (2001) the accumulation of high stresses along the plate interface and the thereby caused fabric development leads to a sealing of the plate interface zone, which

contributes to the trapping of fluids, and the thereby caused increase in fluid pressure (hydrostatic fluid pressure above the seal, lithostatic fluid pressure below the seal; see also Chapter 4.8.4.). Only major earthquakes might be able to break the seal, and allowing fluids to migrate upwards due to the gradient in fluid pressure. Therefore, the amount of water entering the system is crucial for the mechanical properties of the subduction zone interface.

The very low coefficient of friction in the order of 0.25 to 0.08 (Byrne and Fischer 1990) along the plate interface might result from high fluid pressure or material with a low frictional strength. Fluid overpressure will facilitate the development of tensile fractures, such as described by Hashimoto et al. (2006) in sandstone blocks from a tectonic *mélange* of the Shimanto Belt, Japan.

Most of the water is bounded in the incoming sediments or within fracture zones of the downgoing oceanic plate. According to Iwamori (1998) the oceanic crust contains about 6 wt-% water in chlorite, lawsonite and amphibole. This amount is reduced to less than 3 wt-% at 50 km depth. Pore water of the incoming sediments will be expelled at shallow depth < 10 km, and bound water is released in the temperature range between 80°C to 150°C due to the transformation of opal to quartz, and clay minerals to mica (Moore and Saffer 2001, Peacock 2000). Between 100°C and 150°C there is a peak in hydrocarbon production (Selley 1998), where solid organic matter is transferred into fluids. This fluid generation potential ends at ~150°C (Moore and Saffer 2001). Due to the porosity collapse in basalt at 300°C to 500°C, most of its pore water will be expelled or the water might contribute to reactions of high temperature minerals into low temperature minerals such as zeolites, which afterwards starts to dehydrate. Hyndman and Peacock (2003)

pointed out, that water release and water consumption by the growth of hydrous minerals are two competing processes. According to Peacock (2000) most of the water which is liberated > 10 km depth should originate from altered basalts or gabbros of the subducting oceanic plate.

Another important process associated with fluid flow is the serpentinization of the forearc mantle. Fluids required for this process might be released from the downgoing slab, allowing the hydration of the complete forearc mantle over tens of millions of years (Hyndman and Peacock 2003). The fluid flow is assumed to be fracture controlled rather than pervasive (Hyndman and Peacock 2003).

### 3.4. Earthquake distribution

Convergent plate boundaries at continental margins belong to the tectonically most active areas on earth and are endangered by devastating earthquakes. To get information about their spatiotemporal distribution is crucial in improving hazard assessments.

Seismicity at convergent plate margins is distributed within several geotectonic positions, and subdivided into intraplate and interplate earthquakes. Intraplate earthquakes nucleate within the subducting slab (e.g. outer-rise events, events within the Wadati-Benioff zone) or within the back-arc region of the overriding plate. Interplate seismicity at convergent plate margins is concentrated only within a narrow zone in the uppermost part of the subduction channel, i.e. a depth range between ~5 km to ~45 km depth (seismogenic zone). This interplate seismicity is responsible for the largest earthquakes ever recorded (e.g. Chile 1960  $M_w$  9.5, Alaska 1964  $M_w$  9.2, Ruff 1996). To better understand its implications for the studied fossil counterparts, we examined the spatial and temporal

distribution of interplate seismicity based on data gained from the NEIC and Harvard catalogs, and from the combined CINCA '95 and Task Force network. The data were kindly provided by Dietrich Lange (University of Potsdam) and Monika Sobiesiak (GFZ Potsdam), respectively.

In general, interplate earthquakes are distributed along the plate interface zone forming a narrow belt (in a 2D view) up to a few kilometers wide, which depends on the quality in relocation of the single seismic events. They cluster within the subduction channel and the basal parts of the upper plate, and are more diffuse distributed towards greater depths (Figs. 3.2, 3.3, 3.4). Consequently, interplate earthquakes clearly image the subduction plate interface zone.

Additionally, we used seismic data for aftershocks (295 events) from the 1995 Antofagasta earthquake (Northern Chile) in order to analyze a limited time window within the seismic cycle. We carefully evaluated the aftershock sequence by examining the different categories of aftershock focal mechanisms to study the spatiotemporal distribution of recent seismicity at a currently active subduction zone (Figs. 3.4, 3.5). The last big event in northern Chile occurred in 1995 near Antofagasta. This  $M_w$  8.0 event ruptured the subduction interface 180 km along strike with an average slip of about 5 m in the depth interval between 10 km and 50 km. Despite the well defined plate interface the width of the zone of seismic activity defined by the aftershocks corresponds to about 3 km. The main shock was a thrust event, but the succeeding events, which occurred along the seismogenic coupling zone during the narrow time span of the recorded aftershocks (2 month) show all possible kinds of focal mechanisms (thrust faults, normal faults, and strike-slip faults) (Fig. 3.5). This has one critical implication for field-based structural analyses: It makes it

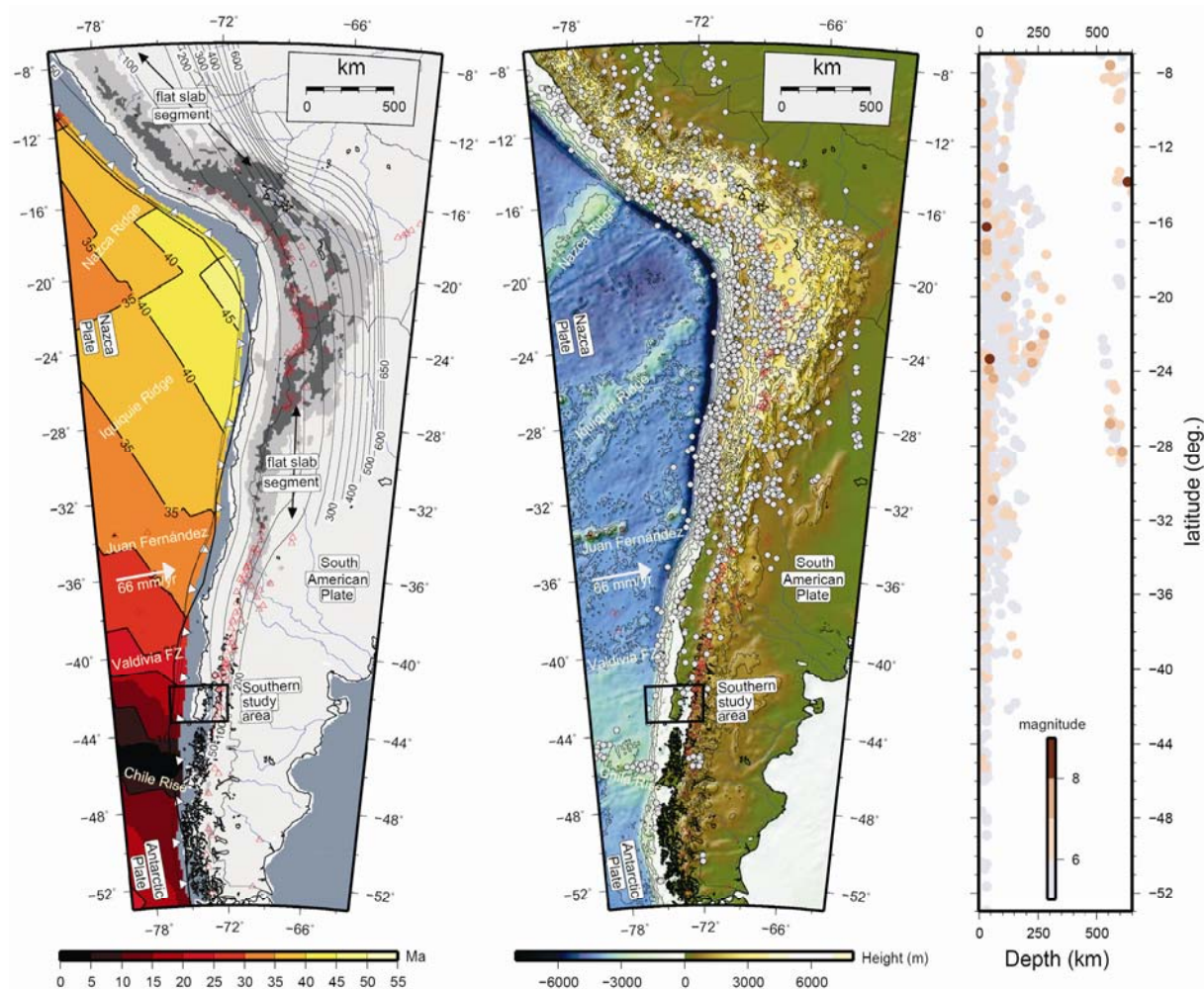


Figure 3.2: Overview of the central and southern Andes between 7°S and 53°S including seafloor ages (Müller et al. 1997), contours of the top of the subducting Nazca plate (Gudmundsson and Sambridge 1998) (left part). Grey dots represent seismicity gained from the NEIC catalog (middle part). The right part shows the seismicity distribution with depth, color coded by magnitude. Note there is a strong clustering of earthquakes within the uppermost part of the plate interface zone. Modified after Lange (2007).

difficult to use fault plane data gained from outcrops of first-order fault zones in order to obtain a relative event chronology on the basis of their kinematics.

We embedded all aftershocks by plotting their spatial distribution in 3D. This resulted in an undulating surface (“earthquake surface”, Fig. 3.6) that indicates a broad area of seismic activity within the depth range of the seismogenic coupling zone outlined by the occurrence of the aftershocks, rather than a single sharp subduction thrust fault being active during the recorded time interval.

The slip accompanying earthquakes accounts only for a part of the total plate tectonic displacement (e.g. Schwartz and Rokosky 2007). In recent times, several studies start to concentrate on other strain releasing processes, such as slow slip events and associated non-volcanic tremors (e.g. Obara 2002, Rogers and Dragert 2003, Brown et al. 2005). However, their physical mechanisms remain questionable. Slow slip events (or silent earthquakes) are thought to be related with fluid migration on or nearby the plate interface, tremors may result from shear failure during slow slip (for an overview see Schwartz and Rokosky 2007). Most of the slow slip

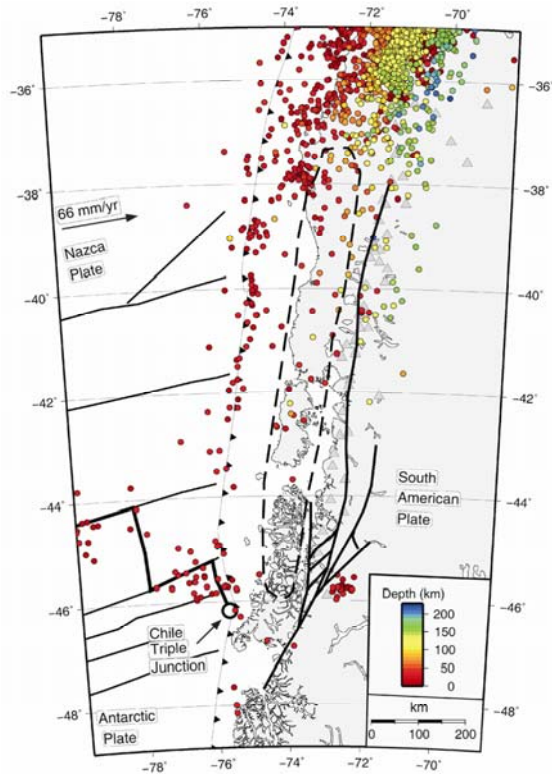


Figure 3.3: Seismicity distribution color coded with depth for Southern Chile based on the NEIC catalog for events between 1990 to 2007. Note there is a strong clustering of earthquakes within the uppermost part of the plate interface zone. Downdip the plate interface there is a more diffuse distribution of seismicity. Modified after Lange (2007).

events occur downdip the seismogenic zone in the transitional or stable sliding region. However, their exact position remains unclear. One of the objectives for this and for future field-based studies is to find possible field expression of ancient slow slip events and associated tremors (see Chapter 4.8.3.).

### 3.5. Geophysical signatures

Seismic reflection and refraction data provide further constraints for the structure of convergent plate margins. The active and passive seismic experiments conducted at the convergent Chile margin ANCORP (Oncken et al. 1999), SPOC (Krawczyk et al. 2003), and TIPTEQ (e.g. Micksch et al. 2006) provide the first complete high

resolution coverage of the entire seismogenic zone of the plate interface (Fig. 3.7). Thereby, the downgoing plate depicts a sharp reflector due to its impedance contrast to the overlying upper plate. In addition, along the southern Chile margin the upper plate is highly reflective showing slightly upward convex continuous reflection bands (see also Fig. 1.6). They are interpreted to represent an ancient accretionary wedge (Krawczyk et al. 2003, Glodny et al. 2005). In general, the reflectivity of the plate interface zone increases to a certain depth and subsequently decreases downdip. According to the ANCORP working group (Oncken et al. 1999), this reduction in reflectivity starts at about 80 km depth, maybe caused by dehydration reactions and eclogitization of the subducting oceanic slab. These proposed processes increase the density of the subducted material, and therefore reduce the impedance contrast to the overlying material, and consequently the ability to resolve structures (Oncken et al. 1999, Krawczyk et al. 2003). Furthermore, along Vancouver Island, Nedimović et al. (2003) reported a transition from a single sharp reflector to a broad zone of reflectivity with varying thickness downdip the plate interface zone in the lower stable sliding region of the plate interface. According to these authors, this reflectivity zone is structurally interpreted as interlayered mafic and/or sedimentary rocks or fluids trapped within intensively sheared sedimentary rocks. A non-structural interpretation refers the reflectivity zone to thin dipping lenses of high porosity (Hyndman 1988). Also Krawczyk et al. (2003) interpreted such reflective elements along the Chilean subduction zone as trapped fluids.

According to Calvert et al. (2003) intense shearing and therewith associated structures (i.e. foliation) are responsible for seismic reflectivity. Therefore, Nedimovic et al. (2003) interpret the broad reflectivity

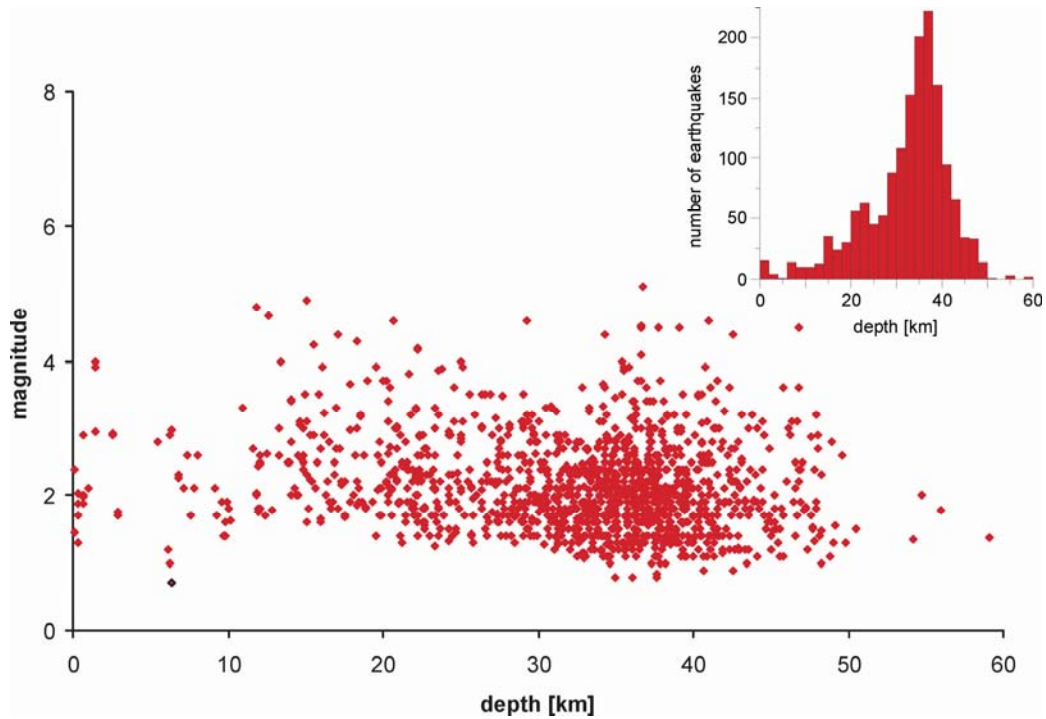


Figure 3.4: Magnitude-frequency-depth distribution for the 1995 Antofagasta aftershock sequence. The majority of the aftershocks occurs in the depth range of the seismogenic coupling zone (see inset of histogram). Data source based on the combined CINCA '95 and Task Force network (e.g. Sobiesiak 2000).

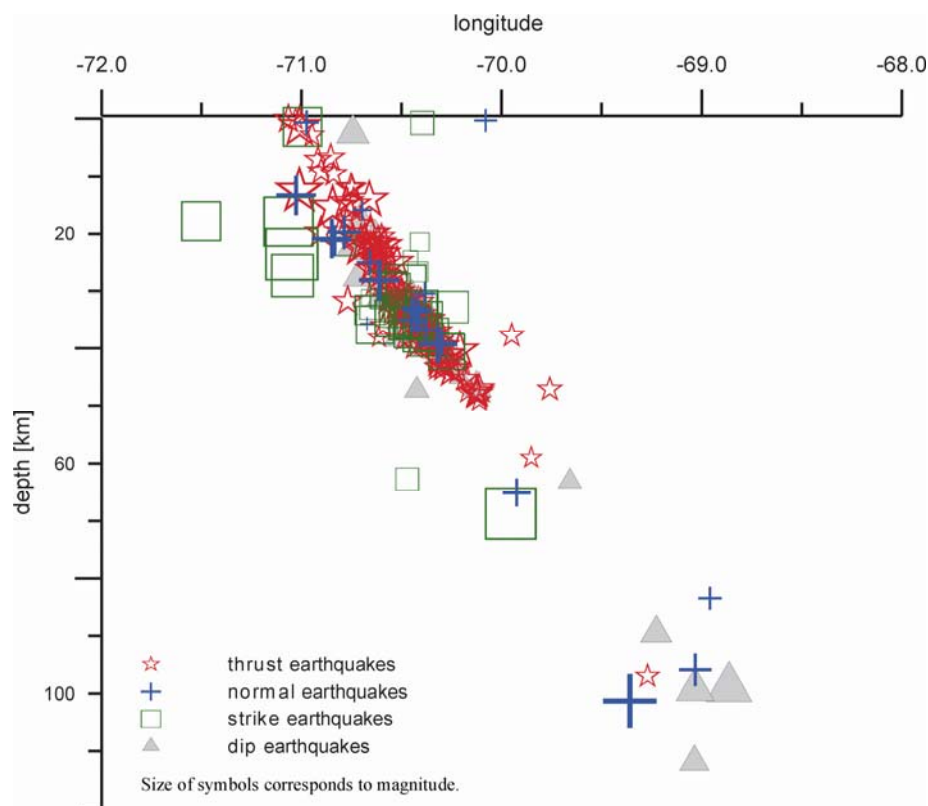


Figure 3.5: Distribution of different focal mechanisms for the 1995 Antofagasta aftershock sequence. There is no preferred appearance of one group of fault plane solutions (thrust faults, normal faults, and strike slip faults) following the main shock event (thrust fault). In contradiction, all possible kinds of focal mechanisms occur along the seismogenic coupling zone during the narrow time span of the recorded aftershocks. This makes it difficult to use fault plane data gained from outcrops of first-order fault zones in order to obtain a relative event chronology on the basis of their kinematics. Data source as above.

DOI: 10.2312/GFZ.b103-08012

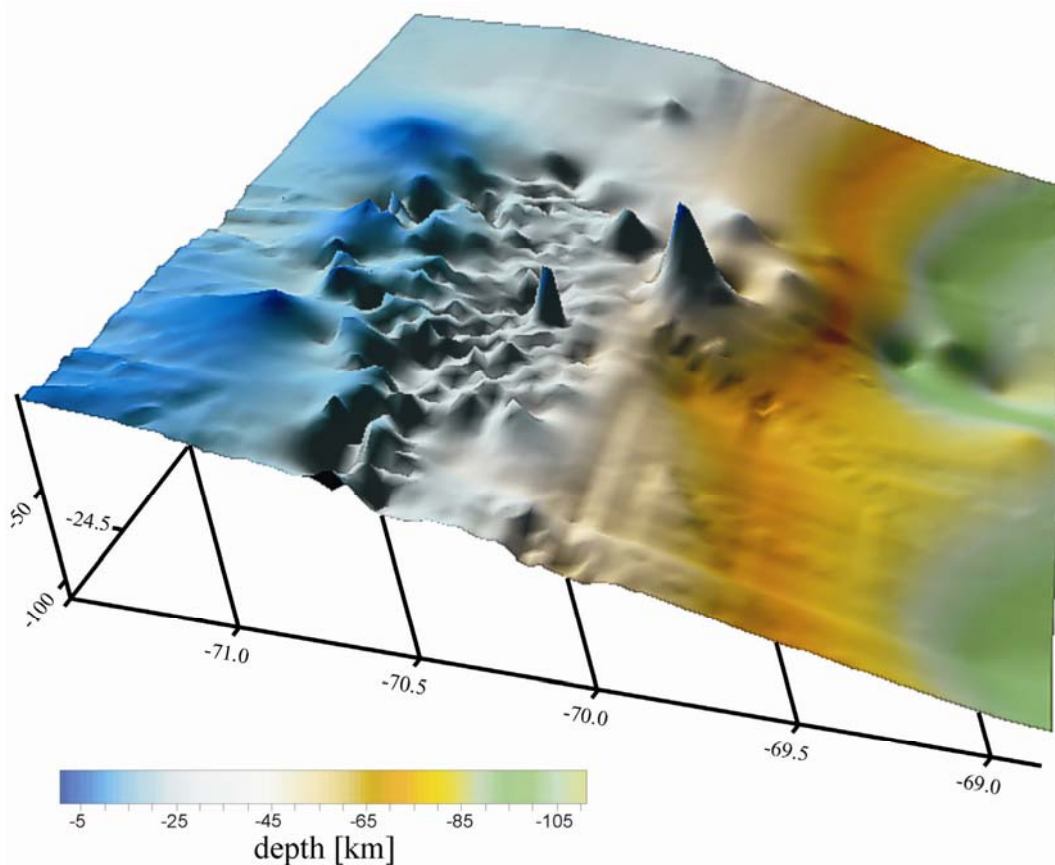


Figure 3.6: Reconstruction of the “earthquake surface” for the 1995 Antofagasta subduction earthquake aftershock sequence. Consider, the undulating surface indicates a broader area of seismic activity within the depth range of the seismogenic coupling zone rather than a single sharp subduction thrust fault being active during recorded aftershocks. Data source based on the combined CINCA’95 and Task Force network (e.g. Sobiesiak 2000).

band downdip the plate interface to be caused by mylonitic rocks, which have been formed where the temperature exceeds the 250°C to 350°C isotherms, and ductile behavior starts to dominate. Consequently, the reflectivity band observable along the plate interface could be the result of both trapped fluids and shearing (see also Chapter 4).

According to Krawczyk et al. (2003, 2006), the assumed subduction channel along the Chile margin is located between the sharp reflector of the downgoing oceanic plate and the highly reflective patches at the base of the accretionary complex. Micksch et al. (2006) reported reflectivity in the uppermost part of the plate interface above the subducting slab,

also reflecting the subduction channel. In consequence, the subduction channel is hardly defined as the area in between the sharp reflector of the oceanic plate, and the highly reflective patches along the base of the upper plate. Additionally, the subduction channel is characterized as a low velocity zone in the area between the base of the upper plate and the top of the oceanic plate along the Chilean subduction zone (Krawczyk et al. 2006, and references therein).

In addition, Calvert (2004) mentioned two important reflectors at the northern Cascadia subduction zone. One reflector is referred to be the top of the downgoing plate, the other reflector is assumed to be the roof thrust of a duplex. The area in



Figure 3.7: Seismic profiles crossing the Chile margin. a) Combined seismic profile crossing marine and onshore domains at about 21° S. Structural and tomographic data are shown to 150 km depth. QBBS: Quebrada Blanca Bright Spot. Data compilation after Krawczyk et al. 2006 and references therein. b) Combined seismic profile crossing marine and onshore domains at about 38.2° S. The wide-angle velocity model is overlain by structural and tomographic information and interpretation to 60 km depth. Data compilation after Krawczyk et al. 2006 and references therein.

between both reflectors is characterized by a  $V_P$  velocity of 6.8 km/s to 7.2 km/s, which is consistent with crustal rocks derived from both the oceanic and the lower continental plate. That gives an additional hint for the presence of a subduction channel transporting slivers from both the lower and the upper plate embedded within a sedimentary matrix towards depth.

The seismic velocity structure of convergent margins clearly highlights the subducting oceanic crust with a  $V_P$  of about 7 km/s, and the oceanic mantle with a  $V_P$  in the range of 8 km/s (Ito et al. 2000). The continental upper crust at 10 km to 15 km depth exhibits a  $V_P$  about 6.3 km/s, whereas the lower continental crust exhibits a  $V_P$  of 7.4 km/s, caused by the change from a felsic to a mafic composition. P-wave velocity of the continental mantle is assumed to achieve 8.0 km/s below 50 km depth and 8.34 km/s at approximately 90 km. Sediments exhibit lower velocities of about 2.0 km/s to 5.8 km/s at a depth range between <1 km and 5 km (Fig. 3.7). Subducted and accreted sediments should be responsible for the low P-wave velocities above the subducted oceanic plate (Husen et al. 2000). This zone of lower seismic velocities should delineate a possible subduction channel (see also Krawczyk et al 2006, and references therein). According to Husen et al. (2000), the base of the upper crust is marked by a strong  $V_P$  increase.

High  $V_P/V_S$  ratios are used as indicators for the presence of fluids (Husen et al. 2000) in the oceanic crust as well as along

the plate interface. This points to possible fractures in the oceanic crust or the presence of water saturated sediments (Husen et al. 2000), respectively. The hydration or serpentinization of the fore-arc mantle wedge (Fig. 3.1) by fluids expelled from the subducting slab is assumed to be responsible for  $V_P$  velocities of about 7.2 km/s to 7.3 km/s, which are too low for normal mantle rocks.



## 4. Anatomy of a Fossil Subduction Channel – a quantitative view on changing structures along the plate interface

### Abstract

Modern concepts on processes of seismically active parts of converging plate interfaces are derived from lab experiments, theoretical inference, and geophysical observations, which have either poor resolution, or are strongly dependent on insufficiently constrained assumptions. We present observations from a continuous exposure of an ancient subduction channel in the depth range of its former seismogenic zone in the Central Alps of Europe related to Late Cretaceous - Early Tertiary subduction and accretion of the South Penninic lower plate underneath the Adriatic upper plate. The exposed plate interface has experienced flow and fracturing over an extended period of time reflecting a multistage evolution. Long-term mass transfer at the base of the Adriatic upper plate is controlled by tectonic erosion and accretion. We identify an unstable slip domain from pseudotachylytes in the temperature range between 200-300°C. This zone coincides with a domain of intense formation of mineralized veins in the subduction mélange. Mineralized veins as well as brittle fractures continue into the conditionally stable region below. The conditionally stable zone above the unstable slip area is devoid of mineralized veins, but displays ample evidence of fluid-assisted processes like the deeper zone: solution-precipitation creep and dehydration reactions in the mélange matrix, hydration and sealing of the base of the upper plate. Seismic rupture is possibly expressed by ubiquitous localized deformation zones. We hypothesize that sealing of parts of the seismogenic portion of the plate interface towards higher parts as well as reaction-enhanced destruction of upper plate permeability (e.g. growth of sheet silicates) is an important component localizing the unstable slip zone.

### 4.1. Introduction

To date, the plate interface of convergent plate boundaries cannot be directly accessed, but has been intensely studied, e.g. in Chile, with geophysical methods (e.g. Oncken et al., 2003; Krawczyk and the SPOC Team, 2003; Haberland et al., 2006), numerical modeling (e.g. Gerya et al., 2002; Gerya and Stöckhert, 2002) and sandbox simulations (e.g. Lohrmann et al., 2006). These, however, either have only poor resolution, or are strongly dependent on a number of poorly constrained assumptions. Hence, direct investigations of exhumed ancient convergent plate boundaries are requested to achieve insights into deformation processes

occurring along the plate interface despite multiple overprinting during exhumation. No continuous exposure exhibiting the complete seismogenic part of a subduction channel has been analyzed as yet. The here presented study contributes to the understanding of convergent plate boundaries in the depth range of their former seismogenic zone aiming at testing inferences and hypotheses of the various kinematic and mechanical concepts presented for the seismogenic zone. We use the complete exposure of this part of a former plate interface in the European Alps (Fig. 4.1), one of the best-studied mountain belts that has resulted from successive subduction, accretion and collision (Froitzheim et al., 1994; Handy, 1996; Schmid et al., 1996; Pfiffner et al., 2000).

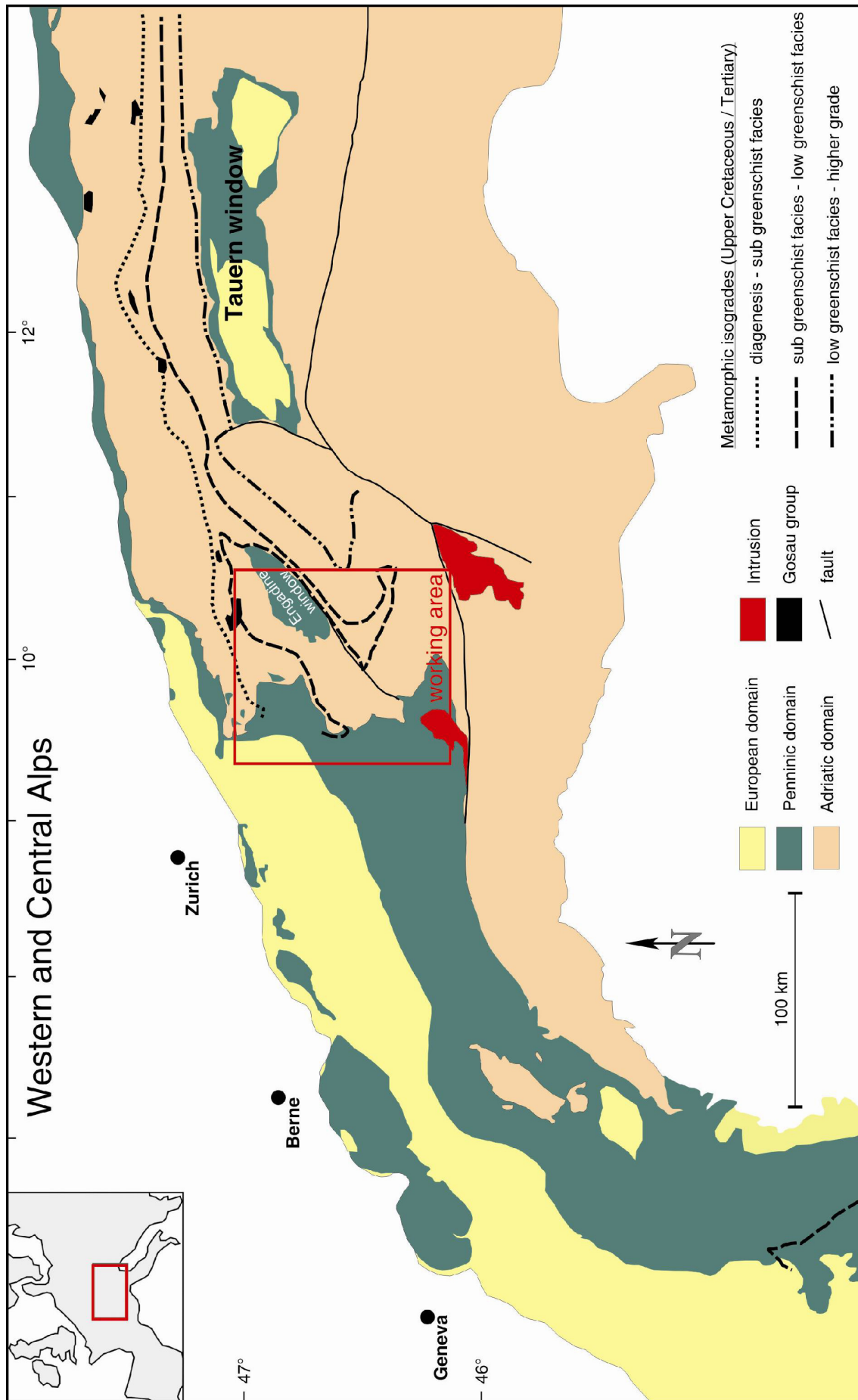


Figure 4.1: Simplified geological map of the European Alps, modified after Frey et al. (1974) and Stampfli et al. (2002). Metamorphic isogrades redrawn after Frey et al. (1999). Rectangle delineates the working area located along the transition of the Western to the Eastern Alps.



We analyzed a *mélange* zone (Fig. 4.1), which traces the plate interface zone of the fossil convergent plate margin.

This zone resulted from subduction of the Penninic ocean beneath the continental realm of the Adriatic plate (Austroalpine nappes) prior to the onset of collision with the European margin (Late Cretaceous - Early Tertiary, e.g. Froitzheim et al., 1996). Large-scale tilting during exhumation of the fossil plate interface provides access to various paleodepths and metamorphic conditions (Figs. 4.1, 4.2). The analysis of 8 transects crossing the former plate interface (Fig. 4.2) aims to identify the downdip variation of features along the former plate interface in terms of composition, deformation, and metamorphism. The exposed ancient plate interface has experienced flow and fracturing over an extended period of time, including minor overprint during collision and exhumation. Although this bears resemblance to active convergent plate margins that have been active over 10s of Myrs, our results invariably contain the effects of a multistage evolution.

## 4.2. Concepts of plate interface processes

### 4.2.1. The subduction channel

Cloos and Shreve (1988 a, b) have introduced the subduction channel concept denoting a zone between the upper and the lower plate of convergent plate margins. This zone may typically be up to a few kilometers wide, its material exhibiting a

velocity gradient towards both plates, and probably extending to a depth of more than 100 km (Gerya and Stöckhert, 2002). Material from both the oceanic and continental plate is transported downwards within the subduction channel, probably reaching mantle depths. Otherwise, material is partly off scraped and may either be accreted to the front of the accretionary wedge (frontal accretion), or to the base of the hanging wall (basal accretion) leading to duplex formation and antiformal stacking (e.g. von Huene and Scholl, 1991). Material may also be removed from the tip (frontal tectonic erosion) or the base (basal tectonic erosion) of the upper plate by tectonic erosion (e.g. Clift and Vannucchi, 2004). Subduction channels developing at erosive margins should be composed of deformed slope sediments, continental basement and cover-rocks in addition to the pelagic and hemipelagic sediments of accretive subduction channels. Strain localization in subduction channels may allow preserving original sedimentary and magmatic textures in blocks of all sizes. These units are bounded by a network of active shear zones or sheared matrix (Ábalos et al., 2003) that promote the downward transport of incoming material. Hence, the active subduction megathrust is not a stationary feature, but composed of transiently active interfaces within and at the boundaries of the subduction channel. While this concept provides a kinematic framework to assess the rock record exposed in an ancient subduction channel that has formed over geological time scales, it requires additional components to account for seismic cycle processes.

At shorter time scales unstable slip in the upper part of subduction channels occurs within a limited depth range along the plate interface, typically between 5 km and 45 km depth (Fig. 4.3, so-called seismogenic coupling zone, e.g. Ruff and Kanamori, 1983; Tichelaar and Ruff, 1993), causing major interplate

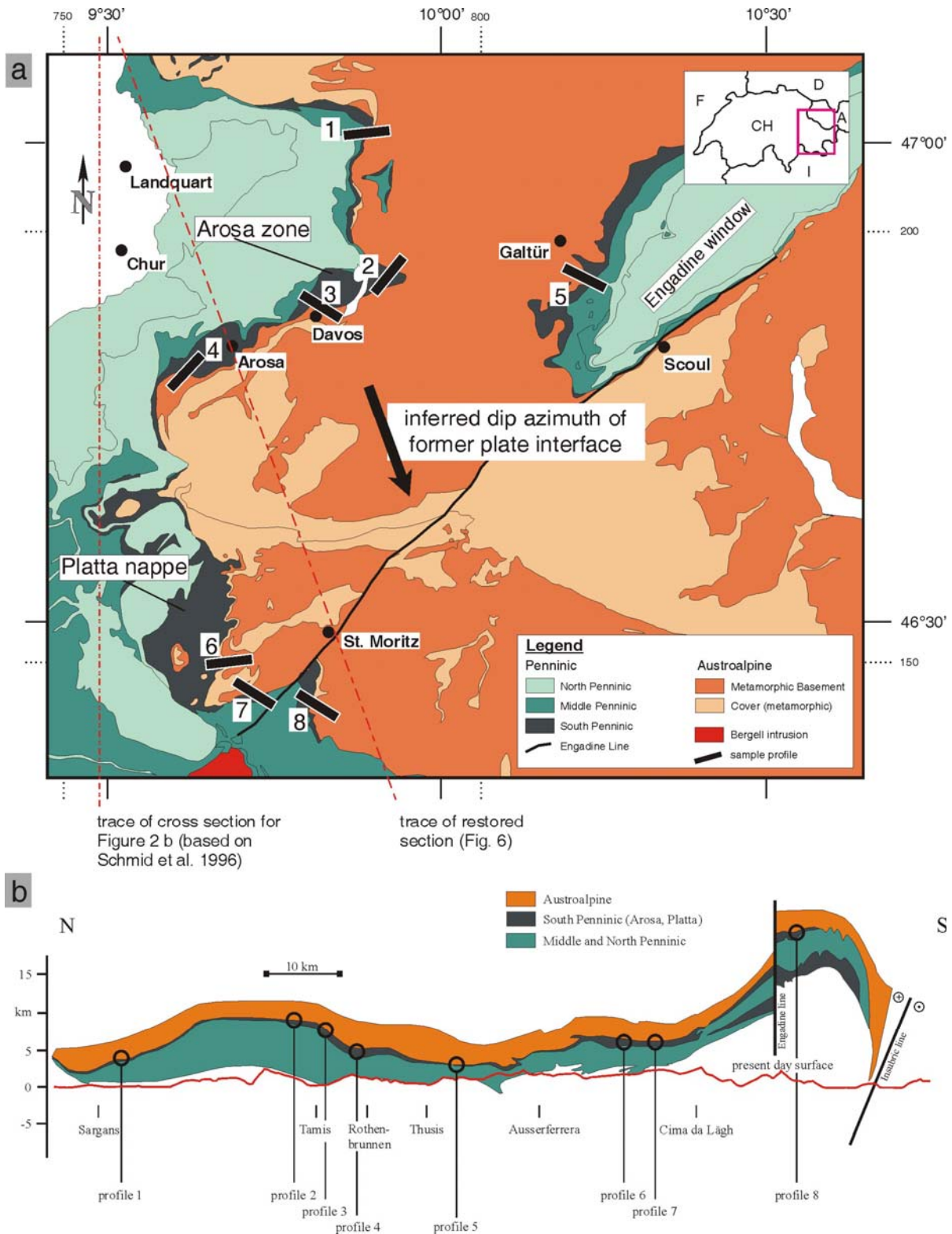


Figure 4.2: a) Tectonic map of the study area emphasizing the boundary zone between the South Penninic (dark green) and the Austroalpine (orange, part of the African plate). Numbers 1 to 8 refer to different profiles extending from domains of South Penninic origin into Austroalpine rocks. Arrow points to the former dip azimuth of the plate interface. Arosa zone and Platta nappe are local names for rocks of South Penninic affinity. Based on the Tectonic map of Switzerland 1:500.000, 2<sup>nd</sup> edition (1980).

b) Schematic profile of the Central Alps based on Schmid et al. (1996). Note the subdivision of the Penninic domain into a North Penninic ocean, Middle Penninic crystalline swell, and a South Penninic ocean.

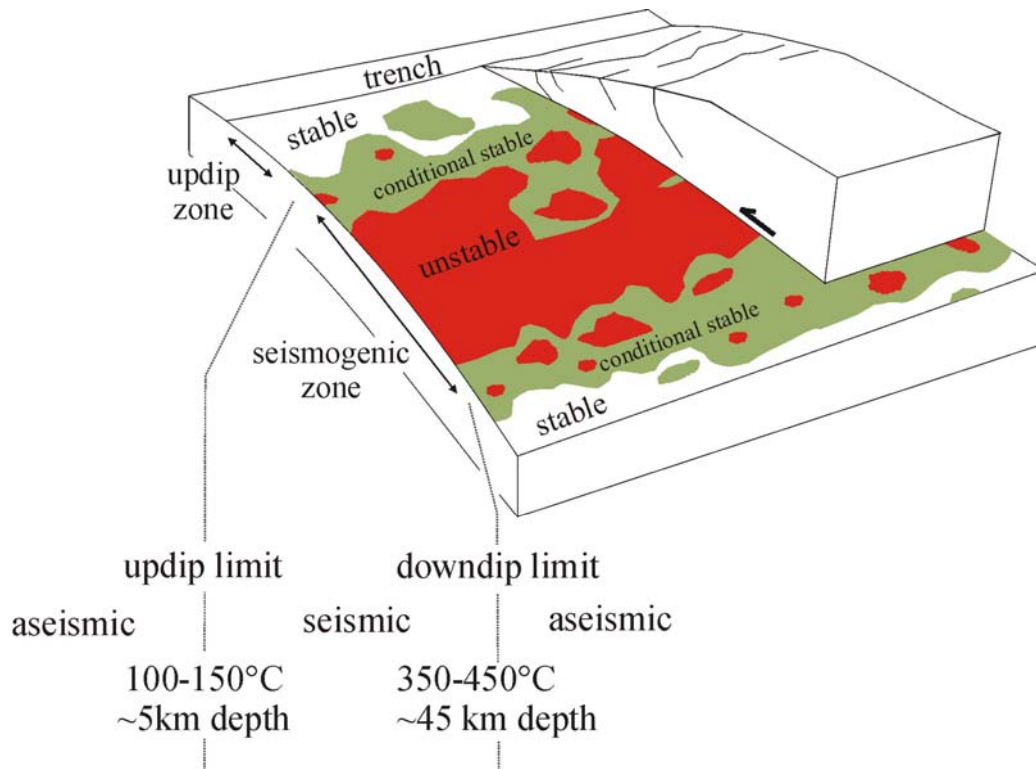


Figure 4.3: Schematic profile of the seismogenic zone of a convergent plate margin. The updip limit of seismogenic coupling (~5 km) is probably caused by consolidation, pressure solution or cementation changing the frictional behavior of the subducted material (Saffer and Marone, 2003). The downdip limit is located at about 45 km, and may be caused by the increasing dominance of ductile behavior (Nedimovic et al., 2003; Oleskevich et al., 1999) or the serpentinization of the forearc mantle (Hyndman et al., 1997; Peacock & Hyndman, 1999). Model of frictional conditions modified and extended downdip following Bilek and Lay (2002) delineating stable areas, conditionally stable and unstable regions. Note, these regions are variable in space and time due to their spatiotemporal-dependent causes (e.g. dehydration reactions). Therefore, no steady state conditions will be achieved along the plate interface zone.

earthquakes. The updip limit of the seismogenic coupling zone may be controlled by one or more of the following factors: dehydration of clay minerals, consolidation, pressure solution, cementation, alignment of sheet silicates, or upper plate geometry (e.g. Saffer and Marone, 2003). The proposed processes take place over a broad range of pressure and temperature conditions. Wang and Hu (2006) therefore state that the updip limit of seismogenic behavior must be a transitional feature. The downdip limit of the seismogenic zone is suggested to be controlled by changes in the geometrical setting of the subduction zone, the onset of viscous behavior of the deforming material (Oleskevich et al., 1999), or stable shearing

of serpentinized forearc mantle (Peacock and Hyndman, 1999).

#### 4.2.2. Mechanical concepts for coseismic and interseismic deformation

Scholz (1998) described different stability regimes along the plate interface (Fig. 4.3): a stable, an unstable, and a conditional stable regime. The stable regime exhibits velocity strengthening behavior, the unstable regime velocity weakening. Conditional stability defines a region, which exhibits a stable regime under quasistatic conditions. These patches are thought to be variable in space and time (Schwartz and Rokosky, 2007, and

references therein). According to Bilek and Lay (1998, 1999) seismic slip cannot be supported in the stable zone. There, elastic strain is relaxed by aseismic creep (Fig. 4.3). Earthquakes are only able to nucleate within unstable regions, but they can propagate into conditionally stable areas (Scholz, 1998; Moore and Saffer, 2001). The distribution of stable, unstable and conditional stable regions may be heterogeneous both downdip and along strike the plate interface producing islands of locked asperities embedded in weaker sedimentary material (Fig. 4.3) due to the heterogeneous character of subducted material, and the continuously occurring processes along the plate interface (e.g. cementation, dehydration).

Repeated thrust earthquakes as a result of a stick-slip frictional instability (Scholz, 1998; Moore and Saffer, 2001) require recovering after any slip event to compensate the coseismic strength drop and allow renewed accumulation of elastic strain. Fault healing by mineral precipitation, compaction, and fluid expulsion is usually invoked as the key process (e.g. Moore and Saffer, 2001).

Downward transported sediments strongly influence the physical properties of the plate interface, because they are less rigid than the rest of the subducting plate. Diverse sediment input in space and over geological times will lead to spatiotemporal modifications of the physical properties along the plate interface (i.e. frictional regimes). Bilek and Lay (1998, 1999) assumed that subducted sediments increase in rigidity and frictional resistance due to compaction, and are therefore responsible for unstable slip, and for the decrease of source durations in earthquake rupturing. Scholz (1998) reported a velocity strengthening behavior for less consolidated sediments, possibly promoting areas of stable sliding (Fig. 4.3). Compaction and phase transitions within both sediments and the subducting slab

lead to dewatering and dehydration, providing fluids to the plate interface system. This water release increases the pore pressure, and therefore reduces normal stress and effective friction increasing the probability of fracture formation. Further down the plate interface loss of fluids increases the strength of the sediments. The replacement of clay minerals by zeolite or quartz enforces velocity weakening due to the velocity weakening behavior of low-porosity rocks and framework silicates (Moore and Saffer, 2001), thus increasing the probability of earthquakes. Whether this change is abrupt or gradual is mostly defined by the general permeability along the plate interface.

### 4.3. Geological setting

#### 4.3.1. *Alpine Evolution*

The European Alps resulted from the collision of the European and the Adriatic continental plates and southeastward to southward subduction and accretion of the intervening Penninic oceanic domain. The oceanic units sandwiched between both continental plates were partly accreted to the base of the overriding continental Adriatic margin (Figs. 4.1, 4.2) (Bousquet et al., 1998). The Penninic domain consists of two oceanic basins related to the Alpine Tethys (North Penninic Valais basin and South Penninic ocean), divided by the so-called Briançonnais continental swell (Middle Penninic) (Fig. 4.2) (e.g. Florineth and Froitzheim, 1994, and references therein). These units were successively subducted and accreted to the Austroalpine domain (Adriatic plate) since the Late Cretaceous until the final collision of the Adriatic plate with the European plate during the Middle Tertiary.

Most models differentiate two phases of subduction during Alpine orogeny:

Cretaceous subduction is defined by an east to southeast dipping subduction zone (e.g. Bousquet et al., 1998; Pfiffner et al., 2000), and associated top-W, locally top-SW and top-NW thrusting (Froitzheim et al., 1994; Handy, 1996). The direction of convergence changed to north – south during the Tertiary with top-N thrusting (Froitzheim et al., 1994; Handy, 1996). According to Ring (1989) structures of top-N thrusting should be more pronounced towards structurally deeper levels of the Penninic domain. The shift between E/SE- to S-directed subduction is associated with NW-SE directed extension, top-SE shearing and normal faulting during the Late Cretaceous affecting the upper plate and partly the structural higher levels of the Penninic domain. This may locally overprint older structures (folds and faults), and reactivate preexisting fault planes (Silvretta basal thrust) of the preceding top-W directed stage of thrusting (Froitzheim et al., 1994). Comparing with recently active convergent plate margins, both orogenic stages can be seen to be the consequence of continuous oblique subduction and accretion of the Penninic domain underneath the Adriatic plate with migration of deformation towards the foreland, which culminated in the collision with the European margin.

#### 4.3.2. *Geology of the working area*

The working area is located along the transition from the Western to the Eastern Alps (Figs. 4.1, 4.2). The main geological units are represented by the Penninic and Austroalpine domain. In the working area remnants of the South Penninic ocean are represented by the Arosa zone (northern area, Fig. 4.2) and Platta nappe (southern area, Fig. 4.2). The upper plate (Adriatic plate) consists of the Austroalpine nappe stack including the Silvretta, Ötztal, Julier and Err-Bernina nappes, all of them built from continental basement covered by Permo-Mesozoic sediments. The boundary

between the South Penninic domain and the Austroalpine is commonly interpreted as a Late Cretaceous suture (e.g. Handy, 1996).

The Arosa and Platta nappes form a *mélange* zone of intensely deformed oceanic and continental material (Deutsch, 1983; Ring et al., 1988; and references therein; we treat “*mélange*” as a scale- and origin-independent descriptive term for an internally fragmented complex that contains blocks of various origin in a sheared matrix; see Ring et al. (1990) and Cowan (1985)), suggesting that the plate interface is a broad deformation zone rather than a discrete suture. The *mélange* is mainly composed of Jurassic ophiolites, radiolarian chert, pelagic limestone, shale and sandstone (Ring et al., 1988). Competent blocks of Austroalpine and Penninic affinity are embedded in the incompetent shaly or serpentized matrix (Ring et al., 1990). The large-scale structures of the Arosa zone are construed by e.g. Ring et al. (1988, 1989, 1990) as the deep parts of an accretionary wedge formed at the tip of and below a thrust belt migrating towards the west.

#### 4.3.3. *Age constraints and metamorphism*

Subduction of the ophiolites from the South Penninic ocean, originally formed during the Jurassic (200 Ma to 180 Ma, Ring, 1989;  $163.5 \pm 1.8$  Ma and  $164.0 \pm 2.7$  Ma, Gebauer, 1999), initiated at around 120 Ma to 100 Ma (Fig. 4.4, Handy and Oberhänsli, 2004, and references therein). Flysch deposits found in the Arosa and Platta nappes show ages ranging from Aptian to Cenomanian (late Early Cretaceous to early Late Cretaceous; Ring, 1989, and references therein). No younger sediments are recorded within the South Penninic domain. The rocks composing the footwall of the South Penninic domain are formed by flysch deposits derived from

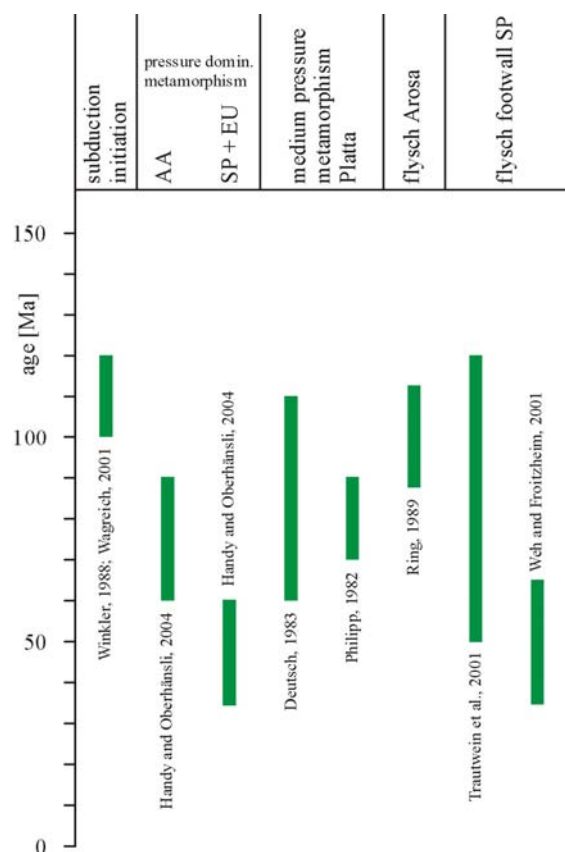


Figure 4.4: Compilation of geochronological data available for the study area concerning the subduction and accretion of the South Penninic domain (SP), deformation within the Austroalpine nappe stack (AA), and flysch deposition within the South Penninic domain and its footwall. EU = European plate.

Middle and North Penninic units, and from the distal European margin (e.g. Rhenodanubian flysch). Biostratigraphic evidence from these flysch deposits yields an Early Cretaceous to early/ middle Eocene age (Trautwein et al., 2001) (Fig. 4.4). In addition, Weh and Froitzeim (2001) reported that the youngest sediments in the footwall of the Arosa zone are Paleocene to possible Eocene in the Middle Penninic Falknis nappe. Hence, subduction-related deformation along the boundary zone between the South Penninic and Austroalpine nappes lasted at least until the Late Cretaceous (end of sedimentation signaling passage through the trench area) to the early/ middle Eocene (where latest sedimentation occurred within the flysch accreted at the

base of the South Penninic units), roughly between 89 Ma to 50 Ma. The northwestward younging of flysch deposition is consistent with a migration of subduction-related accretion towards the northwest (e.g. Handy and Oberhänsli, 2004; and references therein). The general time scheme is also supported by isotopic ages showing 90 Ma to 60 Ma for pressure-dominated metamorphism of the Lower Austroalpine units, and 60 Ma to 35 Ma for the South Penninic and European units, respectively (Handy and Oberhänsli, 2004; and references therein) (Fig. 4.4). Constraints for the timing of pseudotachylyte formation along the fossil plate interface immediately above the base of the Austroalpine nappe stack are given by Thöni (1988). He presented Rb/Sr data from pseudotachylytes collected along the northwestern part of the Engadine window (close to profile 5, Fig. 4.2), which resulted in ages of approximately 75 Ma.

Metamorphic conditions of South Penninic rocks range from upper diagenetic or lowermost greenschist facies in the north of the working area, to middle to upper greenschist facies in the southern parts (Fig. 4.1). A compilation of published geothermobarometric data is given in Table 1. Metamorphic isogrades for the above time span generally trend WSW-ENE in the Central Alps (Frey and Ferreiro Mählmann, 1999; Handy and Oberhänsli, 2004) (Fig. 4.1) providing a crude indication for the trend of the former Adriatic plate margin.

#### 4.4. Methods

We measured foliation, lineation, shear bands, tension gashes, folds, faults, their density, geometric proportions, and their relative age relationships at a series of 8 selected profiles from north to south (Figs. 4.2, 4.5). We additionally used structural data published by numerous authors (e.g. Froitzeim et al., 1994; Ring, 1989). We

Table 1. Compilation of database for section restoration.

distance from corrected trench tip [km]	location	method	comments	R <sub>max</sub> [%]	Si p.f.u.	T [°C]	P [kbar]	P <sub>corr.</sub> [kbar]	converted depth [km]	references
56.8	southern termination of Wägitaler flysch	vitrinite reflectance (effective maturation time 20 Ma)	data converted to depth using different geothermal gradients	1.8		180			7.2 - 12.0	Ferreiro Mähimann 1994
58	south of Bargella	vitrinite reflectance (effective maturation time 20 Ma)	data converted to depth using different geothermal gradients	2.1		190			7.6 - 12.7	Ferreiro Mähimann 1994
60.9	close to Steg	vitrinite reflectance (effective maturation time 20 Ma)	data converted to depth using different geothermal gradients	2.7		225			9.0 - 15.0	Ferreiro Mähimann 1994
65.2	Profile 1	vitrinite reflectance (effective maturation time 20 Ma)	data converted to depth using different geothermal gradients	2.9		230			9.2 - 15.3	Ferreiro Mähimann 1994
65.2	Profile 1	temperature dependent deformation observed at different minerals	pressure solution in carbonates, brittle deformed			150			6.0 - 10.0	
80.5	between profiles 1 and 2	fluid inclusion data	qtz				2.3 - 4.2		8.7 - 15.9	Ring et al. 1989
93.3	Profile 3	vitrinite reflectance (effective maturation time 20 Ma)	data converted to depth using different geothermal gradients	3.2		236			9.4 - 15.4	Ferreiro Mähimann 1994
97	between profiles 3 and 4	illite crystallinity				300 - 350			12.0 - 23.3	Ring 1989
97	between profiles 3 and 4	fluid inclusion data					2.5 - 5.2		9.5 - 19.7	Ring et al. 1989
98.2	Profile 4	vitrinite reflectance (effective maturation time 20 Ma)	data converted to depth using different geothermal gradients	3.9		240			9.6 - 16.0	Ferreiro Mähimann 1994
113.6	close to Tiefencastel	vitrinite reflectance (effective maturation time 20 Ma)	data converted to depth using different geothermal gradients	4.3		245			9.8 - 16.3	Ferreiro Mähimann 1994
114	south of profile 4	illite crystallinity, vitrinite reflectance					2.0 - 4.0		7.6 - 15.1	Frey and Ferreiro Mähimann 1999
125.2	Profile 5	vitrinite reflectance (effective maturation time 20 Ma)	data converted to depth using different geothermal gradients	4.5 - 5.0		247 - 249			9.9 - 16.6	Ferreiro Mähimann 1994
137.8	Profile 6	vitrinite reflectance (effective maturation time 20 Ma)	data converted to depth using different geothermal gradients	5.0 - 5.5		249 - 255			10.0 - 17.0	Ferreiro Mähimann 1994
137.8	Profile 6	chlorite thermometry				308 - 325			12.3 - 21.7	Ferreiro Mähimann 2001
137.8	Profile 6	Si content in phengite	minimum pressure	3.32			3.5 - 6.0		13.2 - 22.7	Ferreiro Mähimann 2001
163.8	Profile 8	temperature dependent deformation observed at different minerals	calcmylonites, intracrystalline deformation of quartz, brittle deformed feldspar			350 - 450			14.0 - 30.0	
163.8	Profile 8	greenschist facies assemblage				300 - 350			12.0 - 23.3	Handy et al. 1996
163.8	Profile 8	Si content in phengite	minimum pressure, recalibrated after Massonne and Szpurka 1997	3.41			8.0 - 9.0	5.0	18.9	Handy et al. 1996

estimated pressure conditions of samples from both the base of the Austroalpine nappe stack and the South Penninic domain in order to restore former plate geometry and the position of the individual profiles. Data for the Austroalpine basement rocks are only useful for our study, where the overprint of the pre-Alpine mineral assemblage is almost complete. This is the case for profiles 6, 7 and 8 (see Chapter 4.5.1.). We make use of the Si-content of phengite due to the Tschermak's substitution with the graphical solution provided by Massonne and Szpurka (1997).

Table 2. Microprobe analyses of phengite of different samples.

sample	B-4	C-15	C-12	B-8	B-13	B-32
Profile	6	7	7	8	8	8
analyses (n)	24	8	4	11	5	22
mineral	phg	phg	phg	phg	phg	phg
SiO <sub>2</sub>	50.12	49.24	51.20	51.26	50.17	47.70
TiO <sub>2</sub>	0.19	0.17	0.06	0.11	0.38	0.13
Al <sub>2</sub> O <sub>3</sub>	25.85	29.78	28.39	25.95	24.81	31.73
MgO	2.37	2.20	3.25	3.18	3.14	2.21
CaO	0.01	0.00	0.01	0.01	0.01	0.07
MnO	0.05	0.04	0.03	0.04	0.03	0.01
FeO	5.14	4.51	3.95	3.88	5.30	2.16
Na <sub>2</sub> O	0.08	0.34	0.15	0.00	0.05	0.29
K <sub>2</sub> O	10.97	9.80	10.77	10.23	10.91	9.51
Total	94.77	96.08	97.81	94.64	94.79	93.80
Formula proportions						
Si	3.421	3.282	3.355	3.457	3.430	3.215
Al <sup>IV</sup>	0.579	0.718	0.645	0.543	0.570	0.785
[Z]	4.000	4.000	4.000	4.000	4.000	4.000
Al <sup>VI</sup>	1.500	1.621	1.547	1.519	1.428	1.735
Ti	0.009	0.009	0.003	0.005	0.019	0.006
Fe <sup>2+</sup>	0.293	0.251	0.216	0.219	0.303	0.122
Mn	0.003	0.002	0.002	0.002	0.002	0.001
Mg	0.241	0.219	0.317	0.320	0.320	0.221
[Y]	2.046	2.102	2.086	2.066	2.072	2.086
Ca	0.001	0.000	0.001	0.000	0.000	0.005
Na	0.011	0.044	0.019	0.000	0.007	0.038
K	0.955	0.833	0.900	0.881	0.952	0.817
[X]	0.966	0.877	0.920	0.881	0.959	0.860
Cat. Charge	22.000	22.000	22.000	22.000	22.000	22.000
Mg#	0.451	0.47	0.59	0.595	0.514	0.647
X <sub>Fe</sub>	0.882	0.90	0.85	0.844	0.844	0.894
X <sub>Mg</sub>	0.118	0.10	0.15	0.155	0.154	0.106

Due to the absence of critical mineral assemblages for which this geobarometer was calibrated (K-feldspar + phlogopite + quartz, quartz + garnet + kyanite, talc + kyanite + quartz), this method only yields minimum pressure conditions. One sample from profile 6, two samples from profile 7,

and three samples from profile 8 were selected for electron microprobe analyses. Mineral analyses were performed using a CAMECA SX100 electron microprobe operating in the wavelength-dispersive mode. Major and minor elements were determined at 15 kV acceleration voltage and a beam current of 20 nA with counting times of 20 s for major elements, and 30 s for minor elements. The beam diameter used for the mineral analyses was 5 µm for all mineral except for plagioclase, where we used 10 µm in order to suppress sodium diffusion. The standard sets of the Smithsonian Institute (cf. Jarosewich et al., 1980) and of MAC<sup>TM</sup> were used for reference. Table 2 lists samples, and the results of analyses. Mineral abbreviation in the text and Tables follow Kretz (1983). Field images were processed with the image-processing software Scion Image for fabric quantification. Afterwards, the software automatically outlined, counted and measured the individual clasts yielding their major and minor axes, and the clast size.

## 4.5. Observations and results

### 4.5.1. Structural data

Rocks of the Arosa zone and Platta nappe close to the contact to the hanging wall Austroalpine nappes (at least in the first few hundred meters) suffered a penetrative deformation with an inferred direction of tectonic transport changing gradually from top-NW in the north of the working area to top-SW in the southernmost parts (Fig. 4.5). Foliation planes dip moderately toward SE to NE and associated stretching lineations plunge smoothly toward SE and ENE, respectively. These structures are best developed in the south of the working area. Embedded clasts within the metasedimentary matrix of the South Penninic domain are partly bounded by

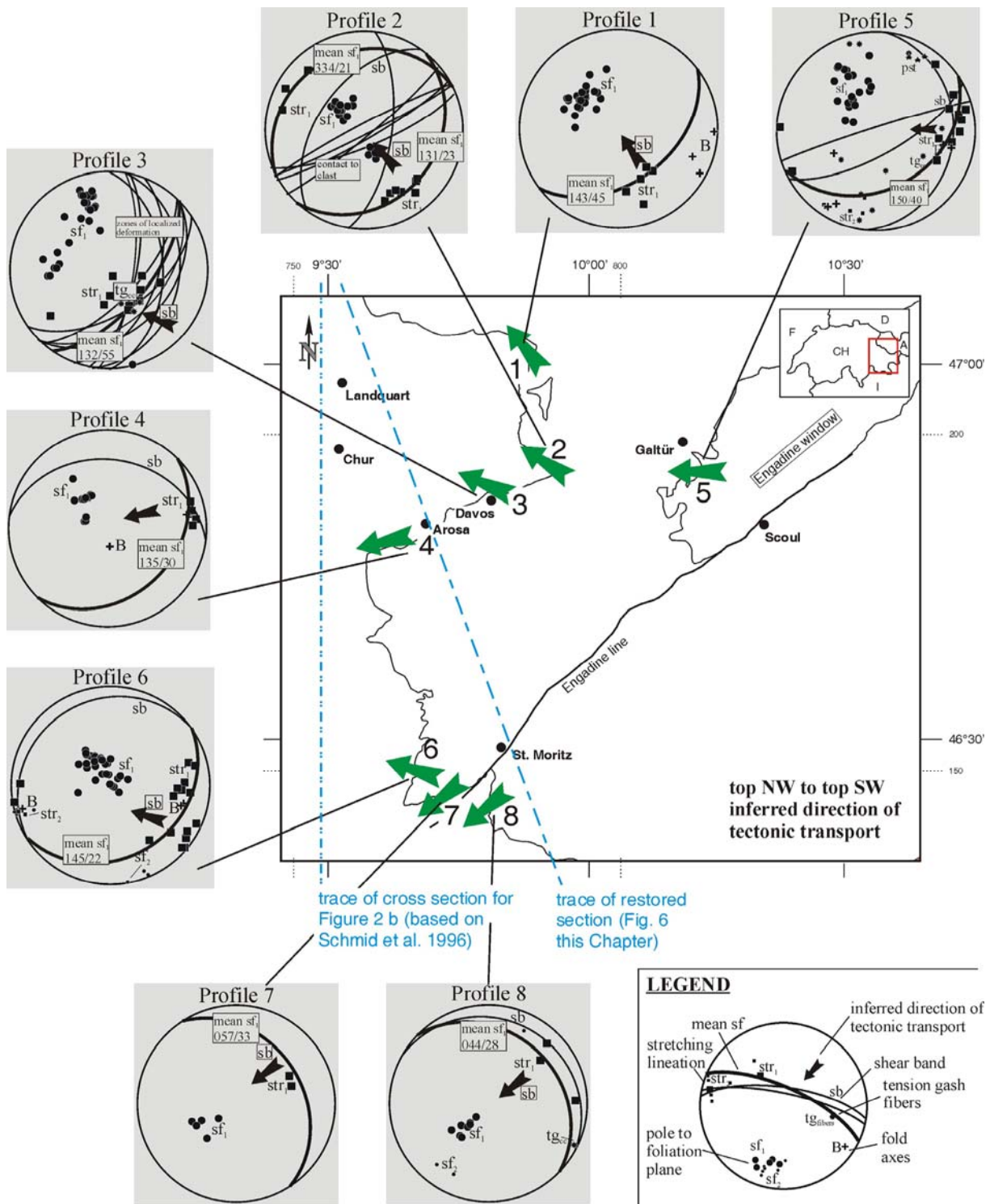


Figure 4.5: Structural data of brittle-ductile to ductile deformation associated with pervasive fabric showing top-NW to top-SW direction of tectonic transport (generally top-W). All plots are Schmidt net lower hemisphere, equal-area diagrams. Due to similarity of structural data along each profile, diagrams are a combination of several outcrops at every profile.

shear zones, which consistently show a general top-W directed tectonic transport.

Deformation with general top-W directed tectonic transport of the Austroalpine basement (upper plate) in the northern part of the study area is expressed by microscale fracture zones reactivating the preexisting foliation of probably Variscan age. This Alpine overprint increases towards the south. At profiles 6, 7 and 8 Alpine deformation pervasively overprints the preexisting foliation within the upper plate basement close to the boundary zone to the South Penninic domain. There, growth and recrystallization of sheet silicates (mainly white mica) occurred parallel to the preexisting foliation. Orientation of foliation in the Austroalpine rocks parallels its corresponding foliation within the South Penninic domain, at least in the first few hundred meters above the base of the hanging wall, and both consistently parallel the base of the Austroalpine nappe stack. Deformation of the South Penninic domain increases towards the south of the working area as expressed by a more distinct foliation with a narrower spacing, and the progressive obliteration of sedimentary structures.

Structures indicating the general top-W tectonic transport are overprinted by subsequent deformation with significantly lower intensity. It is localized in distinct bands or sometimes present as a spaced cleavage (see also Ring, 1989; Dürr, 1992). We also observed brittle-ductile shear bands with top-E to top-SE directed tectonic transport, which are more pronounced towards the south, and seem to reactivate the preexisting top-W structures. These structures are again overprinted by top-N thrusting, which can be inferred from roughly E-W orientated fold axes of open folds at various scales, folding the above older structures. Steeply dipping strike-slip faults (dextral E-W trending faults with offsets of up to 500m, sinistral N-S trending faults with offsets less than

100m) represent the late stage of brittle deformation affecting the whole working area (Ring, 1989).

#### 4.5.2 Geobarometry and temperature estimates

Analyses of white mica (phengite) resulted in a Si-content ranging from 3.215 p.f.u. to 3.457 p.f.u. (Table 2) corresponding to minimum pressures around 3 - 4 kbar at profile 6 and profile 7, and 3 - 6 kbar at profile 8, assuming a temperature of 300°C to 350°C (supported by subgrain rotation recrystallization of quartz). Recalibration of the data provided by Handy et al. (1996) using the graphical solution of Massonne and Szpurka (1997) resulted in about 5 kbar minimum pressure for the base of the upper plate at profile 8, which is substantially lower than the minimum pressures of 8 - 9 kbar suggested by Handy et al. (1996). Deformation temperatures are inferred from macroscopic and microscopic observations concerning the deformational behavior of carbonate minerals, quartz and feldspar. They point to a temperature of about 150°C in the north (pressure solution of carbonates, fractured quartz) and 350°C to 400°C in the south of the working area (calcmylonites, subgrain rotation recrystallization in quartz, brittle deformation of feldspar). These results corroborate published data (Ferreiro Mählmann, 2001; Frey and Ferreiro Mählmann, 1999; Handy et al., 1996; Handy and Oberhänsli, 2004; Ring, 1989; Ring et al., 1989) (Table 1).

#### 4.6. Restoration of the fossil plate interface

In order to relocate plate interface features to their former position along the plate interface we projected the investigated profiles into a composite synthetic section perpendicular to the strike of the former

subduction zone. This restoration is based on the N-S section provided by Schmid et al. (1996), redrawn after the NFP-20-East seismic traverse covering the main geological and tectonical units in the working area (Fig. 4.2b). We used the software 2DMove (Midland Valley) for restoration. The fossil strike of the subduction zone is roughly constrained by the above mentioned orientation of the metamorphic isogrades associated with Late Cretaceous to Early Tertiary subduction and accretion of the Penninic domain, which trends WSW-ENE (Fig. 4.1). In addition, the present day general trend of the external Gosau basins that represent Late Cretaceous forearc basins developed on the Northern Calcareous Alps, show the same trend (Fig. 4.1, Sanders and Höfling, 2000; Wagerich and Krenmayr, 2005). According to Wagerich (1995), Wagerich and Decker (2001) and Wagerich and Krenmayr (2005) the Gosau basins represent subsiding slope basins at the front of the upper plate controlled by oblique dextral convergence. In consequence, we assume the downdip azimuth of the former plate interface to be SSE requiring projection of the geological units and profile positions from the N-S section into a new section rotated by 20°. The first step in restoration was the removal of the vertical offset along the Engadine line (Figs. 4.2, 4.6a) using “fault parallel flow” as deformation algorithm. In a second step “line length unfolding” was applied to the folded South Penninic domain, which resulted in two flat lying horizons (Fig. 4.6a).

The minimum distance of the fossil trench north from profile 1 is given by the present day position of the Wägitaler flysch, which represents remnants of the Early Tertiary accretionary prism, accreted to the tip of the wedge and at the base of the South Penninic domain (Tectonic map of Switzerland 1:500.000, 2<sup>nd</sup> edition, 1980). We assume the exposed northern limit of the Wägitaler flysch as the minimum

position of the former trench because of possible erosion of its toe and of possible syncollisional shortening. We extended the restored section adding the distance between the northern end of the South Penninic domain in Fig. 4.2 and the northern limit of the Wägitaler flysch (Fig. 4.6a).

The dip of the ancient plate interface zone (i.e. the megathrust) is reconstructed from depth conversion of all geobarometric data using a mean density of 2.7 g/cm<sup>3</sup> (i.e. 1 kbar corresponding to 3.78 km below surface) and plotting them into the restored and rotated section assuming a mean topographic slope of 5° for the outer forearc wedge and 3° for the inner forearc wedge (Fig. 4.6b, Table 1) referring to Wang and Hu (2006). They reported a steeper slope for the outer wedge compared to the slope angle of the inner wedge, and the transition between outer and inner wedge is situated close to the updip limit of seismogenic coupling (approximately 30 – 40 km landward of the trench tip). The assumed slope angles are also comparable to values presented by Clift and Vannucchi (2004), which reported a mean forearc slope of 5° for erosive margins (cf. compilation of global forearc slopes by Moores and Twiss, 1995). Landward of the shelf edge (corresponding to about 200m water depth) we used a topographic slope of 0° in order to reach the shoreline close to the downdip limit of the seismogenic coupling zone (Hyndman et al., 1997). Additionally, depth conversion for all geothermometric data was performed assuming different geothermal gradients. For estimating the geothermal gradient we used heat flow data presented by Grevemeyer et al. (2005) with an average value of 30 mW m<sup>-2</sup> for a region landward of the trench, and a thermal conductivity for granites (1.5 to 2.5 W m<sup>-1</sup> K<sup>-1</sup>) and sediments (1.5 to 5 W m<sup>-1</sup> K<sup>-1</sup>) (Clauser and Huenges, 1995), most likely the components of the fossil convergent plate margin within the study

area. This resulted in an average geothermal gradient of 15 to 25 °C km<sup>-1</sup>.

For additional constraints in estimating the dip of the fossil plate interface we reevaluated vitrinite reflectance data provided by Ferreiro Mählmann (2001). We constructed a subsidence curve assuming approximately 10 km of burial for the mean of the used rock samples, and a time range between 90 Ma and 30 Ma for maturation of the organic material (see also Chapter 4.3.3). This resulted in about 20 Ma effective time of maturation assuming a polynomial interpolation of the used data points. Using this value and the diagram provided by Bostick et al. (1979) the vitrinite reflectance data can be transformed into temperature information, and thus, using again different geothermal gradients, into depth values. Vitrinite reflectance data north of profile 1 point to an Early Tertiary overburden of at least 7 km. Therefore, the previously assumed minimum extent of the accretionary prism using the tip of the Wägitaler flysch was underestimated. In consequence, we shifted the adjusted tip of the fossil accretionary prism further towards the north (Fig. 4.6b).

The former plate interface is constructed by pinning the plate interface at the tip of the former wedge, and extending the plate interface through the mean of the geothermobarometric data. Where geobarometry points to minimum pressure

conditions we plotted the interface below the deepest minimum pressure datapoint. This procedure resulted in a constant slab dip angle of approximately 8° (Fig. 4.6c). Global data for slab dips for the first 100 km from the trench are in a similar order of magnitude (Lallemand et al. 1994; Moores and Twiss, 1995; Clift and Vannucchi, 2004). The resultant distances for each profile relative to the trench are shown in Fig. 4.6c.

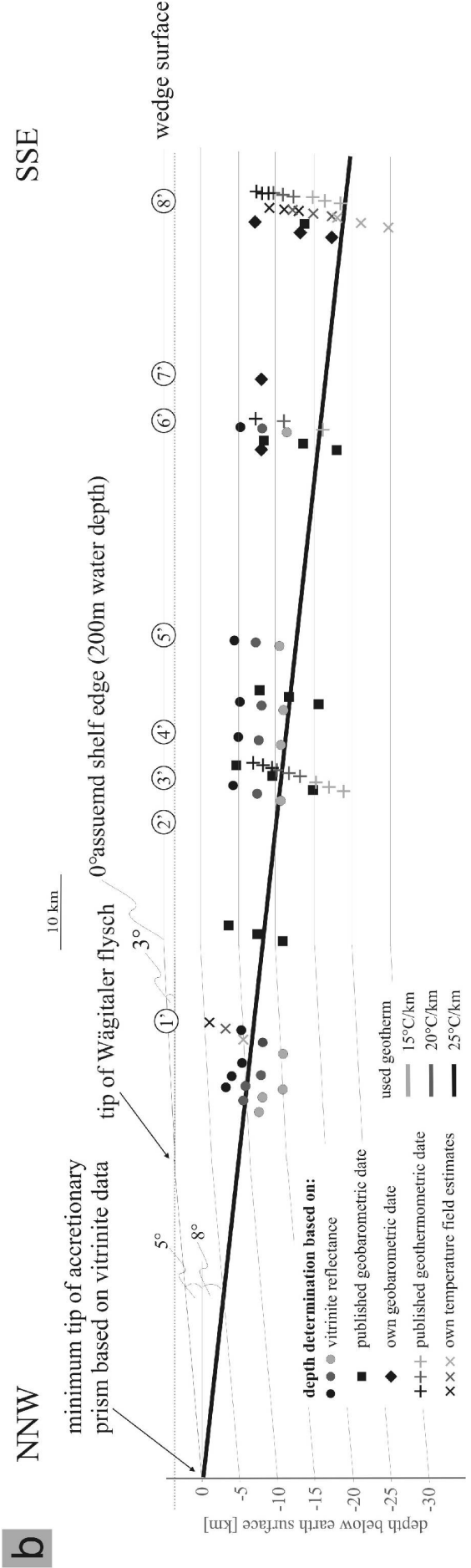
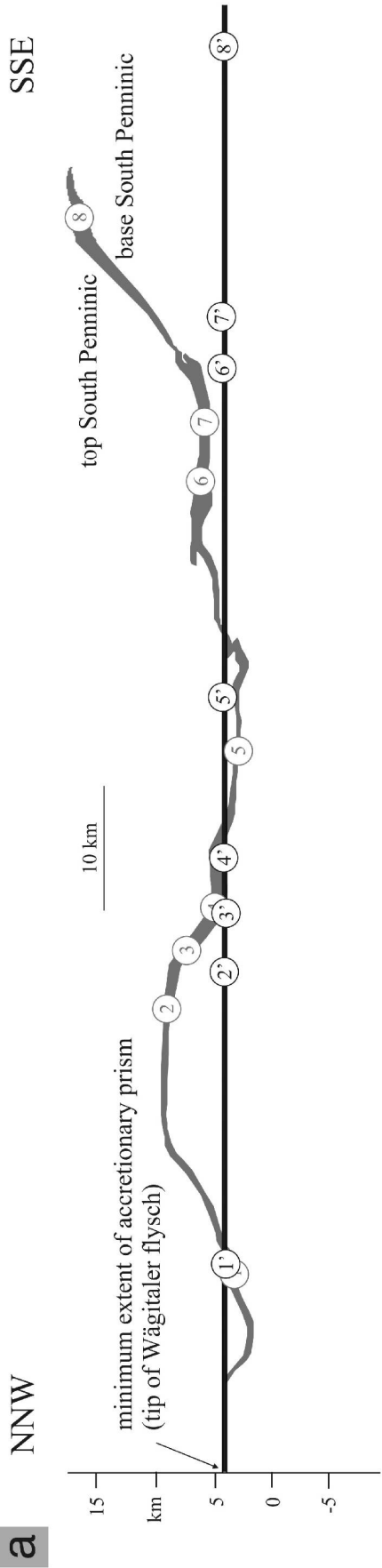
#### 4.7. Spatial variation of characteristics along the fossil plate interface

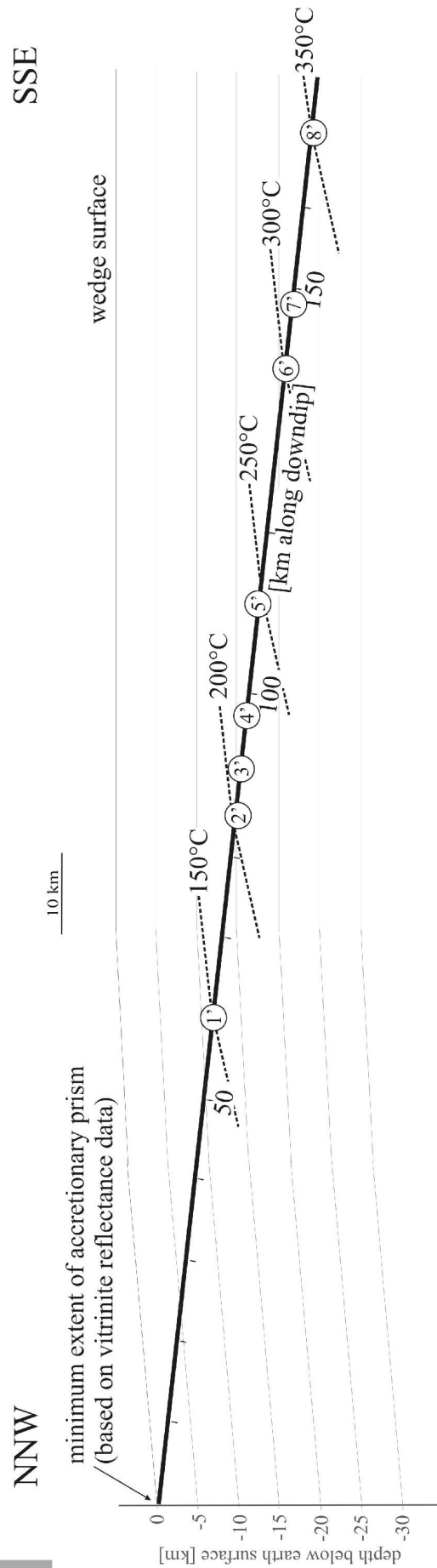
##### 4.7.1. General information

The apparent thickness of the South Penninic mélange varies from a few tens of meters up to more than 2500 m, either reflecting their original thickness after abandoning this shear zone following basal accretion of the mélange or a reduction from subsequent thinning. Within the matrix of shales and serpentinites clasts of more competent material are incorporated, originating either from the Austroalpine upper plate (crystalline basement, its sedimentary cover), or formed by slivers of the lower plate (metagabbros, metabasalts, the sedimentary deposits of the ocean floor, or the trench fill turbidites).

In contrast to the compositional homogeneity in all transects, other features

Figure 4.6: Section restoration using 2DMove (Midland Valley). Green horizon in part (a) shows the restoration of the present day geometry of the fossil plate interface zone after removal of the vertical offset along the Engadine line (Fig. 2b), whereas the black horizon shows the restored South Penninic domain after unfolding. The tip of the Wägitaler flysch (derived from the Tectonic map of Switzerland 1:500.000, 2<sup>nd</sup> edition, 1980) is used as the minimum distance to the tip of the fossil accretionary prism. Part (b) shows the database for reconstructing the dip of the plate interface zone. Depth determination using different geothermal gradients is based on vitrinite reflectance data, published and own geothermobarometric data, as well as field estimates of deformation temperatures. This resulted in a mean dip angle of 8°. Topographic slope is 5° for the outer wedge, 3° for the inner wedge, and 0° for the portion landward of the shelf edge (based on a mean value given by Moores and Twiss, 1995; Clift and Vannucchi, 2004; Wang and Hu, 2006). The minimum extent of the accretionary prism is again shifted towards the NNW in order to fit the vitrinite reflectance data providing an approximation for overburden north of profile 1. Part (c) presents the final restoration of the plate interface for the time window 89 Ma to 50 Ma and the relocated profiles.





Original Figure is DIN A3 and can be obtained from the author.

show a characteristic downdip change (Figs. 4.7, 4.8a-o). This in particular includes the extent of Alpine deformation of the Austroalpine basement close to the contact to the underlying South Penninic *mélange*, the degree of deformation of the South Penninic *mélange* with increasing metamorphism, the quantity and density of localized deformation zones (LDZ), the occurrence of mylonitic textures within the South Penninic *mélange*, the appearance and deformation of embedded clasts, the proportion of pseudotachylytes, as well as the occurrence and quantity of mineralized vein systems.

#### 4.7.2. Deformation

The degree of penetrative deformation within the study area increases downdip, respectively towards the south (Fig. 4.7). The proportion of individual zones of localized deformation (LDZ) per meter increases from profile 1 to profile 8 in the same way (Figs. 4.7, 4.8a, 4.8b). We used distinct surfaces of up to few millimeters width cutting through the outcrops (almost parallel to foliation) as localized deformation zones (LDZ). Sparsely, we observed offsets along the LDZ reaching up to a few cm (Fig. 4.8c). In carbonate-dominated rocks of the South Penninic *mélange* these zones are mainly expressed by pressure solution seams. However, LDZ might possibly evolve into sites of subsequent preferred pressure solution with progressive deformation. We measured the amount of localized deformation zones in outcrops and images using appropriate scale bars. Within the northern profiles (1-4) the number of localized deformation zones (LDZ) per meter measured in outcrops of the South Penninic *mélange* is low (less than 40 LDZ/m, corresponding to 3% of the outcrop). At profile 5 (450 LDZ/m, corresponding to 45 % of the outcrop) and more obviously at profile 7 (880 LDZ/m, corresponding to 88% of the outcrop), the

amount of LDZ within metasedimentary rocks of the South Penninic *mélange* increases drastically (Fig. 4.7). Due to this high amount of LDZ it is difficult to identify individual LDZ at outcrop scale, and we described the outcrops as completely deformed. There, deformation is distributed over the whole outcrop (e.g. at profile 8 amount of LDZ equals 96% of the outcrop). Thus, the increase in amount of LDZ reflects the transition to a distributed deformation towards the south, where especially the metasedimentary matrix of South Penninic origin is intensely sheared (Fig. 4.8b). In addition, LDZ density seems to be lithology dependent. Ultrabasic clasts are characterized by brittle fracturing in the entire working area. Within these rocks we measured less than 20 LDZ/m with no obvious gradient towards the south. The amount of LDZ depends also on the position of the analyzed outcrops relative to the upper plate base. The closer the outcrop to the boundary zone, the higher the total number of LDZ (Fig. 4.9). Even LDZ of the upper plate reflects this behavior in the first tens of meters. Moreover, where the sedimentary cover of the upper plate is in direct contact to the South Penninic *mélange*, it exhibits about tenfold the number of LDZ compared to the crystalline parts of the Austroalpine nappe stack. However, it is still less than the number of LDZ of the South Penninic *mélange* close to the contact to the upper plate (Fig. 4.9).

The volume of rocks with mylonitic textures within the South Penninic *mélange* and the base of the upper plate (related to the Alpine orogeny) increases towards the south. The first appearance can be recognized at profile 6, where rims of carbonatic clasts embedded in the serpentized matrix are mylonitized. In addition, Permian volcanic rocks building the base of the upper plate in parts of profile 6 are intensely deformed close to the contact to the underlying South

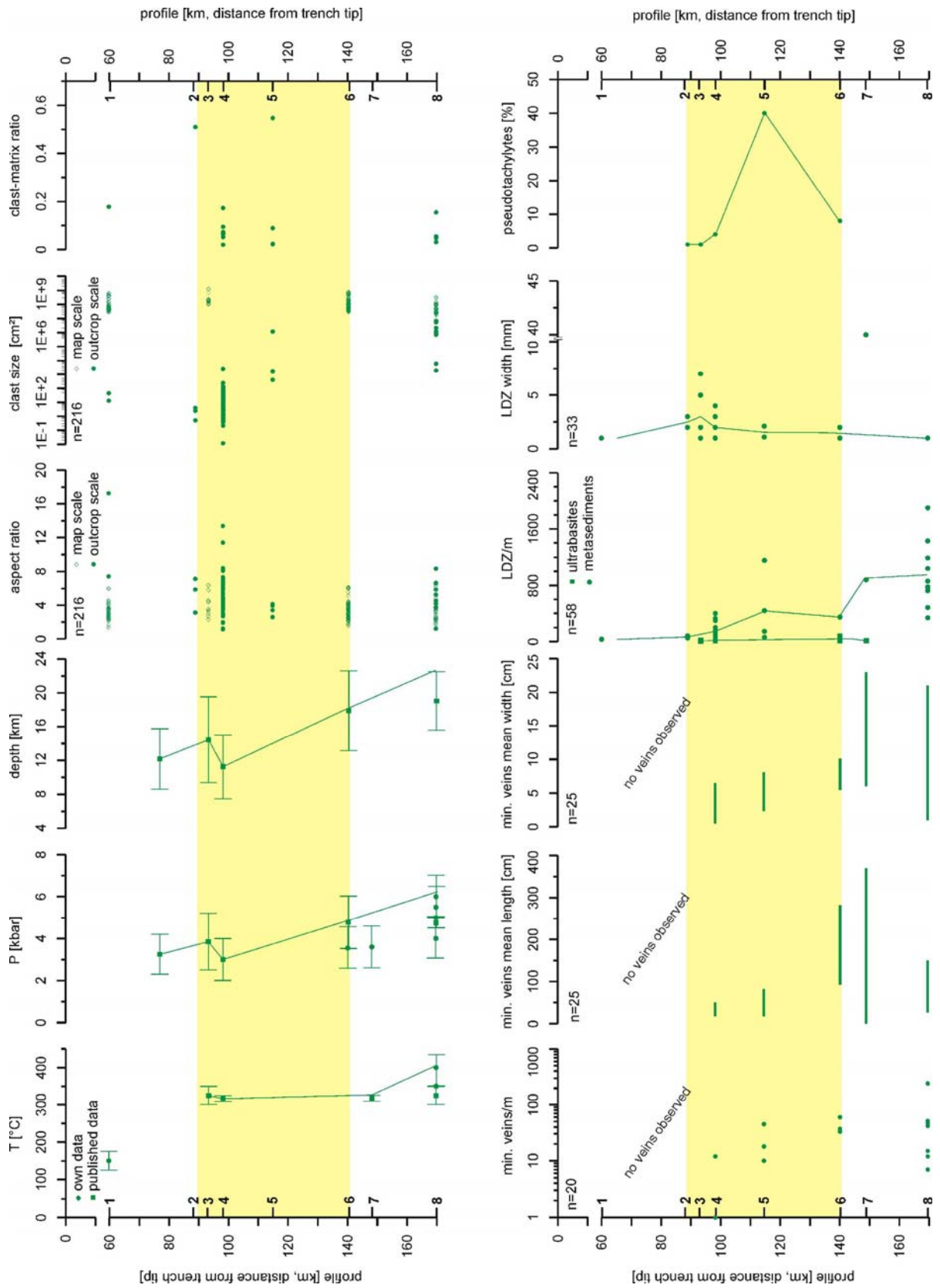


Figure 4.7: Spatial distribution and change of characteristic plate interface zone features. Note, y-axis is corrected using the restored section from Figure 6. Yellow shaded area outlines the extent of the unstable slip region of the fossil seismogenic coupling zone, based on the distribution of pseudotachylytes.



Penninic mélange. At profile 8 also metagabbros as remnants of the South Penninic oceanic crust exhibit mylonitic parts. Limestone layers are deformed to calcmylonites. Crystalplastic deformation of the quartz lattice is dominant towards the south also pointing to activity of slow viscous deformation.

#### 4.7.3. Clasts

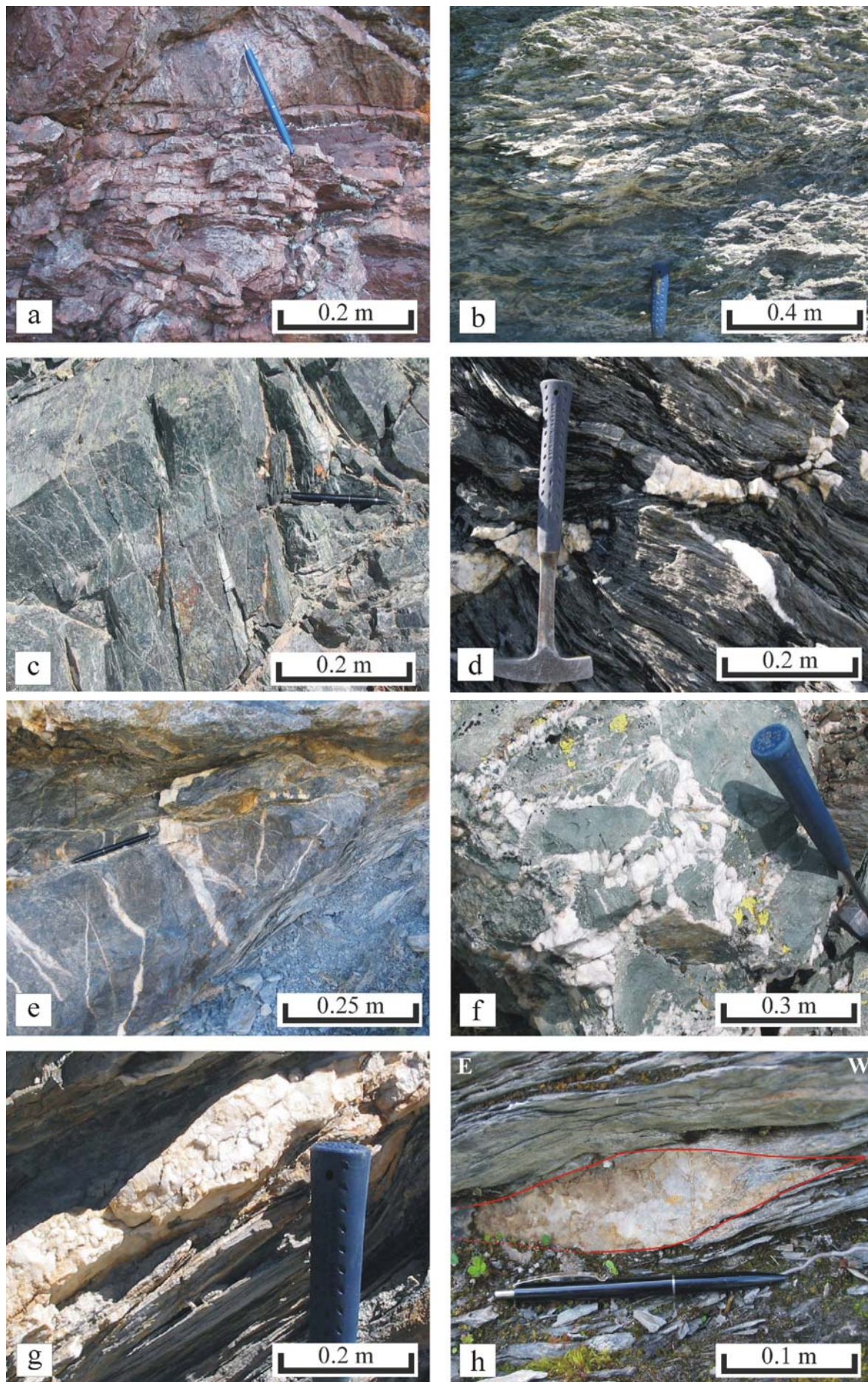
Clast size varies from a few cm up to more than several hundreds of meters (Fig. 4.7). Smaller clasts are nearly completely assimilated into the matrix. Clasts are always oriented with their long axes parallel to the main foliation and their shapes show all transitions between symmetric and asymmetric sigmoidal forms. In general, they mirror the general top-W directed tectonic transport. In order to cover a broad scale of clast sizes we used geological maps presented in Ring et al. (1990) in addition to own outcrop pictures. Note, due to the use of geological maps instead of cross sections, the calculated aspect ratios for map scale clasts represent only minimum values. Aspect ratios for individual clasts are around 5 to 10, which appears to be quite constant for all profiles (Fig. 4.7). There is no obvious contrast between outcrop scale and map scale derived aspect ratios, which indicate that the use of geological maps instead of cross sections is appropriate in our case. The average clast-matrix ratio is about 0.1 and does not change significantly towards the south of the working area (Fig. 4.7). Clast size increases appreciably from the north to the south (Fig. 4.7). The

identification of individual clasts depends strongly on the ratio between clast size and size of the outcrop. In consequence, some clasts are only detectable at map scale. Particularly in the northern part of the working area the identification of individual clasts is problematic. There, outcrops of metasediments or upper plate basement seem to be mega-clasts embedded in a shaly matrix, whereas their boundaries are often not detectable.

Individual layers of sandstone or more pristine carbonates from the sediment pile of the South Penninic ocean are affected by extensional cracking in the north of the working area. With increasing deformation and metamorphism towards the south these layers start to boudinage and progressively separate. Clasts, which are affected by cataclastic deformation in the northern part of the working area, are progressively mylonitized along their rims towards the south. In addition, invading mylonitic shear fractures enforce their disintegration.

#### 4.7.4. Pseudotachylytes

Pseudotachylytes are considered evidence of fossil earthquakes (e.g. Cowan, 1999). These melt veins are formed by frictional heating, preferentially in dry, low porosity rocks, and incorporate angular to subrounded clasts of the wall rock (Sibson, 1975; Spray, 1992). Within the working area pseudotachylytes are present at several localities along the composite N-S section, but are so far found exclusively in the basal section of the crystalline basement of the Austroalpine upper plate (found from the base to a distance of 300m above the base). In addition, we never recognized pseudotachylytes within metasedimentary rocks of the South Penninic mélange, neither in the matrix nor in the clasts. Pseudotachylytes range from mm to several dm in width, and form layers, networks or the matrix of breccia zones (Fig. 4.8i). We determined the



DOI: 10.2312/GFZ.b103-08012

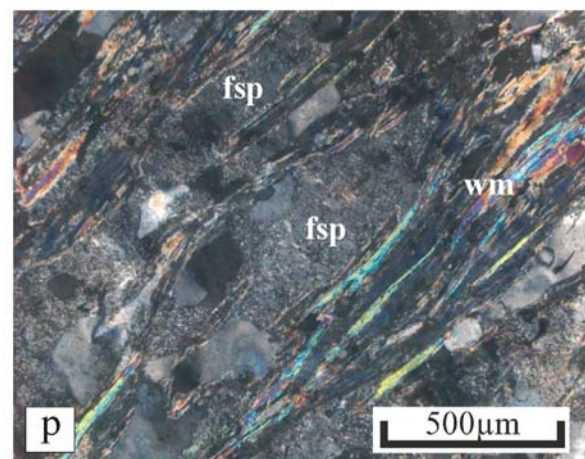
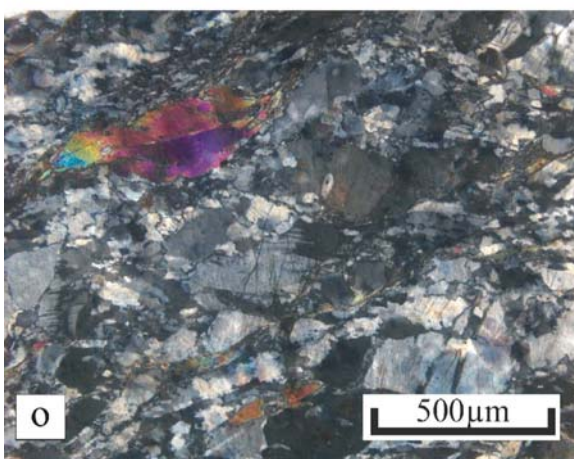
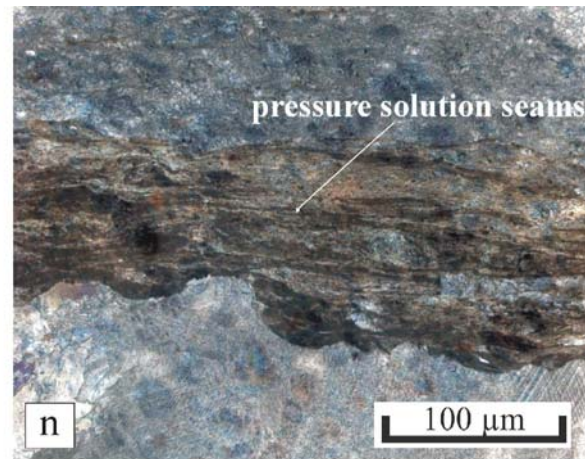
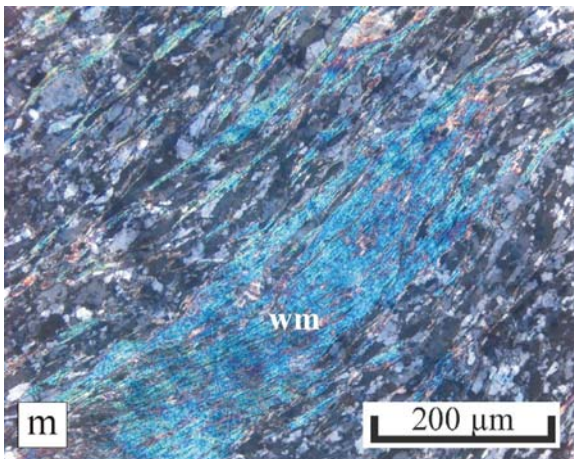
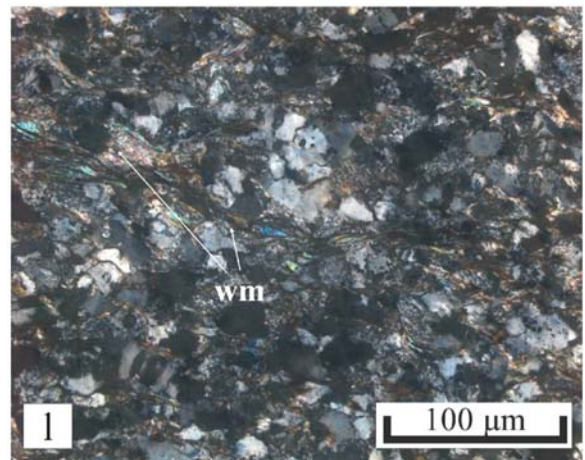
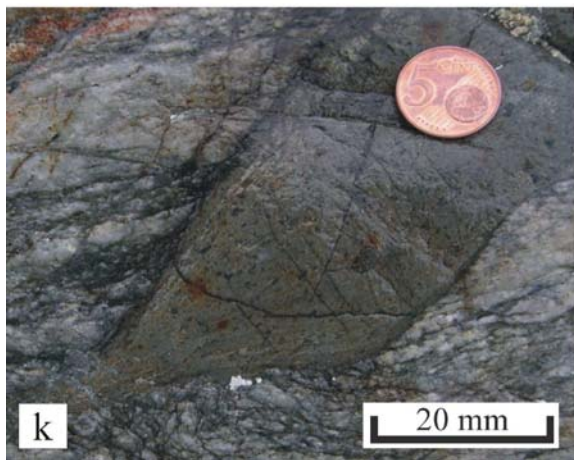
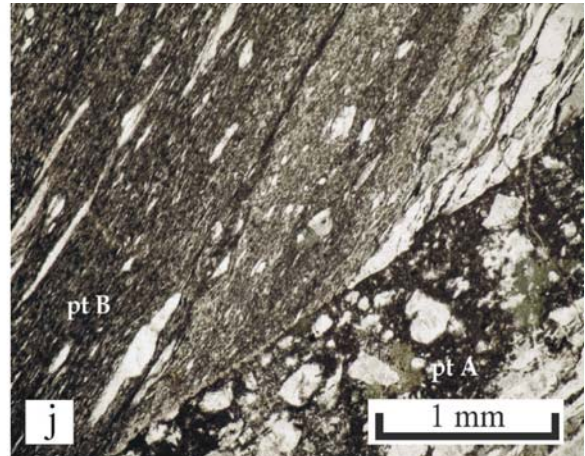
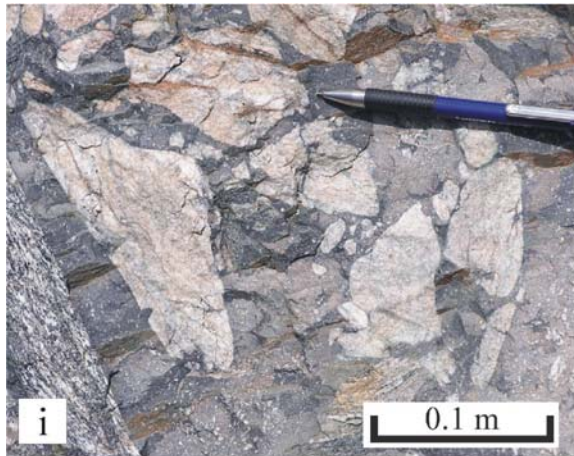


Figure 4.8: Outcrop and thin section images illustrating the change of characteristic features with depth: (a) localized deformation zones (LDZ) in the north of the working area (profile 1), (b) increase in LDZ and distributed deformation over the whole outcrop scale towards the south (profile 6), (c) offset along LDZ in the range of a few cm, (d) mineralized vein subparallel to the foliation and mineralized vein branching off from the main vein, cross-cutting the foliation in a high angle, (e) mineralized vein cutting into competent clast almost perpendicular to its rim, (f) incorporated wall rock fragment within mineralized vein exhibiting a similar texture as pseudotachylytes, (g) mineralized vein running parallel to the foliation and opening into small lentoid fractures, (h) mineralized vein with lentoid shape pointing to top-W hanging wall displacement due to its sigmoidal shape, (i) pseudotachylyte as evidence for unstable slip with incorporated wall rock fragments, (j) mylonitized pseudotachylyte (pt B) cut by a undeformed pseudotachylyte (pt A) pointing to mutual crosscutting relationship between seismic and aseismic deformation, (k) outcrop image of mylonitized pseudotachylyte (alignment of elongated embedded fragments), (l) meta-sandstone with incipient alignment of small white mica and initial formation of foliation (northern part of working area), (m) qtz-mica schist with large white mica aligned within the foliation (southern part of working area), (n) thin section showing pressure solution within deformed limestone, (o) less altered upper plate basement (northern part), and (p) heavily altered upper plate basement (sericitized feldspar with alignment of reaction products) indicating percolating fluids and hydration (southern part).

amount of pseudotachylytes by assessing their relative abundance at outcrop scale (Fig. 4.7). Pseudotachylyte occurrence culminates at profile 5 along the northwestern part of the Engadine window, where partly up to 40% of the outcrops are formed by these melt veins (Fig. 4.7; see also Koch und Masch, 1992; Schmutz, 1995). No pseudotachylytes are found further south than profile 6. At profile 5 we observed an overprint of pseudotachylytes by ductile deformation, maybe promoted by the small grain size of the recrystallized pseudotachylytes favoring viscous grain-size sensitive deformation mechanisms (grain boundary sliding) (Figs. 4.8j, k). In addition, there is a mutual crosscutting relationship between undeformed pseudotachylytes and mylonitized pseudotachylytes (Fig. 4.8j). The wall rock hosting the pseudotachylytes (Austroalpine basement) does not exhibit an Alpine mylonitic overprint. Mylonitic deformation is rather assigned to the higher grade amphibolite facies metamorphism during Variscian orogeny (due to the mineral composition of the mylonitic rocks) (Schmutz, 1995), a metamorphic grade, which was not reached during Alpine orogeny. Chapter 5 deals with pseudotachylytes in more detail.

#### 4.7.5. Mineralized veins

From profile 4 towards the south, the metasedimentary matrix, the metabasic rocks of the South Penninic *mélange*, and dolomite clasts exhibit an increasing amount of mineralized veins, whereas they are rare within the upper plate base throughout the working area (Fig. 4.7). However, an intense alteration of mica and feldspar crystals to chlorite and sericite is widespread in the upper plate basement indicating hydration from percolating fluids. The timing of alteration, however, is not constrained (Fig. 4.8k). The mineralized veins within rocks of the South Penninic *mélange* are generally oriented parallel to sub-parallel to the foliation and fill dilational jogs (mirror top-W hanging wall displacement, Fig. 4.8h), or they cut into more competent clasts embedded in the shaly or serpentized matrix at a high angle to their rims (Fig. 4.8e). Vein filling has a blocky texture of large minerals mostly formed by quartz and calcite, indicative for growth from a free fluid phase into a wide open cavity (Fig. 4.8f, Yardley, 1984; Nüchter and Stöckhert, 2007). In addition, the incorporation of wall rock fragments within the mineralized veins with no or minor contact to the wall rock supports rapid crystallization. Most obviously at

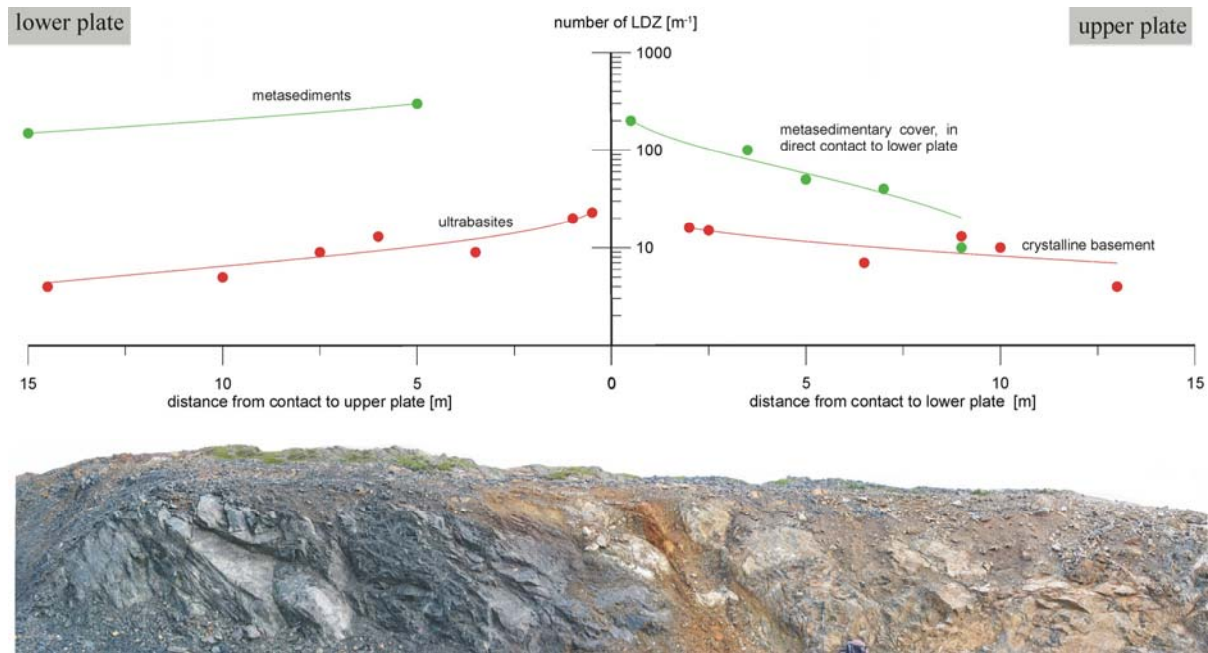


Figure 4.9: Distribution of localized deformation zones (LDZ) along a profile crossing the boundary between the South Penninic domain (lower plate, left side of the figure) and the Austroalpine domain (upper plate, right side of the figure). There is a drastic increase of LDZ towards the base of the upper plate. Therefore, increase in LDZ is not only depth- and lithology-dependent, but also dependent on the distance of the outcrops from the upper plate base as the most prominent shear zone.

profile 5, foliation-parallel mineralized veins within stronger deformed parts of the subduction mélangé are composed of fine-grained dynamically recrystallized calcite. This points to their synkinematic formation with respect to the activity of surrounding shear zones (parallel to the foliation) within the subduction mélangé. Furthermore, veins filled with coarser-grained blocky calcite crystals form either chaotic fracture network or branch off from shear planes with C'-type geometry and cross-cut the foliation at a higher angle (Fig. 4.8d).

Later folds uniformly affect both the foliation and the mineralized veins, which additionally points most likely to vein formation synkinematically to the foliation development. A subsequent set of mineralized veins, unaffected by folding, cuts almost perpendicular to the foliation and the previous veins, and is expressed by a fibrous growth of mostly calcite minerals. These later veins should have

been formed subsequently to the overall deformation along the fossil plate interface.

In order to detect changes in the amount of foliation parallel veins we measured their quantity either directly within outcrops counting them on a tape-measure, or using outcrop images and appropriate scale bars (Fig. 4.7). There are no mineralized veins observable within profiles 1, 2 and 3. At profile 4 and further towards the south the number of foliation parallel veins, as well as their mean length and width, increase (~6 mineralized veins/m at profile 4 and ~55 mineralized veins/m at profile 8; Fig. 4.7) with maximum spread of values south of profile 6. Hence, the trend of increased veining with blocky filling mimics the trend of LDZ density including increasing local variability. In addition, veining in the South Penninic mélangé approximately starts with the occurrence of pseudotachylytes in the basal upper plate, but appears anticorrelated towards and

below the deepest occurrence of pseudotachylytes.

## 4.8. Discussion

### 4.8.1. Post-accretion changes

We rearranged the structural data indicating a pervasive general top-W directed tectonic transport by rotating them into the restored composite section along downdip of the plate interface (rotation axis trends E-W and plunges  $0^\circ$ , rotation angle  $8^\circ$  corresponding to the estimated mean decollement angle, Fig. 4.10). Thereby, the structural data retained their general top-W direction of tectonic transport. At most, measured features such as foliation planes and stretching lineation steepened at the restored dip angle of the plate interface (Fig. 4.10). Furthermore, restoration does not provide hints for a major overprint of the pattern of subduction related metamorphism by younger events exceeding the estimated limits of error (at least 2 kbar vertical, and 5 km horizontal concerning the position of the samples relative to the profiles). All later offsets visible within the section from Schmid et al. (1996) are below 1 km, except for the Engadine line. This is also in agreement with our field observations missing a penetrative overprint of the general top-W directed tectonic transport, which was also reported by Ring (1989) and Dürr (1992).

Nevertheless, the present day fossil subduction channel has been influenced by post-subduction and post-accretion processes during ongoing convergence between both plates. These processes may have involved either both the South Penninic domain and the Austroalpine nappe stack, or only reactivated the direct contact between the lower and the upper plate. Post-subduction shortening of the interface zone would have shifted the

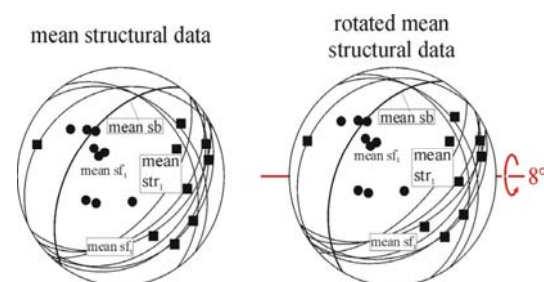


Figure 4.10: Structural data of brittle-ductile to ductile deformation associated with top-NW to top-SW direction of tectonic transport (generally top-W) rotated into the restored composite section perpendicular to the former strike of the plate interface. All plots are Schmidt net lower hemisphere, equal-area diagrams. Note, the structural data retained their general top-W direction of tectonic transport, only e.g. foliation planes and stretching lineation steepened at the restored dip angle of the plate interface.

investigated profiles closer together steepening the dip of the subduction megathrust. Consequently, the estimated megathrust dip would represent a maximum value. In contrast, extension will increase the distance between the analyzed profiles leading to a lower dip angle of the plate interface, and to a minimum megathrust dip angle. In addition, post-subduction motion only along the contact between the South Penninic mélangé and the Austroalpine upper plate would alter the spatial relationship between characteristic features observed along both sides of the suture. NNW-SSE shortening, extension, and displacement on the plate interface have been observed (see e.g. large-scale folding of section). But magnitudes of subsequent deformation are small with respect to the total length and minimum displacement along the plate interface (i.e.  $>170\text{km}$ ), and may even largely cancel out. Moreover, the here calculated dip angle of the plate interface of  $\sim 8^\circ$  is in good agreement with published mean megathrust angles (Lallemand et al., 1994; Moores and Twiss, 1995; Clift and Vannucchi, 2004). In consequence, we consider later modifications irrelevant for the here investigated subduction-related deformation.

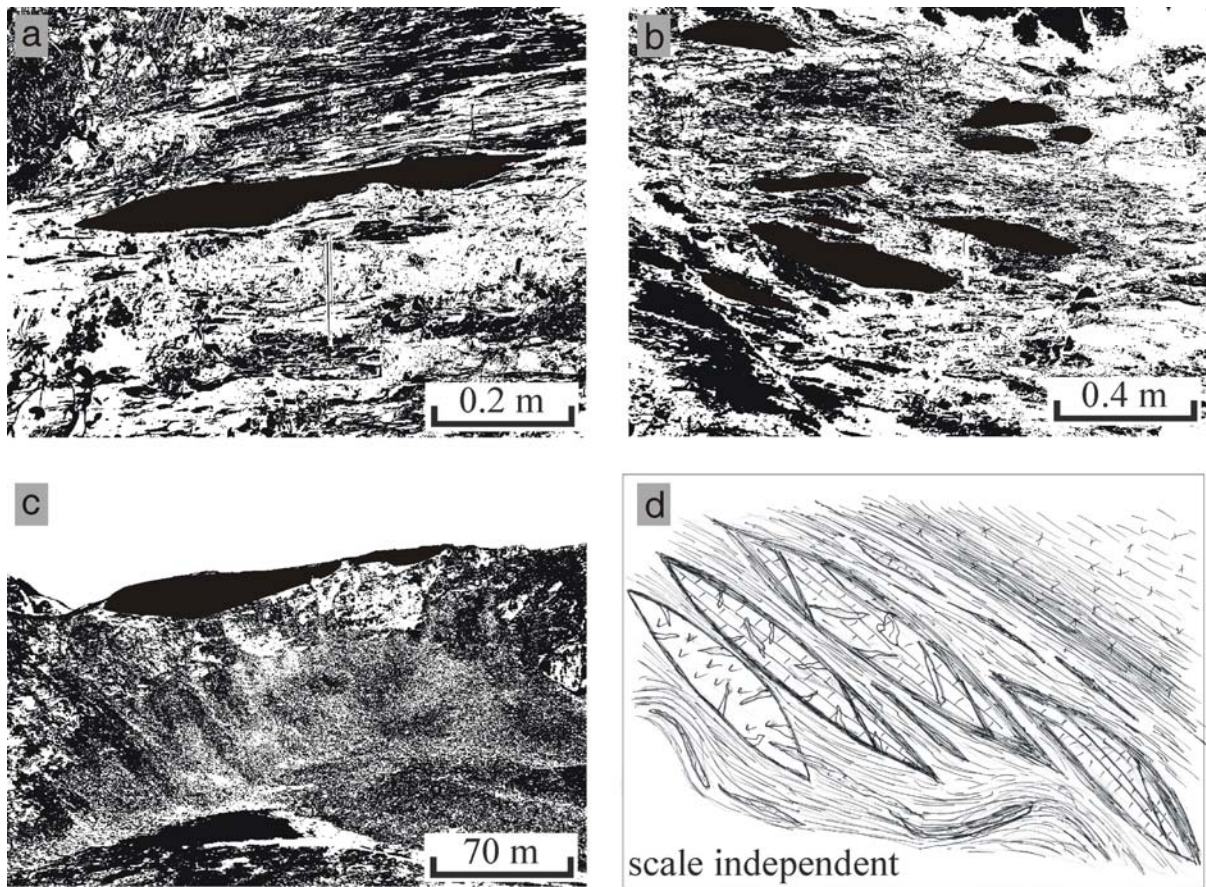


Figure 4.11: Clasts of different size and material are incorporated within the shaly or serpentized matrix. They are elongated with their long axis pointing towards the inferred direction of pervasive tectonic transport, independent of their individual size. This scale independence is shown using outcrop photographs. Clasts are highlighted with the image processing software Scion Image. a) Carbonate clast embedded in shaly matrix at profile 4, b) Carbonate clasts within calcareous and shaly matrix, c) upper plate dolomite clast embedded within subduction mélange at profile 8, d) shows a representative scale independent synthetic section of clasts and matrix.

#### 4.8.2. Long-term kinematics - tectonic erosion vs. accretion

Clasts within the matrix of the subduction mélange provide hints for processes such as tectonic erosion and accretion along the plate interface zone. The strong contribution of upper plate fragments (basement and cover) is a diagnostic criterion for the role of tectonic erosion from the base of the upper plate (Oncken, 1998). Tectonic erosion as a key factor controlling the material input into the fossil subduction channel also explains the lack of upper plate crystalline basement immediately above the plate interface in

some parts of the working area, where upper plate sediments directly rest on the mélange (see also Wagreich, 1995, on reinterpretation of Gosau basins as indicating Late Cretaceous subduction erosion). Basal subduction erosion as prevailing mass transfer mode invariably stopped upon underplating of the mélange, and abandonment of the subduction of the South Penninic ocean (see also Chapter 6).

The process of layer separation, single clast formation, and later assimilation promoted by invading mylonitic shear fractures (see Chapter 4.7.3) would lead to an increase of the aspect ratio as long as the clasts are detectable as independent

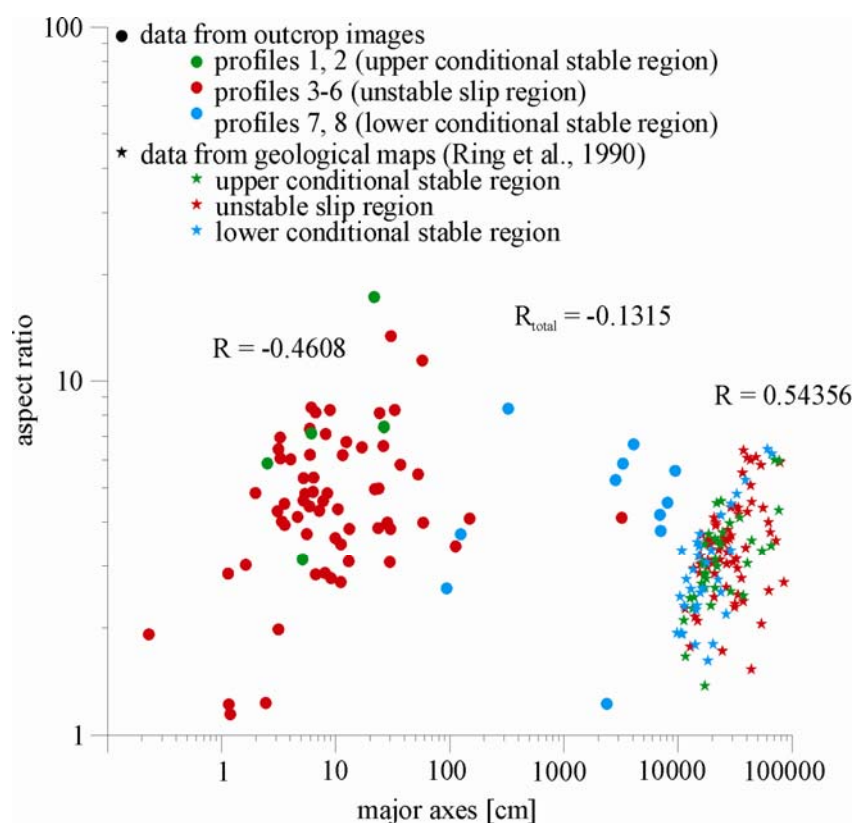


Figure 4.12: Aspect ratio of embedded clasts plotted against major axes. Green dots represent data obtained from outcrop images corresponding to profiles located in the upper conditional stable region, red dots correspond to profiles located within the unstable slip region, whereas blue dots are related to profiles located in the lower conditional stable region. Green stars correspond to data gained from geological maps (Ring et al., 1990) for profiles situated within the upper conditional stable region, red for profiles within the unstable slip region, and blue corresponds to profiles in the lower conditional stable region. There is no obvious trend, expressed by the correlation coefficient  $R$ . Therefore, aspect ratio of clasts is independent of clast size; no hint of the clast's relative position along the fossil plate interface zone is given by a change of the aspect ratio.

objects, and to a decreasing average clast size. An incipient assimilation was observed for both clast types, either slivers of the upper and lower plate or boudinaged clasts of sedimentary layers. But the calculated aspect ratio of individual clasts exhibit no relevant change with depth as would be expected from progressive disintegration (see scale independence of clasts in Fig. 4.11). Additionally, there is no correlation between aspect ratio and clast size (expressed by clasts major axes, Fig. 4.12) suggesting the independence of the aspect ratio compared to the position of the profile along the fossil plate interface, even when taking the limitations by the use of geological maps into account. At most, the average clast size increases towards the

south of the working area (Chapter 4.7.3., Figs. 4.7, 4.12). In all, these observations suggest continuous addition of new clasts from fragmenting the base of the upper plate towards depth indicating tectonic erosion along the entire base of the exposed upper plate and preferential disintegration of smaller fragments until the onset of underplating (Eocene).

A final aspect resulting from long-term material flux merits mentioning: Because of more or less continuous flux of the material in the subduction channel, all features will be displaced downdip once formed, or even updip due to return flow. This will result in (1) offset of mélangé features with regard to the overlying

features at the base of the upper plate (except for first occurrence of features); to (2) an apparent downdip increase in key features when continuously formed during downdip flow; to (3) apparently gradational boundaries that may have been more distinct during formation. None of these aspects will be of significance in the upper plate. The apparent linear increase of e.g. the number of LDZ within the subduction mélange and mineralized veins potentially supports the interpretation of continuing formation paralleling the post-formation displacement of key features towards depth during long-term material flux.

#### *4.8.3. Short-term kinematics - unstable slip vs. stable sliding*

To this date, pseudotachylytes are considered the only unambiguous evidence for faulting at seismic velocities (e.g. Cowan, 1999). Therefore, we interpret their occurrence along the exhumed plate interface as delineating the area of unstable slip (yellow shaded area within Fig. 4.7). From the northernmost occurrence of pseudotachylytes we identify the fossil updip limit of unstable sliding close to profile 2 at a distance of ~90 km from the trench corresponding to a depth of ~15 km, and a temperature of ~200°C (temperature estimate based on deformational behavior of different minerals, see Chapter 4.5.2, Fig. 4.13). Correspondingly, the southernmost occurrence of pseudotachylytes defines the fossil downdip limit of unstable slip, and is located close to profile 6 at a distance of 140 km from the trench equivalent to a depth of ~22 km, and a temperature of ~300°C (temperature estimate based on deformational behavior of different minerals, see Chapter 4.5.2, Fig. 4.13). The conditionally stable segments above and below the unstable segment may continue for some distance up-, but also downdip. Several observations point to the

coincidence of the downdip limit of unstable slip with the start of a transitional zone at the downdip limit of the seismogenic coupling zone (transition from seismic to aseismic and conditionally unstable slip): the observed mylonitic overprint of pseudotachylytes, the mutual crosscutting of overprinted and non-overprinted pseudotachylytes at profile 5 (see Chapter 4.7.4.), the drastic increase in LDZ (see Chapter 4.7.2.), and the onset of mylonitic rocks in the subduction mélange and, slightly deeper, at the base of the upper plate (Fig. 4.13).

Below the downdip end of unstable slip we observe a continuing increase of LDZ in the mélange, progressively observed as distributed over the scale of the whole outcrop (Chapter 4.7.2., Figs. 4.7, 4.8b), jointly occurring with mylonites. This continuous increase requires formation of localized deformation zones that may be seismic also below the zone of unstable slip, when they compete with ductile shearing. Hence, we suggest seismic behavior to be possible in the subduction mélange to temperatures of at least 300°C to 350°C and possible higher. However, formation of LDZ and therefore seismic behavior is strongly lithology dependent (see Chapter 4.7.2, Fig. 4.11). The transition between seismic and aseismic deformation in our studied example is well comparable to the proposed transitional zone downdip of the seismogenic part of active convergent plate interfaces (e.g. Hyndman and Wang, 1995). There, seismic slip in the transitional zone may occur during major coseismic events rupturing the entire unstable slip zone, subsequently overprinted by viscous deformation during postseismic relaxation and interseismic creep. However, we note that recent observations of silent slip events (slip velocity at ~0.1 m/s, Schwartz and Rokosky, 2007) have been reported for the transitional zone. Our observations may well also relate to this observation.

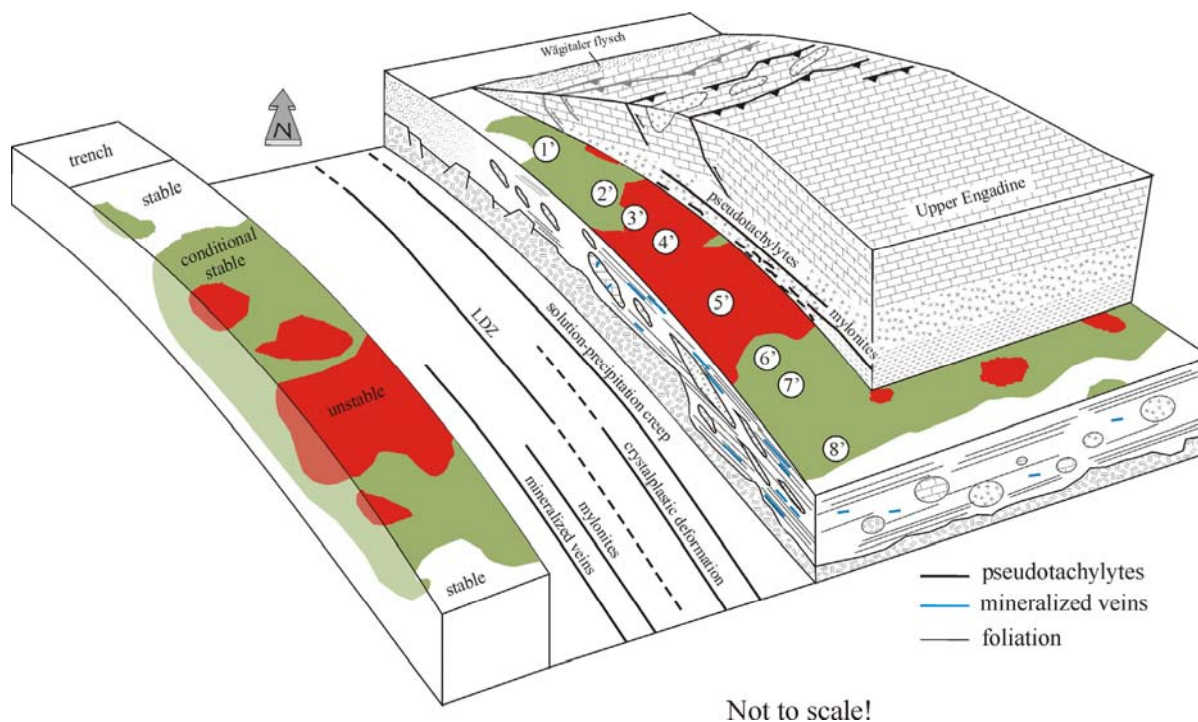


Figure 4.13: Final interpretative section showing the profile positions, as well as the association and interference of the discussed key features. Solution-precipitation creep is dominant in all of the study area, whereas crystalplastic deformation appears towards the south. The number of LDZ increase downdip the plate interface, and in the southern part of the working area the South Penninic mélangé is deformed over the scale of the whole outcrop, closely associated with mylonites. Pseudotachylytes occur within a certain depth range along the fossil plate interface immediately above the base of the upper plate basement delineating the former unstable slip region within the seismogenic coupling zone. Above and below the unstable slip region areas of conditional stability occur, characterized by the coexistence of slow deformation (e.g. solution-precipitation creep in the northern part of the working area, crystalplastic deformation in the southern part) and maybe seismic deformation (e.g. LDZ, mineralized veins). The regions of stable, conditional stable and unstable slip will vary in space and time in accordance to spatiotemporal variance in e.g. sediment input, dewatering and dehydration. Thus, the mechanical conditions within the subduction channel are not characterized by steady state behaviour. Mineralized veins are spatially associated with pseudotachylytes, but exclusively found within the subduction mélangé. This fact points to different rheological behaviour of the subduction mélangé and the crystalline basement of the upper plate. The former prevent the built-up of high effective normal stress and associated shear stress by ongoing hydraulic fracturing and the latter enables the accumulation of higher effective normal stress and associated shear stress. From the spatial coincidence of both pseudotachylytes and mineralized veins and their identical texture we suggest that formation of this type of veins in the subduction channel potentially indicates unstable slip. Model of frictional conditions modified and extended downdip following Bilek and Lay (2002).

The updip extent of the fossil seismogenic coupling zone is probably much wider than the zone of unstable slip outlined by the occurrence of pseudotachylytes. This assumption is supported by the fact that the here estimated updip limit of unstable slip (~15 km depth, 200°C) is below the widely accepted values for the updip limit of the seismogenic coupling zone of active convergent plate margins (~5 km depth, 100°C-150°C, e.g. Oleskevich et al.,

1999). Additionally, we observed localized deformation zones northward (i.e. trenchward) of the estimated upper limit of the unstable slip area. They may also point to slip localization during potentially coseismic events. Otherwise, pressure solution seams, which are widespread in the northern part of the working area, are evidence for aseismic creep (e.g. Kitamura et al., 2005), possibly prevailing in the postseismic relaxation period.

Patches of stable, unstable and conditional stable behavior might change their location not only in space, but also in time. This is caused by spatiotemporally dependent processes, such as compaction, dewatering and dehydration, which influence the frictional properties within the subduction channel. These processes are strongly dependent on other spatiotemporal variable factors, for example the composition and the amount of sediment input, as well as the temperature regime. This variance in space and time might additionally smear out possible distinct boundaries concerning the onset of plate interface key features. This should be of larger influence for features along the upper plate base (e.g. pseudotachylytes resulting from frictional instability within the subduction channel), as the upper plate base is relatively fixed with respect to the material moving within the subduction channel. Otherwise, the effect may be negligible for the subduction channel matrix itself due to the superimposition of continuing downward transport of key features by continuous material flux, which also leads to apparently gradational boundaries (see Chapter 4.8.2). In consequence, the plate interface zone cannot exhibit a steady state behavior.

#### *4.8.4. Fluid flow and constraints for long- and short-term deformation*

Evidence for fluids circulating along the plate interface are widespread in the working area. This is indicated by the ubiquitous presence of foliation-parallel mineralized vein systems in the *mélange* matrix (Fig. 4.8d), and by veins cutting into competent clasts both downdip of profile 4 (Fig. 4.8e, Chapter 4.7.5.). The presence of fluids is also necessary for the observed solution-precipitation creep as dominant deformation mechanism in all of the study area (Fig. 4.8g), including the zone updip of profile 4 (Fig. 4.13). From the absence of mineralized veins updip of

profile 4 we conclude that fluid percolation must have occurred unimpeded through a permeable fracture network, along foliation planes and grain boundaries in the conditionally stable domain (Fig. 4.13). Starting only in the unstable slip domain, formation of mineralized veins clearly requires fluid production rate to exceed percolation rate through an open system building near-lithostatic fluid pressure during parts of the seismic cycle. The hampered fluid flow might be in line with an increase in upper plate alteration and growth of sheet silicates along foliation planes within the subduction *mélange*.

Increasing fluid pressure lowers the effective normal stress, and thus triggers the formation of cracks (e.g. Hubbert and Willis, 1957; Hubbert and Rubey, 1959; Secor, 1965; Sibson, 1981; Atkinson, 1987). According to Husen and Kissling (2001) an increase in fluid pressure is promoted by the concentration of high stress along the plate interface, which leads to sealing, and thus to trapping of fluids. Major earthquakes are thought to be able to break this seal, thus allowing fluids to migrate upwards along the gradient in fluid pressure (hydrostatic fluid pressure above the seal, lithostatic fluid pressure below the seal). This coincides well with our observations that mineralized veins were restricted to rocks within the deeper portions of the subduction channel (South Penninic *mélange*), whereas clear evidence for mineralized veins are missing within the upper plate. However, an intense alteration of mica and feldspar minerals is widespread at the base of the upper plate (Fig. 4.8o). Although, the timing of alteration is poorly constrained, the reaction products may be aligned in a younger foliation of presumable Alpine age in the more southern parts. Alteration processes lead to a consummation of dehydration fluids. Additionally, the observed foliation development makes the base of the upper plate an efficient seal. Within the subduction *mélange* the growth

of sheet silicates (white mica, chlorite, Figs. 4.8l, m) also consumes fluids. In addition, mylonitic overprint of pseudotachylytes immediately above the base of the crystalline hanging wall may also be supported by some fluid circulation enhancing devitrification, formation of hydrate phases, and grain boundary sliding (Fig. 4.8j).

The blocky texture of minerals, which fill the foliation-parallel veins (Fig. 4.8g) starting from the updip end of the unstable slip domain, indicates that fracture opening was faster than mineral growth. Furthermore, this blocky texture is suggested to point to ongoing nucleation during supersaturation of vein-forming minerals (Oliver and Bons, 2001). According to these authors, this might be expected for faults, which exhibit a large, near-instantaneous fluid pressure drop upon fracturing. Nüchter and Stöckhert (2007) concluded that fracturing and cavity formation could reflect a cycle of instantaneous loading followed by stress relaxation within a very short time span. This could point to fluid-induced seismicity or to seismically triggered hydrofracs. However, the relationship of these mineralized veins to deformation at seismic velocities (in the range of 1m/s and more; Cowan, 1999) has yet to be evaluated. Nevertheless, the internal structure of the mineralized veins resembles the structure of pseudotachylyte networks, which are clear evidence for unstable slip (Figs. 4.8f, i). Embedded wall rock fragments within the mineralized veins and within the pseudotachylytes - either without or with minor contact to the wall rock (Figs. 4.8f, i) - point to fast fracturing and subsequent rapid solidification processes. Therefore, from the spatial coincidence of both features (Fig. 4.13) and their identical texture we suggest that formation of this type of veins in the subduction channel potentially indicates unstable slip.

In spite of their mutual association to the seismic process, we conclude that the exclusive restriction of pseudotachylytes and mineralized vein systems to one component of the plate boundary system - i.e. base of upper plate vs. mélange - is most likely due to a different rheological behavior of both, the sedimentary matrix of the subduction channel, and the crystalline basement of the upper plate. Fluids within the mélange (sealed from above) prevent the built-up of high effective normal stress and associated shear stress by ongoing hydraulic fracturing, hence cause a lower potential for shear heating. In contrast, crystalline upper plate rocks (drained from above) support higher effective normal stress and associated shear stress, a prerequisite for the formation of shear fractures and frictional heating, and thus for pseudotachylytes. The mechanical and kinematical key role of the base of the upper plate as the most prominent shear zone is not only underscored by the highest density of pseudotachylytes immediately above the contact, but also by the highest number of LDZ immediately above and below this boundary (Fig. 4.10).

Extensional veins sub-parallel to cleavage formed by compression and/ or shear require variations or a switch of stress directions as well as of the state of fluid pressure. This explains the development of mineralized veins sub-parallel to the maximum compression direction associated with foliation. Transient changes of the state of stress, as expected for repeated seismic loading cycles, may particularly facilitate the development of foliation-parallel veins. In principle, opening of fractures occurs when the minimum principle stress equals the tensile strength of the rock. As proposed in the accretionary model of Meneghini et al. (2007), the stress parallel to subducted sedimentary layers should be larger than the stress normal to the bedding, which is plausible at shallow subduction dip angles, and would promote layer-parallel veining.

In addition, seismically controlled stress cycles at elevated and equally transient fluid pressure lead to the alternating development of foliation-parallel and foliation-normal veins (e.g. Meneghini et al., 2007). In the study presented here, veins parallel to the sedimentary layering are widespread (Fig. 4.8d), whereas veins approximately normal to the sedimentary layering are mainly observed in competent clasts (Fig. 4.8e). However, best developed at profile 5, there are veins filled with blocky calcite crystals, which cross-cut the foliation at a higher angle (branching off from shear planes with a C'-type geometry, Fig. 4.8d). These veins might represent transient upward directed fluid injections resulting from a cyclic build-up of fluid pressure during burial of sediments, dewatering and dehydration (Meneghini et al. 2007). The common observation of foliation-parallel mineralized veins within the subduction mélange of the study area provides hints for the occurrence of pathways for layer-parallel fluid release and transport as required in the model of Meneghini et al. (2007). The heterogeneous internal structure of the subduction mélange governs the transport of released fluids both along and across the foliation, foliation parallel shear planes, and thus, the plate interface. In conclusion, we assume shear deformation and persistent changes of the stress field by cyclic fluid pressure to operate contemporaneously or alternately leading to vein formation synkinematically to the development of foliation.

Last but not least, we note that the abundance of veins increases downdip to the base of the unstable slip zone. Hence, veining therefore probably proceeded along this entire segment. Its geometric style changes deeper down with longer and wider veins, still indicating ongoing hydrofracturing in the lower conditionally stable zone as also observed for the LDZ.

#### 4.9. Conclusions

We analyzed a continuous exposure exhibiting the complete seismogenic part of a subduction channel and its upper plate hanging wall within the Central Alps of Europe. For this purpose we restored the fossil plate interface zone to its subduction geometry resulting in a 170 km long section with a ca. 8° SSE-dipping plate interface for the Late Cretaceous to Eocene period prior to the collision and underplating of the continental Briançonnais domain. During subduction of the South Penninic ocean, material from different sources (continental upper plate, oceanic lower plate) was progressively involved into the subduction factory and transported downwards, forming either the shaly and serpentinitic matrix of the subduction mélange, or competent clasts. Tectonic erosion controlled mass transfer within the subduction channel during the Late Cretaceous to Eocene, while subsequent basal accretion lead to the abandonment of this major shear zone. The internal structure of the studied fossil subduction channel resembles the proposed internal structure of active systems inferred from e.g. seismic and seismological data: less deformed units are bounded by a network of active shear zones or sheared matrix. Therefore, preservation of sedimentary and/ or magmatic textures in blocks of all sizes is supported, unless deformation affects the whole subduction mélange.

Along the SSE-dipping plate interface overprint of the upper plate base by Alpine deformation increases towards depth (respectively towards the south of the working area). The matrix of the subduction channel exhibits an equally increasing deformation and metamorphic grade, and the number of mylonitic shear zones and mylonitic rocks progressively increase as well (including the onset of crystalplastic deformation). The density of LDZ also increases downdip ultimately

involving the entire subduction channel matrix.

Pseudotachylytes along a restricted segment of the upper plate base – delineated by ca. 200°C updip and ca. 300°C downdip – define the limits of the unstable slip region within the fossil seismogenic coupling zone. Foliation-parallel mineralized veins with partly blocky mineralization that occur over the same depth range, but continue to below the unstable slip domain, are suggested to reflect seismic failure in the subduction mélange. The existence of mineralized veins requires fluid production rate exceeding fluid percolation rate, and the thereby caused built up of lithostatic fluid pressures. Growth and alignment of sheet silicates (white mica, chlorite) along foliation planes clearly hampers the percolation of fluids through a co- to postseismically open system that is progressively compacted and cemented during the post- to interseismic stage. In addition, starting from the unstable region downdip, the plate interface zone is characterized by an impermeable upper plate due to fluid assisted alteration processes and fabric development. Therefore, the region of unstable slip within the seismogenic coupling zone has an at least intermittently lithostatic fluid regime effectively sealed off from the higher parts of the subduction channel as well as from the overlying wedge by the hydrated and impermeable upper plate base. Fluid flow supports both long-term interseismic and short-term coseismic deformation by enhancing solution-precipitation creep, mylonitization of pseudotachylytes (by enhancing devitrification, hydrate phase formation, grain boundary sliding) and fracturing, respectively, in the unstable slip zone as well as in the deeper transitional zone. The upper conditionally stable zone shows abundant evidence for brittle localized fracture, but no indication for hydraulic fracturing. The corresponding fluid regime

is sub-lithostatic and probably dewateres the plate interface through an interconnected fracture network, along foliation planes or grain boundaries. The circulation of fluids is indicated by solution-precipitation creep as the dominant deformation mechanism. The lower conditionally stable region is again characterized by hampered fluid flow indicated by the increasing number of mineralized veins even below the unstable slip zone. This may possibly indicate a domain of slow earthquakes and non-volcanic tremors as recently discovered for this depth range along many active convergent margins.

## 5. Temporal constraints for unstable slip – $^{40}\text{Ar}/^{39}\text{Ar}$ geochronology applied to pseudotachylytes

### Abstract

$^{40}\text{Ar}/^{39}\text{Ar}$  isotopic data obtained by stepwise heating using a laser system from pseudotachylytes occurring in the basal parts of the Austroalpine domain in the northwestern part of the Engadine window constrain the timing of unstable slip within the seismogenic zone of a fossil convergent plate interface zone. Formation of pseudotachylyte as unambiguous evidence for fossil seismicity is dated to have occurred during a time span between 60 Ma to 80 Ma. This corroborates previous data obtained by Thöni (1981, 1988). However, the heterogeneous texture of the ultra fine grained pseudotachylyte groundmass, most likely composed of a mixture of amphibole, feldspar and biotite (obtained by defocused beam microprobe bulk analyses), as well as the incorporation of host rock material of comparable size (rock fragments and single minerals) complicate the interpretation of the isotopic data. Therefore, the Ca/K ratio provides first rough indications for the degassing of material enriched in Ca, most probable the inherited host rock material. Due to the temporal similarity between age data for higher pressure metamorphism of South Penninic and Austroalpine rocks and pseudotachylyte formation, and the fact that the pseudotachylytes occur subparallel (i.e. slightly discordant) to the main thrust, we interpret the generation of pseudotachylytes to be related to unstable slip processes occurring along the plate interface zone during the course of subduction of the South Penninic ocean underneath the Austroalpine upper plate.

### 5.1. Introduction

Unstable slip in the upper part of active convergent plate margins occurs within a limited depth range along the plate interface, typically between 5 km and 45 km depth (so-called seismogenic coupling zone, e.g. Ruff and Kanamori 1983, Tichelaar and Ruff 1993), causing major interplate earthquakes. Until now, the plate interface of convergent plate boundaries cannot be directly accessed. Hence, direct investigations of exhumed ancient convergent plate boundaries are requested to achieve insights into deformation processes occurring along the plate interface despite multiple overprinting during exhumation. We use the exposure of a former plate interface in

the European Alps, one of the best-studied mountain belts that has resulted from successive subduction, accretion and collision (Froitzheim et al., 1994; Handy, 1996; Schmid et al., 1996; Pfiffner et al., 2000) to address the question of timing of unstable slip. Therefore, we analyzed pseudotachylytes from the basal parts of the upper plate immediately above a subduction mélange at the northwestern rim of the Engadine window. This suture traces the plate interface zone of a fossil convergent plate margin.

Pseudotachylytes as evidence for unstable slip are the field record of paleoseismic events occurring in the seismogenic zone of large scale crustal faults (e.g. Sibson 1975). Adopting this assumption for

exhumed ancient subduction plate interfaces, the presence of pseudotachylytes constrains the depth range of the exposed fossil counterpart to be situated within the former seismogenic coupling zone. Due to the presence of pseudotachylytes, the here presented study contributes to the understanding of convergent plate interfaces in the depth range of their former seismogenic zone. We shed light on the timing of unstable slip with the help of  $^{40}\text{Ar}/^{39}\text{Ar}$  geochronology applied to the pseudotachylytes. As recommended by Müller et al. (2002), we used stepwise heating with a laser system until total fusion for gas release. According to Maddock (1992) we applied microprobe analyses with a defocused beam to study the bulk composition of the ultra fine grained pseudotachylyte groundmass.

## 5.2. Geological, metamorphical, and structural framework of the working area

The European Alps resulted from collision of the European and the Adriatic continental plates and southeastward to southward subduction and accretion of the intervening Penninic oceanic domain. The Penninic domain consists of two oceanic basins related to the Alpine Tethys (North Penninic Valais basin and South Penninic ocean), divided by the so-called Briançonnais continental swell (Middle Penninic) (e.g. Florineth and Froitzheim 1994, and references therein). These units were successively subducted and accreted to the base of the Adriatic plate (Austroalpine domain in the working area) since the Late Cretaceous until the final collision of the Adriatic plate with the European plate during the Middle Tertiary.

The working area is located at the northwestern rim of the Engadine window (Figs. 5.1, 5.2). The main geological units are represented by the South Penninic and

Austroalpine domain. The South Penninic domain forms a tectonic subduction mélange caused by the Late Cretaceous to Eocene subduction of the South Penninic ocean underneath the Austroalpine upper plate. This mélange zone is composed of intensely deformed oceanic and continental material (Deutsch 1983, Ring et al. 1988, and references therein) comprising Jurassic ophiolites, radiolarian chert, pelagic limestone, shale and sandstone (Ring et al. 1988). Competent blocks of Austroalpine and Penninic affinity are embedded in the incompetent shaly matrix (Ring et al. 1990). The large-scale structures of the whole South Penninic mélange are construed by e.g. Ring et al. (1988, 1989, 1990) as the deep parts of an accretionary wedge formed at the tip of and below a thrust belt migrating towards the west. The Austroalpine upper plate consists of a suite of gneissic to amphibolitic, mainly upper crustal rocks, which experienced pre-Alpine (mainly Permo-Carboniferous) and Early (Eo-) Alpine deformation (e.g. Florineth and Froitzheim 1994, Manatschal et al. 2003, Ring et al. 1988). Metamorphic conditions of South Penninic rocks in the working area are in the range from lower greenschist facies to middle greenschist facies. The Austroalpine domain was metamorphosed to lower greenschist facies conditions during Alpine deformation in the working area (e.g. Handy and Oberhänsli 2004).

The South Penninic subduction mélange close to the contact to the Austroalpine upper plate experienced a penetrative deformation with an inferred top-W direction of tectonic transport (see Chapter 4, e.g. Bachmann et al. submitted). Deformation with general top-W directed tectonic transport of the Austroalpine nappe stack is expressed by microscale fracture zones reactivating the preexisting foliation of probably Variscan age. Orientation of these fracture zones and the preexisting foliation in the Austroalpine rocks parallels the corresponding foliation

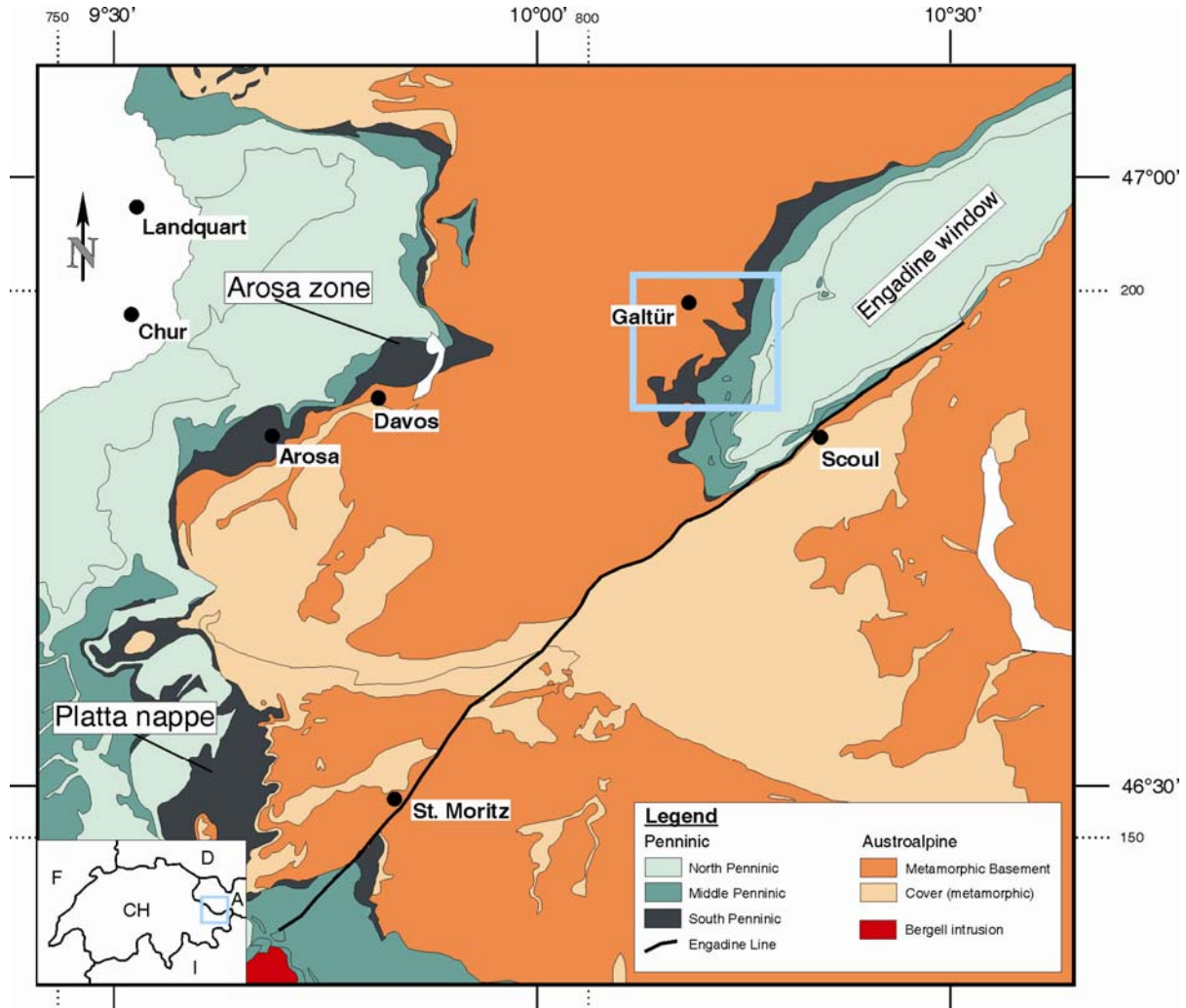


Figure 5.1: Geological map of the study area emphasizing the suture zone between the South Penninic (dark green) and the Austroalpine (orange, part of the Adriatic plate). Arosa zone and Platta nappe are local names for rocks of South Penninic affinity. Based on the Tectonic map of Switzerland 1:500,000, 2<sup>nd</sup> edition (1980). Blue rectangle emphasizes the working area located at the northwestern rim of the Engadine window.

within the South Penninic *mélange*, at least in the first few hundred meters above the base of the hanging wall. In general, orientation of structural data and the therewith assessed direction of tectonic transport are similar in both the South Penninic *mélange* and the basal parts of the Austroalpine upper plate. This is also the case for their metamorphic conditions reached during Alpine deformation. Subsequent localized deformation with significant lower intensity overprints the top-W structures, but a complete erasure of the top-W structures in both the South Penninic *mélange* and the Austroalpine

nappes by younger deformational processes cannot be observed (see also Ring 1989, Dürr 1992).

The boundary between the South Penninic *mélange* in the footwall and the Austroalpine upper plate in the hanging wall represents a large scale thrust zone, where Austroalpine rocks were thrust onto the South Penninic *mélange*. The most prominent feature within the study area are pseudotachylytes, which occur in the first ~300 m above the base of the upper plate, which are previously described by a number of authors (e.g.

Gürler and Schmutz 1995, Masch 1970, 1974, Koch and Masch 1992, Thöni 1988). The frequency of these brittle fault rocks decreases with increasing distance from the base of the upper plate. Therefore, they are supposed to be related to the emplacement of the Austroalpine nappe stack onto the South Penninic domain (e.g. Gürler and Schmutz 1995). Pseudotachylytes occur both concordant and discordant to the preexisting layering, preferentially formed along lithological boundaries. Pseudotachylytes occur slightly discordant to the main thrust fault (Gürler and Schmutz 1995). However, we never recognized pseudotachylytes within metasedimentary rocks of the South Penninic mélangé, neither in the matrix nor in the clasts.

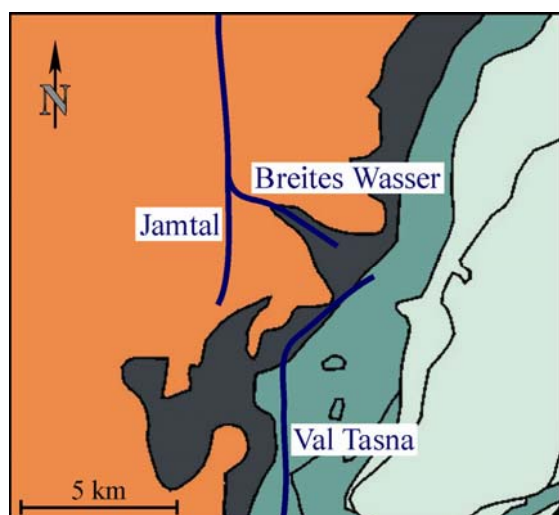


Figure 5.2: Close-up of the working area indicating the sampling areas Jamtal valley, valley Breites Wasser, and valley Val Tasna. Close-up equals blue rectangle in Figure 5.1. For explanation of signatures see legend in Figure 5.1.

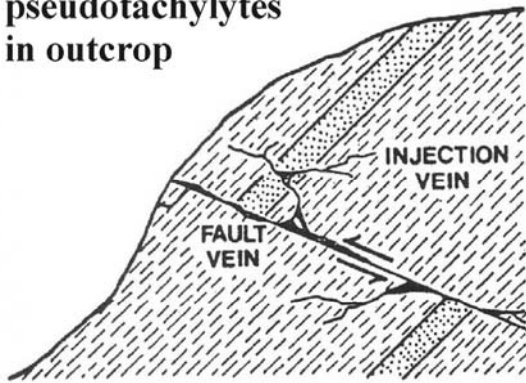
Additionally, we observed an overprint of pseudotachylytes by viscous deformation, maybe promoted by the small grain size of the recrystallized pseudotachylytes favoring viscous grain-size sensitive deformation mechanisms (grain boundary sliding) (see Chapter 4). This overprint is most prominent just above the main thrust plane. The wall rock hosting the pseudotachylytes (Austroalpine basement)

does not exhibit an Alpine mylonitic overprint. Mylonitic deformation is rather assigned to the higher grade amphibolite facies metamorphism during Variscian orogeny (due to the mineral composition of the mylonitic rocks) (Schmutz 1995), a metamorphic grade, which was not reached during Alpine orogeny. Moreover, there is a mutual crosscutting relationship between undeformed pseudotachylytes and mylonitized pseudotachylytes pointing to spatiotemporal changes of brittle and viscous deformation.

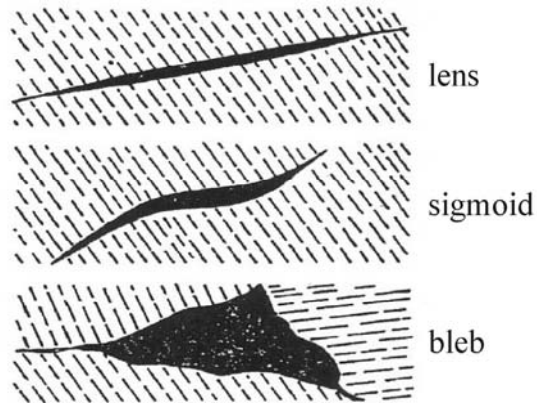
### 5.3. Pseudotachylytes – General information

The term “pseudotachylyte” was originally introduced by Shand (1916) due to the resemblance of dark veins in the Vredefort area (South Africa) to tachylytes, which represent mafic volcanic glass. Today, pseudotachylytes describe cohesive glassy or very fine grained brittle fault rocks. According to Cowan (1999), they are the only unambiguous evidence for deformation at seismic velocity ( $\geq 1$  m/s). Pseudotachylytes represent melt veins due to frictional heating produced by sliding (e.g. Sibson 1975, Spray 1987). In addition, Wenk (1978) proposed that pseudotachylytes result from fluidization of material due to frictional-induced ultracataclasis, rather than from friction-induced melting. According to results from high-speed slip experiments conducted by Spray (1995), comminution by ultracataclasis and frictional melting may take place in fully transitional stages, not explicitly excluding each other. However, both require high deformation rates. Therefore, pseudotachylytes are thought to be associated with either hyper-velocity impact events, or high-velocity coseismic slip along crustal fault zones (Spray 1992). Additionally, pseudotachylytes are reported to have been produced at the base of large landslides (Legros et al. 2000).

**principle sketch of  
pseudotachylytes  
in outcrop**



**discordant veins**



**concordant veins**

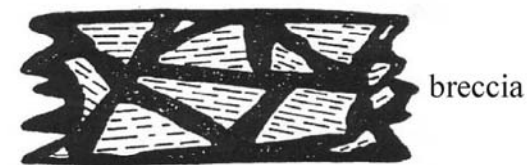
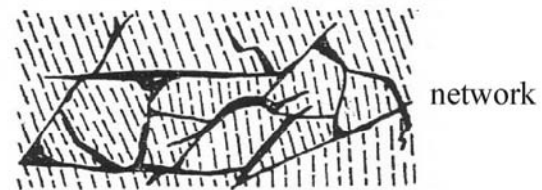
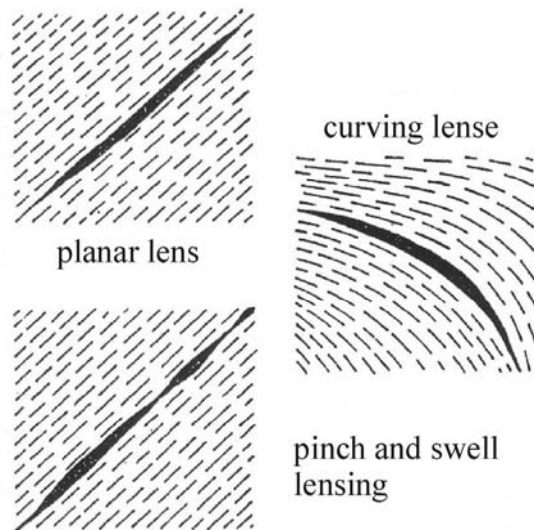


Figure 5.3: Principle drawing of main pseudotachylyte geometries and textures. Modified after Sibson (1975).

In general, pseudotachylytes form along so-called generation surfaces (fault veins, Fig. 5.3). Veins inject into the host rock with a high angle (roughly  $90^\circ$ ) to this main surface (injection veins, Fig. 5.3) (Sibson 1975). Fault veins are situated along planar shear fractures, whereas injection veins represent tensile fractures and voids, in which the melt was squeezed-off from the generation surface (e.g. Sibson 1975). According to e.g. Sibson (1975) other key geometric characteristics are: sharp boundaries to the host rock, and a dark matrix with mineral and wall rock fragments. Pseudotachylytes occur as networks, layers or form the matrix of

breccia zones (Figs. 5.3, 5.4). They are oriented concordant or discordant to a pre-existing layering, but they are preferentially formed along lithological contrasts (e.g. Kenkmann et al. 2000).

Formation of pseudotachylytes occurs mainly in dry and low porosity rocks. Fluids would prevent the built-up of high effective normal stress and associated shear stress by ongoing hydraulic fracturing, hence cause a lower potential for shear heating. In contrast, dry crystalline rocks support higher effective normal stress and associated shear stress, a prerequisite for the formation of shear

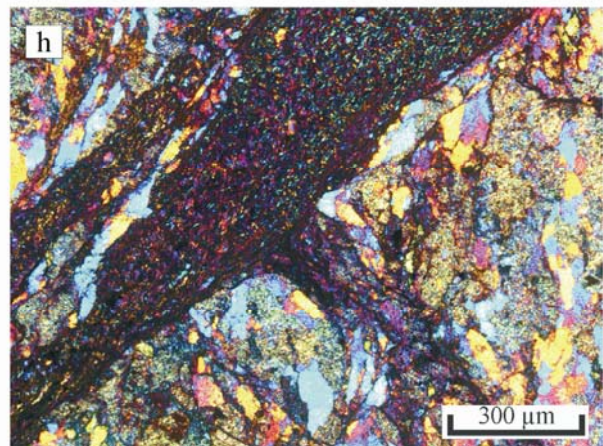
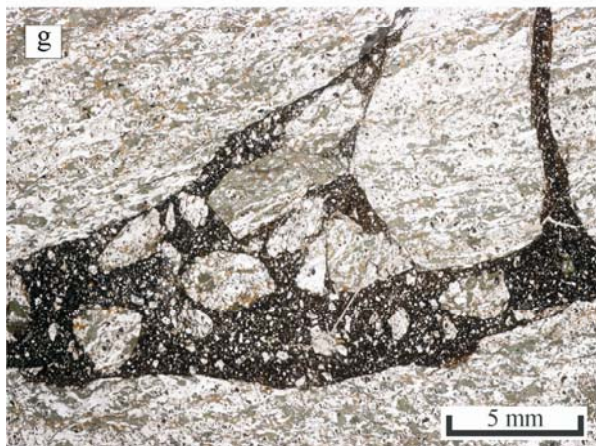
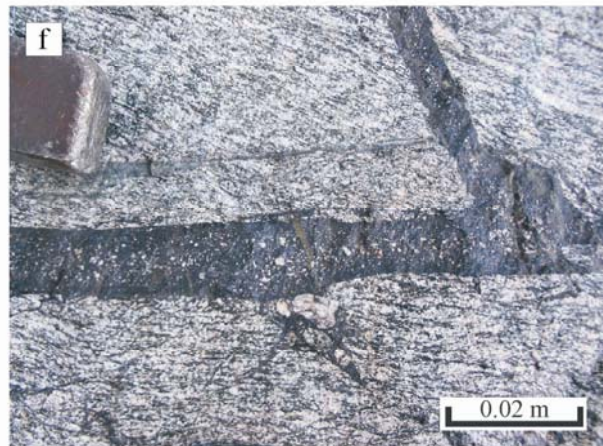


Figure 5.4: Outcrop and thin section images of pseudotachylytes from the northwestern rim of the Engadine window. a) pseudotachylyte exhibiting a ladder network, b) pseudotachylyte forming the matrix of a breccia zone, c) pseudotachylyte with fault vein and injection vein ( $\sim 90^\circ$  from the main surface), d) pseudotachylyte with embedded wall rock fragments of different size, e) pseudotachylyte exhibiting a large number of wall rock fragments. Note the sharp boundaries to the wall rock, f) pseudotachylyte with only small fragments from the host rock, aligned within the center of the pseudotachylyte, most likely due to flow processes, g) scanned thin section showing wall rock fragments of different size embedded in the dark ultra fine grained pseudotachylyte matrix, and h) thin section image (with  $\lambda$ -filter) of pseudotachylyte with injection vein.

fractures and frictional heating, and thus for pseudotachylytes. Melting temperatures are inferred from the absence of host rock minerals as inclusions within the ultra fine grained pseudotachylyte matrix. Therefore, temperatures between  $750^\circ\text{C}$  (melting of biotite, muscovite) up to  $1600^\circ\text{C}$  (melting of high-Ca-feldspar, quartz) are predicted on the main fault (Spray 1992). In consequence, there is a preferred melting of Fe-Mg-Al silicates, which are almost completely absent as mineral inclusions in the pseudotachylyte matrix. Rapid quenching might lead to the crystallization of spherulites, which represents in composition the former melted paragenesis.

#### 5.4. Published age data

Subduction of the South Penninic ocean initiated at around 120 Ma to 100 Ma (Handy and Oberhänsli 2004, and references therein). Pressure-dominated metamorphism in the Lower Austroalpine units occurred at around 90 Ma to 60 Ma, and in the South Penninic and European units at around 60 Ma to 35 Ma (Handy and Oberhänsli 2004, and references therein). Schmid et al. (2004) reported HP metamorphism of South Penninic rocks during the Tertiary, at least for the Western Alps. Handy and Oberhänsli (2004, and references therein) reported thrusting and accretion under HP-greenschist facies conditions during a time span between 88 Ma and 76 Ma for the Austroalpine domain to the south of our study area. These data show the migration of subduction related deformation towards the foreland, which

finally culminated in the collision with the European margin.

The pseudotachylytes occurring along the northwestern margin of the Engadine window have been already dated by Thöni (1981, 1988) using K/Ar geochronology on whole rock pseudotachylyte samples and Rb/Sr geochronology with the thin slab method, respectively. The K/Ar method resulted in different age groups ranging between 53 Ma to 58 Ma, 73 Ma to 78 Ma, and 114 Ma. Thöni (1981) interpreted these ages to reflect Cretaceous pseudotachylyte formation at around 75 Ma. The younger ages should be caused by later thermal or tectonic processes favoring a loss of radiogenic Ar. The older age group is interpreted to be caused by the analyses of older clasts remained within the pseudotachylyte groundmass. The Rb/Sr analyses (Thöni 1988) resulted in two ages around 75 Ma. Together, both methods are thought to reflect pseudotachylyte formation at roughly 75 Ma along the base of the Austroalpine nappe stack.

#### 5.5. Methods

We used different methods to shed light on the timing of unstable slip within the study area. At first, we analyzed the relevant samples with a petrographic microscope. Due to their ultra fine grain size (at least in the groundmass of the pseudotachylytes) we subsequently used scanning electron microscopy (SEM). Microprobe analyses were conducted to identify the bulk

composition of the pseudotachylyte groundmass and the embedded clasts.

Mineral analyses were performed using both a CAMECA SX100 electron microprobe operating in the wavelength-dispersive mode at the GFZ Potsdam and a JEOL JXA-8200 electron microscope at the FU Berlin. Major and minor elements were determined at 15 kV acceleration voltage and a beam current of 11 nA to 20 nA with counting times of 20 s for major elements, and 30 s for minor elements. The standard sets of the Smithsonian Institute (cf. Jarosewich et al. 1980) and of MAC<sup>TM</sup> were used for reference. In addition to focused beam analyses (beam diameter 1 µm to 10 µm) we used defocused beams with a beam diameter ranging from 30 µm up to 100 µm. This variation was necessary due to differences in the internal structure of the samples regarding to size, concentration and distribution of embedded clasts in order to cover exclusively groundmass material. Microprobe analytical data are given in the appendix A. The JEOL JXA-8200 microprobe was additionally used to obtain back-scattered electron images (BSE). In addition, we used a DSM 962 scanning electron microscope (SEM) at the GFZ Potsdam to obtain secondary electron images (SE), as well as BSE images.

The study of Müller et al. (2002) pointed out that reliable results for pseudotachylyte formation ages can be best achieved using the  $^{40}\text{Ar}/^{39}\text{Ar}$  method, both with stepwise heating or laser ablation. Therefore, we conducted  $^{40}\text{Ar}/^{39}\text{Ar}$  geochronology with stepwise heating using a laser on pseudotachylytes from the northwestern part of the Engadine window to further constrain their formation ages, and to relate them to the overall geological evolution of the South Penninic-Austroalpine plate interface zone. Argon, which is expelled from the sample in the different temperature steps, was simultaneously

measured in a mass spectrometer, and Ar isotopes were calculated for each step.

In an initial phase, we macroscopically selected pseudotachylytes, which appear to be undeformed and less altered. Petrographic microscopy was used to study the chosen samples in more detail in terms of amount and petrography of clasts embedded within the ultra fine grained pseudotachylyte matrix. Care was taken to exclude material altered by weathering or fluid-rock interaction. Afterwards, 300 µm thick slices of pseudotachylytes were produced and highly polished on both sides. Then, these slices were cut into small pieces of roughly 5 x 5 mm, and were checked using a binocular microscope to avoid embedded clasts, which would represent an error source for excess argon. Samples were washed in de-ionized water to remove fine powder on the surface of grains (health risk after irradiation). After washing, grains were dried in an oven at roughly 100°C.

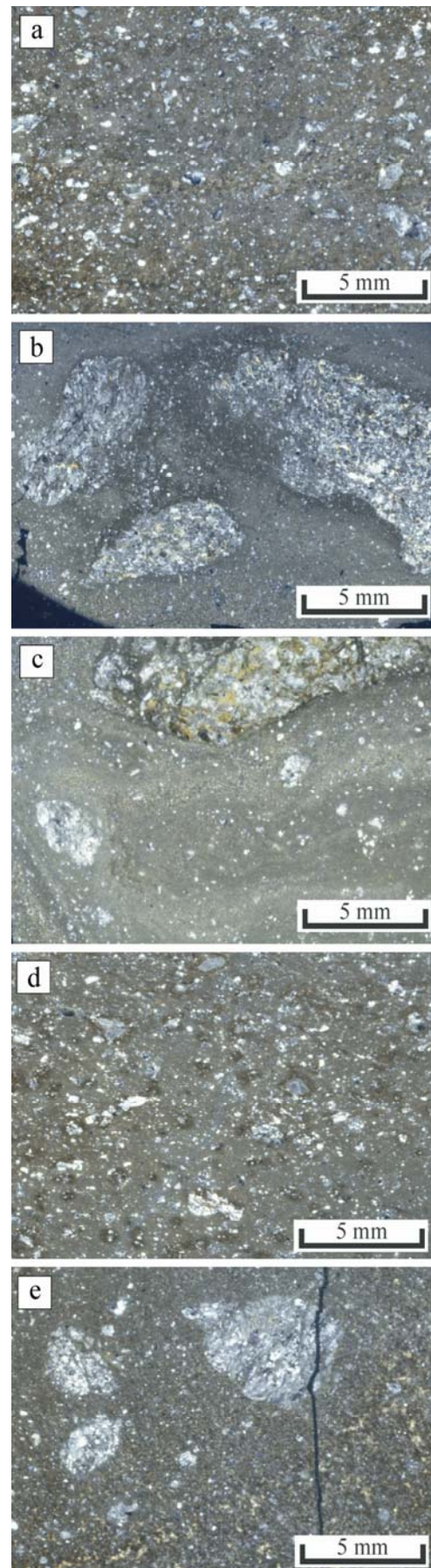
For irradiation, samples were individually wrapped in Al foil and then packed into holes within a 99.999 % pure Al disk. Samples were irradiated for four days in a reactor at the GKSS Geesthacht. After the irradiated samples returned from the reactor, the Al foils were opened and the samples were recollected for subsequent argon isotope analyses. The grains were loaded into holes within a Cu disk. This disk was finally introduced into a vacuum line at the Ar laboratory of the University of Potsdam. We used an automated laser extraction and gas cleanup system operating with both a Merchantek LUV266X quadrupled laser emitting UV at 266 nm and a Merchantek floating MIR10IR (CO<sub>2</sub>) (20W Nd-YAG) laser. These laser systems allow both in-situ ablation of small spots on the samples and bulk step-heating. After extraction of Ar gas from the sample by step heating (several steps until total fusion), the gas was purified in the ultra high vacuum

analytical line. Ar gas was introduced into a Micromass 5400 Static Vacuum Mass Spectrometer. Then, the isotopic ratios were obtained. Finally, obtained data were used to produce plateau and isochron plots, both normal and inverse. Ages were calculated using the Isoplot/Ex program of Ludwig (1999). The use of degassing steps to define a plateau age is defined in several ways, e.g. by a contiguous gas fraction comprising more than 50% of total  $^{39}\text{Ar}$  released (Fleck et al. 1977), or by a sequence of five or more steps, where all data agree within  $2\sigma$  error (Berger and York 1981). Analytical errors were applied within the calculation using weighted errors. Data point errors are  $2\sigma$  standard deviation. Data of the different analyses are summarized in the appendix B.

### 5.6. Sampling and petrography

Throughout the working area (Figs. 5.1, 5.2) we sampled pseudotachylytes, which appeared macroscopically fresh and unaltered. They occur in veins of up to 20 cm width (Fig. 5.4). Freshness of samples was subsequently checked by using petrographical and binocular microscopes. In consequence, we selected five samples for further analyses. In general, the pseudotachylytes exhibit a dark ultra fine grained groundmass with embedded clasts, both comprising wall rock fragments and single minerals, mostly quartz and minor feldspar (Fig. 5.4). Description of the samples is organized geographically; first introducing samples from the Jamtal, followed by the Val Tasna, and the valley Breites Wasser (Fig. 5.2).

Figure 5.5: Scanned thin sections of samples used for  $^{40}\text{Ar}/^{39}\text{Ar}$  geochronology. a) sample 1b, b) sample 5, c) sample 16, d) sample J96-1, and e) sample J96-2. See text for details.



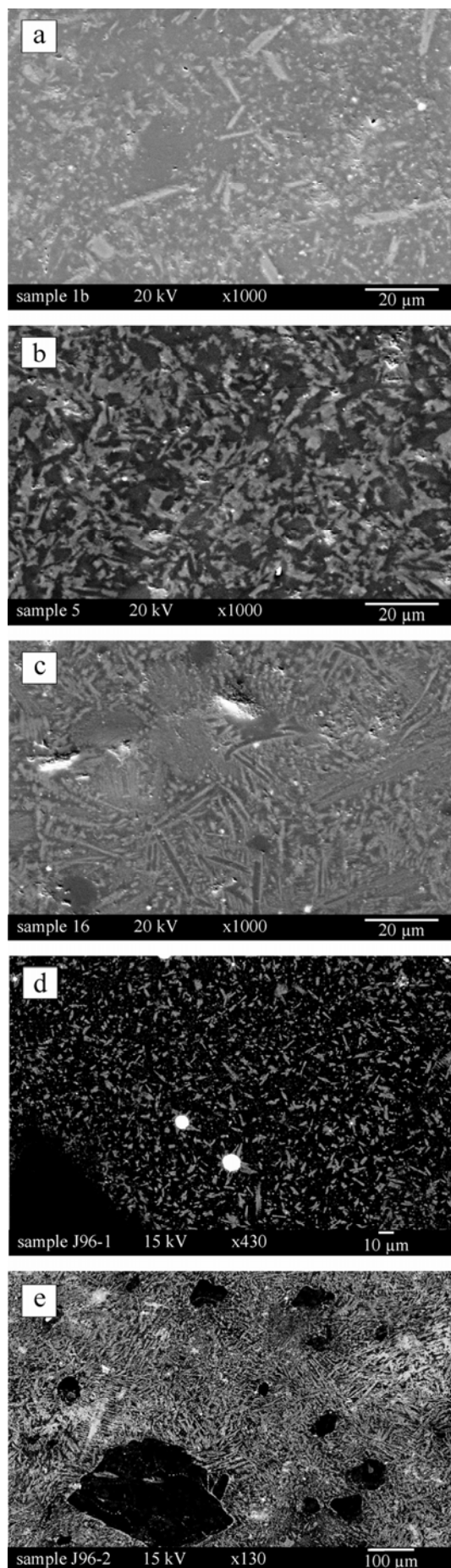


Figure 5.6: BSE and SE images obtained by microprobe and SEM of samples used for  $^{40}\text{Ar}/^{39}\text{Ar}$  geochronology. a) sample 1b, b) sample 5, c) sample 16, d) sample J96-1, and e) sample J96-2. See text for details. Acceleration voltage is 15 kV and 20 kV, respectively. Magnification is 130, 430, and 1000, respectively.

Sample 1b represents a pseudotachylyte taken from the basal parts of the Austroalpine upper plate at the northwestern rim of the Engadine window in the Jamtal valley (Fig. 5.2). On a macroscopic scale, the pseudotachylyte appears to be dark with only minor inclusions within a dense matrix. On a microscopic scale, the sample exhibits a large number of small inclusions of both wall rock fragments and single minerals (Fig. 5.5a). While using 300  $\mu\text{m}$  thin polished slices and a binocular microscope we avoided to probe these clasts. The SE image obtained by the SEM shows small lasts of only 20  $\mu\text{m}$  length comprising the dense ultra fine grained groundmass (Fig. 5.6a). A microprobe analyses of its bulk composition exhibits roughly 60 mole-%  $\text{SiO}_2$ , 19 mole-%  $\text{Al}_2\text{O}_3$ , 7 mole-%  $\text{FeO}$ , and minor amounts of  $\text{TiO}_2$ ,  $\text{MgO}$ ,  $\text{CaO}$ ,  $\text{Na}_2\text{O}$  and  $\text{K}_2\text{O}$ . This might point to a mixture between amphibole and feldspar, both reflecting the paragenesis of the host gneisses.

Sample 5 is a pseudotachylyte sampled in the Val Tasna (NW part of Engadine window, Fig. 5.2). Macroscopically, it exhibits a dark and dense groundmass with large wall rock fragments. A few single mineral inclusions are visible. Microscopically, an ultra fine grained matrix with minor inclusions, smaller in comparison to sample 1b, and some large wall rock fragment are visible (Fig. 5.5b). The BSE image of the matrix shows the growth of very small (a few  $\mu\text{m}$  thick) lasts of single crystals (Fig. 5.6b). The bulk microprobe analysis points again to a possible mixture between amphibole and

feldspar. Here, the groundmass is enriched in Ca.

Sample 16 represents a pseudotachylyte from the Val Tasna in the northwestern part of the Engadine window (Fig. 5.2). The macroscopic dark and dense matrix contains small wall rock fragments, and single minerals. A few larger fragments from the host gneiss are also visible. This is also reflected in the microscopic view. In addition, flow textures from the primary melting stage might be present (Fig. 5.5c). The BSE image exhibits needles and partly spherulites, approved signs for crystallization from a melt (Fig. 5.6c). Bulk analysis points to a mixture of amphibole and feldspar as well. The groundmass is enriched in FeO compared to the previous analyzed samples.

J96-1 is a pseudotachylyte sample taken from the valley Breites Wasser, a side valley of the Jamtal (Fig. 5.2). This sample originates about 20 m above the main thrust plane. The host rock is an amphibole bearing layered gneiss. On the macroscopic scale, the matrix is dense and dark. Only a few inclusions of both wall rock fragments and single minerals are visible. This is also valid for the microscopic scale. There, the matrix exhibits parts with less frequent wall rock fragments and single minerals (Fig. 5.5d). These areas were subsequently used for further preparation. The BSE image shows ultra fine grained needles within the matrix. Partly, these needles form dendritic and spherulitic structures starting to growth on clast surfaces. In addition, sulfide droplets are visible within this sample, formed due to the immiscibility of a silicate and a sulfide melt (Fig. 5.6d). This is interpreted as to occur during pseudotachylyte formation (Magloughlin 2005). They also represent sites of preferred nucleation of newly crystallized lasts. The microprobe bulk analysis of this sample resulted in a mixture of amphibole and plagioclase comprising the groundmass. According to the microprobe

analysis, the lasts are most likely amphibole.

Sample J96-2 represents a sample from the vicinity of sample J96-1 showing comparable macroscopic and microscopic structures (Figs. 5.5e, 5.6e). Here, the individual lasts are a little bit coarser grained (individual dendritical needles up to 100  $\mu\text{m}$  in length). Therefore, the structures indicating initial growth from a melt phase (dendrites, spherulites) are best visible. Microprobe bulk composition points to a mixture of feldspar and amphibole as well.

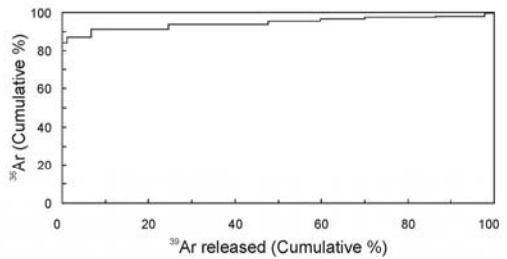
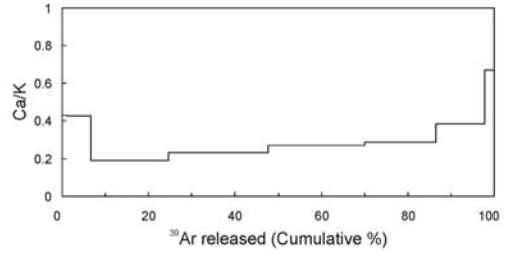
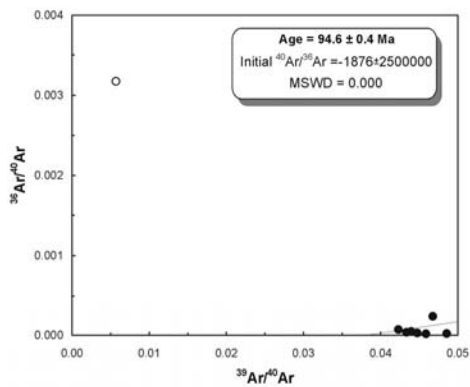
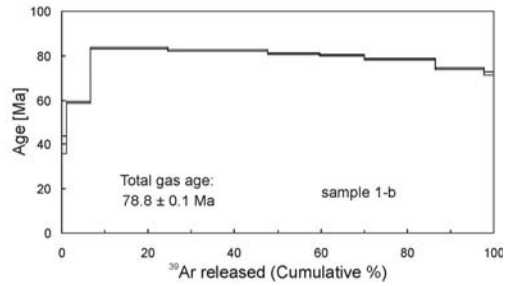
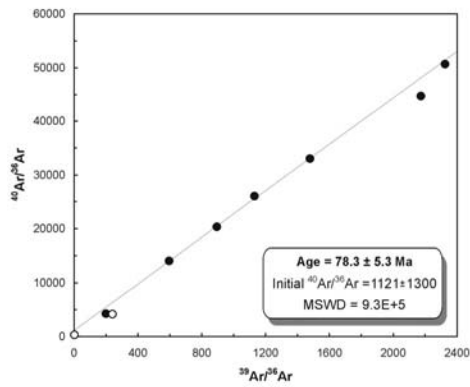
One fact has to be mentioned. Due to the ultra fine grained texture of the groundmass, the analysed bulk composition could reflect the incorporation of other minerals beside amphibole and feldspar, such as biotite. But this fact could not be solved due to analytical limitations.

## 5.7. Results

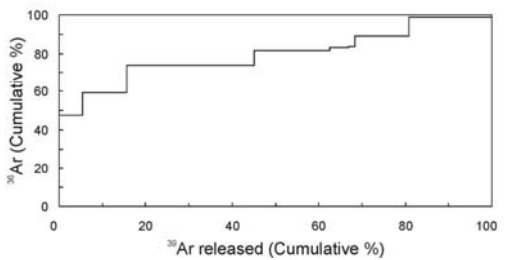
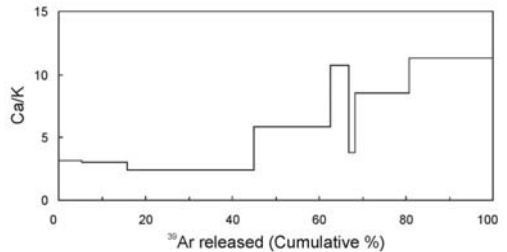
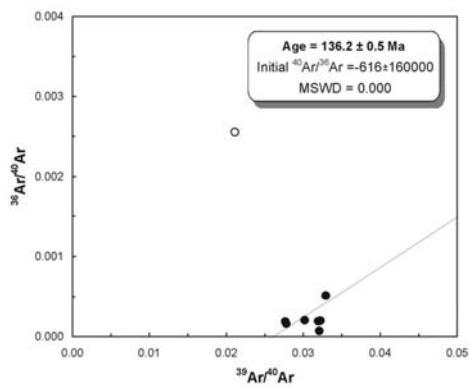
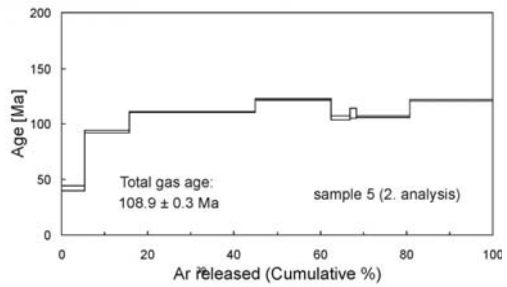
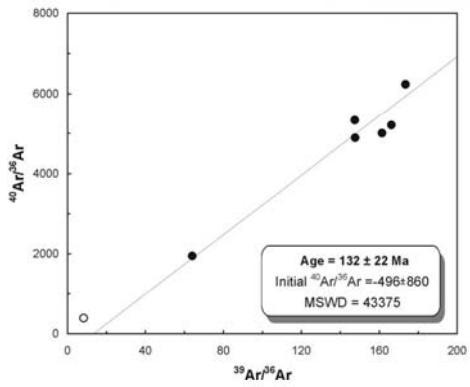
To obtain  $^{40}\text{Ar}/^{39}\text{Ar}$  isotopic data, groundmass grains were heated up with the laser system until total fusion, and the gas was purified and subsequently discharged into the mass spectrometer. There, isotopic ratios were obtained for each gas release step. These data were used to produce isochron and plateau plots, and ages were calculated with the Isoplot/Ex program of Ludwig (1999). Table 1 gives an overview about the ages calculated for each sample.

Sample 1b (Jamtal valley, Figs. 5.2, 5.7a) yielded a total gas age of  $78.8 \pm 0.1$  Ma. For isochron calculation we omitted the first two steps of degassing, because of possible influence of radiogenic Ar loss due to diffusion, which would result in too low ages. Calculating the isochron age with the remaining data points resulted in  $78.3 \pm 5.3$  Ma, which is similar to the total gas age. The inverse isochron age resulted in  $94.6 \pm 0.4$  Ma. A plateau age was not obtained, because individual gas release

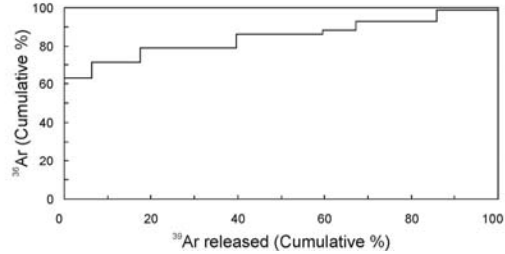
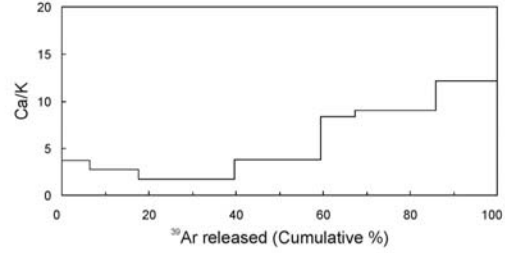
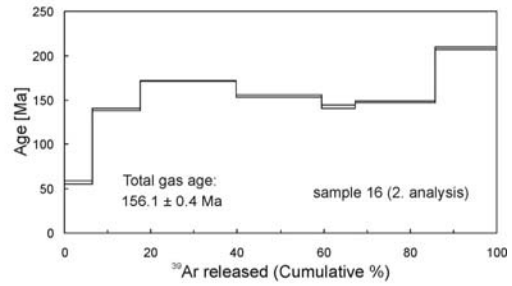
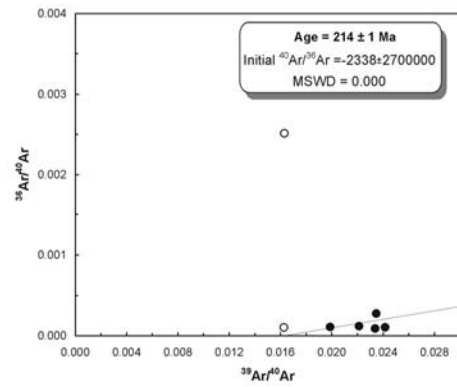
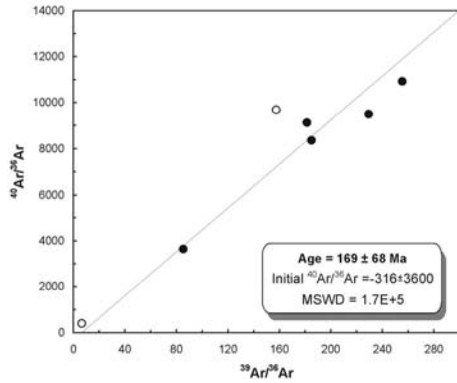
**a 1b**



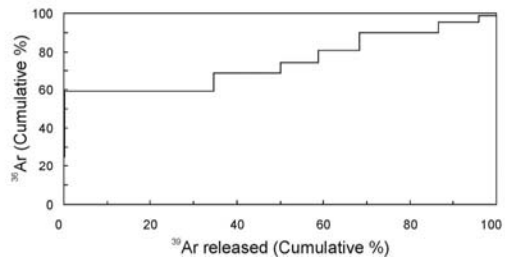
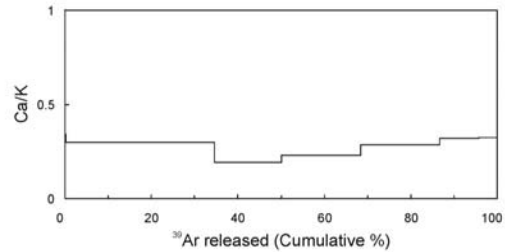
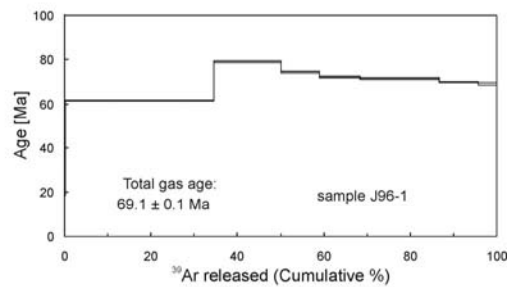
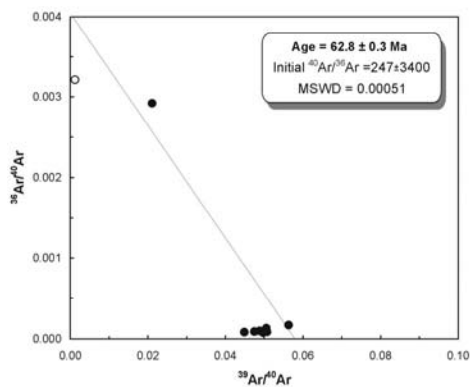
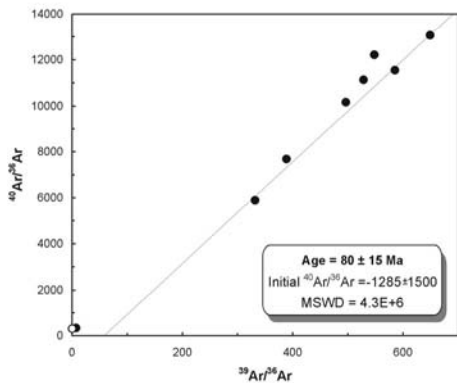
**b 5**



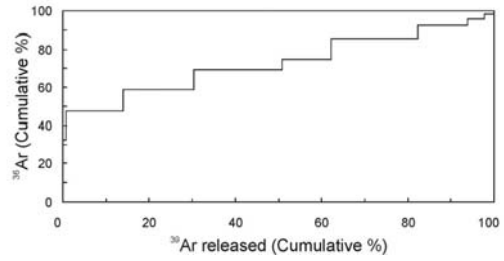
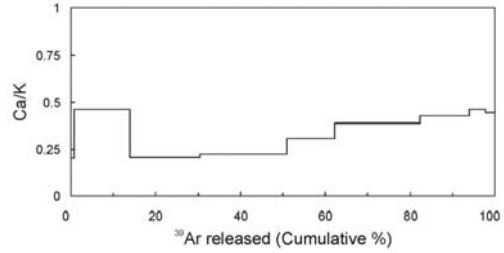
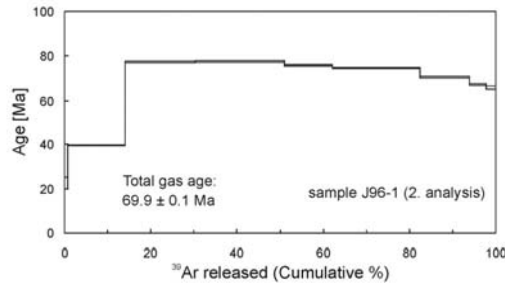
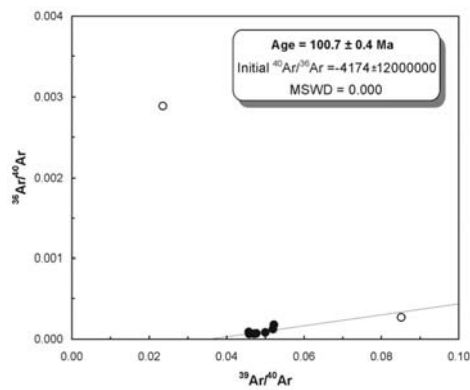
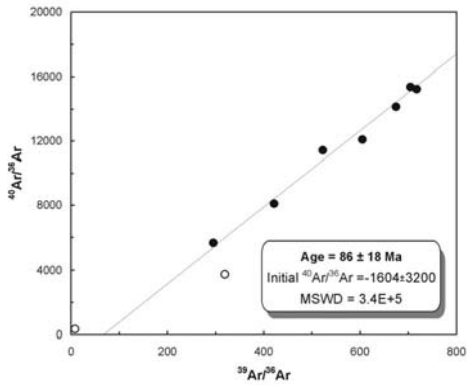
**c 16**



**d J96-1**



**e J96-1 (2)**



**f J96-2**

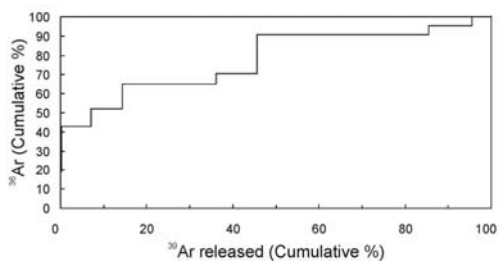
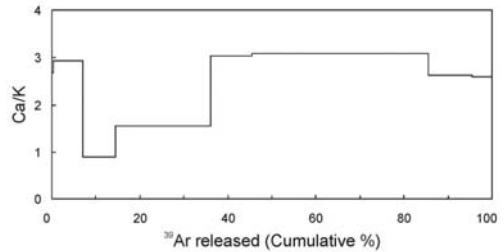
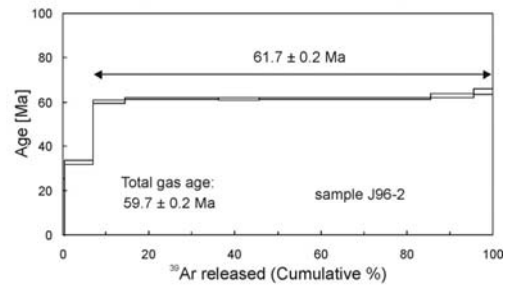
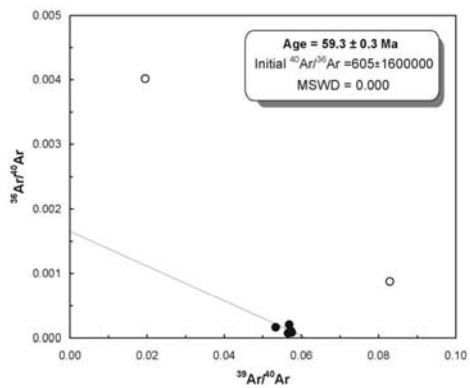
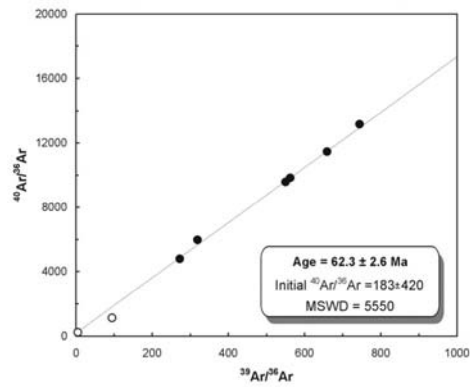


Figure 5.7: Normal isochron, inverse isochron, and plateau diagrams for the analysed samples. Evolution of Ca/K ratios and cumulative Ar release is also given. In addition, different calculated ages are indicated. a) sample 1b, b) sample 5, c) sample 16, d) sample J96-1, e) second measurement of sample J96-1, and f) sample J96-2. See text for details and discussion of data.

steps violated the standards in defining plateau steps (see Chapter 5.5). The Ca/K ratio is quite low, ranging between 0.2 and 0.4. It increases in the last step (total fusion) to roughly 0.7.

Sample 5 (Val Tasna, Figs. 5.2, 5.7b) yielded a total gas age of  $108.9 \pm 0.3$  Ma. We omitted the first gas release step for isochron calculation due to possible excess Ar or Ar loss. The thereby obtained isochron age is  $132 \pm 22$  Ma. The inverse isochron yields an age of  $136.2 \pm 0.5$  Ma. The calculation of a plateau age was not possible for the same reasons as for sample 1b. The Ca/K ratio (between 4 and 11) is slight increased in the last few degassing steps.

Sample 16 (Val Tasna, Figs. 5.2, 5.7c) resulted in a total gas age of  $156.1 \pm 0.4$  Ma. We rendered the first and the last degassing steps for isochron calculation due to the individual too low and too high ages, respectively. The normal isochron age resulted in  $169 \pm 68$  Ma. The inverse isochron yields an age of  $214 \pm 1$  Ma. In addition, no plateau age was defined. Ca/K ratios are around 5, increasing to around 10 in the last few steps of Ar release.

Sample J96-1 (Breites Wasser, Figs. 5.2, 6.7d) yielded a total gas age of  $69.1 \pm 0.1$  Ma. Again, the first degassing step was disregarded for isochron calculation due to possible excess or loss Ar. The obtained isochron age is  $80 \pm 15$  Ma. The inverse isochron resulted in  $62.8 \pm 0.3$  Ma. No plateau steps were defined. The Ca/K ratios are generally low around 0.4. In order to check to quality of separation and Ar measurements we conducted a second measurement for the same sample (Fig. 5.7e). This resulted in a total gas age of  $69.9 \pm 0.1$  Ma. We omitted the first two steps in gas release for isochron calculation, which resulted in  $86 \pm 18$  Ma.

The inverse isochron age is  $100.7 \pm 0.4$  Ma. No plateau age was obtained. Ca/K ratios are again low, ranging between 0.25 and 0.5.

Sample J96-2 (Breites Wasser, Figs. 5.2, 5.7f) yielded a total gas age of  $59.7 \pm 0.2$  Ma. The first two steps of Ar release were not included into isochron calculation. Normal isochron resulted in an age of  $62.3 \pm 2.6$  Ma. The inverse isochron yielded an age of  $59.3 \pm 0.3$  Ma. Steps 3 to 8 define a plateau. Therefore, the calculated plateau age is  $61.7 \pm 0.2$  Ma. The Ca/K ration is between 1 and 3.

## 5.8. Discussion

Due to the melt origin of pseudotachylytes a resetting of the Ar isotope system is generally expected by degassing of the melt (e.g. Müller et al. 2002). This argues for the use of the  $^{40}\text{Ar}/^{39}\text{Ar}$  isotope system to assess pseudotachylyte generation ages. Potassium bearing phases such as biotite, amphibole, or, to a lesser extend, K-feldspar and low-Ca-plagioclase, are preferentially melted due to their lower melting points (Spray 1992, Müller et al. 2002). Newly crystallized phases would represent the mineralogy of the previously molten paragenesis, also exhibiting K-bearing phases as a prerequisite for the use of the  $^{40}\text{Ar}/^{39}\text{Ar}$  isotope system. This is in accordance with our microprobe bulk analyses of the pseudotachylyte groundmass pointing to a mixture of amphibole, feldspar and possibly biotite, which equal the paragenesis of the host rocks (see Chapter 5.6). As long as the newly formed minerals recrystallized from a completely degassed melt, they do not incorporate initial Ar, and therefore providing correct  $^{40}\text{Ar}/^{39}\text{Ar}$  ages (Müller et

Table 1. Summary of Ar/Ar geochronological data.

sample	mineral	J value	total gas age [Ma]	isochron age [Ma]	MSWD	inverse isochron age [Ma]	MSWD	plateau age [Ma]	age interpretation [Ma]
<i>Jamtal valley</i>									
1b	gm	0.00205	78.8 ± 0.1	78.3 ± 5.3	9.3 E+5	94.6 ± 0.4	0.00	no plateau	78
<i>Val Tasna</i>									
5	gm	0.002049	108.9 ± 0.3	132 ± 22	43375	136.2 ± 0.5	0.00	no plateau	> 110 (?)
16	gm	0.002049	156.1 ± 0.4	169 ± 68	1.7 E+5	214 ± 1	0.00	no plateau	> 150 (?)
<i>Breites Wasser</i>									
J96-1	gm	0.00205	69.1 ± 0.1	80 ± 15	4.3 E+6	62.8 ± 0.3	0.01	no plateau	65
	gm	0.00205	69.9 ± 0.1	86 ± 18	3.4 E+5	100.7 ± 0.4	0.00	no plateau	70
J96-2	gm	0.00205	59.7 ± 0.2	62.3 ± 2.6	5550	59.3 ± 0.3	0.00	61.7 ± 0.2	60

gm = groundmass

al. 2002). However, the very short time span expected for frictional melting is supposed to result in only partial isotopic homogenization and the incorporation of inherited  $^{40}\text{Ar}$  (Müller et al. 2002). This makes the use of the  $^{40}\text{Ar}/^{39}\text{Ar}$  method and the interpretation of the data a quite challenging task.

We tried to omit wall rock fragments and single minerals by the investigation of the 300  $\mu\text{m}$  thick polished slices using a binocular microscope while cutting the pieces for subsequent analyses, as long as they were recognizable at that scale. According to Shimamoto and Nagahama (1992), pseudotachylytes are characterized by the absence of the finest fraction of clasts incorporated within the matrix, when compared to e.g. cataclasites or ultracataclasites. This might be caused by the preferential melting of smaller fragments (e.g. Spray 1992). Therefore, our approach to omit visible fragments might be appropriate to render most of the inherited and distracting clasts. Otherwise, the BSE and SE images obtained with the microprobe and SEM show small newly crystallized lasts, and older fragments (in the range of a few tens of  $\mu\text{m}$ ), which act as nucleation sites. In consequence, we cannot argue for a complete leave out of wall rock fragments and single crystals. They provide a source for inherited  $^{40}\text{Ar}$ ,

complicating the interpretation of the obtained isotopic data.

The use of a laser system in order to degas Ar results in a rather localized heating of the sample. Despite of the small spot size, we expect the degassing of Ar to occur from a mixture of the ultra fine grained newly crystallized lasts of possible amphibole, feldspar, and biotite, as well as from wall rock fragments and single crystals, rather than from a homogeneous solidified melt. Therefore, the source for the degassed Ar cannot be tightly constrained, providing an additional error source for analyses. In consequence, the assessment of the potassium content and the thereby constrained minimum weight of the sample to obtain an ample amount of degassed Ar and therefore reliable age results are complicated, if not completely impossible. This might be an additional cause for the badly constrained plateau plots, which failed to produce plateau ages in most cases. In addition, the discrepancy between the different isochron ages and the total gas ages can thereby be explained. In consequence, considering the inhomogeneous texture of the pseudotachylyte matrix, we used the obtained ages to define an “interpreted age” of the individual samples. In addition, the Ca/K ratios provide further hints for the incorporation of wall rock fragments,

which are most likely composed of quartz and feldspar (probably high-Ca-feldspar, e.g. Spray 1992)). As the Ca/K ratio increases for the total fusion step, the incorporation of wall rock fragments is assumed resulting in an apparently too old age for pseudotachylyte generation.

Considering all limitations, we interpreted the age of sample 1b to be roughly 78 Ma due to the similarity of the total gas and normal isochron ages. We excluded the inverse isochron age, because of the clustering of data points resulting in problems constraining the regression line. Therefore, generation of the pseudotachylyte is assumed at ~ 78 Ma. The development of Ca/K ratios might point to the degassing of Ca bearing phases in the higher temperature steps (probably inherited from the wall rock).

Sample 5 is more difficult to evaluate. The total gas age, and both isochron ages differ, not overlapping within errors. Therefore, we interpret the obtained Ar result to point to an age greater than ~ 109 Ma. If this represents a real pseudotachylyte generation age cannot be confirmed. Ca/K ratios strongly alternate for the analysed steps, which points to the incorporation of Ca phases, probably inherited wall rock fragments or single minerals. Microprobe bulk analyses resulted in an elevated Ca content as well.

For sample 16, all individual calculated ages mismatch. The total gas age and the normal isochron age overlap within errors, which is caused by the large error of the latter. The high Ca/K ratios and their development during stepwise heating might point to the involvement of material from the wall rock, degassed at least in the last few steps. Therefore, we interpret the obtained values to result in an age greater than 150 Ma, probably reflecting an age obtained from a disturbed isotope system, rather than a generation age.

Normal isochron and total gas ages for sample J96-1 overlap within errors. In addition, the inverse isochron is roughly

comparable to the total gas age. Ca/K ratios are low and do not differ significantly. The second analysis resulted in comparable values, despite of the older inverse isochron age. In consequence, we interpret an age of ~ 65 Ma for this sample. This might reflect a pseudotachylyte generation age.

The best values were obtained for sample J96-2. Total gas age, normal isochron age, and inverse isochron age overlap within the quite small errors. In addition, a plateau age could be defined, which is in a similar range. Ca/K ratio did not provide a clear hint for the incorporation of material from the host rock. Therefore, we interpret that this sample reflects pseudotachylyte generation at roughly 60 Ma.

The Ca/K ratios for samples, from which we obtained the most reliable pseudotachylyte generation ages are much lower than from the samples without a meaningful age. Therefore, monitoring the Ca/K ratio provide an additional hint for the reliability of the obtained ages in terms of possible incorporation of host rock material, both rock fragments and single minerals.

Finally, our obtained  $^{40}\text{Ar}/^{39}\text{Ar}$  ages, as erroneous they might be, point to unstable slip and therewith associated pseudotachylyte formation within the basal parts of the Austroalpine nappe stack during a prolonged time span between 60 Ma to roughly 80 Ma. The data of Thöni (1981, 1988) fall into the bracketed time frame. During that time, South Penninic oceanic crust was subducted underneath the Austroalpine upper plate.

## 5.9. Conclusion

In the here presented study we show  $^{40}\text{Ar}/^{39}\text{Ar}$  ages obtained by stepwise heating using a laser system, which constrain the generation of pseudotachylytes within the basal parts of the Austroalpine nappe stack at the

northwestern rim of the Engadine window. Samples were gained directly above the main thrust plane, where the Austroalpine overrides the South Penninic domain. This occurred during the subduction of the South Penninic ocean underneath the Austroalpine upper plate in the Late Cretaceous to the Eocene.

The heterogeneous texture of the ultra fine grained pseudotachylyte groundmass, most likely composed of a mixture of amphibole, feldspar and biotite, as well as the incorporation of host rock material of comparable size (rock fragments and single minerals) complicate the interpretation of the isotopic data. The Ca/K ratio provides first roughly indications for the degassing of material enriched in Ca, most probable the inherited host rock material.

Taking all analytical and sample derived limitations into account, the assessment of the possible pseudotachylyte generation age is feasible; at least a certain time range can be constrained. For our study area, formation of pseudotachylytes as unambiguous evidence for fossil seismicity is dated to have occurred during a time span between 60 Ma to 80 Ma. This equals isotopic ages for the same working area obtained by Thöni (1981, 1988), which point to unstable slip at roughly 75 Ma. Additionally, our age data expand the time window for the occurrence of unstable slip. Due to the temporal similarity between subduction and pseudotachylyte formation, and the fact that the pseudotachylytes occur subparallel (i.e. slightly discordant) to the main thrust, we interpret the generation of pseudotachylytes to be related to unstable slip processes occurring along the plate interface zone during the course of subduction of the South Penninic ocean underneath the Austroalpine upper plate.

According to Müller et al. (2002) our approach ( $^{40}\text{Ar}/^{39}\text{Ar}$  method, stepwise

heating with laser ablation) might be the most suitable methodology in dating pseudotachylytes. There, we were able to exclude most of the inherited host rock material. Due to the heterogeneous texture of the pseudotachylyte matrix (mixture of different recrystallized minerals, host rock fragments, inherited host rock single crystals) the approach of Thöni (1981, 1988) using whole rock material for K/Ar analyses or thin slabs of pseudotachylyte material for Rb/Sr analyses (which is *sensu stricto* also a whole rock approach) might be erroneous, because of including inherited material to different and undetermined amounts. Nevertheless, his results are comparable to our results, making K/Ar and Rb/Sr a possible option for dating pseudotachylytes as well. However, the dating of pseudotachylytes will remain challenging and erroneous due to the texture of the solidified, and, in most cases, recrystallized melt veins.

## 6. Abandonment of the South Penninic-Austroalpine paleosubduction plate interface zone, Central Alps: constraints from Rb/Sr geochronology

### Abstract

The suture zone between lower-plate South Penninic and upper-plate Austroalpine units is crucial for understanding the early stages of plate convergence in the Central European Alps. Rb/Sr deformation ages for mylonitized rocks of the South Penninic paleosubduction *mélange* and for deformed Austroalpine basement shed light on the pre-Alpine and Alpine deformation history along the suture, as well as on the mode of syn-subduction interplate mass transfer. Rb/Sr age data define two age groups. The first group reflects the pre-Alpine, Paleozoic to Jurassic deformation within the upper plate basement, with varying degree of resetting by subsequent Alpine deformation. The second group marks the termination of subduction-related deformation along the South Penninic-Austroalpine suture zone at ~50 Ma. A foliation-parallel prograde *mobilisate*, precipitated at ~50 Ma within the subduction *mélange*, testifies to the presence of free fluids in the subduction channel. Identical Rb/Sr ages for pervasively deformed Austroalpine and South Penninic lithologies point to tectonic erosion of the upper plate during subduction. Elevated Sr isotope signatures of (meta-) carbonates from the South Penninic *mélange* are due to interaction of syn-subduction fluids with old continental crust. Lack of a metamorphic contrast between the South Penninic *mélange* and the Austroalpine upper plate favors exhumation of the suture zone due to a combination of tectonic underplating and erosion. Most likely, this underplating occurred when the Middle Penninic micro-continent entered the subduction zone. We propose that this process, at ~50 Ma, led to the cessation of deformation within the South Penninic *mélange*, shifted the zone of active deformation into the footwall, and also caused a contemporaneous upper plate uplift and shutoff of sedimentation in Alpine Gosau forearc basins.

### 6.1. Introduction

One key to understand the temporal evolution of fossil orogenic systems as analogues to recently active counterparts is isotopic dating of deformation processes. In this study we provide time constraints, based on Rb/Sr multimineral data, for the end of subduction-related deformation along the suture zone between the basal parts of the upper plate Austroalpine nappe stack and the South Penninic subduction *mélange* in the European Central Alps. Due to the scarcity of suitable mineral assemblages, related to the only low-grade metamorphism during Alpine deformation in the working area (diagenetic grade for

northernmost outcrops, higher greenschist grade for southernmost outcrops), a detailed study of the precise timing of Alpine deformation across and along this paleosubduction plate interface was still lacking. Hence, we investigated outcrops located in the eastern part of Switzerland (Fig. 6.1) along the fossil suture zone, representing samples from both the basal parts of the Austroalpine nappe stack and from the South Penninic *mélange* to clarify the timing of subduction-related deformation. For that purpose we made use of the Rb/Sr system of white mica and coexisting phases (feldspar, apatite, calcite, epidote) in intensely deformed rocks from both tectonic units. In our samples,

deformation and related white mica recrystallization occurred at temperatures well below 500°C - 550°C, ensuring preservation of Rb/Sr signatures related to dynamic recrystallization without major postdeformative diffusional resetting. Additionally, we studied the Rb/Sr isotope signature of 8 marine (meta-) carbonatic samples from the fossil plate interface zone for comparison with the Sr seawater evolution curve to get information about their age relationships and possible interaction with either crustal- or mantle-derived fluids.

The here studied plate interface zone resulted from subduction of the Penninic oceanic domain beneath the continental realm of the Adriatic plate (Austroalpine nappes) in Late Cretaceous - Early Tertiary (e.g. Froitzheim et al. 1996), prior to the onset of Alpine collision with the European margin. Froitzheim et al. (2003) suggested that the subduction zone of the South Penninic ocean was locked at ~50 Ma by the collision of the Middle Penninic micro-continent with the Adriatic margin, leading to the end of deformation along this suture zone at that time. Unfortunately, the authors provide no geochronological data for their time constraints. Large-scale differential tilting during exhumation of the fossil plate interface enables us to study this zone in present day outcrops, and provides access to various paleodepths (Figs. 6.1, 6.2). The exposed fossil plate interface has experienced flow and fracturing over an extended period of time, including minor overprint during Alpine continent-continent collision and subsequent exhumation. Nevertheless, it is shown that the fossil plate interface zone preserved its structural and isotopic record from the time when subduction-related deformation was terminated.

## 6.2. Geological framework

### 6.2.1. Alpine evolution

The European Alps, one of the best-studied mountain belts worldwide, resulted, in their present form, from the collision of the European and the Adriatic continental plates (Austroalpine nappe stack), preceded by southeastward to southward subduction and accretion of the intervening Penninic oceanic domain (Fig. 6.1). Most models differentiate between two 'Alpine' orogenic cycles: A Cretaceous orogenic cycle (referred to as 'Eoalpine', e.g. Wagerich 1995) is characterized by an east to southeast dipping subduction zone resulting in the closure of the Meliata ocean and leaving signatures of subduction-related deformation within the Austroalpine nappes (belonging to the Adriatic plate, e.g. Schmid et al. 2004). Stacking within the Austroalpine units is associated with top-W, locally top-SW and top-NW thrusting (Froitzheim et al. 1994, Handy 1996). The direction of convergence changed to north - south during the Tertiary orogenic cycle (referred to as 'Mesoalpine' to 'Neoalpine', e.g. Wagerich 1995) with top-N thrusting and closure of the Alpine Tethys in between the European and Adriatic plates (Froitzheim et al. 1994, Handy 1996, Schmid et al. 2004). According to Froitzheim et al. (1994) the transition between top-W thrusting and top-N thrusting is marked by a Late Cretaceous extensional phase with top-SE directed normal faulting, which partly reactivates deformation features of the former deformational stages. This clear separation between the Cretaceous and the Tertiary orogenic cycle is only well observable in the Austroalpine nappes of the Eastern Alps (e.g. Schmid et al. 2004). However, subduction and accretion of oceanic units in the Western Alps represents a continuous process from the Late Cretaceous to the Paleogene, transforming a passive continental margin into an active

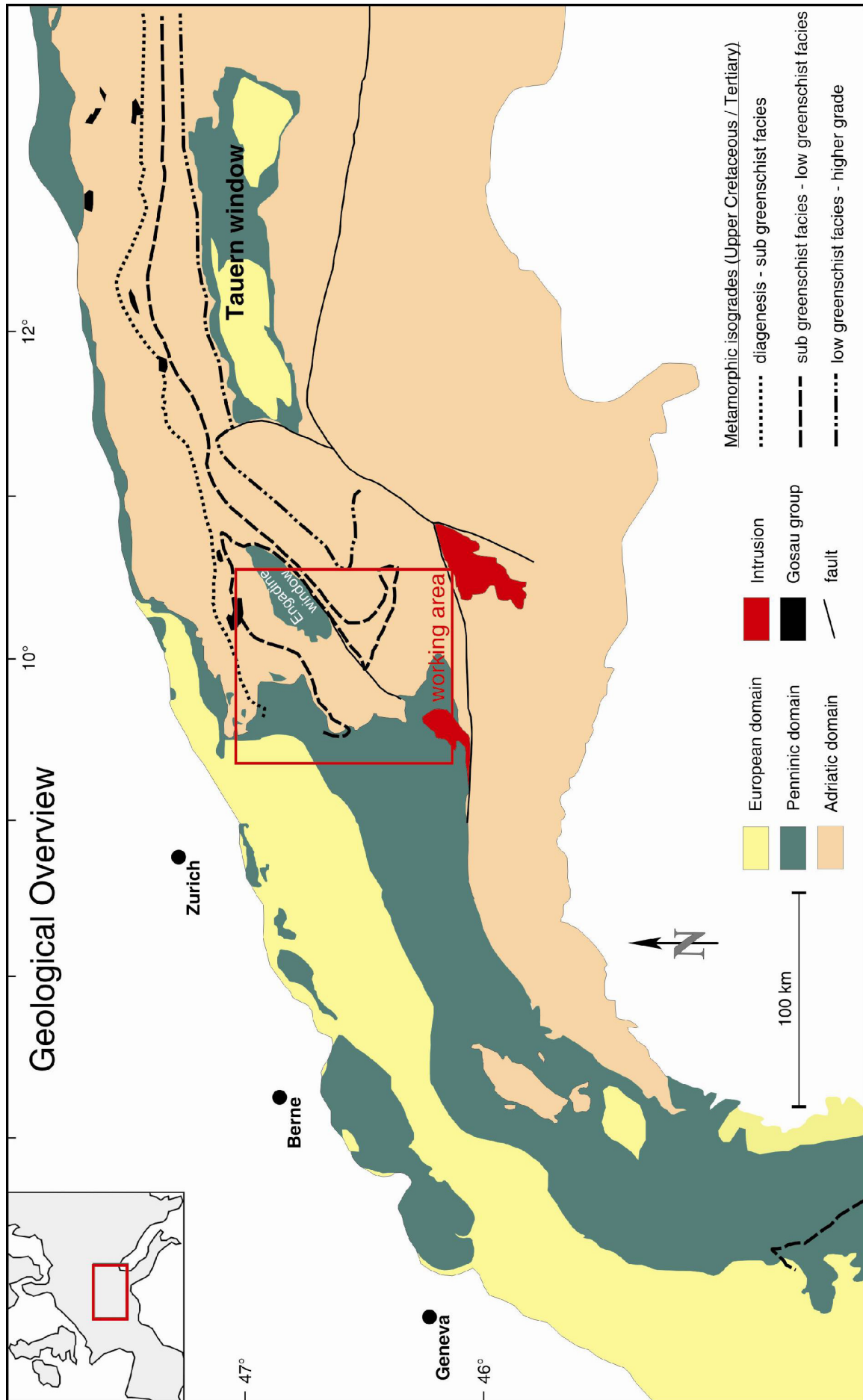


Figure 6.1: Simplified geological map of the European Alps, modified after Frey et al. (1974) and Stampfli et al. (2002). Metamorphic isogrades redrawn after Frey et al. (1999). Rectangle delineates the working area in the Central Alps. Note, the Adriatic domain comprises the Austroalpine nappe stack.



one (i.e. with an active subduction zone, e.g. Schmid et al. 2004).

The oceanic units in between both continental realms (European and Adriatic plate), the Penninic units (Fig. 6.1), were progressively subducted and deformed during convergent plate motion and partly accreted to the front and / or the base of the Adriatic plate. Palinspastic restoration of the Penninic units resulted in two separate oceanic basins divided by a micro-continent (e.g. Florineth & Froitzheim 1994, Schmid et al. 2004). This so-called Briançonnais terrane (or Middle Penninic) separates the northern basin (North Penninic or Valais ocean) from the southern basin (South Penninic or Piemont-Liguria ocean). Fragments from the Piemont-Liguria ocean experienced high pressure metamorphism in the Western Alps during the Tertiary, whereas South Penninic units in the Eastern Alps are characterized by a Cretaceous tectonic imprint associated with variable grades of metamorphism ranging from diagenesis to blueschist facies (Schmid et al. 2004). Owing to the fact that the paleosubduction interface has been tilted and differentially exhumed from original depth, we are able to study it in present day outcrops.

### 6.2.2. *Geology of the working area*

The working area is located in the Central Alps of Eastern Switzerland (Figs. 6.1, 6.2). The main geological units in the area belong to either the South Penninic or the Austroalpine units. In various plate tectonic models the Austroalpine domain

overrides the South Penninic domain during Cretaceous/ Tertiary subduction (e.g. Ring et al. 1988, Schmid et al. 2004). Therefore, the immediate plate interface zone between the South Penninic domain (Arosa zone and the Platta nappe as its direct equivalent to the south [Biehler 1990], Fig. 6.2) and the Austroalpine represents a Late Cretaceous/ Tertiary continent-ocean suture (e.g. Handy 1996, Schmid et al. 2004) of a convergent plate margin. The large-scale structures of the Arosa zone are interpreted by e.g. Ring et al. (1988, 1989, 1990) as the deep parts of an accretionary wedge formed at the tip of and below a thrust belt migrating towards the west. The apparent thickness of the South Penninic domain in the study area varies from a few tens of meters up to more than 2500 m, either reflecting the original thickness or a reduction by subsequent thinning processes.

Ring et al. (1990) pointed out that the lithofacies and the internal structures of the Arosa zone are comparable to characteristics of mélanges found within subduction complexes. Therefore, the South Penninic domain is discussed as a (subduction) mélange of both oceanic material (derived from the South Penninic ocean) and continental fragments (derived from the Austroalpine domain) (Deutsch 1983, Ring et al. 1988 and references therein). Within the subduction mélange, competent blocks of Austroalpine and South Penninic affinity are embedded in a less competent matrix composed of serpentinites or calcareous shales (Ring et al. 1990). Deformation is partitioned into brittle and ductile due to competence contrasts between clasts and matrix (Ring et al. 1988). Metamorphic conditions of South Penninic rocks range from upper diagenetic or lowermost greenschist facies in the north of the working area, to middle to upper greenschist facies in the southern parts (Figs. 6.1, 6.2). The Austroalpine domain consists of a suite of gneissic to amphibolitic, mainly upper crustal rocks

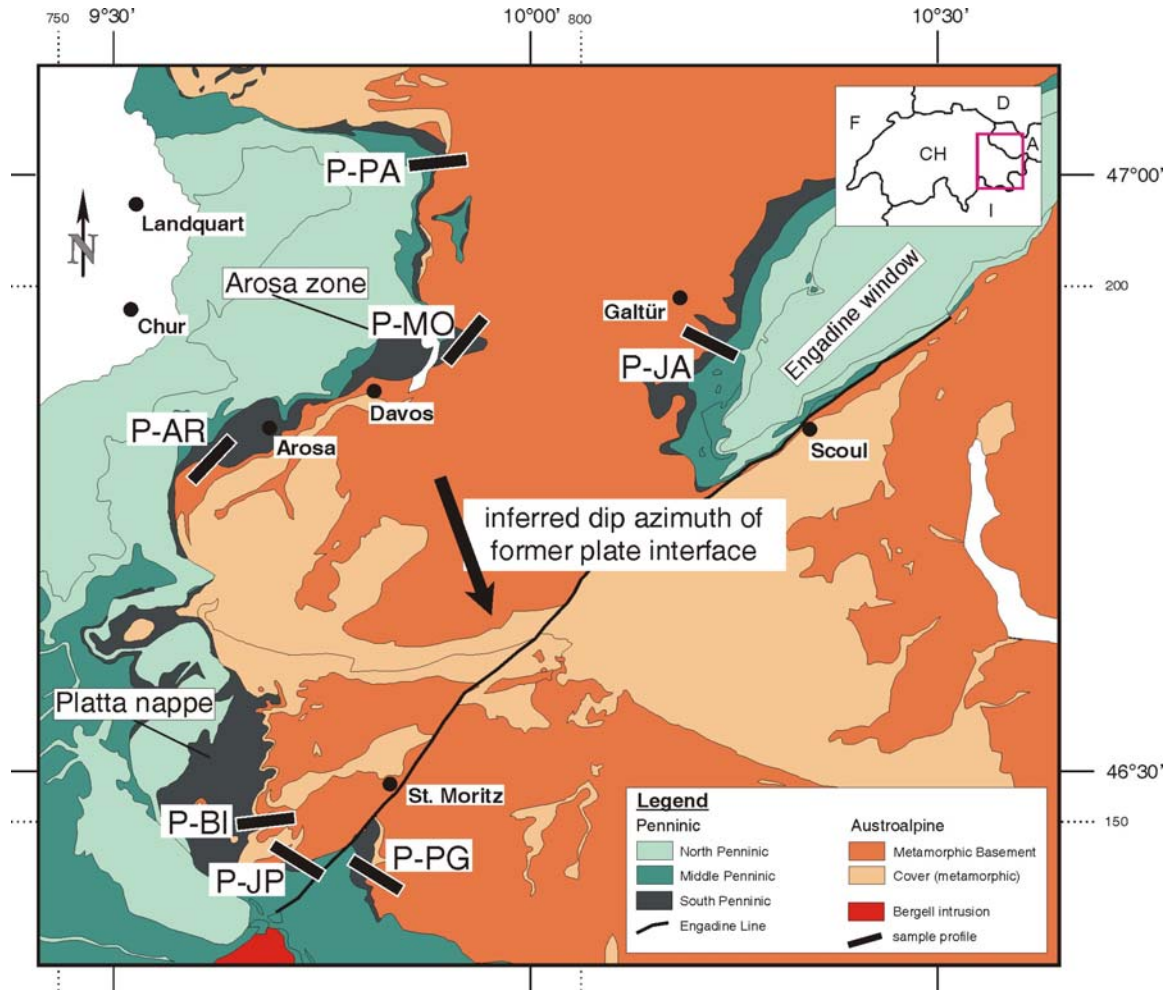


Figure 6.2: a) Tectonic map of the study area emphasizing the suture zone between the South Penninic (black) and the Austroalpine (dashed, part of the Adriatic plate). Black lines indicate different profiles extending from domains of South Penninic origin into Austroalpine rocks. Arrow points to the former dip azimuth of the plate interface. Arosa zone and Platta nappe are local names for rocks of South Penninic affinity. Based on the Tectonic map of Switzerland 1:500.000, 2<sup>nd</sup> edition (1980).

which experienced pre-Alpine (mainly Permo-Carboniferous) and Early (Eo-) Alpine deformation, overlain by and intercalated with variably deformed and metamorphosed Permo-Carboniferous clastic rocks, and Mesozoic sediments (e.g. Florineth & Froitzheim 1994, Manatschal et al. 2003, Ring et al. 1988). Due to large scale differential post-subduction tilting and exhumation of the fossil plate interface zone formerly deeper parts are accessible towards the south.

In analogy to active convergent plate margins we consider the South Penninic subduction mélangé to resemble material of a so-called subduction channel (e.g.

Cloos and Shreve, 1988 a, b; Chapter 4). Cloos and Shreve (1988 a, b) have introduced the subduction channel concept denoting a zone between the upper and the lower plates of convergent plate margins. This zone may typically be up to a few kilometers wide, its material exhibiting a velocity gradient towards both plates, and it probably extends to a depth of more than 100 km (Gerya and Stöckhert 2002). Within the subduction channel, material from both the oceanic and continental plates is intermingled and transported downwards. The channel material may then either get lost into the earth's mantle, it may be partly off-scraped and accreted to the front of a growing accretionary wedge

(frontal accretion), or accreted to the base of the hanging wall (basal accretion) (von Huene and Scholl 1991). Material may also be removed from the tip (frontal tectonic erosion) or the base (basal tectonic erosion) of the upper plate by tectonic erosion (e.g. Clift and Vannucchi 2004). Clasts within the matrix of the subduction mélange provide hints for dominance of tectonic erosion or accretion. According to Oncken (1998) abundance of upper plate fragments in the channel material is a diagnostic criterion for the role of tectonic erosion. Basal tectonic erosion as prevailing mass transfer mode along the South Penninic-Austroalpine plate interface zone is indicated by numerous clasts of upper plate material embedded within the South Penninic mélange (Chapter 4).

### 6.2.3. Structural aspects of the fossil plate interface zone

We measured foliation, lineation, shear bands, tension gashes, folds, faults, and assessed their relative age relationships in a series of profiles across the plate interface, sampling different paleodepths of the paleosubduction zone (Fig. 6.3). The South Penninic mélange close to the contact to the Austroalpine upper plate experienced a penetrative deformation with an inferred direction of tectonic transport changing gradually from top-NW in the north of the working area via top-W in the central parts to top-SW in the southernmost parts (e.g. Chapter 4). This might be explained by oblique subduction, which favors partitioning of deformation. We observed foliation planes dipping moderately toward SE to NE and associated stretching lineations plunging smoothly toward SE and ENE (Fig. 6.3, see also Fig. 4.5 in Chapter 4). These structures are best developed in the south of the working area. Embedded clasts within the matrix of the South Penninic mélange are partly bounded by shear zones

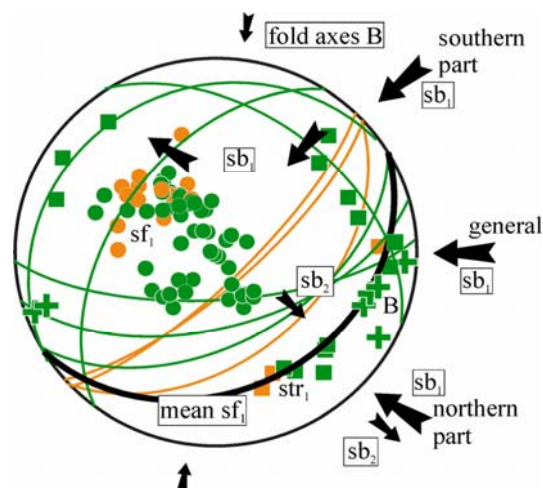


Figure 6.3: Combination of structural data of brittle-ductile to ductile deformation associated with top-NW (northern part of the working area) to top-SW (southern part of the working area) direction of tectonic transport (general top-W, large black arrows). Data are subdivided in: green corresponding to outcrops located within the South Penninic mélange, orange corresponding to outcrops located within the basal parts of the Austroalpine upper plate. Plot is a Schmidt net lower hemisphere, equal-area diagram. In addition, subsequent non-pervasive deformation is indicated (top-SE extension and top-N thrusting, small black arrow). Note that there is no obvious difference in the structural data obtained from outcrops in the South Penninic mélange and the Austroalpine upper plate. See text for data. str = stretching lineation, sf = foliation, B = fold axes, sb = shear bands

also pointing to a general top-W direction of tectonic transport. Deformation of the South Penninic mélange increases towards the south of the working area, which is expressed by a more distinct and tighter foliation, and by the obliteration of sedimentary structures. Deformation with general top-W directed tectonic transport of the Austroalpine nappe stack is expressed by microscale fracture zones reactivating the preexisting foliation of probably Variscan age in the northern part of the working area (Chapter 4). This overprint increases towards the south, where Alpine deformation pervasively overprints the preexisting foliation within at least the basal parts of the upper plate basement. This is expressed by growth and recrystallization of platy minerals (mainly

white mica) parallel to the preexisting foliation. Orientation of foliation in the Austroalpine rocks parallels the corresponding foliation within the South Penninic mélange, at least in the first few hundred meters above the base of the hanging wall. In general, orientation of structural data and the therewith assessed direction of tectonic transport are similar in both the South Penninic mélange and the basal parts of the Austroalpine upper plate (Fig. 6.3).

Subsequent localized deformation with significantly lower intensity overprints the top-W structures, but a complete erasure of the top-W structures in both the South Penninic mélange and the Austroalpine nappes by younger deformational processes cannot be observed (see also Ring 1989, Dürr 1992). There is a superimposed set of brittle-ductile shear bands indicating top-E to top-SE directed tectonic transport, a feature becoming more prominent towards the south (Fig. 6.3). All the above structures are overprinted by top-N thrusting. This shortening direction can be inferred from roughly E-W orientated fold axes of open folds at various scales (Fig. 6.3, Chapter 4).

### 6.3. Published age data

Time constraints on the evolution of the South Penninic mélange are sparse; the few existing data are summarized below (Fig. 6.4). Ocean spreading, and thus opening of the South Penninic ocean, is dated to have occurred at least since the Early to Middle Jurassic ( $186 \pm 2$  Ma Ar/Ar bt, Ratschbacher et al. 2004, 165 Ma Ar/Ar phl, Gebauer 1999). According to Waggreich (2001) and references therein, the transition to an overall convergent setting and the initiation of oblique southward subduction of the Penninic domain beneath the Austroalpine occurred during the Aptian/ Albian, at  $\sim 110$  Ma.

Biostratigraphic ages provide additional constraints on the timing of subduction-related deformation of the South Penninic mélange. Latest sedimentation within the Arosa zone (South Penninic) is documented to have occurred within the Early Coniacian, at  $\sim 90$  Ma (Late Cretaceous, Ring 1989). Flysch deposits from the Platta nappe (South Penninic) show sedimentation ages ranging from Aptian to Albian (late Early Cretaceous; Ring 1989). Overall, no sediments younger than  $\sim 90$  Ma are known from the South Penninic mélange. Biostratigraphic ages for the flysch deposits comprising the footwall of the South Penninic mélange (derived from Middle and North Penninic units, and from the distal European margin, Figs. 6.2, 6.4) range from Early Cretaceous to Early/ Middle Eocene (Trautwein et al. 2001). In addition, Stampfli et al. (2002) reported distal flysch deposition until 43 Ma. In consequence, subduction-related sedimentation lasted at least until the Late Cretaceous to the Early/ Middle Eocene, a time span between  $\sim 90$  Ma to 43 Ma (passage through the subduction channel from termination of sedimentation within the South Penninic ocean to latest sedimentation within the flysch accreted at the base of the South Penninic domain).

Constraints on the timing of subduction-related deformation are also given by isotopic ages pointing to 90 Ma - 60 Ma for a pressure-dominated metamorphism of the Lower Austroalpine units, and 60 Ma to 35 Ma for the South Penninic and European units, respectively (Handy and Oberhänsli 2004, and references therein). Schmid et al. (2004) reported HP metamorphism of South Penninic rocks during the Tertiary, at least for the Western Alps. Handy and Oberhänsli (2004, and references therein) reported thrusting and accreting under HP-greenschist facies conditions during a time span between 88 Ma and 76 Ma for the Austroalpine domain in the southern part of our study area. Earliest high-pressure metamorphism for

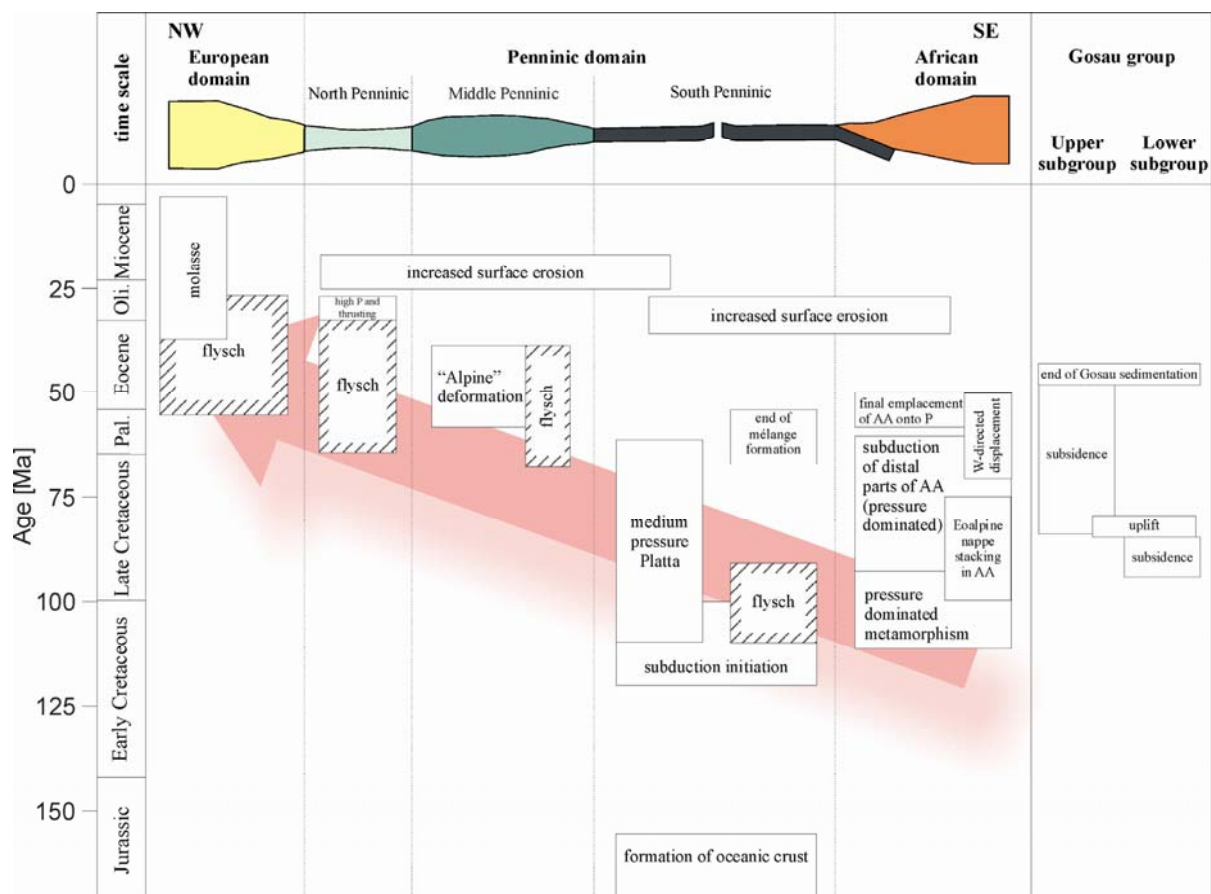


Figure 6.4: Compilation of geochronological data available for the study area concerning the subduction and accretion of the South Penninic domain, deformation within the Austroalpine nappe stack, flysch deposition within the South Penninic domain and its footwall, and deformation within the Middle Penninic, North Penninic and European units. Subsidence and sedimentation history of the Gosau group is also indicated. Light red arrow indicates shift in subduction-related deformation towards the foreland (i.e. towards NW). See text for details and source of data.

parts of the Penninic domain further to the east (Tauern Window) is constrained to  $57 \pm 3$  Ma for the subduction-accretion Rechnitz complex (Ar/Ar amphibole, Ratschbacher et al. 2004). Additionally, Markley et al. (1995) used Ar/Ar geochronology on synkinematic white mica from Middle Penninic (Briançonnais domain) rocks. They obtained ages at around 38 Ma. Together, these data show the migration of subduction and therewith related deformation towards the foreland (i.e. towards NW in modern coordinates), which finally culminated in the collision with the European margin (Fig. 6.4). The northwestward younging of flysch deposition ages is consistent with this

migration (e.g. Handy and Oberhänsli 2004, and references therein).

Constraints for the timing of unstable slip within the basal parts of the Austroalpine upper plate are given by Thöni (1981, 1988). The author presented K/Ar and Rb/Sr data from pseudotachylytes collected along the northwestern part of the Engadine window. Presence of pseudotachylytes is considered as evidence for paleoearthquakes (Cowan 1999). These pseudotachylytes yielded ages of approximately 75 Ma. Additionally, we obtained  $^{40}\text{Ar}/^{39}\text{Ar}$  ages using stepwise heating with a laser system, in order to better constrain the generation of pseudotachylytes within the basal parts of

the Austroalpine nappe stack at the northwestern rim of the Engadine window. This resulted in an expanded time window for the occurrence of unstable slip between 60 Ma and 80 Ma (see Chapter 5).

#### 6.4. Analytical procedures for Rb/Sr geochronology and Sr isotope signature

For the purpose of Rb/Sr isotope analyses we used the internal mineral isochron approach (Glodny et al. 2002, 2005). Samples of small size (approximately 20 - 100 g) were chosen, carefully selected as, wherever viable, texturally exclusively recording a specific recrystallization-inducing tectonic and metamorphic event. In our study this is the pervasive general top-W directed tectonic transport within the South Penninic mélangé and basal parts of the Austroalpine domain, related to the subduction of Penninic units underneath the Austroalpine nappe stack. We focused on samples containing white mica as a high Rb/Sr phase. The Rb/Sr isotope system of white mica is assumed to be thermally stable to temperatures  $>500^{\circ}\text{C} - 550^{\circ}\text{C}$ , but may be fully reset by dynamic recrystallization even at lower temperature (Inger and Cliff 1994, Freeman et al. 1997, Villa 1998). According to Müller et al. (1999) isotopic reequilibration between white mica and coexisting phases during mylonitization may occur at temperatures as low as  $350^{\circ}\text{C}$ . Careful study of the correlation between microtextures and isotopic signatures, both by conventional mineral separation techniques (Müller et al. 1999, Glodny et al. submitted) and Rb/Sr microsampling (Müller et al. 2000, Cliff and Meffan-Main 2003) has shown that complete synkinematic recrystallization in mylonites is usually accompanied by isotopic reequilibration. Therefore, Rb/Sr isotopic data from penetratively deformed rocks can be used to date the waning stages of mylonitic deformation, as long as deformation occurred below the temperature range for

diffusional resetting. In our samples, deformation and related white mica recrystallization occurred at temperatures well below  $500^{\circ}\text{C}$  to  $550^{\circ}\text{C}$  (calcmylonites, subgrain rotation recrystallization in quartz, brittle deformation of feldspar, Chapter 4), which makes sure that Rb/Sr isotopic signatures record dynamic recrystallization under greenschist facies conditions without subsequent diffusional resetting. To detect possible Sr isotope inhomogeneities resulting from isotopic inheritance, from long-term or incomplete dynamic recrystallization, from diffusional Sr redistribution, and/or from alteration processes, white mica was analysed in several, physically different (in terms of magnetic properties and/or grain size) fractions whenever possible. According to Müller et al. (1999) this approach ensures control on possible presence of unequilibrated, pre-deformational white mica relics. In addition, mineral concentrates of feldspar, apatite, calcite, and epidote were produced. Care was taken to exclude material altered by weathering or by late fluid-rock interaction. White mica sieve and magnetic fractions were ground in ethanol in an agate mortar, and then sieved in ethanol to obtain pure, inclusion-free separates. All mineral concentrates were checked, and finally purified by hand-picking under a binocular microscope. Rb and Sr concentrations were determined by isotope dilution using mixed  $^{87}\text{Rb} - ^{84}\text{Sr}$  spikes. Determinations of Rb and Sr isotope ratios were carried out by thermal ionization mass spectrometry (TIMS) on a VG Sector 54 multicollector instrument (GeoForschungsZentrum Potsdam). Sr was analyzed in dynamic mode. The value obtained for  $^{87}\text{Sr}/^{86}\text{Sr}$  of NBS standard SRM 987 was  $0.710268 \pm 0.000015$  ( $n = 19$ ). The observed Rb isotopic ratios were corrected for 0.25% per a.m.u. mass fractionation. Total procedural blanks were consistently below 0.15 ng for both Rb and Sr. Because of generally low and highly variable blank

values, no blank correction was applied. Isochron parameters were calculated using the Isoplot/Ex program of Ludwig (1999). Standard errors, as derived from replicate analyses of spiked white mica samples, of  $\pm 0.005\%$  for  $^{87}\text{Sr}/^{86}\text{Sr}$  ratios, and of  $\pm 1.5\%$  for Rb/Sr ratios were applied in isochron age calculations (cf. Kullerud 1991). Individual analytical errors were generally smaller than these values. Rb/Sr analytical data are given in Table 1.

Additionally, we studied the Rb/Sr isotope signatures of 8 originally marine (meta-) carbonatic samples from the fossil plate interface zone. The Sr-isotopic ratio of seawater is known to vary with time (e.g. Wickman 1948, Gast 1955), so that Sr isotopic compositions of seawater precipitates (e.g. biogene carbonates) may directly be converted to absolute age information ('strontium isotope stratigraphy', Howarth and McArthur 1997, McArthur et al. 2001). In our analytical protocol we dissolved the carbonate samples with 2.5N HCl and monitored Rb contents and Rb/Sr ratios of the samples, to be able to correct for potential in-situ radiogenic ingrowth of Sr.

### 6.5. Petrography and sampling

The South Penninic subduction *mélange* exhibits a N-S gradient in metamorphic grade. In the northern part of the working area, Alpine metamorphism did not exceed diagenetic grades, or lower greenschist facies (see also Chapters 4, 6.2). In the southern part, rocks of the *mélange* as well as the basal parts of the Austroalpine nappe stack were metamorphosed at middle to upper greenschist-facies conditions during Alpine orogeny (as inferred from Si contents in phengitic white mica, e.g. Chapter 4). Along this N-S profile, we sampled calcsilicates, calcmylonites, quartz-mica schists and a quartz-mobilisate (mineralized vein) from the South Penninic *mélange*, as well as quartz mylonites,

mylonitized Permian meta-volcanics and quartz-mica schists from the basal parts of the Austroalpine nappe stack (Figs. 6.5a-i). Samples used for Rb/Sr dating are fine grained, strongly foliated or mylonitized, except for the qtz-mobilisate. Minerals found in these rocks include quartz, feldspar, white mica, biotite, calcite, apatite, opaque minerals, and epidote. Locally, retrograde chlorite occurs. The mineral assemblages in general testify to greenschist-facies conditions during deformation in both the basal parts of the upper plate and the subduction *mélange*. The strong deformation (Figs. 6.5e, f) caused, in most samples, optically complete to nearly complete recrystallization of white mica, apatite, calcite, and albite. Samples show a general top-W direction of tectonic transport (Fig. 6.3). However, overprint by subsequent deformation (top-SE, top-N) is visible to some extent in the field, which is expressed by e.g. a crenulated foliation. We omitted samples with stronger overprint by identifying overprinting relationships at outcrop scale or within thin sections in order to date only a single deformation event (top-W). In the following, the description of the different samples is organized from north to south, and separated between samples for Rb/Sr geochronology, and Sr isotope signature. Mineral abbreviations follow Kretz (1983). The locations of the geochronological samples are shown in Figure 6.6, locations of samples used for Sr isotope signature analyses are shown in Figure 6.7.

Sample 4d represents a mylonite from the base of the upper plate at the northernmost profile P-PA (Fig. 6.6). It consists of heavily sericitized fs (kfs 50 mole-%, ab 45 mole-%, an 5 mole-%), qtz showing subgrain rotation recrystallization, ms (Si p.f.u. 3.15 – 3.24), and minor ap. Foliation is expressed by the alignment of both white mica and feldspar-quartz rich layers. Larger feldspar grains form clasts, which are oriented subparallel to the foliation.

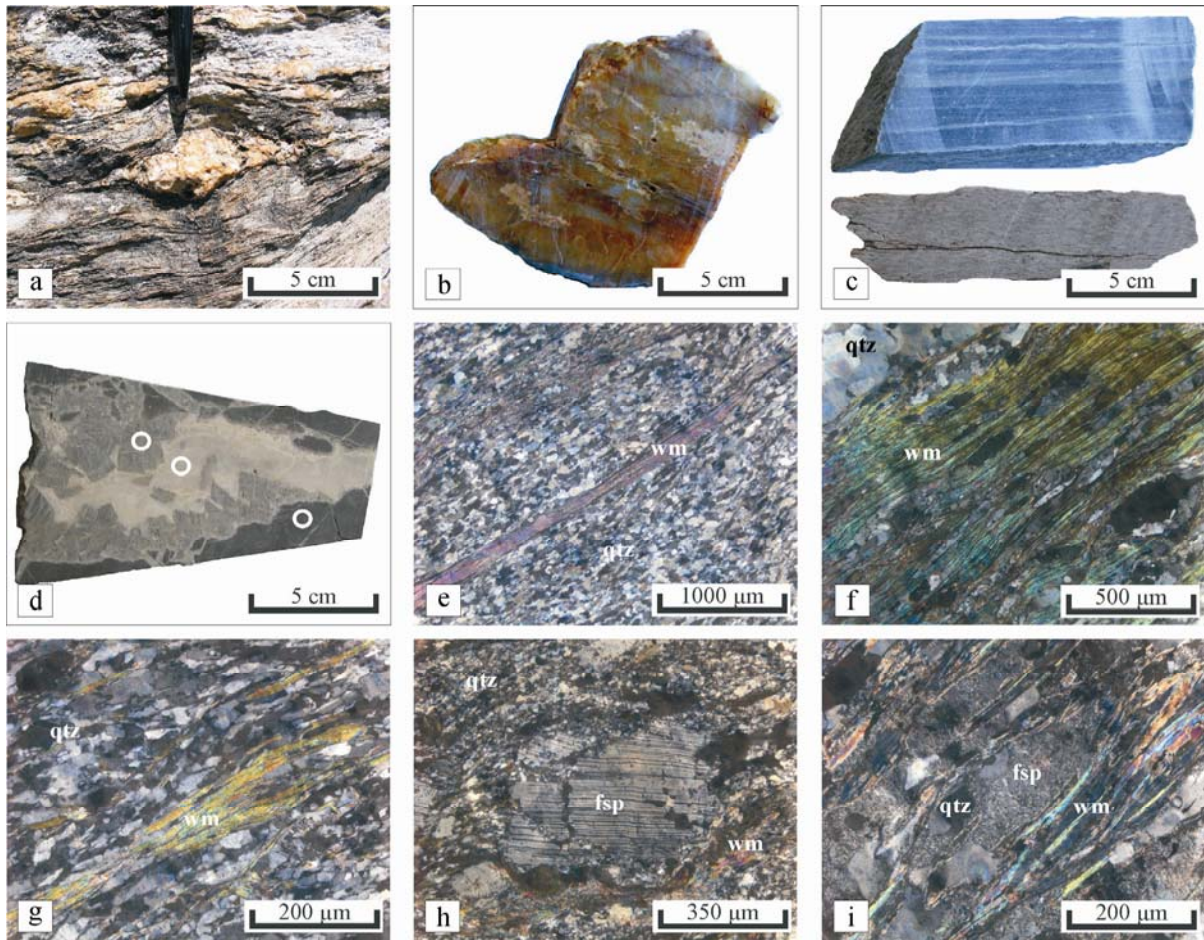


Figure 6.5: Outcrop, hand specimen and thin section images illustrating the different samples analysed for the present study (a) outcrop of foliation parallel prograde mobilisate at profile P-PG, (b) hand specimen of analyses sample B-8 (prograde mobilisate), (c) hand specimen of calcmylonite B-14 exhibiting tight foliation (upper part) and B-11 (qtz rich mylonite, upper plate, lower part of figure), (d) host rock (dark grey) and two vein generations of carbonatic sample 16b (lighter grey areas), white open dots indicate the position of microsampling for Sr isotope analyses, (e) thin section of sample C-15 showing strong foliation expressed by the alignment of white mica (wm), (f) thin section of sample B-11 also indicating deformation-induced recrystallization of white mica in the foliation, (g) thin section showing foliation parallel white mica with large variability of mica grain size (sample B-13), (h) thin section of sample C-12. Presence of some large feldspar clasts within dynamically recrystallized matrix as a possible reason for Sr-isotopic intermineral disequilibrium (see MSWD = 22), (i) thin section of sample J91 showing heavily sericitized feldspar minerals contributing to less complete isotopic reequilibration (see MSWD = 2185).

Sample 10c was taken from a shear zone within the upper plate basement at profile P-MO (Fig. 6.6). This sample represents a quartz-mica schist composed of qtz with bulging and subgrain rotation recrystallization, brownish bt, few heavily sericitized fs (pl with ab ~73 mole-%, an 27 mole-%), and minor ap. The tight foliation is formed by the alignment of fine-grained biotite and quartz-feldspar rich domains. In a few parts, larger biotite forms mica fish.

J91 represents a gneiss from the upper plate basement (Austroalpine nappe stack) sampled at profile P-JA (Fig. 6.6). It yields a paragenesis of qtz with subgrain rotation recrystallization, extremely sericitized fs (ab 68 mole-%, an 23 mole-%, or 9 mole-%) (Fig. 6.5i), ms (Si p.f.u. 3.12), and ap. Strong foliation is expressed by the alignment of white mica and quartz-feldspar domains.

Sample C-5 represents a Permian meta-volcanic rock exposed at the base of the

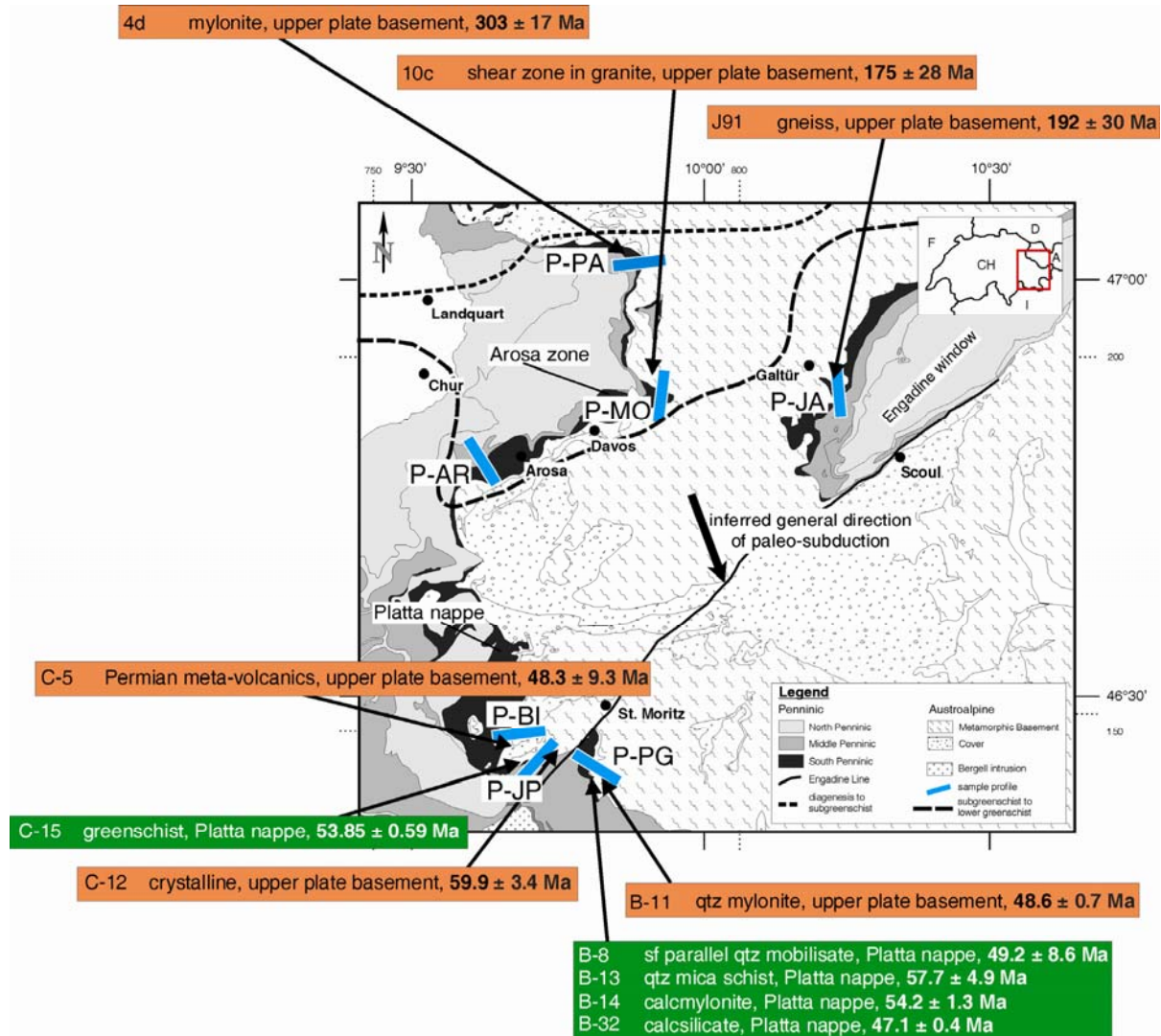


Figure 6.6: Tectonic map of the working area with profiles and sample positions for Rb/Sr geochronology, with new Rb/Sr deformation ages for the base of Austroalpine upper plate (orange) and the South Penninic subduction mélangé (green). Metamorphic isogrades redrawn after Frey et al. (1999).

upper plate at profile P-BI (Fig. 6.6). It is strongly deformed, and exhibits a closely spaced foliation. Its paragenesis is mainly composed of fs, ms, qtz showing undulose extinction, ap and minor mgt. In part, the mica rich layers are crenulated.

C-15 was sampled at profile P-JP (Fig. 6.6). It represents a quartz mica schist from the South Penninic mélangé, and contains qtz, which is partly recrystallized, fs, ms (Si p.f.u. 3.28) and minor ap. The tight foliation is defined by alternating quartz-feldspar and mica rich layers (Fig. 6.5e).

Sample C-12 represents a quartz mica schist from the base of the Austroalpine

upper plate at profile P-JP (Fig. 6.6). It is composed of qtz, almost pure ab, phg (Si p.f.u. 3.36) and ep. Quartz exhibits bulging recrystallization, whereas feldspar forms larger clasts in some parts (Fig. 6.5h).

Sample B-11 derives from the basal parts of the Austroalpine nappe stack at profile P-PG (Fig. 6.6). It represents a fine-grained quartz rich mylonite (Figs. 6.5c, f). The paragenesis is composed of qtz with subgrain rotation recrystallization, almost pure ab, phg (Si p.f.u. 3.41 – 3.43), and ap. The microtexture is characterized by the alternation of quartz-feldspar rich and mica

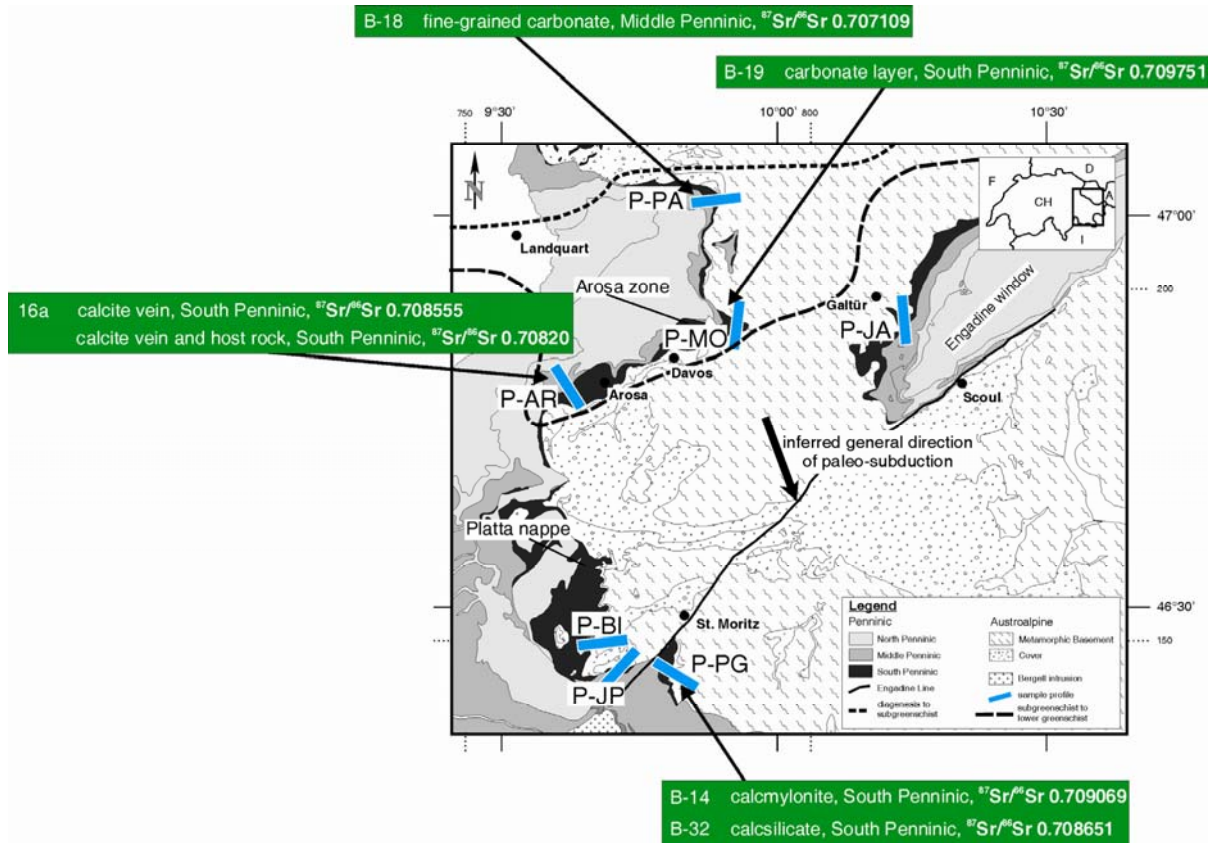


Figure 6.7: Tectonic map of the working area with profiles and sample positions for analyses of Sr isotope signatures, indicating  $^{87}\text{Sr}/^{86}\text{Sr}$  values for marine (meta-) carbonates from the South Penninic subduction mélangé and the Middle Penninic domain. Metamorphic isogrades redrawn after Frey et al. (1999).

rich domains exhibiting a strong alignment of white mica (Fig. 6.5f).

Sample B-8 is a foliation-parallel quartz mobilisate (mineralized vein) taken from the South Penninic mélangé (Platta nappe) at profile P-PG (Figs. 6.5a, b, 6.6). It exhibits a blocky texture with coarse-grained qtz, finer-grained ab, ap and phg (Si p.f.u. ranging from 3.38 to 3.51). Quartz microstructure is dominated by subgrain rotation recrystallization.

The quartz-mica schist B-13 was taken from an outcrop of the South Penninic mélangé (Platta nappe) at profile P-PG (Fig. 6.6). It contains qtz, almost pure ab, phg (Si p.f.u. 3.42 – 3.44), and ap. Strong foliation is due to the alternation of quartz-feldspar rich and mica rich layers (Fig. 6.5g). Quartz microstructure is characterized by subgrain rotation recrystallization. Some larger feldspar

grains float within the finer-grained matrix. White mica is partly crenulated.

Sample B-14 was also sampled at profile P-PG, and represents a calcmylonite (Figs. 6.5c, 6.6). The sample was taken from the mylonitic outer parts of a large dolomite (?) clast (upper plate sedimentary cover) embedded within the South Penninic mélangé with its long axis apparently parallel to the main foliation. The rock is composed of cal (? dol), and ms. The strongly deformed sample exhibits an alternation of fine-grained and coarser-grained calcite, which highlights the foliation. Larger calcite grains exhibit tabular thick twins and rarely undulose extinction. Sparsely white mica grew along the foliation.

B-32 represents a calcsilicate from the South Penninic mélangé (Platta nappe) sampled at profile P-PG (Fig. 6.6). Its

paragenesis is composed of cal (with minor amounts of Fe, Mg and Mn), phg (Si p.f.u. ranging from 3.19 to 3.23), and ap. The strong foliation is caused by the alternation of mica, quartz and coarser grained calcite domains. Calcite shows tabular thick twins and subgrain rotation recrystallization in some cases. Quartz exhibits undulose extinction and incipient subgrain rotation recrystallization.

To sum up, samples for Rb/Sr isotopic dating yield very similar metamorphic conditions (middle to upper greenschist grade, as far as it can be constrained by the limited paragenesis), kinematic indicators (generally top-W) and microstructures (quartz showing bulging and subgrain rotation recrystallization, strongly aligned calcmylonites) for both the base of the upper plate Austroalpine domain and the South Penninic subduction mélange.

In addition, we sampled marine (meta-) carbonatic rocks from both the South Penninic mélange and the Middle Penninic (a few tens of meters below the base of the South Penninic subduction mélange) (Fig. 6.7) in order to conduct Sr isotope analyses for comparison with the Sr seawater evolution curve (cf. Howarth and McArthur 1997, McArthur et al. 2001). Sample B-18 represents a massive, nearly undeformed fine-grained carbonate from profile P-PA (Fig. 6.7). It was sampled from the Middle Penninic Sulzfluh unit for reference, because it was never part of the fossil South Penninic-Austroalpine plate interface zone. Sample B-19 is a carbonatic layer within a less deformed sediment pile at profile P-MO (Fig. 6.7). Samples 16a and 16b represent calcite-filled mineralized veins and the host rock (sample 16b black) (Fig. 6.5d). These samples were taken at profile P-AR (Fig. 6.7). Sample B-14 is a calcmylonite sampled at the rim of a carbonate clast of probably Triassic/Jurassic depositional age (Geological map of Switzerland, 1:500.000, 1980) embedded in the South Penninic mélange

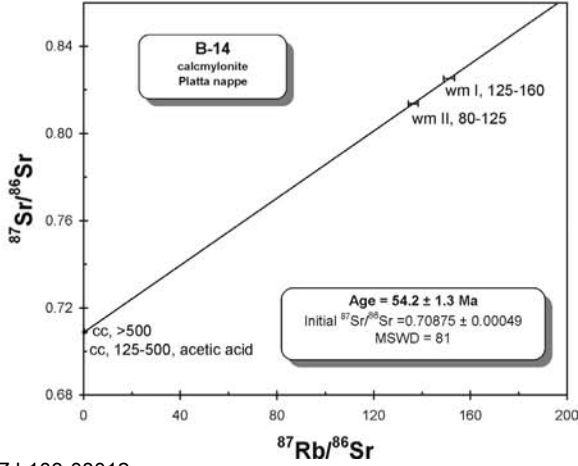
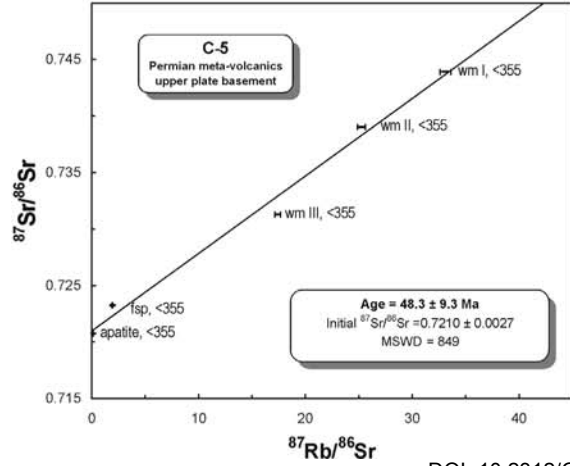
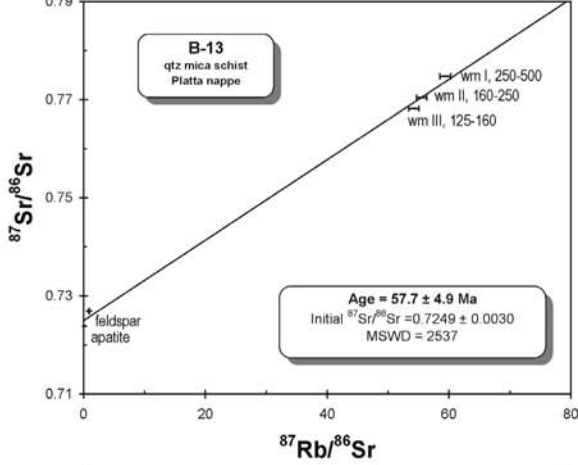
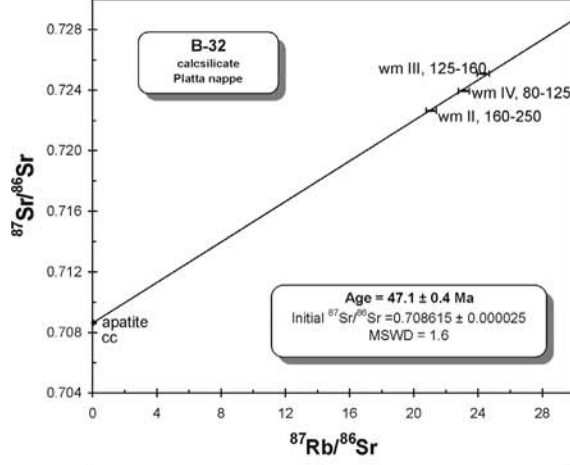
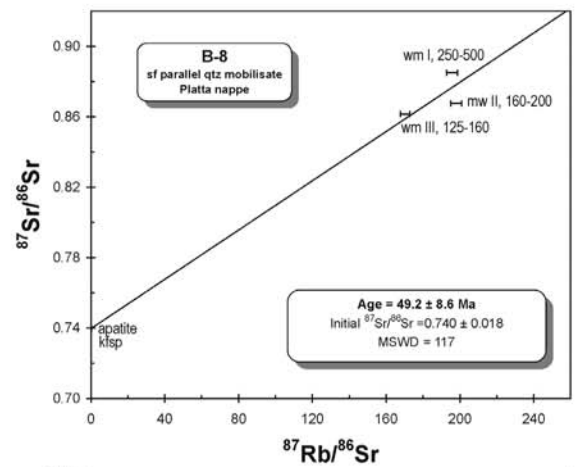
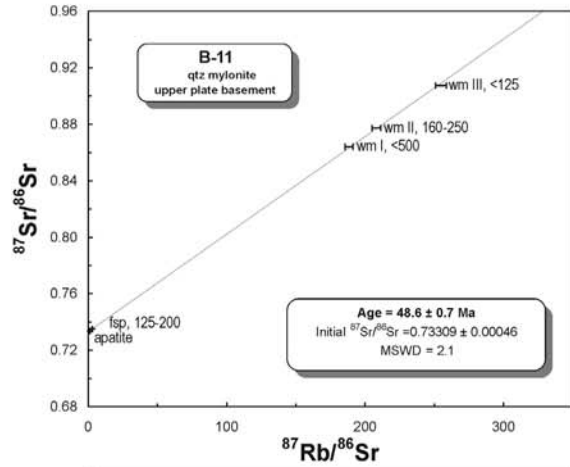
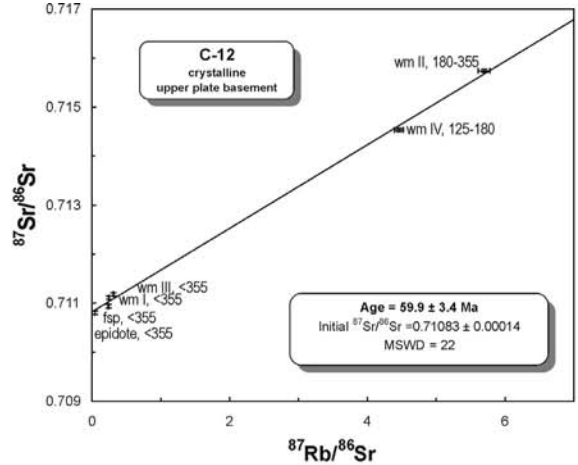
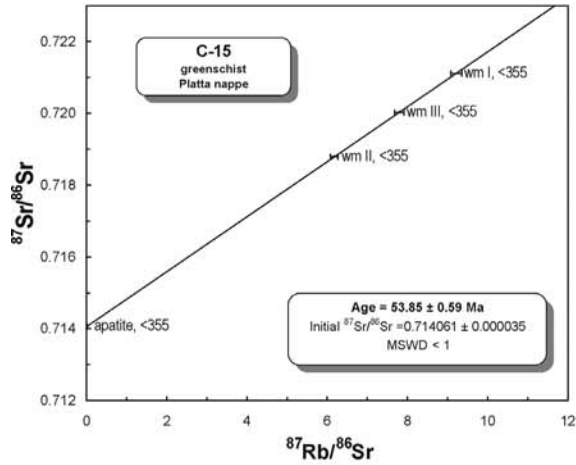
at profile P-PG (Figs. 6.5c, 6.7). B-32 represents a calcsilicate from the same profile (Fig. 6.7).

## 6.6. Results

### 6.6.1. Rb/Sr Data

Isotopic ages have been calculated using Rb/Sr isotope data for white mica, and cogenetic feldspar, apatite, calcite and epidote. We obtained well-defined isochron ages for three samples from the southern part of the working area, originating both from the basal parts of the Austroalpine upper plate and the South Penninic mélange. Sample C-15 (quartz mica schist, P-JP, South Penninic mélange) yielded a four-point isochron age of  $53.85 \text{ Ma} \pm 0.59 \text{ Ma}$ , sample B-11 (quartz rich mylonite, P-PG, Austroalpine) yielded a five-point isochron age of  $48.6 \text{ Ma} \pm 0.7 \text{ Ma}$  (Fig. 6.8). The five-point isochron of sample B-32 (calcsilicate, P-PG, South Penninic mélange) resulted in a slightly younger age of  $47.1 \pm 0.4 \text{ Ma}$  (Fig. 6.8). Additionally, for five samples from the upper plate and the South Penninic mélange, as well as for a quartz mobilisate we obtained correlations in Rb/Sr isochron plots which reveal minor apparent initial isotopic disequilibria between the analyzed mineral fractions (evident from elevated MSWD values of regression) (Fig. 6.8). Nevertheless, these samples give good hints on the age of their last important overprint. Sample C-5 (Permian meta-volcanic rock, P-BI, Austroalpine) resulted in an age of  $48.3 \text{ Ma} \pm 9.3 \text{ Ma}$ , based on a five-point correlation. A six-point

Figure 6.8: Internal mineral isochrons for samples from the South Penninic mélange and the Austroalpine upper plate. Analytical data are given in Table 1. Mineral abbreviations follow Kretz (1983). Grain size is indicated when different grain size fraction were analyzed.



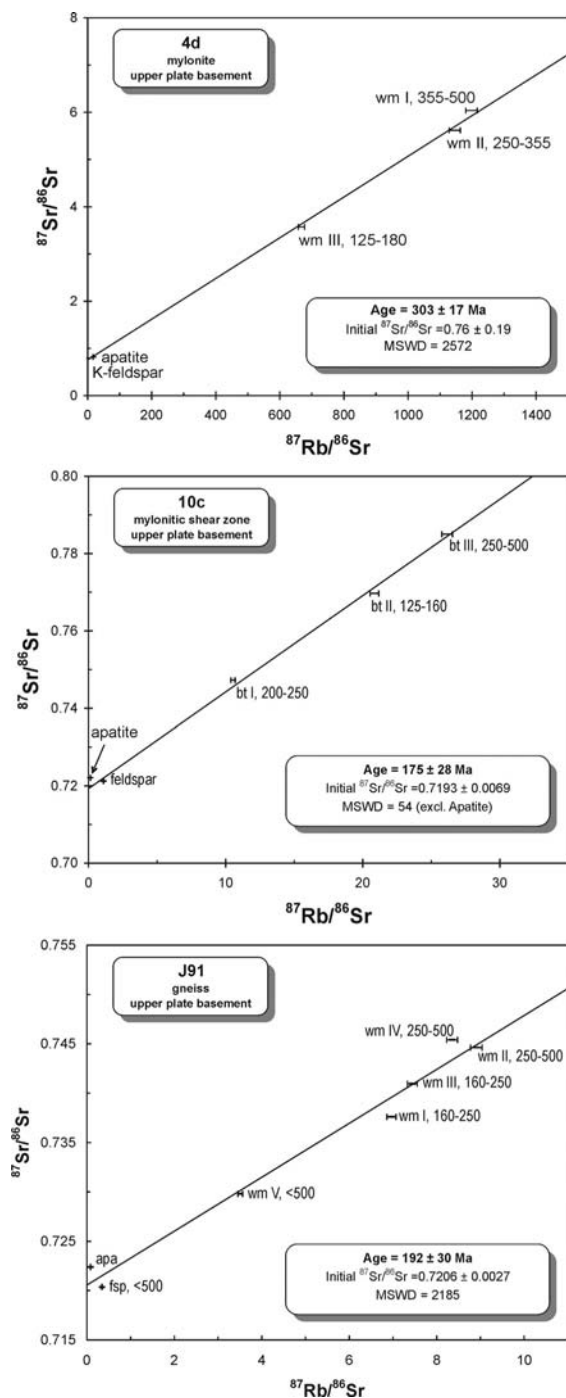


Figure 6.9: Rb/Sr mineral data for samples taken at the base of the crystalline upper plate in the northern part of the working area. Significance of isotopic disequilibria is discussed in the text. Analytical data are given in Table 1. Mineral abbreviations follow Kretz (1983). Grain size is indicated when different grain size fraction were analyzed.

correlation for sample C-12 (quartz mica schist, P-JP, Austroalpine) yielded an age value of  $59.9 \text{ Ma} \pm 3.4 \text{ Ma}$ . The quartz mobilisate B-8 (P-PG, South Penninic

mélange) resulted in a correlation based on five points corresponding to an age of  $49.2 \text{ Ma} \pm 8.6 \text{ Ma}$ . For sample B-13 (quartz mica schist, P-PG, South Penninic mélange), a five-point regression resulted in an age of  $57.7 \pm 4.9 \text{ Ma}$ . A four-point correlation was obtained for sample B-14 (calcmylonite, P-PG, South Penninic mélange) corresponding to an age of  $54.2 \text{ Ma} \pm 1.3 \text{ Ma}$ . In summary, there is a signal for a deformation process ending at  $\sim 50 \text{ Ma}$ .

Beside the above isotopic ages around 50 Ma, we obtained Rb/Sr mineral data pointing to considerably older, pre-Cretaceous events for some samples from the base of the crystalline upper plate (Austroalpine) in the northern part of the working area (Fig. 6.9). These samples are all characterized by Sr-isotopic disequilibria. Disequilibria are probably related to incomplete resetting of the mineral isotope systems due to incomplete deformation-induced recrystallization during younger overprints, for which indications are visible in thin sections (Fig. 6.5i). For sample 4d (mylonite, P-PA, the northernmost sample) regression of five Rb/Sr mineral data yielded  $303 \text{ Ma} \pm 17 \text{ Ma}$  (Fig. 6.9). Sample 10c (mylonitic shear zone, P-MO) yields an apparent age of  $175 \text{ Ma} \pm 28 \text{ Ma}$  ( $n = 4$ , MSWD = 54, excl. apatite; Fig 6.9). For sample J91 (gneiss, P-JA), regression of seven mineral data pairs points to an apparent age of  $192 \text{ Ma} \pm 30 \text{ Ma}$  (Fig. 6.9).

### 6.6.2. Sr isotope signatures

Sr isotope signatures for our 8 marine (meta-) carbonate samples are plotted in Fig. 6.10, together with the Sr seawater evolution curve (cf. Howarth and McArthur 1997, McArthur et al. 2001). Two groups of samples can be distinguished, a) with  $^{87}\text{Sr}/^{86}\text{Sr}$  of  $\sim 0.7071$ , and b) with ratios above 0.708171. Group a) is represented by one sample from the

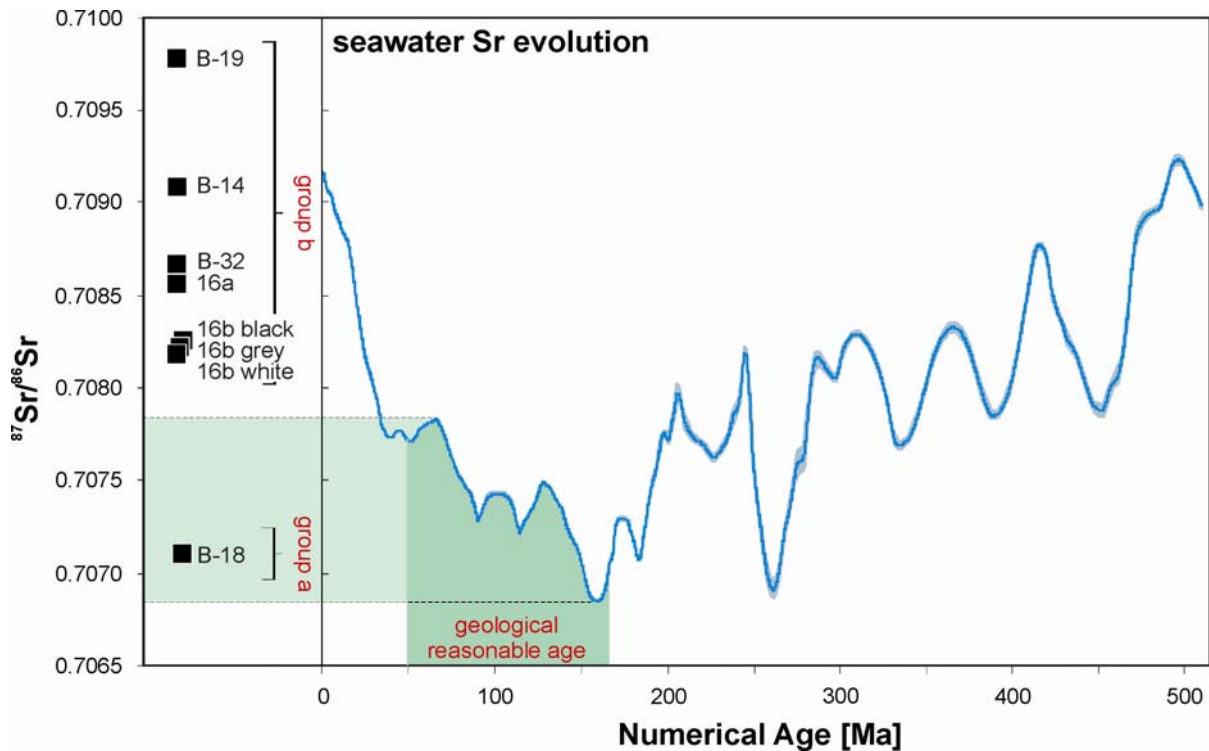


Figure 6.10: Diagram showing the Sr seawater evolution curve (McArthur et al. 2001) and the Sr data for 8 marine (meta-) carbonate samples. Two groups can be distinguished: Group a) was taken from the Middle Penninic unit, a few tens of meters below the base of the South Penninic subduction mélangé, and did not undergo deformation within the subduction channel. Its  $^{87}\text{Sr}/^{86}\text{Sr}$  ratio indicates carbonate deposition during the Upper Jurassic, and no evidence for later alteration. Group b) comprises samples taken from the subduction channel with elevated  $^{87}\text{Sr}/^{86}\text{Sr}$  ratios, incompatible with the Sr seawater ratios during the geologically reasonable carbonate deposition interval (dark green area).

Middle Penninic Sulzfluh unit (B-18), which did not undergo deformation or recrystallization within the fossil South Penninic-Austroalpine plate interface zone. Its  $^{87}\text{Sr}/^{86}\text{Sr}$  ratio is 0.707109. Group b) comprises samples taken from the South Penninic mélangé with  $^{87}\text{Sr}/^{86}\text{Sr}$  ratios between 0.708171 and 0.709751, which are consistently higher than  $^{87}\text{Sr}/^{86}\text{Sr}$  ratios of geologically reasonable (Jurassic to Paleocene) segments of the Sr seawater evolution curve (Fig. 6.10, Table 2). Sample B-19 yields a Sr isotope value of 0.709751; sample 16a has an  $^{87}\text{Sr}/^{86}\text{Sr}$  signature of 0.708555.  $^{87}\text{Sr}/^{86}\text{Sr}$  ratios of sample 16b (16b black, 16b grey, 16b white, Fig. 6.5d) are analytically indistinguishable at around 0.70820. Sample B-14 exhibits an  $^{87}\text{Sr}/^{86}\text{Sr}$  ratio of 0.709069, whereas sample B-32 shows an  $^{87}\text{Sr}/^{86}\text{Sr}$  ratio of 0.708651.

## 6.7. Discussion

### 6.7.1. Rb/Sr ages

To determine the absolute timing of penetrative deformation within the South Penninic mélangé and the basal parts of the Austroalpine nappe stack we used Rb/Sr geochronology on pervasively deformed rocks from both tectonic units. In addition, we dated one mineralized vein running subparallel to the foliation within the South Penninic mélangé to relate the formation of these vein systems to the overall deformation.

As outlined above, all samples are taken from outcrops reflecting a general top-W direction of tectonic transport (see Chapter 6.2.3.), although they may exhibit relics of former deformational stages, or may have

Table 1. Rb/Sr analytical data.

sample	material	Rb [ppm]	Sr [ppm]	$^{87}\text{Rb}/^{86}\text{Sr}$	$^{87}\text{Sr}/^{86}\text{Sr}$	$^{87}\text{Sr}/^{86}\text{Sr} \ 2s_m$ (%)
<i>4d (mylonite; 303 ± 17 Ma; MSWD = 2572, <math>Sr_i = 0.76 ± 0.19</math>)</i>						
PS1355	wm I, 355-500	896	3.29	1198	6.038448	0.0078
PS1354	wm II, 250-355	885	3.31	1146	5.616657	0.0050
PS1353	wm III, 125-180	783	4.35	668	3.572638	0.0116
PS1426	fsp	197	33.7	17.1	0.820349	0.0030
PS1356	apatite	9.67	91.7	0.307	0.797647	0.0018
<i>10c (mylonite; 175 ± 28 Ma; MSWD = 54 (excl. ap), <math>Sr_i = 0.7193 ± 0.0069</math>)</i>						
PS1376	bt I, 200-250	230	63.3	10.5	0.747277	0.0018
PS1375	bt II, 125-160	242	33.8	20.9	0.769687	0.0038
PS1372	bt III, 250-500	251	27.9	26.2	0.785026	0.0016
PS1374	fsp	34.4	90.7	1.10	0.721254	0.0020
PS1373	apatite	8.01	171	0.136	0.722105	0.0014
<i>J91 (gneiss; 192 ± 30 Ma; MSWD = 2185, <math>Sr_i = 0.7206 ± 0.0027</math>)</i>						
PS1511	wm I, 160-250	188	78.4	6.97	0.737618	0.0014
PS1512	wm II, 250-500	194	63.3	8.90	0.744635	0.0012
PS1513	wm III, 160-250	189	73.6	7.44	0.740965	0.0014
PS1514	wm IV, 250-500	186	64.7	8.35	0.745408	0.0014
PS1515	wm V, <500	148	122	3.51	0.729797	0.0016
PS1517	fsp, <500	70.9	599	0.343	0.720367	0.0016
PS1516	apatite	6.21	217	0.0829	0.722397	0.0018
<i>C-5 (Permian metavolcanic rock; 48.3 ± 9.3 Ma; MSWD = 849, <math>Sr_i = 0.7210 ± 0.0027</math>)</i>						
PS1505	wm I <355 µm	282	24.7	33.1	0.743921	0.0014
PS1506	wm II <355 µm	260	29.9	25.2	0.739032	0.0014
PS1507	wm III <355 µm	192	32.0	17.4	0.731291	0.0012
PS1510	fsp <355 µm	318	480	1.92	0.723244	0.0014
PS1509	apatite	12.8	312	0.119	0.720741	0.0016
<i>C-15 (quartz mica schist; 53.85 ± 0.59 Ma; MSWD &lt; 1, <math>Sr_i = 0.714061 ± 0.000035</math>)</i>						
PS1518	wm I <355 µm	110	34.4	9.22	0.721113	0.0016
PS1519	wm II <355 µm	48.0	22.5	6.17	0.718788	0.0016
PS1520	wm III <355 µm	78.4	29.1	7.80	0.720022	0.0014
PS1521	apatite	10.3	3194	0.00935	0.714068	0.0018
<i>C-12 (quartz mica schist; 59.9 ± 3.4 Ma; MSWD = 22, <math>Sr_i = 0.71083 ± 0.00014</math>)</i>						
PS1490	wm I <355 µm	12.8	151	0.247	0.711112	0.0014
PS1491	wm II 180-355 µm	274	139	5.70	0.715743	0.0014
PS1493	wm III <355 µm	11.9	110	0.313	0.711180	0.0016
PS1494	wm IV 125-180 µm	179	116	4.46	0.714533	0.0014
PS1496	fsp <355 µm	3.42	41.3	0.239	0.710940	0.0014
PS1492	epi <355 µm	19.3	1318	0.0424	0.710808	0.0012
<i>B-11 (qtz mylonite; 48.6 ± 0.7 Ma; MSWD = 2.1, <math>Sr_i = 0.73309 ± 0.00046</math>)</i>						
PS1405	wm I <500 µm	533	8.31	188	0.864115	0.0020
PS1404	wm II 160-250 µm	549	7.76	208	0.877306	0.0020
PS1403	wm III <125 µm	557	6.45	255	0.907476	0.0030
PS1427	fsp 125-200 µm	27.2	27.3	2.90	0.735181	0.0062
PS1378	apatite	445	1301	0.991	0.733649	0.0012
<i>B-8 (foliation parallel qtz mobilisate; 49.2 ± 8.6 Ma; MSWD = 117, <math>Sr_i = 0.740 ± 0.018</math>)</i>						
PS1369	wm I 250-500 µm	515	7.74	196	0.884915	0.0022
PS1368	wm II, 160-200 µm	541	8.03	198	0.867532	0.0020
PS1367	wm III 125-160 µm	453	7.81	170	0.861505	0.0036
PS1371	kfsp >500 µm	4.00	55.0	0.211	0.739813	0.0014
PS1370	apatite	2.15	1157	0.00539	0.739322	0.0018
<i>B-13 (qtz mica schist; 57.7 ± 4.9 Ma; MSWD = 2537, <math>Sr_i = 0.7249 ± 0.0030</math>)</i>						
PS1409	wm I 250-500 µm	479	23.5	59.4	0.774758	0.0024
PS1408	wm II 160-250 µm	477	25.0	55.5	0.770414	0.0020
PS1407	wm III 125-160 µm	461	24.7	54.2	0.768190	0.0043
PS1428	fsp 90-160 µm	9.88	31.8	0.900	0.726888	0.0016
PS1410	apatite	6.29	1303	0.0140	0.723852	0.0014
<i>B-14 (calcmylonite; 54.2 ± 1.3 Ma; MSWD = 81, <math>Sr_i = 0.70875 ± 0.00049</math>)</i>						
PS1412	wm I 125-160 µm	149	2.89	151	0.825256	0.0022
PS1411	wm II 80-125 µm	73.4	1.57	136	0.813684	0.0062
PS1359	cc >500 µm	32.6	294	0.321	0.709157	0.0014
PS1377	cc 125-500 µm	2.06	115	0.0520	0.708628	0.0016
<i>B-32 (calcsilicate; 47.1 ± 0.4 Ma; MSWD = 1.6, <math>Sr_i = 0.708615 ± 0.000025</math>)</i>						
PS1415	wm II 160-250 µm	283	38.9	21.1	0.722641	0.0012
PS1414	wm III 125-160 µm	333	39.7	24.3	0.725086	0.0014
PS1413	wm IV 80-125 µm	182	22.9	23.1	0.723945	0.0014
PS1429	cc >500 µm	6.71	308	0.0631	0.708651	0.0016
PS1417	apatite	1.67	477	0.0101	0.708629	0.0016

Table 2. Rb/Sr analytical data, carbonates and metacarbonates.

sample	material	weight (mg)	Rb (ppm)	Sr (ppm)	$^{87}\text{Rb}/^{86}\text{Sr}$	$^{87}\text{Sr}/^{86}\text{Sr}$	$^{87}\text{Sr}/^{86}\text{Sr}$ $2\sigma_m$ (in %)
16a	carbonate	10.5	1.03	176	0.0169	0.708555	0.0012
16b black	host rock carbonate	8.5	2.21	106	0.0602	0.708246	0.0012
16b grey	vein generation I	9.4	0.04	315	0.00039	0.708200	0.0014
16b white	vein generation II	10.0	0.29	1245	0.00068	0.708171	0.0016
B-14	calcmylonite	8.3	0.36	345	0.00300	0.705000	0.0014
B-18	carbonate Sulzfluh	8.8	0.09	198	0.00135	0.707109	0.0016
B-19	carbonate	11.5	2.85	427	0.0193	0.709751	0.0014
B-32	calcsilicate	3.8	6.71	308	0.0631	0.708651	0.0016

been exposed to later overprints. The analyses of Rb/Sr data for the different samples resulted in 2 age groups (Fig. 6.11a). The first group is exclusively comprised of samples from the base of the upper plate Austroalpine nappe stack. Here, the oldest apparent age of  $303 \text{ Ma} \pm 17 \text{ Ma}$  (sample 4d, Fig. 6.9) is within the range of ‘Variscan’ ages known from the Austroalpine of the region (cf. Thöni 1999 for review), while the data for sample J91 (disequilibria; poorly constrained apparent age of  $192 \pm 30 \text{ Ma}$ , Fig. 6.9) might reflect partial resetting of pre-Alpine signatures, probably by Alpine-age overprints. The fact that the apparently ‘younger’ sample originates from a more southern (deeper) position within the fossil plate interface is consistent with the observed increasing intensity of Alpine imprints on textures and mineral assemblages towards the S (see Chapter 4). A low degree of Alpine impact on the northernmost sample correlates with only sub-greenschist-facies Alpine imprint, whereas the more strongly affected sample was located already in a lower greenschist facies Alpine environment (Figs. 6.6, 6.11a), an observation pointing to more effecting resetting of the isotope system by deformation at higher metamorphic conditions. Sample 10c from a mylonitic

shear zone within the upper plate resulted in an age of  $175 \text{ Ma} \pm 28 \text{ Ma}$  (Fig. 6.9). It remains unclear whether this (biotite-based) age value may also reflect the incomplete reset of Variscan isotope signature by Alpine deformation. It is worth noting that this age is in accordance to published age data for the breakup of the continent finally leading to the opening of the Alpine Tethys in between Europe and Africa (e.g. Schmid et al. 2004 and references therein). The here sampled shear zone may, therefore, alternatively represent a deformation zone related to the above Jurassic continental extension and breakup (e.g. Froitzheim and Rubatto 1998, Manatschal et al. 2006 for the interpretation of the ocean-continent transition in the Swiss Alps).

The second group comprising samples from both the base of the Austroalpine nappe stack and the South Penninic mélange in the southern part of the working area, resulted in ages roughly around  $50 \text{ Ma}$  (Fig. 6.11a). For the samples from the basal parts of the upper plate we interpret these ages to reflect the final stages of mylonitization-related isotopic reequilibration from penetrative Alpine deformation, under greenschist grade conditions (at least close to the boundary to

the underlying South Penninic *mélange*). There is a striking similarity between the deformation ages calculated for the basal parts of the upper plate, and for the South Penninic *mélange*, in the southern part of the study area (Fig. 6.11b). We therefore interpret the ages obtained for the South Penninic *mélange* to reflect the same deformation-induced recrystallization as observed in the upper plate samples. It appears that deformation along the plate interface zone of the South Penninic *mélange* and the Austroalpine nappe stack (and affecting rocks from both tectonic units) occurred over a prolonged period, at least over a time span bracketed by our isochron age data ( $53.85 \pm 0.59$  Ma to  $47.1 \pm 0.4$  Ma). Possibly even somewhat earlier increments of deformation are recorded by the samples C-12 (Fig. 6.8) and B13 (Fig. 6.8). These samples show higher apparent ages ( $59.9 \pm 3.4$  and  $57.7 \pm 4.9$  Ma, respectively), combined with positive correlations between white mica grain sizes and apparent ages (e.g. sample B13: large white mica crystals plotting above, and smaller white micas below the regression line, Fig. 6.8). This grain size – age correlation reflects some kind of isotopic inheritance. It is consistent with protracted deformation, with incomplete isotopic resetting of early-recrystallized grains during the latest stages of deformation. Finally, there is no hint in the dataset to any ductile overprint postdating the Lower Eocene (~50 Ma) record of waning deformation.

The dated foliation parallel prograde mobilisate (B-8) resulted in an (imprecisely constrained) apparent age of  $49.2 \pm 8.6$  Ma (Fig. 6.8), pointing to the activity of fluids along the active paleosubduction zone. Pseudotachylytes from the base of the Austroalpine upper plate in the northern part of the working area has previously been dated by Thöni (1988) to ~75 Ma (Figs. 6.11a, b). Own Ar/Ar data point to pseudotachylyte formation within a prolonged time frame

of 60 Ma to 80 Ma (see Chapter 5). We interpreted the formation of pseudotachylyte to be related to the subduction of the South Penninic *mélange* underneath the Austroalpine upper plate (Chapter 5), giving another hint for the time frame of subduction-related deformation. Material accreted to the base of the South Penninic subduction *mélange* (i.e. the Middle Penninic domain) yield synkinematic white mica ages around 38 Ma (Markley et al. 1995), which point to subduction related deformation at that time in the footwall of the South Penninic subduction *mélange* (Fig. 6.11a). In summary, our Rb/Sr isotopic data provide the first precise geochronological constraints on the end of subduction related deformation along the South Penninic-Austroalpine suture zone in the Eastern Swiss Alps, i.e. on the abandonment of this paleosubduction interface.

One fact has to be pointed out: The deformational and isotopic record of a subduction channel is persistently renewed due to continuous processes such as sediment subduction, deformation, and tectonic erosion. Only when material finally leaves the active parts of the subduction channel and becomes accreted to the base of the hanging wall, the deformational and isotopic record can be preserved. Deformation-induced isotopic resetting during accretion of material to the base of the upper plate is caused by permanent strain accumulation due to velocity gradient between material flow within the channel and the upper plate. Depending on the degree of coupling between upper and lower plate, deformation and consequently a zone of deformation-induced isotopic resetting may even penetrate into the base of the overriding plate. As outlined above, we interpret our Rb/Sr age data as indicating the removal of material out of the active parts of the subduction channel and as dating the abandonment of the South

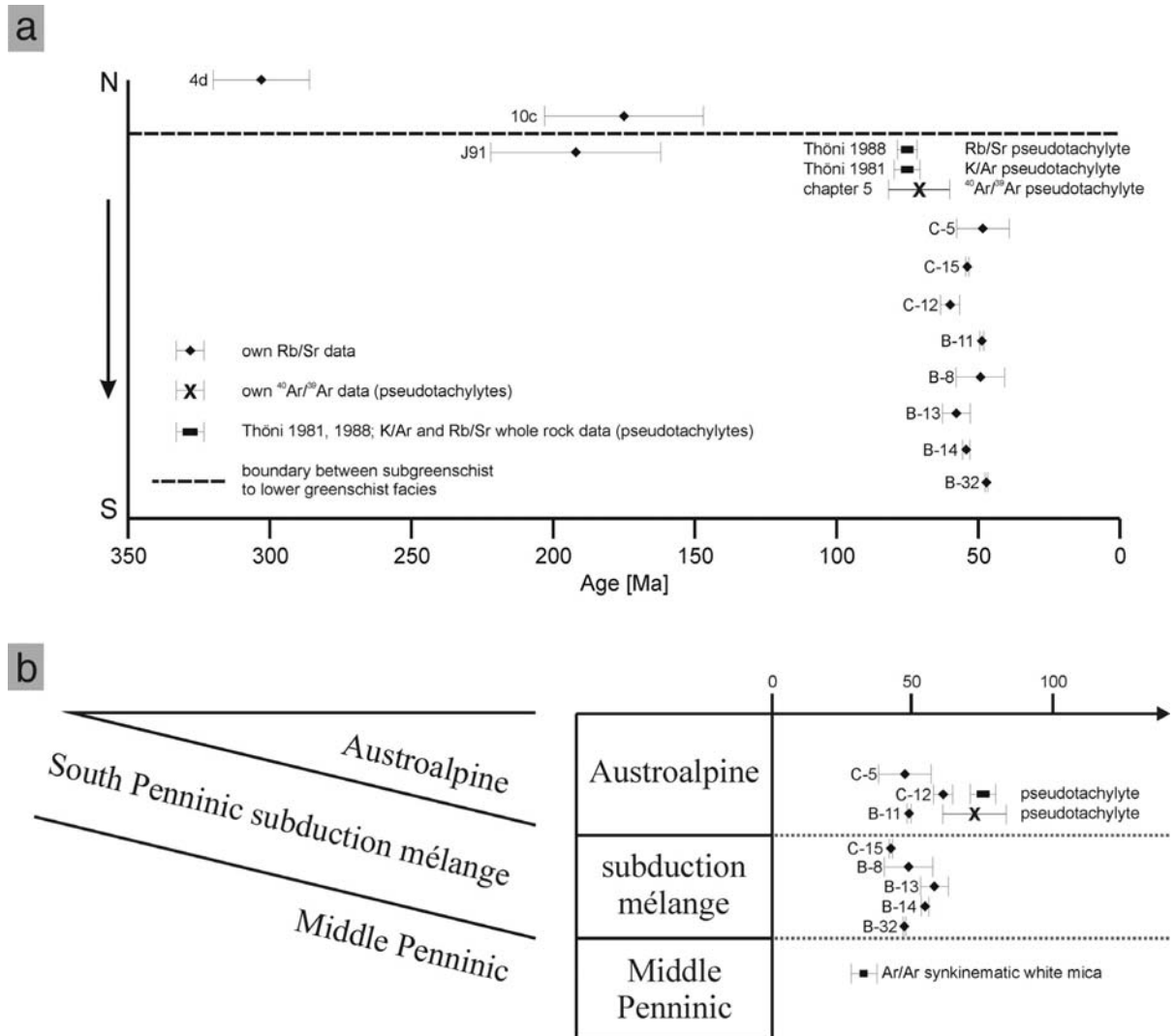


Figure 6.11: a) Distribution of Rb/Sr age data from N to S. There is a clear subdivision into two group of ages, the first group  $> 175$  Ma and the second group at  $\sim 50$  Ma. Position of metamorphic isograds taken from Frey et al. (1999). b) Position of own Rb/Sr data relative to either the Austroalpine upper plate or the South Penninic mélangé showing the similarity of deformation ages obtained for both units. Additionally, Rb/Sr ages (Thöni 1988), K/Ar ages (Thöni 1981), and own  $^{40}\text{Ar}/^{39}\text{Ar}$  ages (see Chapter 5) for pseudotachylyte formation within the basal part of the upper plate, as well as Ar/Ar synkinematic white mica ages for the Middle Penninic domain (Markley et al. 1995) are indicated.

Penninic-Austroalpine suture zone at around 50 Ma. This is in accordance with results of Liu et al. (2001), dating the final emplacement of Austroalpine units onto the Penninic domain at around 55-50 Ma using Ar/Ar muscovite ages for the area east of the Tauern window. Furthermore, Liu et al. (2001) associate the Cretaceous to Early Tertiary deformation within the lower part of the Austroalpine nappe complex with top-WNW directed transport, which is well comparable to our

structural data (see Chapter 2.3.) pointing to a general top-W direction of tectonic transport during the Cretaceous to Early Eocene subduction-related deformation.

### 6.7.2. Sr isotopes

We studied the Rb/Sr isotope signature of 8 originally marine (meta-) carbonate samples from the fossil plate interface zone to get information about both their age

relationships and possible interaction with either crustal or mantle derived fluids. The carbonates are believed to have formed in a seawater environment (South Penninic ocean), and thus should record the syn-precipitational  $^{87}\text{Sr}/^{86}\text{Sr}$  ratio of seawater, given that no later, post-depositional fluid-rock interaction occurred. The Sr-isotopic ratio of seawater is known to vary with time (e.g. Wickman 1948, Gast 1955), so that Sr isotopic compositions of seawater precipitates (e.g. biogene carbonates) may directly be converted to absolute age information ('strontium isotope stratigraphy', cf. Howarth and McArthur 1997, McArthur et al. 2001). For reliable age information to be extracted from Sr isotope signatures, several preconditions have to be met, namely that no detrital components contaminate the seawater precipitates, that the Sr isotopic signature is not changed by in-situ decay of Rb, and that no secondary exchange of Sr with external fluids ever occurred. Monitoring of Rb contents and Rb/Sr ratios and microscopic examination of the studied samples has shown that siliciclastic detrital components are virtually absent, and Rb/Sr ratios are very low (Table 2), indicating that in-situ radiogenic ingrowth of  $^{87}\text{Sr}$  in the carbonate samples is negligible. Therefore, the Sr isotope data either provide information on primary Sr isotopic signatures or give hints to possible interaction and Sr exchange with fluids during syn-subduction metamorphism.

We distinguished the analyzed samples into two groups (see Chapter 6.7.2). Group a) yields Sr isotope values around 0.7071 for a reference sample from the Middle Penninic (Sulzfluh, close to the base to the overlying South Penninic subduction mélange). This value corresponds with either a Permian or Upper Jurassic Sr isotope stratigraphy age (Fig. 6.10). This fits well with geological constraints indicating an Upper Jurassic (Malm) age (Geological map of Switzerland, 1:500.000, 1980) of marine carbonate

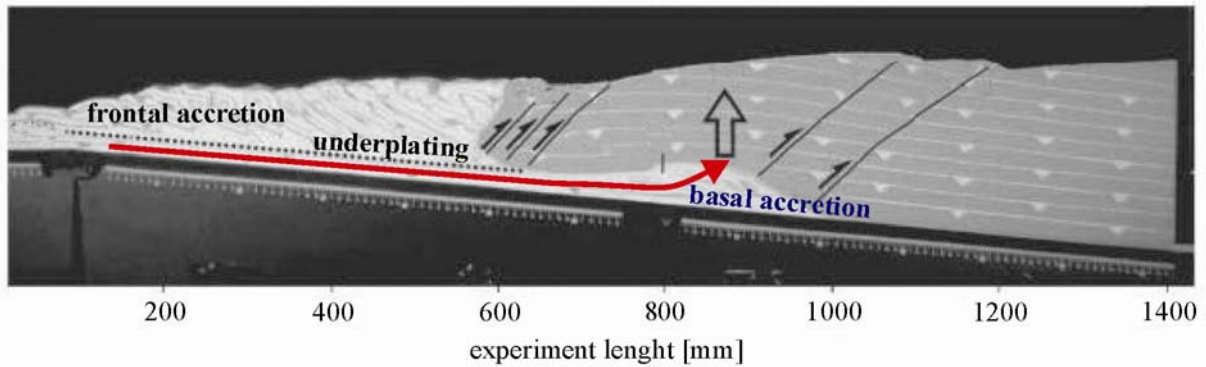
deposition on top of the submerged Middle Penninic micro-continent. There is no evidence for influence of fluids or deformation-related recrystallization, which altered the  $^{87}\text{Sr}/^{86}\text{Sr}$  subsequently. The isotopic data thus confirm the Malm age of the rock, and show that it escaped from subduction-related overprints.

Group b) yielded elevated Sr isotope signature ( $>0.708171$ ) for samples from the South Penninic mélange. Similar  $^{87}\text{Sr}/^{86}\text{Sr}$  ratios in seawater prevailed only in Ordovician, Permian, or Miocene to Recent times, and all these potential deposition intervals are incompatible with the geological setting of the carbonates. This suggests a significant interaction of the carbonates of this group with fluids carrying Sr with  $^{87}\text{Sr}/^{86}\text{Sr} > 0.708171$ , i.e., with fluids interacting with old continental crustal material. Most likely, the dominant source for the syn-subduction fluids, which altered the samples, is prograde dehydration of continent-derived sediments during subduction. Contributions to the subduction fluids from other sources, like from dehydration of oceanic crust, cannot be ruled out, but must have been minor due to the low  $^{87}\text{Sr}/^{86}\text{Sr}$  ratios expected for such fluids. Such fluids would range between MORB values around 0.703 and Paleogene seawater values of  $< 0.7078$ , i.e. their isotopic composition would be in marked contrast with the compositions observed in the mélange samples.

### 6.7.3. Exhumation of the South Penninic-Austroalpine plate interface zone

The suture zone between the South Penninic mélange (Arosa zone, Platta nappe) and the Austroalpine nappe stack does not exhibit a clear metamorphic contrast between hanging wall and footwall (Figs. 6.1, 6.6, 6.7) (e.g. Nievergelt et al. 1996). In terms of possible exhumation mechanisms this would argue for erosion as the principle driving force (see discussion in Froitzheim et al. 2003).

## a Sandbox model



## b Schematic drawing of underplated Middle Penninic units (~55-45 Ma)

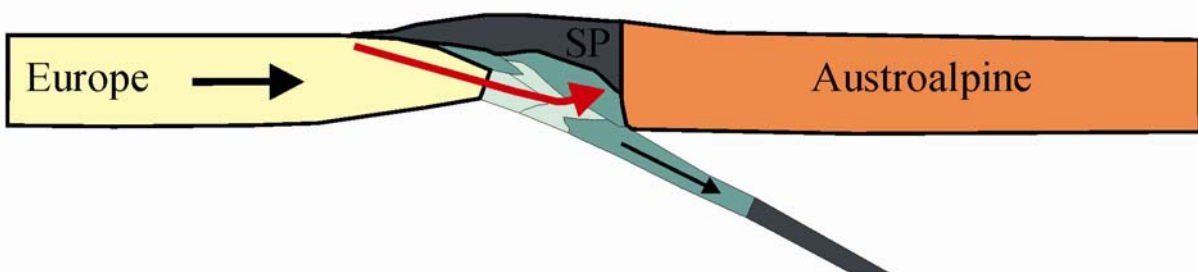


Figure 6.12: (a) Sandbox model indicating processes of frontal and basal accretion (modified after Glodny et al. 2005). (b) Schematic drawing of underplating of the Middle Penninic micro-continent at around 55 Ma to 45 Ma (redrawn after von Blanckenburg and Davies (1995).

However, differential exhumation of the suture zone (diagenetic to lowest greenschist facies conditions in the northern part, roughly upper greenschist facies conditions towards the south, Figs. 6.6, 6.7, e.g. Chapter 4), the observation of underfilled foreland basins during the initial time of subduction (prior to Oligocene) reported by Ford et al. (2006), as well as the initial onset of major sediment input into the foreland basins between 31 Ma and 20 Ma due to erosion of the rapidly emerging orogen (von Eynatten et al., 1999; Schlunegger et al., 1998; Spiegel et al., 2000; Liu et al., 2001, Kuhlemann et al. 2006) would favor additional processes than erosion, which contributed to the exhumation at least prior to the Oligocene.

In addition to erosion, we propose the accretion of subducted material to the base of the upper plate (Austroalpine nappes) as the key mechanism accounting for the exhumation of the studied suture zone. Such a process is theoretically predicted from numerical and analogue modeling (Fig. 6.12a) (Allemand and Lardeaux 1997, Kukowski et al. 2002, Lohrmann 2002). This would also require no metamorphic contrast between hanging wall and footwall. Basal accretion would lead to basal wedge growth by antiformal stacking of the subducted and underplated material (Glodny et al. 2005, and references therein). Ongoing basal accretion roughly at the same position in space would lead to extension of the accreted material simply caused by doming. Following a principle particle path down the subduction plate interface would

be as follows (Fig. 6.12a): 1. Entering the subduction zone at the tip of the accretionary wedge, 2. Passing down the plate interface zone within the subduction channel, and prograde metamorphism, 3. Accretion to the base of the upper plate, removal from the active subduction channel, and thereby caused penetrative deformation due to velocity contrast of particle flow within the subduction channel and the upper plate, 4. Uplift, extension and retrogressive metamorphism due to ongoing basal accretion. The hypothetical sample would receive its isotopical and structural record when it finally left the active subduction channel and became accreted to the base of the hanging wall.

Von Blanckenburg and Davies (1995) suggest the underplating of continental Penninic material (most likely the Middle Penninic micro-continent) below the overriding plate in a time span between 55 Ma and 45 Ma (Fig. 6.12b). Our Rb/Sr age data are in line with these suggestions. They clearly show the end of deformation along the South Penninic-Austroalpine suture zone at roughly 50 Ma, which should be caused by the locking of the South Penninic subduction zone by the incoming Middle Penninic micro-continent. This might have transferred the zone of active deformation further into the footwall, making the South Penninic subduction mélange a part of the upper plate, which subsequently overrides the Middle Penninic domain.

#### *6.7.4. Gosau group – additional evidence for abandonment of the Alpine subduction zone*

Additional constraints for timing of subduction and for the subduction-associated mass transfer mode are given by Wagneich (e.g. 1991, 1995) referring to the initial development of the Late Cretaceous Gosau basins as slope basins at the northward deepening slope at the front of

the orogenic wedge (Wagneich and Krenmayr 2005). According to these authors the Gosau basins represent synorogenic sedimentation along a broad transform zone, and are the consequence of oblique subduction of the South Penninic ocean underneath the Austroalpine nappe stack starting in the Late Cretaceous with dextral transpression and strike-slip faulting. The Gosau basins comprise a stratigraphic record from the Upper Turonian to the Eocene evolving from terrestrial and shallow marine deposits (Lower Gosau subgroup) into deep marine sediments (Upper Gosau subgroup). The Upper Gosau subgroup is associated with tectonic erosion and a thereby caused large scale subsidence pulse during the Late Cretaceous to the Eocene (e.g. Wagneich 1991). The change from an accretive to a tectonically erosive margin with the onset of Gosau group sedimentation might be due to the subduction of a SW-NE trending topographic high (Wagneich 1995). This explains the observed time shift in uplift, deformation and subsidence from northwest to southeast throughout the Gosau group depocenters (Fig. 6.13, Wagneich 1995). According to Wagneich (1995) this observation is comparable to active convergent plate margins, where seamount chains (e.g. Tonga Trench, Balance et al. 1989) or spreading ridges (e.g. Peru-Chile trench, Nelson and Forsythe 1989) collide obliquely with the upper plate. Another resemblance to active convergent plate margins is reported by Sanders and Höfling (2000). According to these authors the carbonatic depositional systems of the Gosau group are similar with respect to physiographic settings, scale, and facies to Holocene mixed siliciclastic-carbonate environments in active convergent settings. In addition, subsidence curves for the Miocene to Recent record of the erosive Japan margin are well comparable in shape, magnitude and duration to the Upper Gosau subgroup subsidence curves (von Huene and Lallemand 1990, Wagneich 1995).

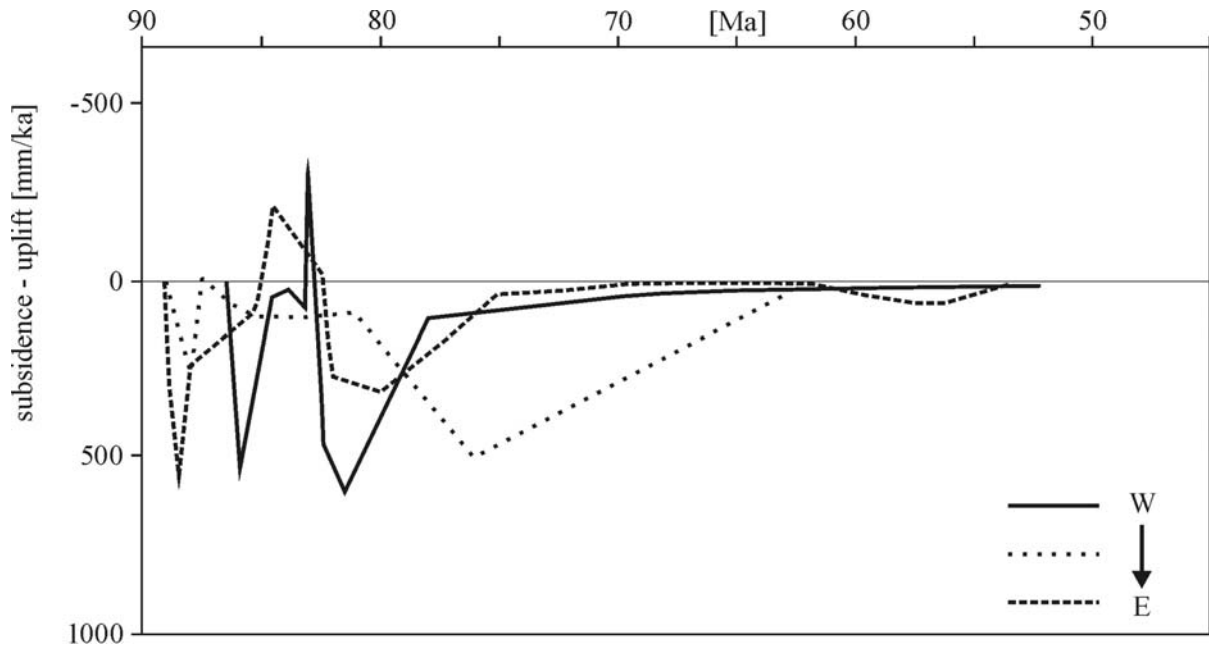


Figure 6.13: Subsidence and uplift curves for different localities (from W to E) of the Gosau group depocenters. Redrawn after Wagreich 1995. Sedimentation of the Gosau group terminated at around 50 Ma.

There is a striking similarity between our Rb/Sr deformation ages for the abandonment of the South Penninic paleosubduction interface, and the timing of the end of subsidence and sedimentation within the Gosau group depocenters, both at around 50 Ma (Eocene). Therefore, it is likely that there is a causal relationship between the end of deformation along the South Penninic-Austroalpine suture zone, and termination of Gosau group sedimentation. According to Wagreich (1995) the termination of the Gosau group sedimentation is associated with the end of tectonic erosion and the transformation of the erosive margin again back into an accretive one. We suggest that tectonic underplating and accretion of the Middle Penninic micro-continent, roughly at 50 Ma (e.g. von Blanckenburg and Davies 1995), accounts for the locking of the South Penninic subduction zone and associated termination of tectonically erosive mass transfer mode. Such accretive underplating may have resulted in the termination of Gosau group sedimentation, due to an accretion-related pulse of uplift.

#### 6.7.5. Isotopic dating – a hint for mass transfer mode

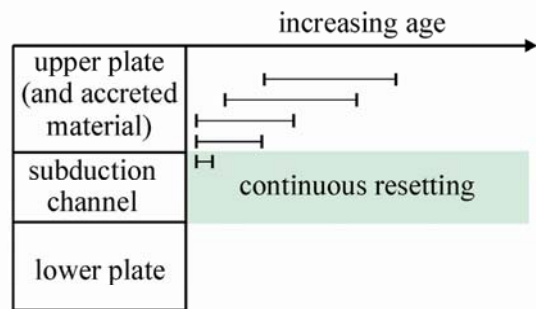
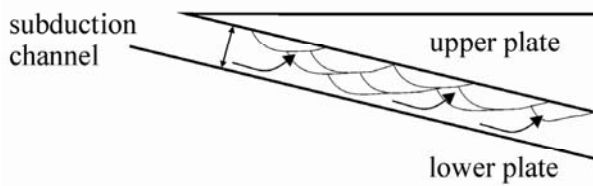
Our Rb/Sr isotopic age data provide another hint for the temporal evolution of mass transfer within the fossil subduction system. As illustrated in Figure 6.14 (a, b, c), hypothetical endmember scenarios for mass transfer mode within subduction channels comprise: 1) continuous underplating (addition of material to the base of the upper plate, i.e. basal accretion) (Fig. 6.14a), 2) continuous tectonic erosion removing material from the base of the upper plate (Fig. 6.14c), or 3) steady state, in a sense of continuous material flow neither adding nor removing material (Fig. 6.14b). For the isotopic record of deformation-sensitive isotopic systems in such endmember scenarios, the following predictions can be made:

Scenario a): A case scenario of continuous underplating (Fig. 6.14a) would result in a broad range of isotopic ages within the upper plate,

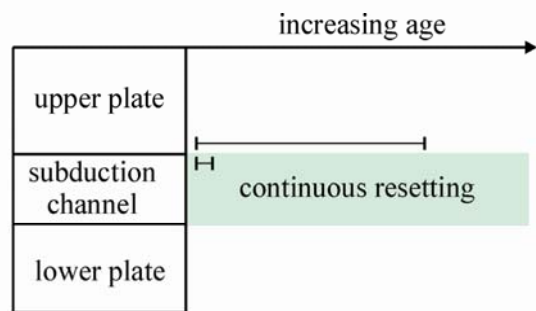
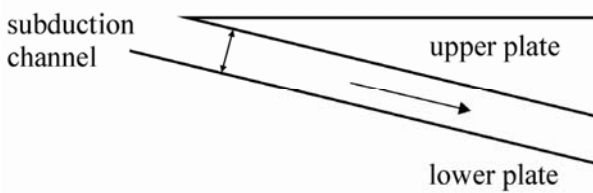
- getting systematically younger towards the subduction channel. Additionally, there would be a discrepancy between the ages obtained for the subduction mélange (comprising the subduction channel) and for the upper plate rocks at some distance from the channel. This would be caused by continuous accumulation of material at the base of the upper plate, and by associated transport of material out of the region of possible deformation-induced isotopic resetting.
- Scenario b): In the case of steady-state (continuous) material flow, isotopic ages for the upper plate would reflect the pre-subduction geological history, possibly with a domain of partial, subduction-related reset of age information at the base of the upper plate. A large non-systematic discrepancy between deformation ages from the subduction mélange (reflecting the latest stage of deformation), and the upper plate age record is expected (Fig. 6.14b). Continuous material flow within the subduction channel would constantly reset the isotopic systems, so that only the latest increment before abandonment would be preserved within the channel.
- Scenario c): Continuous tectonic erosion would result in nearly identical isotopic ages for both the basal parts of the upper plate and the subduction mélange due to ongoing mobilization of material at the base of the upper plate followed by tectonic removal to depth, which persistently shifts the region of deformation-induced isotopic resetting into the upper plate (Fig. 6.14c).
- Our Rb/Sr isotopic data are roughly identical for both the basal parts of the upper plate and the subduction mélange at

Figure 6.14: Hypothetical endmember scenarios for mass transfer mode within subduction channels. a) Continuous underplating adding material to the base of the upper plate (basal accretion). Assuming a snapshot in the evolution of such a system and analyzing the isotopic record, continuous underplating would result in a large spectrum of obtained isotopic ages within the upper plate, getting younger towards the subduction channel. Additionally, there would be a discrepancy between the ages obtained for the subduction mélange and the upper plate. b) Steady state continuous material flow neither adding nor removing material. Continuous material flow would result in a large spread of isotopic ages for the upper plate depending on its previous geological history. Additionally, a large discrepancy to the isotopic ages from the subduction mélange would be observable. c) continuous tectonic erosion removing material from the base of the upper plate. Continuous tectonic erosion would result in nearly identical isotopic ages for both the basal parts of the upper plate and the subduction mélange. d) Proposed temporal evolution path for material comprising the plate interface zone (red path): At first, tectonic erosion at the base of the upper plate removed constantly material. Thereby, the region of deformation induced resetting is shifted further into the upper plate, resulting in an identical isotopic record. At a certain time, the material may be located completely within the area of isotopic resetting. Abandonment of the subduction channel is caused by the basal accretion of the Middle Penninic micro-continent. Thereby, material from both the upper plate and the subduction mélange of the terminated South Penninic subduction zone are shifted out of the area of deformational resetting. This allows the preservation of the isotopical and deformational. Alternatively, material may have continuously entered and left the area of isotopic resetting by spatiotemporal changes of tectonic erosion and accretion, until it finally got resetted, accreted and removed out of the actively deforming system (blue path).

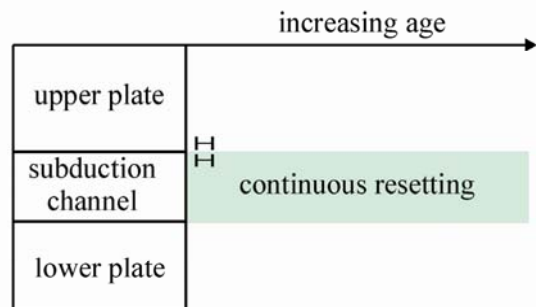
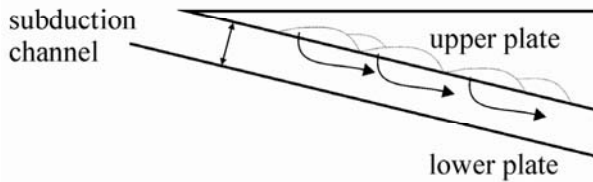
**a continuous underplating (basal accretion)**



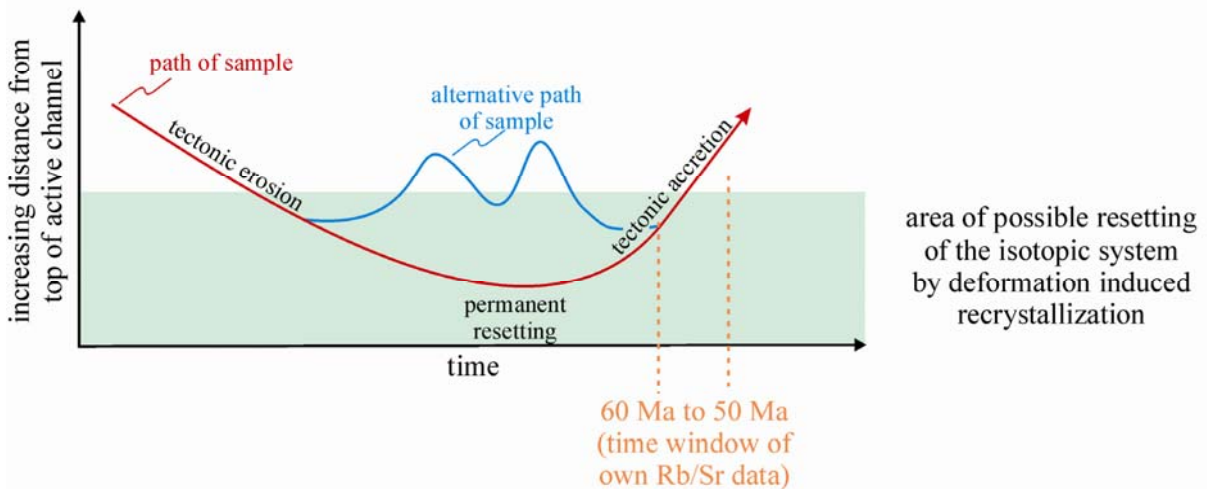
**b continuous material flow**



**c continuous tectonic erosion**



**d model of suggested temporal evolution**



around 50 Ma (Fig. 6.11b). Referring to the endmember scenarios above, this favors tectonic erosion as the main material transfer mode active within the subduction channel until the time of abandonment of this major suture zone. This is also in line with the observed numerous upper plate clasts embedded within the subduction mélange (e.g. Oncken 1998, Chapter 4) and the postulation by e.g. Wagneich (1991, 1995) that tectonic erosion is required for the formation of the Gosau group basins contemporaneously to the activity of the South Penninic subduction zone. Abandonment of the South Penninic-Austroalpine plate interface zone is most likely caused by the underplating of the Middle Penninic micro-continent (see Chapter 6.8.3.), leading to a transfer of the zone of active deformation further into the footwall. Thenceforward, the South Penninic-Austroalpine suture zone formed part of the upper plate, now passively overriding the Middle Penninic domain. This resulted in the preservation of the isotopic record of the final increment of subduction-related mass transfer along the South Penninic-Austroalpine plate interface zone.

Therefore, we propose the following temporal evolution path for material comprising the plate interface zone (red path in Fig. 6.14d): At first, tectonic erosion at the base of the upper plate constantly removed material from here. Thereby, the region of deformation-induced resetting is shifted further into the upper plate, resulting in an identical isotopic record for both the upper plate base and the subduction mélange. At a certain time, the material may be located completely within the area of isotopic resetting. Abandonment of the subduction channel is caused by the basal accretion the South Penninic subduction mélange. Thereby, material from both the upper plate and the subduction mélange of the terminated South Penninic subduction zone

is shifted out of the area of deformational resetting. Further on, the accretion of the Middle Penninic domain to the base of the South Penninic subduction mélange supports this process. This allows the preservation of the isotopic and deformational record for the final increment of subduction of the South Penninic ocean underneath the Austroalpine upper plate. Since the here proposed material path is simplified, alternatively, material may have continuously entered and left the area of isotopic resetting by spatiotemporal changes of tectonic erosion and accretion, until it finally got resetted, accreted and removed out of the actively deforming system (blue path in Fig. 6.14d). The slightly older Rb/Sr ages obtained for unstable slip in the basal part of the Austroalpine upper plate (pseudotachylyte ages ~75 Ma, Thöni 1988), and our own pseudotachylyte Ar/Ar data (60 Ma to 80 Ma, see Chapter 5) support this assumption (Fig. 6.11b). Ages obtained in the footwall of the abandoned South Penninic-Austroalpine suture zone for the Middle Penninic domain point to deformation at around 38 Ma (Ar/Ar synkinematic white mica ages, Markley 1995) (Fig. 6.11b). This is slightly younger than the ages obtained for the South Penninic-Austroalpine plate interface zone, which later on formed the hanging wall passively overriding the Middle Penninic domain. This would argue, at least partly, for continuous material flow along the newly developed deformation zone in the footwall of the South Penninic mélange subsequent to the termination of the South Penninic subduction zone resulting in an age gap between the hanging wall and footwall (Figs. 6.11b, 6.14). This provides an additional hint for spatiotemporal changes of material transfer mode and thereby caused changes of the position of the area of possible isotopic resetting (Fig. 6.14d).

Therefore, precise studies of the isotopic record of fossil subduction complexes have the potential to constrain the long term evolution of mass transfer in terms of tectonic erosion, basal accretion and steady state material flow.

## 6.8. Conclusion

In this study we show first precise Rb/Sr age data for the termination of subduction-related deformation along the South Penninic-Austroalpine suture zone in the Eastern Swiss Alps. Rb/Sr multimineral data for strongly foliated rocks of both the South Penninic subduction *mélange* and the immediate hanging wall (Austroalpine) resulted in two age groups. The first group reflects pre-Alpine (Paleozoic to Jurassic) deformation events in the upper plate Austroalpine basement, the age information being disturbed by subsequent (Alpine?) overprint to apparently southward increasing degrees. The second group resulted in ages consistently around 50 Ma both in the *mélange* and the overlying Austroalpine, interpreted to reflect recrystallization in both units in response to late increments of deformation along the paleosubduction interface. A ~50 Ma metamorphic mobilisate points to syn-subductional dehydration, fluid activity and mineral precipitation. The dated waning of deformation along the paleosubduction interface is inferred to be due to final basal accretion of the former subduction channel material to the upper plate. According to our structural data, the latest increment of deformation at ~50 Ma is characterized by a roughly top-W direction of tectonic transport. Referring to published paleogeographic reconstructions, the end of subduction related deformation is best explained by the locking of the South Penninic paleosubduction interface due to underplating of the Middle Penninic micro-continent, a process that caused a relocation of convergence-related strain from the paleosubduction *mélange* into the

new, Middle Penninic footwall. The shutoff of sedimentation in the forearc Gosau basins is contemporaneous with basal accretion of the South Penninic *mélange* and the Middle Penninic units, both processes occurring in the Lower Eocene (~50 Ma). We hypothesize a causal link between the two events, with the change from tectonic erosion to basal accretion being responsible for a regional pulse of uplift, leading to inversion of the forearc basins.

Sr isotope signatures of marine (meta-) carbonates are shown to be governed by both the depositional and by the syn-subduction recrystallization histories. Strontium isotope stratigraphy for an undeformed reference sample from the Middle Penninic points to Upper Jurassic carbonate deposition onto this unit. In contrast, metamorphosed carbonate samples from the subduction *mélange* exhibit clear evidence for syn-metamorphic alteration by fluids. Elevated  $^{87}\text{Sr}/^{86}\text{Sr}$  ratios of the metacarbonates indicate that the dominant source of syn-subduction fluids has been the devolatilization of old continental crustal material, probably of subducted continental detritus.

We propose that the mass transfer mode of a paleosubduction system can be constrained using the deformation age record of both the upper plate and the subduction channel *mélange*. In our case, combined evidence from identical Rb/Sr ages for the Austroalpine upper plate and the South Penninic subduction *mélange*, from the presence of upper plate clasts in the subduction *mélange*, and from the syn-subduction evolution of Gosau forearc basins, points to tectonic erosion as prevailing mass transfer mode during the time of subduction.



## 7. Final discussion and conclusions

Most of the world's seismicity, and nearly all of the earthquakes with magnitudes  $>8$ , are generated along convergent plate margins. To date, processes occurring along the plate interface of convergent plate margins (i.e. within a subduction channels) cannot be directly accessed by drilling nor through surface observations, but has been intensely studied with geophysical methods, numerical modeling, and sandbox simulations. However, these methods have either poor resolution, or are strongly dependent on insufficiently constrained assumptions. Hence, direct investigations of exhumed ancient convergent plate margins are requested to achieve insights into structures and processes which occurred along the plate interface. The here presented study contributes to the understanding of convergent plate margins in the depth range of their former seismogenic zone aiming at testing inferences and hypotheses of the various kinematic and mechanical concepts presented for the seismogenic zone. Therefore, we use the complete exposure of this part of a fossil plate interface in the European Alps, one of the best-studied mountain belts worldwide that has resulted from successive subduction, accretion and collision. Here, we analyzed a *mélange* zone tracing the plate interface zone of the fossil convergent plate margin (Chapter 4). Additionally, we included information from Southern Chile, where material, which formerly underwent deformation along the plate interface, was exhumed to the surface by large scale accretion to the base of the upper plate (Chapter 1). We compare our field observation also with the assumptions from active convergent plate margins (Chapter 3). Therefore, the study is twofold, not even providing new aspects for the regional geology in the European Alps, but also providing constraints for inferences of structures and processes, which might be

subsequently tested at active convergent plate margins.

At first, we analyzed the South Penninic domain in the European Alps, which resulted from subduction of the Penninic oceanic domain underneath the Adriatic (Austroalpine) upper plate. Due to its comparability in lithofacies and internal structures to *mélanges* from subduction complexes (Ring et al. 1990) we treat the South Penninic domain as a subduction *mélange*, which resembles material from a so-called subduction channel. The thickness of the South Penninic subduction *mélange* varies from a few tens of meters up to more than 2500 m, reflecting their original thickness or a reduction from subsequent thinning. The matrix of shales and serpentinites incorporates clasts of more competent material, originating either from the Austroalpine upper plate (crystalline basement, its sedimentary cover), or formed by slivers of the lower plate (metagabbros, metabasalts, the sedimentary deposits of the ocean floor, or the trench fill turbidites). Therewith, it resembles the proposed internal structure of recently active subduction systems inferred from e.g. seismic and seismological data: less deformed units are bounded by a network of active shear zones or sheared matrix (e.g. Ábalos et al. 2003).

The South Penninic subduction *mélange* exhibits a N-S gradient in metamorphic grade. In the northern part of the working area, Alpine metamorphism did not exceed diagenetic grades, or lower greenschist facies (Chapters 4, 6). In the southern part, rocks of the *mélange* as well as the basal parts of the Austroalpine nappe stack were metamorphosed at middle to upper greenschist-facies conditions during Alpine orogeny. Due to large scale differential post-subduction tilting and exhumation of the fossil plate interface zone formerly deeper parts are accessible towards the south.

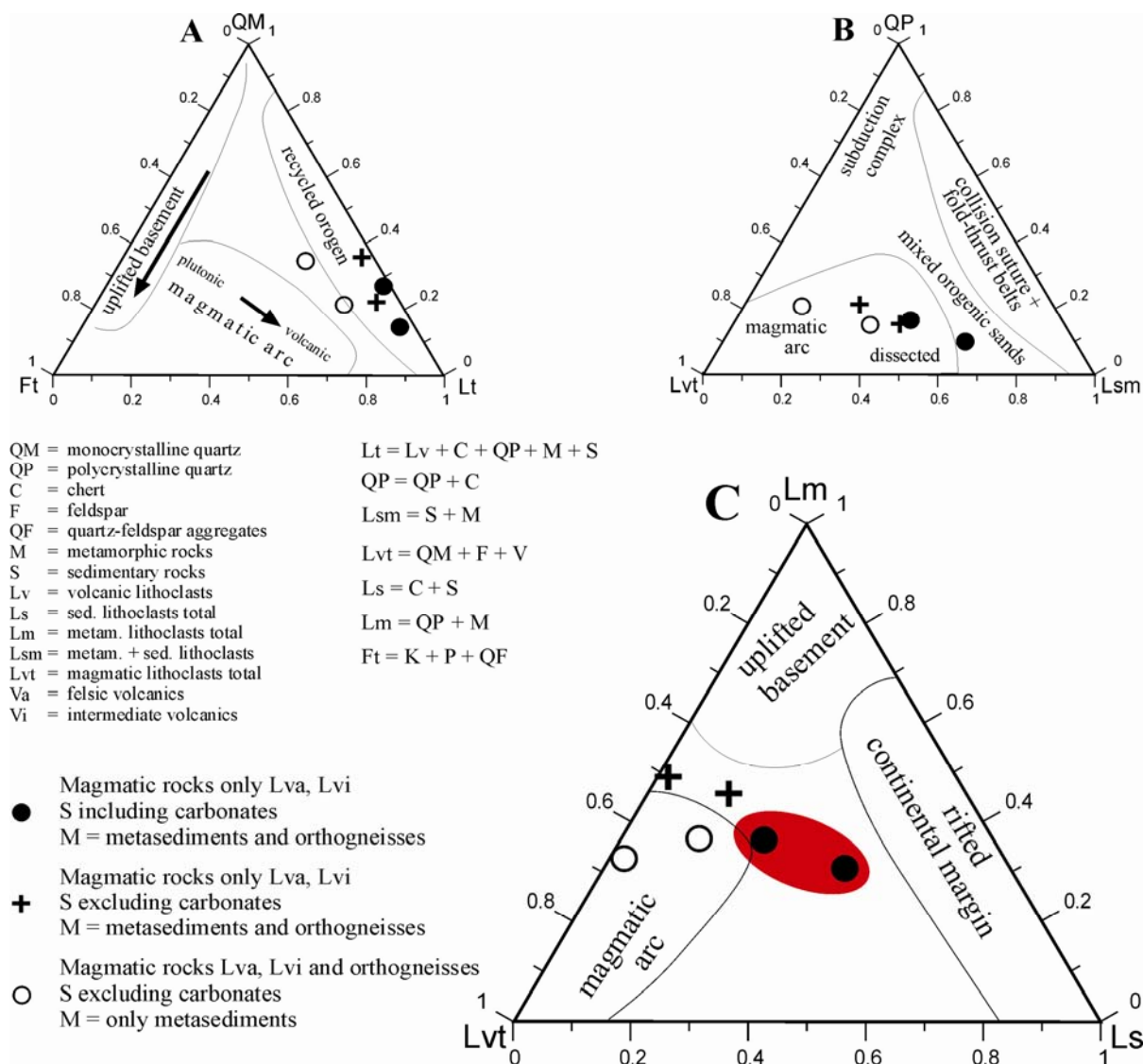


Fig. 7.1. Discrimination diagrams used for provenance analyses, based on Dickinson and Suczek (1979), Graham et al. (1993), and Ingersoll and Suczek (1979). Red shaded area denotes most reliable sample discrimination.

To better constrain the composition and the tectonic background of the subducted material in the study area, we applied provenance analyses to two samples from very-low grade sediment layers (profile 2). The discrimination diagrams (Fig. 7.1) show that the lithoclasts of both samples mainly consist of exhumed rock material of older orogenic origin. Metamorphic fragments with greenschist degree of overprint are thought to represent the dissected magmatic arc of the Paleozoic basement. In addition, 25% to 40% of the material is of magmatic-arc input. Because

of dominating rhyolitic fragments, it presumably may be related to Jurassic rifting. The high degree of recrystallized glassy matrix of these fragments rather excludes derivation from the Tertiary magmatic arc. Carbonatic fragments may derive either from Cretaceous basin sediments associated with rifting, which started in Middle Jurassic times (Ring et al. 1989; von Eynatten and Gaupp 1999), or to the Triassic cover of the basement prior to the onset of rifting processes. Due to the abundance of variegated components, minor tectonic and metamorphic overprint,

as well as the low degree of the component's rounding (subangular to subrounded) we conclude that the studied sediments are derived from the sedimentary cover of the South Penninic ocean. They might represent proximal turbiditic greywackes, which have been subducted to shallow depths and later accreted to the base of the overlying Austroalpine nappe stack.

The material comprising the fossil subduction channel is comparable to material thought to be subducted at recently active convergent plate margins (Chapter 3). According to Hashimoto et al. (2006), this material should be composed of clay mineral, trench-filling sand and carbonates. Also, the extension of sandstone blocks and layers, as proposed by these authors, is well visible throughout the study area (Chapter 4). In consequence, the exposed fossil subduction plate interface zone resembles active plate interface zones, despite of overprint during collision and exhumation, at least in terms of its compositional setup. We propose that in addition to the comparable composition, the behavior of the fossil plate interface zone was equivalent to recently active systems in terms of stable, unstable and conditional stable areas, as this is governed by the divers sediment input over time (Chapters 4, 5). Even spatiotemporal varying mass transfer mode is similar to presently active systems (Chapter 6).

We restored the fossil plate interface zone in the Swiss Alps to its former subduction geometry resulting in a 170 km long section with a ca.  $8^\circ$  SSE-dipping plate interface for the Late Cretaceous to Eocene period, prior to collision and underplating of the continental Briançonnais domain. This restoration does not provide hints for a major overprint of the pattern of subduction-related metamorphism by younger events. All later offsets visible within the section from Schmid et al. (1996) are below 1 km, except for the

oblique-slip Engadine line (Chapter 4). This is also in agreement with our field observations missing a penetrative overprint of the general top-W directed tectonic transport. Nevertheless, the present day fossil subduction channel has been influenced by post-subduction and post-accretion processes during ongoing convergence between both plates. These processes may have involved either both the South Penninic domain and the Austroalpine nappe stack, or only reactivated the direct contact between the lower and the upper plate. Magnitudes of subsequent deformation are small with respect to the total length and minimum displacement along the plate interface, and may even largely cancel out. The here calculated dip angle of the plate interface ( $\sim 8^\circ$ ) is in good agreement with published average megathrust angles (Lallemand et al., 1994; Moores and Twiss, 1995; Clift and Vannucchi, 2004). Therefore, we consider later modifications irrelevant at the here applied scale of observation.

In contrast to the compositional homogeneity in all studied transects, other features show a characteristic downdip change: the overprint of the upper plate base by Alpine deformation increases towards depth (respectively towards the south of the working area), the matrix of the subduction channel exhibits an equally increasing deformation and metamorphic grade, and the number of mylonitic shear zones and mylonitic rocks progressively increases as well. The density of LDZ also increases downdip ultimately involving the entire subduction channel matrix (Fig. 7.2). Because of more or less continuous flux of material in the subduction channel, all features will be displaced downdip once formed, or even updip due to return flow. This will result in (1) an offset of mélange features with regard to the overlying features at the base of the upper plate (except for first occurrence of features); (2) an apparent downdip increase in key features; and (3) apparently gradational

boundaries that may have been more distinct during formation. However, none of these aspects will be of significance in the upper plate. There, spatial and temporal varying frictional conditions within the plate interface zone caused by spatiotemporal variable sediment input might additionally smear out distinct boundaries for the onset of plate interface key features (e.g. pseudotachylytes formed within the basal parts of the crystalline upper plate resulting from frictional instability within the subduction channel). In consequence, the plate interface zone cannot exhibit a steady state behavior.

We interpret the occurrence of pseudotachylytes along the exhumed plate interface as delineating the area of unstable slip within the ancient subduction channel (Chapter 4) (Fig. 7.2). The fossil updip limit of unstable slip is located at a distance of ~90 km from the trench corresponding to a depth of ~15 km, and a temperature of ~200°C (Fig. 7.2). The fossil downdip limit of unstable slip is located at a distance of 140 km from the trench equivalent to a depth of ~22 km, and a temperature of ~300°C (Fig. 7.2). The conditionally stable segments above and below the unstable segment may continue for some distance updip and downdip. Below the downdip end of unstable slip we observe a continuing increase of LDZ in the *mélange* that may be seismic, jointly occurring with mylonites (Chapter 4). Therefore, we postulated seismic behavior to be possible in the subduction *mélange* to temperatures of at least 300°C to 350°C and possibly higher. However, formation of LDZ and associated seismic behavior is strongly lithology dependent (Chapter 4). The mylonitic overprint of pseudotachylytes, the mutual crosscutting of overprinted and non-overprinted pseudotachylytes, the drastic increase in LDZ, and the onset of mylonitic rocks in the subduction *mélange* and, slightly deeper, at the base of the upper plate, point to the coincidence of the

downdip limit of unstable slip with the start of a transitional zone at the downdip limit of the seismogenic coupling zone.

The updip extent of the fossil seismogenic coupling zone is proposed to be much wider than outlined by the zone of unstable slip, because the here estimated updip limit of unstable slip (~15 km depth, 200°C) is below the widely accepted values for active convergent plate margins (~5 km depth, 100°C-150°C, e.g. Oleskevich et al., 1999). Additionally, we observed localized deformation zones trenchward of the estimated upper limit of the unstable slip area. Otherwise, pressure solution seams, which are widespread in the northern part of the working area, are evidence for aseismic creep (e.g. Kitamura et al., 2005), possibly prevailing in the postseismic relaxation period.

Evidence for fluids circulating along the plate interface are widespread in the study area: foliation-parallel blocky-textured mineralized veins in the *mélange* matrix, veins cutting into competent clasts both downdip of profile 4 (Chapter 4), solution-precipitation creep as dominant deformation mechanism in all of the study area, dehydration reactions in the *mélange* matrix, and hydration as well as sealing of the upper plate base. Fluid percolation must have occurred unimpeded through a permeable fracture network, along foliation planes and grain boundaries in the upper conditionally stable domain because of the absence of mineralized veins updip of profile 4 (Fig. 7.2). Starting in the unstable slip area, formation of mineralized veins clearly requires fluid production rate to exceed percolation rate building near-lithostatic fluid pressure during parts of the seismic cycle. The internal structure of the mineralized veins resembles the structure of pseudotachylyte networks. Embedded wall rock fragments within the mineralized veins and within the pseudotachylytes - either with or without minor contact to the wall rock - point to fast fracturing and

subsequent rapid solidification processes. From the spatial coincidence of both features and their identical texture we postulate that formation of the mineralized veins potentially indicates unstable slip in the subduction *mélange*. The exclusive restriction of pseudotachylytes and mineralized vein systems to one component of the plate boundary system - i.e. base of upper plate vs. *mélange* - is most likely due to a different rheological behavior of the subduction *mélange*, and the crystalline basement of the upper plate.

Additionally, we observed blocky-textured mineralized veins, which are aligned sub-parallel to the overall foliation, in both metasediments and metabasic rocks in our second working area in Southern Chile (Chapter 1.3.2.). They are identical in texture and occurrence compared to the observed mineralized veins within the European Alps. However, according to PT estimates by Glodny et al. (2005) they have been formed deeper along the plate interface zone (8-9 kbar in Southern Chile). This also indicates proceeding vein formation along the plate interface, deeper down as observable in the European Alps. Its geometric style changes deeper down with longer and wider veins, still indicating ongoing hydrofracturing in the lower conditionally stable zone, as also observed for the LDZ. The heterogeneous internal structure of the subduction *mélange* governs the transport of released fluids both along and across the foliation, foliation parallel shear planes, and thus, the plate interface.

The transition between seismic and aseismic deformation in our studied example is well comparable to the proposed transitional zone downdip of the seismogenic part of active convergent plate interfaces (e.g. Hyndman and Wang, 1995). There, seismic slip in the transitional zone may occur during major coseismic events rupturing the entire unstable slip zone, subsequently

overprinted by viscous deformation during postseismic relaxation and interseismic creep. However, we note that our observations of proceeding vein formation, formation of LDZ, and the viscous overprint of brittle structures in the lower conditionally stable segment (Fig. 7.2) might also be indicators for a domain of slow earthquakes (slow slip events) and associated non-volcanic tremors, as proposed for many active subduction zones in a comparable depth range (e.g. Schwartz and Rokosky 2007).

We analyzed Sr isotope signatures of marine (meta-) carbonates. They are shown to be governed by both depositional and syn-subduction recrystallization history. Metamorphosed carbonate samples from the subduction *mélange* exhibit clear evidence for syn-metamorphic alteration by fluids. Increased  $^{87}\text{Sr}/^{86}\text{Sr}$  ratios of the metacarbonates indicate devolatilization of old continental crustal material as dominant source of syn-subduction fluids, probably of subducted continental detritus. This is in line with the prediction by e.g. Moore and Saffer (2001) highlighting the fluid production potential of subducted sediments at active subduction zones (Chapter 3) (Fig. 7.2) Subduction fluids from other sources, like dehydration of oceanic crust (e.g. Peacock 2000, Chapter 3), cannot be ruled out, but must have been minor due to the low  $^{87}\text{Sr}/^{86}\text{Sr}$  ratios expected for such fluids, which is in strong contrast with the compositions observed in the subduction *mélange* samples.

To determine the absolute timing of subduction-related deformation (Chapter 6), we used Rb/Sr geochronology on pervasively deformed rocks from both the South Penninic subduction *mélange* and the Austroalpine upper plate. Results of Rb/Sr isotope analyses shed light on the pre-Alpine and Alpine deformation history along the suture. The deformational and isotopic record of a subduction channel is persistently renewed due to continuous

processes such as sediment subduction and tectonic erosion. Only when material finally left the active parts of the subduction channel and became accreted to the base of the hanging wall, the deformational and isotopic record can be preserved. Deformation induced isotopic resetting during accretion of material to the base of the upper plate is caused by permanent strain accumulation due to velocity gradient between material flow within the channel and the upper plate. Due to a missing overprint of the isotopic system by later deformation events, our Rb/Sr isotopic ages date the removal of material out of the active parts of the subduction channel and the abandonment of the South Penninic-Austroalpine suture zone at roughly 50 Ma (Fig. 7.2). Rb/Sr ages are identical for pervasively deformed Austroalpine and South Penninic rocks. Metamorphic mobilisation, which is dated to 50 Ma, points to syn-subductional dehydration, fluid activity and mineral precipitation. According to our structural data, the latest increment of subduction-related deformation (at ~50 Ma) is characterized by a roughly top-W direction of tectonic transport.

Referring to published paleogeographic reconstructions, the end of subduction-related deformation is best explained by the locking of the South Penninic paleosubduction interface due to underplating of the Middle Penninic micro-continent, a process that caused a relocation of convergence-related strain from the paleosubduction *mélange* into the new, Middle Penninic footwall. The shutoff of sedimentation in the forearc Gosau basins is contemporaneous with basal accretion of the South Penninic *mélange* and the Middle Penninic units, both processes occurring in the Lower Eocene (~50 Ma). We therefore hypothesize a causal link between the two events, with the change from tectonic erosion to basal accretion being responsible for a regional pulse of uplift,

leading to inversion of the forearc basins. Von Blanckenburg and Davies (1995) suggest the underplating of continental Penninic material (most likely the Middle Penninic micro-continent) below the overriding plate in a time span between 55 Ma and 45 Ma (Fig. 6.12b). Our Rb/Sr age data are in line with these suggestions.

Rb/Sr deformation ages additionally have the potential to constrain the mode of syn-subduction interplate mass transfer. Hypothetical endmember scenarios for such mass transfer modes within subduction channels (Chapter 6) would result in: 1) continuous underplating adding material to the base of the upper plate (basal accretion), 2) continuous tectonic erosion removing material from the base of the upper plate, or 3) steady state continuous material flow neither adding nor removing material. Nearly identical Rb/Sr ages for pervasively deformed Austroalpine and South Penninic rocks point to tectonic erosion of the upper plate during subduction. This is also evidenced by the lack of upper plate crystalline basement immediately above the plate interface in some parts of the working area where upper plate sediments directly rest on the *mélange*, by the presence of upper plate clasts in the subduction *mélange* (e.g. Oncken 1998, Chapter 4), and from the syn-subduction evolution of Gosau forearc basins pointing to tectonic erosion as prevailing mass transfer mode during the time of subduction. Basal subduction erosion invariably stopped upon underplating of the *mélange*, and abandonment of the subduction of the South Penninic ocean. Lack of a metamorphic contrast between the South Penninic *mélange* and the Austroalpine upper plate favors exhumation of the suture zone due to a combination of tectonic underplating and surface erosion.

Another part of the study was  $^{40}\text{Ar}/^{39}\text{Ar}$  geochronology on pseudotachylytes to

constrain the timing of occurrence of unstable slip (Chapter 5). Defocused beam microprobe bulk analyses of the pseudotachylyte groundmass point to a mixture of amphibole, feldspar and possibly biotite, which equal the paragenesis of the host rocks. In addition, rock fragments and single minerals from the host rock of comparable size are incorporated in the pseudotachylyte groundmass. They provide a source for inherited argon, and thus complicating the interpretation of the isotopic data. We omitted visible wall rock fragments and single crystals inherited from the host rocks, but we cannot argue for a complete leave out of distracting inclusions. The use of a laser system in order to degas Ar by stepwise heating resulted in a rather localized heating of the sample. Despite of the small spot size, we expect the degassing of Ar to occur from a mixture of the ultra fine grained newly crystallized lasts and from wall rock fragments and single crystals, rather than from a homogeneous solidified melt. Our obtained  $^{40}\text{Ar}/^{39}\text{Ar}$  ages, as erroneous they might be, point to unstable slip and therewith associated pseudotachylyte formation within the basal parts of the Austroalpine nappe stack during a prolonged time span between 60 Ma to roughly 80 Ma (Fig. 7.2). The data of Thöni (1981, 1988) fall into the bracketed time frame. Due to the temporal similarity between subduction and pseudotachylyte formation, and the fact that the pseudotachylytes occur subparallel to the main thrust where Austroalpine rocks were overthrust onto South Penninic rocks, we interpret the generation of pseudotachylytes to be related to unstable slip processes occurring along the plate interface zone during subduction of the South Penninic ocean underneath the Austroalpine upper plate (Chapter 5).

The slightly difference between our Rb/Sr deformation ages for the southern parts of the working area (~50 Ma), and the

$^{40}\text{Ar}/^{39}\text{Ar}$  ages for pseudotachylyte formation within the central part of the working area (80 Ma to 60 Ma) might be either caused by methodological limitations or by changes in the mass transfer mode. While using Rb/Sr isotopic data we dated last increments of deformation induced resetting, and thus the end of a deformation process. The use of the Ar isotopic system constrain the obtained ages to a temperature sensitive degassing step during formation and recrystallization of the melt veins, which could be somewhat older then the last increment of deformation captured by the Rb/Sr system. Otherwise, the difference can also be explained by the incorporation of wall rock fragments and single minerals within the pseudotachylyte matrix leading the inherited argon, and thus to apparently too old ages. Additionally, according to our proposed endmember scenarios of material flux within the subduction channel, which we postulated to be elucidated using isotope geochronology, the difference in both geochronological methods could provide additional hints for spatiotemporal changes in tectonic erosion and accretion. Assuming tectonic erosion, the last increments of unstable slip might be erased from the base of the upper plate and transported towards depth, continuously shifting the area of isotopic resetting into the upper plate (Chapter 5). The mylonitization of pseudotachylytes at the immediate base of the upper plate might favor this explanation. Only geochronological studies of the mylonitic overprinted pseudotachylytes have the potential to finally answer this question.

The potential of this study is the possibility to draw direct connection from field-based observations to their proposed counterparts from active convergent plate margins. The distribution of earthquakes within the subduction channel as well as the basal part of the upper plate proposed for active subduction zones (Chapter 3) is comparable to the observed

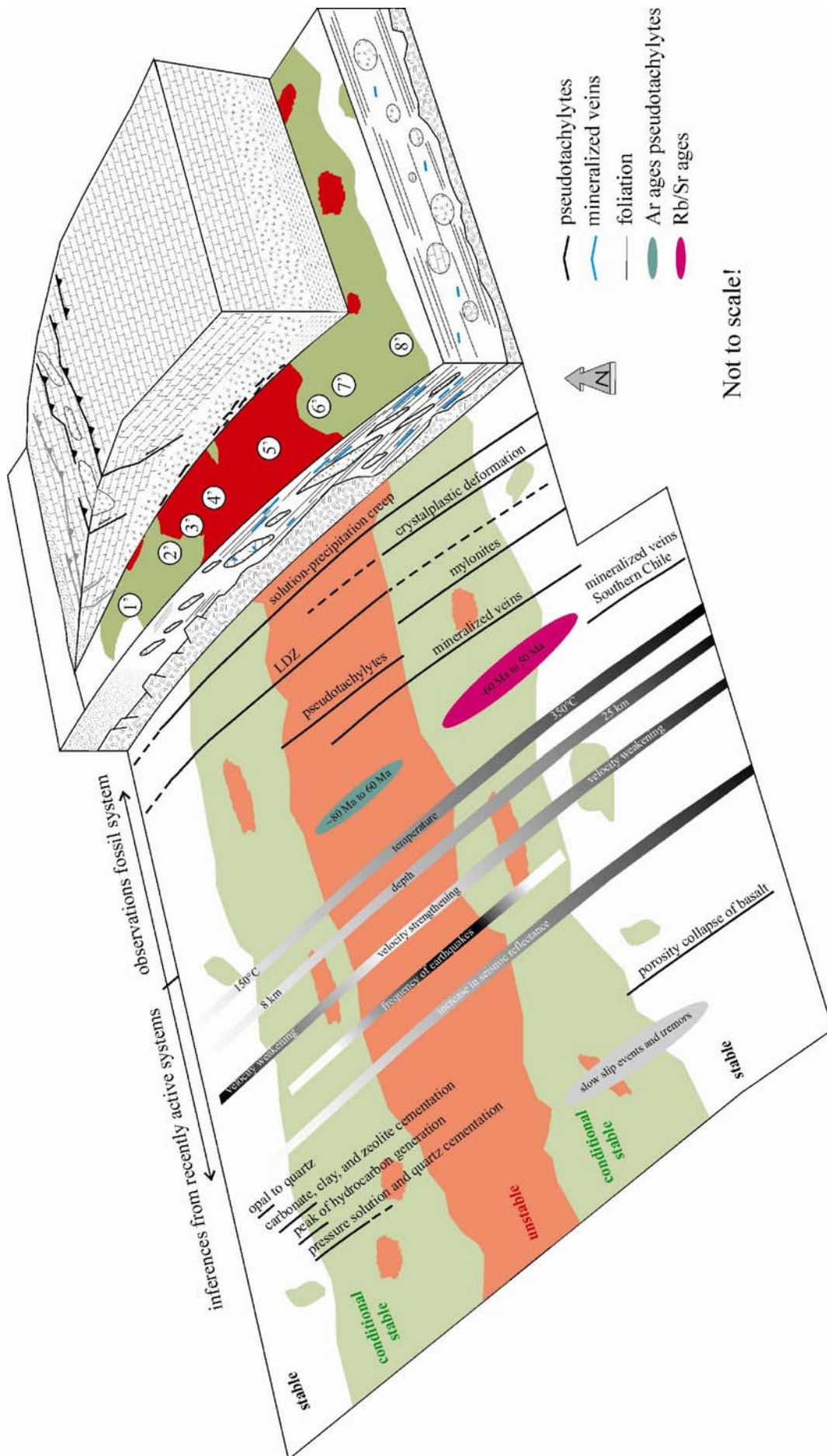


Figure 7.2: Final interpretative section showing the profile positions (number in circles), as well as the association and interference of the observed key features. Areas of conditional stability occur above and below the unstable slip region, characterized by the coexistence of slow deformation and maybe seismic deformation (e.g. LDZ, mineralized veins). The regions of stable, conditional stable and unstable slip will vary in space and time in accordance to spatiotemporal variance in e.g. sediment input, dewatering and dehydration. Thus, the mechanical conditions within the subduction channel are not characterized by steady state behaviour. Model of frictional conditions modified and extended downdip following Bilek and Lay (2002). Results of Rb/Sr and  $^{40}\text{Ar}/^{39}\text{Ar}$  geochronology are indicated. Additionally, we summarized key observations from recently active convergent plate interfaces. See text for details.

pseudotachylytes along the base of the Austroalpine upper plate, and the potentially seismicity-indicating mineralized veins and LDZ within the subduction mélangé (Fig. 7.2). The reported increase in seismic reflectivity towards depth (until a certain threshold) from active subduction zones (e.g. Oncken et al. 1999, Calvert et al. 2003) might be due to the increase in fabric development (foliation planes, shear zones, mineralized vein systems) observable at the fossil counterpart, in line with the prediction from active systems (Fig. 7.2). The broad reflector downdip the Cascadian subduction zone is interpreted to be related to mylonitic rocks in the temperature range between 250°C to 350°C (e.g. Nedimovic et al. 2003). In a comparable depth range with our fossil analogue we observed the increase in deformation, progressively involving the whole subduction channel (metasedimentary rocks intermingled with slivers of both oceanic and continental origin) and basal parts of the upper plate (Fig. 7.2). This might provide a structural evidence for the observed broad zone of reflectivity (e.g. Nedimovic et al. 2003 for Cascadia). Trapped fluids causing reflectivity e.g. along the Chilean subduction zone (e.g. Krawczyk et al. 2003) are widespread downdip the fossil plate interface, forming partly lentoid bodies. Furthermore, the low velocity zone being interpreted as a subduction channel (Krawczyk et al. 2006, and references therein) might be caused by the mixture of subducted sediments (with low  $V_P$  values)

with material from the upper and the lower plate – a composition equally to the observations with the fossil counterparts (Fig. 7.2). The observed intermingling of metasediments and slivers of upper and lower plate origin was also postulated by Calvert (2004) to be responsible for the observed  $V_P$  values (Chapter 3). High  $V_P/V_S$  ratios along the plate interface zone are assumed to be indicators for the presence of water saturated sediments (Husen et al. 2000), also in line with our field observations showing ubiquitous evidence for subducted sediments and dewatering and dehydration reactions, as well as fluid circulation.

Finally, the plate interfaces of the studied fossil convergent plate margins experienced flow and fracturing over an extended period of time reflecting a multistage evolution (especially the European Alps), but resemble active convergent plate margins in terms of e.g. sediment input, earthquake distribution, fluid circulation, and possible slow slip events and associated tremors. We suggest the testing of our field-based subduction plate interface setup with synthetic seismograms in order to prove the resolvability of the observed structures and lithological contrasts (i.e. clasts, duplexes). This would finally help to better constrain synthetic geophysical, numerical and analogue modelling, and offers the chance for a more detailed identification of processes within ancient and active subduction channels.



## References

- Ábalos, B., Puelles, P. & Gil Ibarguchi, J. I. 2003. Structural assemblage of high-pressure mantle and crustal rocks in a subduction channel (Cabo Ortegal, NW Spain). *Tectonics* **22**(2), 1-1 - 1-21.
- Allemand, P. & Lardeaux, J. M. 1997. Strain partitioning and metamorphism in a deformable orogenic wedge; application to the Alpine belt. In: *Thermal and mechanical interactions in deep-seated rocks* **280**; 1-2. Elsevier, Amsterdam, Netherlands, 157-169.
- Angermann, D., Klotz, J. & Reigber, C. 1999. Space-geodetic estimation of the Nazca-South America Euler vector. *Earth and Planetary Science Letters* **171**(3), 329-334.
- Atkinson, B. K. 1987. Introduction to fracture mechanics and its geophysical applications. In: *Fracture mechanics of rock*. Acad Press, London, United Kingdom.
- Bachmann, R., Oncken, O., Seifert, W. & Georgieva, V. submitted. Anatomy of a Fossil Subduction Channel - a quantitative view on changing structures along the plate interface.
- Ballance, P. F., Scholl, D. W., Vallier, T. L., Stevenson, A. J., Ryan, H. F. & Herzer, R. H. 1989. Subduction of a Late Cretaceous seamount of the Louisville Ridge at the Tonga Trench; a model of normal and accelerated tectonic erosion. *Tectonics* **8**(5), 953-962.
- Barazangi, M. & Isacks, B. L. 1976. Spatial distribution of earthquakes and subduction of the Nazca Plate beneath South America. *Geology (Boulder)* **4**(11), 686-692.
- Beaumont, C., Ellis, S. & Pfiffner, A. 1999. Dynamics of sediment subduction-accretion at convergent margins: Short-term modes, long-term deformation, and tectonic implications. *Journal of Geophysical Research B: Solid Earth* **104**(8), 17,573-17,601.
- Berger, G. W. & York, D. 1981. Geothermometry from  $^{40}\text{Ar}/^{39}\text{Ar}$  dating experiments. *Geochimica et Cosmochimica Acta* **45**(6), 795-811.
- Biehler, D. 1990. Strukturelle Entwicklung der penninisch-ostalpinen Grenzzone am Beispiel der Arosa-Zone im Ost-Raetikon (Vorarlberg, Oesterreich). *Eclogae Geologicae Helveticae* **83**(2), 221-239.
- Bilek, S. L. & Lay, T. 1998. Variation of interplate fault zone properties with depth in the Japan subduction zone. *Science* **281**(5380), 1175-1178.
- Bilek, S. L. & Lay, T. 1999. Rigidity variations with depth along interplate megathrust faults in subduction zones. *Nature (London)* **400**(6743), 443-446.
- Bilek, S. L. & Lay, T. 2002. Tsunami earthquakes possibly widespread manifestations of frictional conditional stability. *Geophysical Research Letters* **29**(14), 18-1 - 18-4.
- Birch, F. S. 1986. Isostatic, thermal, and flexural models of the subsidence of the north coast of Puerto Rico. *Geology (Boulder)* **14**(5), 427-429.
- Bostick, N. H., Cashman, S. M., McCulloh, T. H. & Waddell, C. T. 1979. Vitrinite reflectance, present rock temperature, laumontite occurrence, and burial history in Los Angeles and Ventura basins, California. *AAPG Bulletin* **63**(3), 421-422.
- Bousquet, R., Oberhänsli, R., Goffe, B., Jolivet, L. & Vidal, O. 1998. High-pressure-low-temperature metamorphism and deformation in the Bündnerschiefer of the Engadine window: implications for the regional evolution of the eastern central Alps. *Journal of Metamorphic Geology* **16**(5), 657-674.
- Brown, K. M., Tryon, M. D., DeShon, H. R., Dorman, L. M. & Schwartz, S. Y. 2005. Correlated transient fluid pulsing and seismic tremor in the Costa Rica subduction zone. *Earth and Planetary Science Letters* **238**(1-2), 189-203.
- Byrne, T. & Fisher, D. 1990. Evidence for a weak and overpressured decollement beneath sediment- dominated accretionary prisms. *Journal of Geophysical Research* **95**(B6), 9081-9097.
- Calvert, A. J., Fisher, M. A., Ramachandran, K. & Trehu, A. M. 2003. Possible emplacement of crustal rocks into the forearc mantle of the Cascadia Subduction Zone. *Geophysical Research Letters* **30**(23), SDE 3-1 - SDE 3-4.
- Chemenda, A. I., Hurpin, D., Tang, J. C., Stephan, J. F. & Buffet, G. 2001. Impact of arc-continent collision on the conditions of burial and exhumation of UHP/LT rocks: Experimental and numerical modelling. *Tectonophysics* **342**(1-2), 137-161.
- Chemenda, A. I., Mattauer, M. & Bokun, A. N. 1996. Continental subduction and a mechanism for exhumation of high-pressure metamorphic rocks; new modelling and field data from Oman. *Earth and Planetary Science Letters* **143**(1-4), 173-182.
- Chemenda, A. I., Mattauer, M., Malavieille, J. & Bokun, A. N. 1995. A mechanism for syn-collisional rock exhumation and associated normal faulting: results from physical modelling. *Earth and Planetary Science Letters* **132**(1-4), 225-232.
- Clauser, C. & Huenges, E. 1995. Thermal conductivity of rocks and minerals. In: *Rock physics & phase relations; a handbook of physical constants 3*; American Geophysical Union, Washington, DC, United States, 105-126.

- Cliff, R. A. & Meffan-Main, S. 2003. Evidence from Rb-Sr microsampling geochronology for the timing of Alpine deformation in the Sonnblick Dome, SE Tauern Window, Austria. In: *Geochronology: linking the isotopic record with petrology and textures* **220**; Geological Society of London, London, United Kingdom, 159-172.
- Clift, P. & Vannucchi, P. 2004. Controls on tectonic accretion versus erosion in subduction zones: Implications for the origin and recycling of the continental crust. *Reviews of Geophysics* **42**(2), RG2001 1-31.
- Cloos, M. & Shreve, R. L. 1988a. Subduction-channel model of prism accretion, mélange formation, sediment subduction, and subduction erosion at convergent plate margins: 1. Background and description. *Pure and Applied Geophysics* **128**(3-4), 455-500.
- Cloos, M. & Shreve, R. L. 1988b. Subduction-channel model of prism accretion, mélange formation, sediment subduction, and subduction erosion at convergent plate margins; Part II, Implications and discussion. *Pure and Applied Geophysics* **128**(3-4), 501-545.
- Cowan, D. S. 1985. Structural styles in Mesozoic and Cenozoic mélanges in the Western Cordillera of North America. *Geological Society of America Bulletin* **96**(4), 451-462.
- Cowan, D. S. 1999. Do faults preserve a record of seismic slip? A field geologist's opinion. *Journal of Structural Geology* **21**, 995-1001.
- Dallmeyer, R. D., Handler, R., Neubauer, F. & Fritz, H. 1998. Sequence of thrusting within a thick-skinned tectonic wedge: evidence from  $^{40}\text{Ar}/^{39}\text{Ar}$  and Rb-Sr ages from the Austroalpine nappe complex of the eastern Alps. *Journal of Geology* **106**(1), 71-86.
- DeMets, C., Gordon, R. G., Argus, D. F. & Stein, S. 1994. Effect of recent revisions to the geomagnetic reversal time scale on estimates of current plate motions. *Geophysical Research Letters* **21**(20), 2191-2194.
- Deutsch, A. 1983. Datierungen an Alkalamphibolen und Stilpnomelan aus der Suedlichen Platta-Decke (Graubuenden). *Eclogae Geologicae Helveticae* **76**(2), 295-308.
- Dickinson, W. R. 1970. Interpreting detrital modes of graywacke and arkose. *Journal of Sedimentary Petrology* **40**(2), 695-707.
- Dickinson, W. R. & Suczek, C. A. 1979. Plate tectonics and sandstone compositions. *AAPG Bulletin* **63**(12), 2164-2182.
- Dürr, S. B. 1992. Structural history of the Arosa Zone between Platta and Err nappes east of Marmorera (Grisons): multi-phase deformation at the Penninic-Austroalpine plate boundary. *Eclogae Geologicae Helveticae* **85**(2), 361-374.
- Eppinger, K. J., and Rosenfeld, U. 1996. Western margin and provenance of sediments of the Neuquén Basin (Argentina) in the Late Jurassic and Early Cretaceous. *Tectonophysics*, **259** (1-3), 229-244.
- Faupl, P. & Wagneich, M. 1996. Basin analysis of the Gosau Group of the northern Calcareous Alps (Turonian-Eocene, Eastern Alps). In: *Oil and gas in Alpidic thrustbelts and basins of Central and Eastern Europe* **5**; [publisher varies], [location varies], Federal Republic of Germany, 127-135.
- Faure, G. 1986. *Principle of Isotope Geology*. Wiley, New York.
- Ferreiro Mählmann, R. 1994. *Zur Bestimmung von Diagenesehöhe und beginnender Metamorphose - Temperaturgeschichte und Tektogenese des Austroalpins und Südpenninikums in Vorarlberg und Mittelbünden*.
- Ferreiro Mählmann, R. 2001. Correlation of very low grade data to calibrate a thermal maturity model in a nappe tectonic setting, a case study from the Alps. *Tectonophysics* **334**(1), 1-33.
- Fleck, R. J., Sutter, J. F. & Elliot, D. H. 1977. Interpretation of discordant  $^{40}\text{Ar}/^{39}\text{Ar}$  age-spectra of Mesozoic tholeiites from Antarctica. *Geochimica et Cosmochimica Acta* **41**(1), 15-32.
- Florineth, D. & Froitzheim, N. 1994. Transition from continental to oceanic basement in the Tasna nappe (Engadine window, Graubunden, Switzerland): evidence for early Cretaceous opening of the Valais Ocean. *Schweizerische Mineralogische und Petrographische Mitteilungen* **74**(3), 437-448.
- Ford, M., Duchene, S., Gasquet, D. & Vanderhaeghe, O. 2006. Two-phase orogenic convergence in the external and internal SW Alps. *Journal of the Geological Society of London* **163**(5), 815-826.
- Forsythe, R. 1982. The late Paleozoic to early Mesozoic evolution of Southern South America: a plate tectonic interpretation. *J. Geol. Soc. London*, **139**, 671-682.
- Freeman, S. R., Inger, S., Butler, R. W. H. & Cliff, R. A. 1997. Dating deformation using Rb-Sr in white mica; greenschist facies deformation ages from the Entrelor shear zone, Italian Alps. *Tectonics* **16**(1), 57-76.
- Frey, M. & Ferreiro Mählmann, R. 1999. Alpine metamorphism of the Central Alps. In: *The new metamorphic map of the Alps; 1:500000; 1:1000000* **79**; 1. Staebli Verlag AG, Zurich, Switzerland, 135-154.
- Frey, M., Hunziker, J. C., Frank, W., Bocquet, J., Dal, P. G. V., Jager, E. & Niggli, E. 1974. Alpine metamorphism of the Alps; a review. *Schweizerische Mineralogische und Petrographische Mitteilungen = Bulletin Suisse de Mineralogie et Petrographie* **54**(2-3, Alpidische Metamorphosen in den Alpen), 247-290.

- Froitzheim, N., Conti, P. & Van Daalen, M. 1997. Late Cretaceous, synorogenic, low-angle normal faulting along the Schlinig fault (Switzerland, Italy, Austria) and its significance for the tectonics of the Eastern Alps. *Tectonophysics* **280**(3-4), 267-293.
- Froitzheim, N., Müntener, O., Puschig, A., Schmid, S. M. & Trommsdorff, V. 1996. Der penninisch-ostalpine Grenzbereich in Graubünden und in der Val Malenco. *Eclogae geol. Helv.* **89**(1), 617-634.
- Froitzheim, N., Pleuger, J., Roller, S. & Nagel, T. 2003. Exhumation of high- and ultrahigh-pressure metamorphic rocks by slab extraction. *Geology* **31**(10), 925-928.
- Froitzheim, N. & Rubatto, D. 1998. Continental breakup by detachment faulting; field evidence and geochronological constraints (Tasna Nappe, Switzerland). *Terra Nova The European Journal of Geosciences*. **10**(4), 171-176.
- Froitzheim, N., Schmid, S. M. & Conti, P. 1994. Repeated change from crustal shortening to orogen-parallel extension in the Austroalpine units of Graubünden. *Eclogae Geologicae Helveticae* **87**(2), 559-612.
- Gast, P. W. 1955. Abundance of Sr (super 87) during geologic time. *Geological Society of America Bulletin* **66**(11), 1449-1454.
- Gebauer, D. 1999. Alpine geochronology of the central and western alps: New constraints for a complex geodynamic evolution. *Schweizerische Mineralogische und Petrographische Mitteilungen* **79**(1), 191-208.
- Gerya, T. V. & Stöckhert, B. 2002. Exhumation rates of high pressure metamorphic rocks in subduction channels: The effect of Rheology. *Geophysical Research Letters* **29**(8), 102-1 - 102-4.
- Gerya, T. V., Stöckhert, B. & Perchuk, A. L. 2002. Exhumation of high-pressure metamorphic rocks in a subduction channel: A numerical simulation. *Tectonics* **21**(6), 6-1 - 6-19.
- Glodny, J., Bingen, B., Austrheim, H., Molina, J. F. & Rusin, A. 2002. Precise eclogitization ages deduced from Rb/Sr mineral systematics: The Maksyutov complex, Southern Urals, Russia. *Geochimica et Cosmochimica Acta* **66**(7), 1221-1235.
- Glodny, J., Lohrmann, J., Echter, H., Graefe, K., Seifert, W., Collao, S. & Figueroa, O. 2005. Internal dynamics of a paleoaccretionary wedge; insights from combined isotope tectonochronology and sandbox modelling of the south-central Chilean forearc. *Earth and Planetary Science Letters* **231**(1-2), 23-39.
- Glodny, J., Ring, U. & Kühn, A. submitted. High-pressure metamorphism, thrusting, strike-slip and extensional shearing in the Tauern Window, Eastern Alps: All starting at the same time? *Tectonics*.
- Graham, S. A., Hendrix, M. S., Wang, L. B. & Carroll, A. R. 1993. Collisional successor basins of western China; impact of tectonic inheritance on sand composition. *Geological Society of America Bulletin* **105**(3), 323-344.
- Grevemeyer, I., Kaul, N., Diaz, N. J. L., Villinger, H. W., Ranero, C. R. & Reichert, C. 2005. Heat flow and bending-related faulting at subduction trenches; case studies offshore of Nicaragua and central Chile. *Earth and Planetary Science Letters* **236**(1-2), 238-248.
- Gudmundsson, O. & Sambridge, M. 1998. A regionalized upper mantle (RUM) seismic model. *Journal of Geophysical Research B: Solid Earth* **103**(B4), 7121-7136.
- Gürler, B. & Schmutz, H.-U. 1995. *Geologische Untersuchungen im SW-Teil des Unterengadiner Fensters*.
- Haberland, C., Rietbrock, A., Lange, D., Bataille, K. & Hofmann, S. 2006. Interaction between forearc and oceanic plate at the south-central Chilean margin as seen in local seismic data. *Geophysical Research Letters* **33**(23), ; L23302.
- Hahn, O., Strassmann, F., Mattauch, J. & Ewald, H. 1943. Geologische Altersbestimmung mit der Strontiummethode. *Chem. Zeitung* **67**, 55-56.
- Handy, M. R. 1996. The transition from passive to active margin tectonics: a case study from the Zone of Samedan (eastern Switzerland). *Geologische Rundschau* **85**(4), 832-851.
- Handy, M. R., Herwegh, M., Kamber, B. S., Tietz, R. & Villa, I. M. 1996. Geochronologic, petrologic and kinematic constraints on the evolution of the Err-Platta boundary, part of a fossil continent- ocean suture in the Alps (eastern Switzerland). *Schweizerische Mineralogische und Petrographische Mitteilungen* **76**(3), 453-474.
- Handy, M. R. & Oberhänsli, R. 2004. Explanatory notes to the map: Metamorphic structure of the Alps, age map of the metamorphic structure of the Alps - tectonic interpretation and outstanding problems. In: *Metamorphic structure of the Alps* (edited by Oberhänsli, R.). *Mitteilungen der Österreichischen Mineralogischen Gesellschaft*, Wien, 227.
- Hashimoto, Y., Nakaya, T., Ito, M. & Kimura, G. 2006. Tectonolithification of sandstone prior to the onset of seismogenic subduction zone: Evidence from tectonic mélange of the Shimanto Belt, Japan. *Geochemistry Geophysics Geosystems* **7**.
- Howarth, R. J. & McArthur, J. M. 1997. Statistics for strontium isotope stratigraphy; a robust LOWESS fit to marine Sr-isotope curve for 0 to 206 Ma, with look-up table for derivation of numeric age. *Journal of Geology* **105**(4), 441-456.

- Hubbert, M. K. & Rubey, W. W. 1959. Mechanics of fluid-filled porous solids and its application to overthrust faulting, [Part] 1 of Role of fluid pressure in mechanics of overthrust faulting. *Geological Society of America Bulletin* **70**(2), 115-166.
- Hubbert, M. K. & Willis, D. G. 1957. Mechanics of hydraulic fracturing. *Jpt Journal of Petroleum Technology*, **9**(6), 153-168.
- Husen, S. & Kissling, E. 2001. Postseismic fluid flow after the large subduction earthquake of Antofagasta, Chile. *Geology* **29**(9), 847-850.
- Husen, S., Kissling, E. & Flueh, E. R. 2000. Local earthquake tomography of shallow subduction in north Chile: A combined onshore and offshore study. *Journal of Geophysical Research B: Solid Earth* **105**(12), 28183-28198.
- Hyndman, R. D. 1988. Dipping seismic reflectors, electrically conductive zones, and trapped water in the crust over a subducting plate. *Journal of Geophysical Research, B, Solid Earth and Planets* **93**(11), 13,391-13,405.
- Hyndman, R. D. & Peacock, S. M. 2003. Serpentinization of the forearc mantle. *Earth and Planetary Science Letters* **212**, 417-432.
- Hyndman, R. D. & Wang, K. 1995. The rupture zone of Cascadia great earthquakes from current deformation and the thermal regime. *Journal of Geophysical Research, B, Solid Earth and Planets* **100**(11), 22,133-22,154.
- Hyndman, R. D., Yamano, M. & Oleskevich, D. A. 1997. The seismogenic zone of subduction thrust faults. *Island Arc* **6**(3), 244-260.
- Inger, S. & Cliff, B. 1994. Dating high pressure metamorphism in the Western Alps; refining isotopic and tectonic interpretations. In: *Abstracts of the Eighth international conference on Geochronology, cosmochronology, and isotope geology* **S. Geological Survey Circular**. U S, Geological Survey, 149.
- Ingersoll, R. V. & Suczek, C. A. 1979. Petrology and provenance of Neogene sand from Nicobar and Bengal fans, DSDP sites 211 and 218. *Journal of Sedimentary Petrology* **49**(4), 1217-1228.
- Ito, S., Hino, R., Matsumoto, S., Shiobara, H., Shimamura, H., Kanazawa, T., Sato, T., Kasahara, J. & Hasegawa, A. 2000. Deep seismic structure of the seismogenic plate boundary in the off-Sanriku region, northeastern Japan. *Tectonophysics* **319**(4), 261-274.
- Iwamori, H. 1998. Transportation of H<sub>2</sub>O and melting in subduction zones. *Earth and Planetary Science Letters* **160**(1-2), 65-80.
- Jarosewich, E., Nelen, J. A. & Norberg, J. A. 1980. Reference samples for electron microprobe analysis. *Geostandards Newsletter* **4**(1), 43-47.
- Kenkmann, T., Hornemann, U. & Stoffler, D. 2000. Experimental generation of shock-induced pseudotachylites along lithological interfaces. *Meteoritics and Planetary Science* **35**(6), 1275-1290.
- Kitamura, Y., Sato, K., Ikesawa, E., Ikehara, O. K., Kimura, G., Kondo, H., Ujiie, K., Onishi, C. T., Kawabata, K., Hashimoto, Y., Mukoyoshi, H. & Masago, H. 2005. Mélange and its seismogenic roof decollement; a plate boundary fault rock in the subduction zone; an example from the Shimanto Belt, Japan. *Tectonics*.
- Koch, N. & Masch, L. 1992. Formation of Alpine mylonites and pseudotachylites at the base of the Silvretta nappe, Eastern Alps. *Tectonophysics* **204**, 289-306.
- Krawczyk, C. & SPOC-Team. 2003. Amphibious seismic survey images plate interface at 1960 Chile earthquake. *EOS* **84** (32)(301), 304-305.
- Krawczyk, C. M., Mechie, J., Lüth, S., Tašárová, Z., Wigger, P., Stiller, M., Brasse, H., Echter, H. P., Araneda, M. & Bataille, K. 2006. Geophysical Signatures and Active Tectonics at the South-Central Chilean Margin. In: *The Andes - Active Subduction Orogeny* (edited by Oncken, O., Chong, G., Franz, G., Giese, P., Götze, H.-J., Ramos, V. A., Strecker, M. R. & Wigger, P.). Springer, Berlin, 171-192.
- Kretz, R. 1983. Symbols for rock-forming minerals. *American Mineralogist* **68**(1-2), 277-279.
- Kuhlemann, J., Dunkl, I., Bruegel, A., Spiegel, C. & Frisch, W. 2006. From source terrains of the Eastern Alps to the Molasse Basin; detrital record of non-steady-state exhumation. *Tectonophysics* **413**(3-4), 301-316.
- Kukowski, N., Lallemand, S. E., Malavieille, J., Gutscher, M. A. & Reston, T. J. 2002. Mechanical decoupling and basal duplex formation observed in sandbox experiments with application to the western Mediterranean Ridge accretionary complex. In: *The accretionary complex of the Mediterranean Ridge; tectonics, fluid flow, and the formation of brine lakes* **186; 1-2**. Elsevier, Amsterdam, Netherlands, 29-42.
- Kullerud, L. 1991. On the calculation of isochrons. *Chemical Geology* **87**, 115-124.
- Lallemand, S. E., Schnuerle, P. & Malavieille, J. 1994. Coulomb theory applied to accretionary and nonaccretionary wedges; possible causes for tectonic erosion and/ or frontal accretion. *Journal of Geophysical Research, B, Solid Earth and Planets* **99**(6), 12,033-12,055.
- Lange, D. 2007. The Southern Chilean Subduction Zone between 41° and 43.5°S: Seismicity, Structure and State of Stress. Unpublished PhD thesis, University Postdam.

- Legros, F., Cantagrel, J. M. & Devouard, B. 2000. Pseudotachylite (frictionite) at the base of the Arequipa volcanic landslide deposit (Peru); implications for emplacement mechanisms. *Journal of Geology* **108**(5), 601-611.
- Linares, E., Cagnoni, M. C., DoCampo, M., and Oстера, H. A. 1988. Geochronology of metamorphic and eruptive rocks of southeastern Neuquén and northwestern Río Negro Provinces, Argentine Republic. *J. S. Am. Earth Sci.*, **1** (1), 53-61.
- Liu, Y., Genser, J., Handler, R., Friedl, G. & Neubauer, F. 2001.  $^{40}\text{Ar}/^{39}\text{Ar}$  muscovite ages from the Penninic-Austroalpine Plate boundary, Eastern Alps. *Tectonics* **20**(4), 526-547.
- Lohrmann, J. 2002. Identification of parameters controlling the accretive and tectonically erosive mass-transfer mode at the South-Central and North Chilean forearc using scaled 2D sandbox experiments. In: *Scientific Technical Report*, 236.
- Lohrmann, J., Kukowski, N., Krawczyk, C. M., Oncken, O., Sick, C., Sobiesiak, M. & Rietbrock, A. 2006. Subduction Channel Evolution in Brittle Fore-Arc Wedges - a Combined Study with Scaled Sandbox Experiments, Seismological and Reflection Seismic Data and Geological Field Evidence. In: *The Andes - Active Subduction Orogeny* (edited by Oncken, O., Chong, G., Franz, G., Giese, P., Götze, H.-J., Ramos, V., Strecker, M. & Wigger, P.). *Frontiers in Earth Sciences*. Springer, Berlin, 237-262.
- Ludwig, K. R. 1999. Isoplot/Ex Ver 2.06: a Geochronological Toolkit for Microsoft Excel. *Berkeley Geochronology Center Special Publications* **1a**.
- Maddock, R. H. 1992. Effects of lithology, cataclasis and melting on the composition of fault-generated pseudotachylites in Lewisian gneiss, Scotland. In: *Frictional melting processes and products in geological materials* **204**; 3-4. Elsevier, Amsterdam, Netherlands, 261-278.
- Manatschal, G., Engstrom, A., Desmurs, L., Schaltegger, U., Cosca, M., Müntener, O. & Bernoulli, D. 2006. What is the tectono-metamorphic evolution of continental break-up; the example of the Tasna ocean-continent transition. *Journal of Structural Geology* **28**(10), 1849-1869.
- Manatschal, G., Müntener, O., Desmurs, L. & Bernoulli, D. 2003. An ancient ocean-continent transition in the Alps: The Totalp, Err-Platta, and Malenco units in the eastern Central Alps (Graubünden and northern Italy). *Eclogae Geologicae Helvetiae* **96**(1), 131-146.
- Markley, M., Teyssier, C. & Cosca, M. 1995. Deformation vs. cooling ages; the application of the  $^{40}\text{Ar}/^{39}\text{Ar}$  method to synkinematic white micas. In: *Geological Society of America, 1995 annual meeting* **27**; 6. Geological Society of America (GSA), Boulder, CO, United States, 217-218.
- Martin, M. W., Kato, T. T., Rodriguez, C., Godoy, E., Duhart, P., McDonough, M. & Campos, A. 1999. Evolution of the late Paleozoic accretionary complex and overlying forearc-magmatic arc, south central Chile (38< degrees >-41< degrees >S): Constraints for the tectonic setting along the southwestern margin of Gondwana. *Tectonics* **18**(4), 582-605.
- Masch, L. 1970. Die Pseudotachylite der Silvretta. *Dissertation*.
- Masch, L. 1974. Untersuchung der Aufschmelzung und Deformation der Pseudotachylite der Silvretta (Österreich, Schweiz). *Neues Jahrbuch Mineralogie* **11**, 485-509.
- Massonne, H. J. & Szpurka, Z. 1997. Thermodynamic properties of white micas on the basis of high-pressure experiments in the systems  $\text{K}_2\text{O}-\text{MgO}-\text{Al}_2\text{O}_3 - \text{SiO}_2 - \text{H}_2\text{O}$  and  $\text{K}_2\text{O} - \text{FeO} - \text{Al}_2\text{O}_3 - \text{SiO}_2 - \text{H}_2\text{O}$ . In: *High pressure metamorphism in nature and experiment* **41**; 1-3. Elsevier, Amsterdam, International, 229-250.
- McArthur, J. M., Howarth, R. J. & Bailey, T. R. 2001. Strontium isotope stratigraphy; LOWESS Version 3; best fit to the marine Sr-isotope curve for 0-509 Ma and accompanying look-up table for deriving numerical age. *Journal of Geology* **109**(2), 155-170.
- Melnick, D. 2007. Neogene seismotectonics of the south-central Chile margin: Subduction-related processes over various temporal and spatial scales. Unpublished PhD thesis, University Potsdam.
- Meneghini, F. & Moore, J. C. 2007. Deformation and hydrofracture in a subduction thrust at seismogenic depths; the Rodeo Cove thrust zone, Marin Headlands, California. *Geological Society of America Bulletin* **119**(1-2), 174-183.
- Merrihue, C. & Turner, G. 1966. Potassium-argon dating by activation with fast neutrons. *Journal of Geophysical Research* **78**, 2852-2857.
- Micksch, U., Krawczyk, C. M., Ryberg, T., Groß, K., Buske, S., Stiller, M., Wigger, P. & Group, T. R. 2006. The Seismogenic Coupling Zone in Southern Central Chile, 38° S: Structure and state of the convergent margin between surface and down-dip end. *AGU Fall Meeting (San Francisco, USA 2006)*.
- Mitchel, J. G. 1968. The argon-40/argon-39 method for potassium-argon age determination. *Geochimica et Cosmochimica Acta* **64**, 73-98.
- Moore, J. C. & Saffer, D. 2001. Updip limit of the seismogenic zone beneath the accretionary prism of southwest Japan: An effect of diagenetic to low-grade metamorphic processes and increasing effective stress. *Geology* **29**(2), 183-186.
- Moores, E. M. & Twiss, R. J. 1995. *Tectonics*. W. H. Freeman, New York.

- Müller, R. D., Roest, W. R., Royer, J.-Y., Gahagan, L. M. & Sclater, J. G. 1997. Digital isochrons of the world's ocean floor. *Journal of Geophysical Research* **102**, 3211-3214.
- Müller, W., Dallmeyer, R. D., Neubauer, F. & Thoeni, M. 1999. Deformation-induced resetting of Rb/ Sr and  $^{40}\text{Ar}/^{39}\text{Ar}$  mineral systems in a low-grade, polymetamorphic terrane (Eastern Alps, Austria). *Journal of the Geological Society of London*.
- Müller, W., Kelley, S. P. & Villa, I. M. 2002. Dating fault-generated pseudotachylytes: comparison of  $^{40}\text{Ar}/^{39}\text{Ar}$  stepwise-heating, laser-ablation and Rb-Sr microsampling analyses. *Contributions to Mineralogy and Petrology* **144**, 57-77.
- Müller, W., Mancktelow, N. & Meier, M. 2000. Rb-Sr microchrons of synkinematic mica in mylonites; an example from the DAV Fault of the Eastern Alps. *Earth and Planetary Science Letters* **180**(3-4), 385-397.
- Nedimovic, M. R., Hyndman, R. D., Ramachandran, K. & Spence, G. D. 2003. Reflection signature of seismic and aseismic slip on the northern Cascadia subduction interface. *Nature* **424**(6947), 416-420.
- Nelson, E. P. & Forsythe, R. D. 1989. Ridge collision at convergent margins; implications for Archean and post-Archean crustal growth. In: *Growth of the continental crust* **161**; 3-4. Elsevier, Amsterdam, Netherlands, 307-315.
- Nievergelt, P., Liniger, M., Froitzheim, N. & Ferreiro-Mählmann, R. 1996. Early to mid Tertiary crustal extension in the central Alps: the Turba mylonite zone (eastern Switzerland). *Tectonics* **15**(2), 329-340.
- Nüchter, J.-A. & Stöckhert, B. 2007. Vein quartz microfabrics indicating progressive evolution of fractures into cavities during postseismic creep in the middle crust. *Journal of Structural Geology* **In Press, Accepted Manuscript**.
- Obara, K. 2002. Nonvolcanic deep tremor associated with subduction in southwest Japan. *Science* **296**(5573), 1679-1681.
- Oleskevich, D. A., Hyndman, R. D. & Wang, K. 1999. The updip and downdip limits to great subduction earthquakes: Thermal and structural models of Cascadia, south Alaska, SW Japan, and Chile. *Journal of Geophysical Research* **104**(B7), 14965-14991.
- Oliver, N. H. S. & Bons, P. D. 2001. Mechanisms of fluid flow and fluid-rock interaction in fossil metamorphic hydrothermal systems inferred from vein-wallrock patterns, geometry and microstructure doi:10.1046/j.1468-8123.2001.00013.x. *Geofluids* **1**(2), 137-162.
- Oncken, O. 1998. Evidence for precollisional subduction erosion in ancient collisional belts; the case of the mid-European Variscides. *Geology (Boulder)* **26**(12), 1075-1078.
- Oncken, O., Luschen, E., Mechie, J., Sobolev, S., Schulze, A., Gaedicke, C., Grunewald, S., Bribach, J., Asch, G., Giese, P., Wigger, P., Schmitz, M., Lueth, S., Scheuber, E., Haberland, C., Rietbrock, A., Gotze, H. J., Brasse, H., Patzwahl, R., Chong, G., Wilke, H. G., Gonzalez, G., Jensen, A., Araneda, M., Vieytes, H., Behn, G., Martinez, E., Rossling, R., Amador, J., Ricaldi, E., Chumacero, H. & Luterstein, R. 1999. Seismic reflection image revealing offset of Andean subduction-zone earthquake. *Nature* **397**(6717), 341-344.
- Oncken, O., Sobolev, S., Stiller, M., Asch, G., Haberland, C., Mechie, J., Yuan, X., Luschen, E., Giese, P., Wigger, P., Lueth, S., Scheuber, E., Goetze, J., Brasse, H., Buske, S., Yoon, M. K., Shapiro, S., Rietbrock, A., Chong, G., Wilke, H. G., Gonzalez, G., Bravo, P., Vieytes, H., Martinez, E., Rossling, R. & Ricaldi, E. 2003. Seismic imaging of a convergent continental margin and plateau in the central Andes (Andean Continental Research Project 1996 (ANCORP'96)). *Journal of Geophysical Research, B, Solid Earth and Planets*.
- Pacheco, J. F., Sykes, L. R. & Scholz, C. H. 1993. Nature of seismic coupling along simple plate boundaries of the subduction type. *Journal of Geophysical Research* **98**(B8), 14,133-14,159.
- Parada, M. A., Palacios, C., and Lahsen, A. 1997. Jurassic extensional tectono-magmatism and associated mineralization of the El Faldeo polymetallic district, Chilean Patagonia: geochemical and isotopic evidence of crustal contribution. *Min. Dep.*, **32**, 547-554.
- Peacock, S. M. 2000. Thermal Structure and Metamorphic Evolution of Subducting Slabs.
- Peacock, S. M. & Hyndman, R. D. 1999. Hydrous minerals in the mantle wedge and the maximum depth of subduction thrust earthquakes. *Geophysical Research Letters* **26**(16), 2517-2520.
- Pfiffner, O. A., Ellis, S. & Beaumont, C. 2000. Collision tectonics in the Swiss Alps: Insight from geodynamic modeling. *Tectonics* **19**(6), 1065-1094.
- Platt, J. P. 1993. Exhumation of high-pressure rocks; a review of concepts and processes. *Terra Nova* **5**(2), 119-133.
- Ratschbacher, L., Dingeldey, C., Miller, C., Hacker, B. R. & McWilliams, M. O. 2004. Formation, subduction, and exhumation of Penninic oceanic crust in the Eastern Alps; time constraints from  $^{40}\text{Ar}/^{39}\text{Ar}$  geochronology. *Tectonophysics* **394**(3-4), 155-170 2 sheets.
- Renard, F., Gratier, J. P. & Jamtveit, B. 2000. Kinetics of crack-sealing, intergranular pressure solution, and compaction around active faults. *Journal of Structural Geology* **22**(10), 1395-1407.

- Ring, U. 1989. Tectonogenesis of the Penninic/ Austroalpine boundary zone: The Arosa Zone (Grisons-Rätikon area, Swiss-Austrian Alps). *Tübinger Geowissenschaftliche Arbeiten Reihe A*(1), 1-177.
- Ring, U., Brandon, M. T., Willett, S. D. & Lister, G. S. 1999. Exhumation processes. In: *Exhumation processes; normal faulting, ductile flow and erosion* **154**; Geological Society of London, London, United Kingdom, 1-27.
- Ring, U., Ratschbacher, L. & Frisch, W. 1988. Plate-boundary kinematics in the Alps: Motion in the Arosa suture zone. *Geology* **16**, 696-698.
- Ring, U., Ratschbacher, L., Frisch, W., Biehler, D. & Kralik, M. 1989. Kinematics of the Alpine plate-margin: structural styles, strain and motion along the Penninic-Austroalpine boundary in the Swiss-Austrian Alps. *Journal, Geological Society (London)* **146**(5), 835-849.
- Ring, U., Ratschbacher, L., Frisch, W., Durr, S. & Borchert, S. 1990. The internal structure of the Arosa Zone (Swiss-Austrian Alps). *Geologische Rundschau* **79**(3), 725-739.
- Rogers, G. & Dragert, H. 2003. Episodic tremor and slip on the Cascadia subduction zone: The chatter of silent slip. *Science* **300**(5627), 1942-1943.
- Rosenau, M. R. 2004. Tectonics of the Southern Andean intra-arc zone (38°-42°S). Unpublished PhD thesis, FU Berlin.
- Rubatto, D., Gebauer, D. & Fanning, M. 1998. Jurassic formation and Eocene subduction of the Zermatt-Saas-Fee ophiolites; implications for the geodynamic evolution of the Central and Western Alps. *Contributions to Mineralogy and Petrology* **132**(3), 269-287.
- Ruff, L. & Kanamori, H. 1983. Seismic coupling and uncoupling at subduction zones. *Tectonophysics* **99**(2-4), 99-117.
- Ruff, L. J. 1996. Large earthquakes in subduction zones; segment interaction and recurrence times. In: *Subduction top to bottom* **96**; American Geophysical Union, Washington, DC, United States, 91-104.
- Ruff, L. J. 1999. Dynamic stress drop of recent earthquakes: Variations within subduction zones. *Pure and Applied Geophysics* **154**(3-4), 409-431.
- Saffer, D. M. & Marone, C. 2003. Comparison of smectite- and illite-rich gouge frictional properties: Application to the updip limit of the seismogenic zone along subduction megathrusts. *Earth and Planetary Science Letters* **215**(1-2), 219-235.
- Sanders, D. & Höfling, R. 2000. Carbonate deposition in mixed siliclastic-carbonate environments on top of an orogenic wedge (Late Cretaceous, Northern Calcareous Alp, Austria). *Sedimentary Geology* **137**(3-4), 127-146.
- Schlunegger, F., Slingerland, R. & Matter, A. 1998. Crustal thickening and crustal extension as controls on the evolution of the drainage network of the central Swiss Alps between 30 Ma and the present; constraints from the stratigraphy of the North Alpine Foreland basin and the structural evolution of the Alps. *Basin Research* **10**(2), 197-212.
- Schmid, S. M., Fügenschuh, B., Kissling, E. & Schuster, R. 2004. Tectonic map and overall architecture of the Alpine orogen. *Eclogae geol. Helv.* **97**, 93-117.
- Schmid, S. M., Pfiffner, O. A., Froitzheim, N., Schönborn, G. & Kissling, E. 1996. Geophysical-geological transect and tectonic evolution of the Swiss-Italian Alps. *Tectonics* **15**(5), 1036-1064.
- Schmutz, H.-U. 1995. Die makroskopische Geometrie der Pseudotachylite in der Silvretta-Decke am NW-Rand des Unterengadiner Fensters. In: *Geologische Untersuchungen im SW-Teil des Unterengadiner Fensters. Beiträge zur geologischen Karte der Schweiz*. **166**, 73-123.
- Scholz, C. H. 1998. Earthquakes and friction laws. *Nature (London)* **391**(6662), 37-42.
- Schwartz, S. Y. & Rokosky, J. M. 2007. Slow slip events and seismic tremor at circum-pacific subduction zones. *Reviews of Geophysics* **45**(RG3004), doi:10.1029/2006RG000208.
- Secor, D. T., Jr. 1965. Role of fluid pressure in jointing. *American Journal of Science* **263**(8), 633-646.
- Selley, R. C. 1998. *Elements of petroleum geology*. Academic Press, San Diego.
- Shand, S. J. 1916. The pseudotachylite of Parijs (Orange Free State), and its relation to trap-shotten gneis and flinty crush-rock. *Geological Society of London Quarterly Journal*, 198-221.
- Shimamoto, T. & Nagahama, H. 1992. An argument against the crush origin of pseudotachylites based on the analysis of clast-size distribution. *Journal of Structural Geology* **14**(8-9), 999-1006.
- Sibson, R. H. 1975. Generation of pseudotachylite by ancient seismic faulting. *The Geophysical Journal of the Royal Astronomical Society* **43**(3), 775-794.
- Sibson, R. H. 1981. Fluid flow accompanying faulting; field evidence and models. In: *Earthquake prediction; an international review* **4**. American Geophysical Union, Washington, DC, United States, 593-603.
- Sobiesiak, M. 2000. Fault plane structure of the Antofagasta, Chile earthquake of 1995. *Geophysical Research Letters* **27**(4), 577-580.
- Sobolev, S. V., Babeyko, A. Y., Koulakov, I. & Oncken, O. 2006. Mechanism of the Andean Orogeny: Insight from Numerical Modeling. In: *The Andes - Active Subduction Orogeny* (edited by Oncken, O., Chong, G.,

- Franz, G., Giese, P., Götze, H.-J., Ramos, V., Strecker, M. & Wigger, P.). *Frontiers in Earth Sciences*. Springer, Berlin, 513-535.
- Spear, F. S. 1995. Metamorphic Phase Equilibria and Pressure-Temperature-Time Paths. *Mineralogical Society of America Monograph*, 799.
- Spicher, A. 1980. Tectonic map of Switzerland 1:500.000. In: *Atlas der Schweiz*. Bundesamt für Landestopographie, 3084 Wabern.
- Spiegel, C., Kuhlemann, J., Dunkl, I., Frisch, W., von, E. H. & Balogh, K. 2000. The erosion history of the Central Alps; evidence from zircon fission track data of the foreland basin sediments. *Terra Nova* **12**(4), 163-170.
- Spray, J. G. 1987. Artificial generation of pseudotachylite using friction welding apparatus; simulation of melting on a fault plane. *Journal of Structural Geology* **9**(1), 49-60.
- Spray, J. G. 1992. A physical basis for the frictional melting of some rock-forming minerals. *Tectonophysics* **204**(3-4), 205-221.
- Spray, J. G. 1995. Pseudotachylite controversy: fact or friction? *Geology* **23**(12), 1119-1122.
- Stampfli, G. M., Borel, G. D., Marchant, R. & Mosar, J. 2002. Western Alps geological constraints on western Tethyan reconstructions. *Journal of the Virtual Explorer (online)*.
- Thöni, M. 1981. Degree and evolution of the Alpine metamorphism in the Austroalpine Unit W of the Hohe Tauern in the light of K/ Ar and Rb/ Sr age determinations on micas. *Jahrbuch der Geologischen Bundesanstalt Wien* **124**(1), 111-174.
- Thöni, M. 1988. Rb-Sr Isotopic Resetting in Mylonites and Pseudotachylites: Implications for the Detachment and Thrusting of the Austroalpine Basement Nappes in the Eastern Alps. *Jb. Geol. B.-A.* **131**(1), 169-201.
- Thöni, M. 1999. A review of geochronological data from the Eastern Alps. *SMPM* **79**, 209-230.
- Tichelaar, B. W. & Ruff, L. J. 1993. Depth of seismic coupling along subduction zones. *Journal of Geophysical Research* **98**(B2), 2017-2037.
- Trautwein, B., Dunkl, I., Kuhlemann, J. & Frisch, W. 2001. Cretaceous-Tertiary Rhenodanubian flysch wedge (Eastern Alps); clues to sediment supply and basin configuration from zircon fission-track data. *Terra Nova* **13**(5), 382-393.
- Villa, I. M. 1998. Isotopic closure. *Terra Nova* **10**(1), 42-47.
- von Blanckenburg, F. & Davies, J. H. 1995. Slab breakoff: a model for syncollisional magmatism and tectonics in the Alps. *Tectonics* **14**(1), 120-131.
- von Eynatten, H. & Gaupp, R. 1999. Provenance of cretaceous synorogenic sandstones in the Eastern Alps: Constraints from framework petrography, heavy mineral analysis and mineral chemistry. *Sedimentary Geology* **124**(1-4), 81-111.
- von Huene, R. & Scholl, D. W. 1991. Observations at convergent margins concerning sediment subduction, subduction erosion, and the growth of continental crust. *Reviews of Geophysics* **29**(3), 279-316.
- Wagreich, M. 1991. Subsidenzanalyse an kalkalpinen Oberkreidesebenen der Gosau-Gruppe (Oesterreich). In: *Sediment '90; 5 Treffen deutschsprachiger Sedimentologen 1990; 11*. E Schweizerbart'sche Verlagsbuchhandlung, Stuttgart, Federal Republic of Germany, 1645-1657.
- Wagreich, M. 1995. Subduction tectonic erosion and late Cretaceous subsidence along the northern Austroalpine margin (eastern Alps, Austria). *Tectonophysics* **242**(1-2), 63-78.
- Wagreich, M. 2001. A 400-km-long piggyback basin (upper Aptian-lower Cenomanian) in the Eastern Alps. *Terra Nova* **13**(6), 401-406.
- Wagreich, M. & Decker, K. 2001. Sedimentary tectonics and subsidence modelling of the type Upper Cretaceous Gosau basin (Northern Calcareous Alps, Austria). *International Journal of Earth Sciences* **90**(3), 714-726.
- Wagreich, M. & Krenmayr, H. G. 2005. Upper Cretaceous oceanic red beds (CORB) in the Northern Calcareous Alps (Nierental Formation, Austria): Slope topography and clastic input as primary controlling factors. *Cretaceous Research* **26**(1), 57-64.
- Wang, K. & Hu, Y. 2006. Accretionary prisms in subduction earthquake cycles; the theory of dynamic Coulomb wedge. *Journal of Geophysical Research*.
- Weh, M. & Froitzheim, N. 2001. Penninic cover nappes in the Prattigau half-window (Eastern Switzerland): Structure and tectonic evolution. *Eclogae Geologicae Helveticae* **94**(2), 237-252.
- Wenk, H. R. 1978. Are pseudotachylites products of fracture or fusion? *Geology (Boulder)* **6**(8), 507-511.
- Wickman, F. E. 1948. Isotope ratios, a clue to the age of certain marine sediments. *Journal of Geology* **56**(1), 61-66.
- Winkler, W. 1988. Mid-to early Late Cretaceous flysch and melange formations in the western part of the Eastern Alps; palaeotectonic implications. *Jahrbuch der Geologischen Bundesanstalt Wien* **131**(2), 341-389.

Yardley, B. 1984. Fluid migration and veining in the Connemara Schists, Ireland. In: *Fluid-rock interactions during metamorphism* (edited by Walther, J. V. & Wood, B. J.). Springer, New York, 109-131.

[www.worldwind.arc.nasa.gov](http://www.worldwind.arc.nasa.gov)



## **Appendix A**

### Microprobe bulk analyses of pseudotachylyte groundmass

Table 1. Microprobe bulk analysis of sample 1b.

SiO <sub>2</sub>	TiO <sub>2</sub>	Al <sub>2</sub> O <sub>3</sub>	MgO	CaO	MnO	FeO	Na <sub>2</sub> O	K <sub>2</sub> O	total
59.51	1.00	18.72	2.75	1.89	0.11	6.97	3.38	3.68	98.14
58.21	0.98	20.07	2.61	1.85	0.08	6.86	5.12	2.38	98.23
58.68	1.13	19.85	2.40	1.78	0.11	6.06	2.85	4.16	97.16
59.18	1.08	19.12	2.51	1.55	0.12	6.91	3.09	4.06	97.75
57.96	1.05	19.98	2.47	1.40	0.07	6.84	4.00	4.16	98.04
62.81	1.10	16.55	2.75	0.89	0.17	7.16	0.56	5.08	97.14
60.03	1.08	19.25	2.33	1.80	0.13	5.92	3.60	3.94	98.20
59.52	1.05	20.01	2.00	1.93	0.10	5.81	5.98	2.43	98.91
58.26	1.08	19.85	2.37	1.48	0.10	6.38	5.89	2.69	98.28
58.49	0.99	18.44	3.05	1.95	0.11	7.69	2.12	4.26	97.25
51.85	1.36	21.80	3.21	1.42	0.13	7.93	1.98	6.21	96.04
57.55	0.99	20.18	2.64	1.43	0.11	6.36	2.93	4.99	97.30
59.47	1.06	19.90	2.21	1.97	0.10	5.72	4.39	3.38	98.30
57.01	1.16	20.61	2.83	1.56	0.12	7.20	2.96	4.45	98.05
51.21	1.21	22.36	3.06	1.64	0.14	7.99	4.66	4.82	97.23
59.46	0.99	18.97	2.67	1.51	0.07	6.75	2.48	4.42	97.45
62.28	0.81	18.08	1.77	1.27	0.07	6.39	3.49	4.00	98.20
58.28	0.96	18.99	2.94	1.82	0.12	7.18	2.73	4.29	97.42
61.69	0.93	19.19	1.95	2.01	0.03	4.93	5.12	2.70	98.62
61.06	0.92	18.82	2.14	1.88	0.07	5.87	4.01	3.34	98.19
58.57	0.86	18.95	3.49	1.62	0.06	7.58	3.50	3.12	97.80
60.47	1.16	19.87	1.80	1.62	0.10	5.67	4.40	3.83	99.08
60.98	0.91	19.27	2.18	2.05	0.14	5.36	5.51	2.65	99.13
59.75	1.21	19.36	2.64	1.50	0.16	6.34	2.86	4.12	98.03
61.18	0.98	18.42	2.67	1.69	0.11	6.58	3.71	3.38	98.79
67.19	0.92	17.35	1.22	1.25	0.02	3.80	5.82	1.96	99.63
60.31	1.14	18.57	2.49	1.66	0.11	6.31	4.50	3.48	98.67
62.20	0.96	18.00	2.09	1.64	0.14	6.02	3.78	3.39	98.36
57.67	1.07	19.55	2.89	1.88	0.10	7.35	3.52	3.94	98.06
60.07	1.07	19.37	2.20	1.45	0.14	6.34	4.79	3.41	98.98

Table 2. Microprobe bulk analysis of sample 5.

SiO <sub>2</sub>	TiO <sub>2</sub>	Al <sub>2</sub> O <sub>3</sub>	MgO	CaO	MnO	FeO	Na <sub>2</sub> O	K <sub>2</sub> O	total
58.63	0.63	15.91	4.18	6.83	0.20	7.66	3.34	1.33	98.80
54.59	0.53	18.24	4.50	8.25	0.20	7.67	3.83	0.97	98.90
54.81	0.63	16.93	4.98	7.63	0.18	8.43	3.57	1.31	98.54
57.09	0.41	18.27	3.44	7.46	0.12	6.90	4.47	0.74	99.08
56.96	0.51	17.94	4.01	7.56	0.16	7.06	4.06	1.29	99.61
56.17	0.47	17.74	4.20	7.94	0.15	7.14	4.08	0.77	98.77
57.00	0.63	17.56	4.29	7.89	0.16	6.90	3.83	0.95	99.28
55.03	0.66	16.67	5.29	7.87	0.14	8.38	3.30	1.27	98.67
49.85	0.76	19.43	5.56	8.54	0.23	9.41	3.78	1.35	99.04
57.41	0.56	17.58	4.36	7.62	0.12	6.88	4.00	0.85	99.55
54.57	0.31	20.47	3.75	7.32	0.07	6.35	5.18	0.29	98.33
50.80	0.63	19.32	5.11	8.64	0.13	8.60	4.29	0.63	98.27
48.94	0.59	18.58	5.80	8.95	0.19	10.15	3.54	0.98	97.82
56.72	0.43	17.19	4.26	8.47	0.18	7.30	4.07	0.50	99.17
48.48	0.98	18.71	5.42	7.81	0.21	10.41	3.71	1.11	96.94
53.60	0.66	18.27	4.66	6.55	0.11	8.92	4.96	0.79	98.60
56.65	0.66	18.89	3.64	7.10	0.17	6.32	4.78	0.67	98.90
56.85	0.79	16.94	4.24	6.50	0.15	8.01	5.03	0.51	99.06
57.29	0.78	16.61	4.12	7.85	0.12	8.20	3.54	0.78	99.38
52.30	0.57	17.51	5.08	7.73	0.20	9.93	4.25	0.71	98.40
69.55	0.40	14.52	1.99	4.63	0.08	4.15	4.65	0.37	100.42
52.93	0.22	19.11	5.67	9.71	0.18	7.54	3.37	0.93	99.82
56.58	0.58	17.54	4.35	8.49	0.15	7.49	3.56	0.71	99.59
66.20	1.25	13.69	3.00	5.23	0.12	6.08	3.53	0.77	99.90
60.49	0.41	18.93	3.01	7.37	0.09	4.99	3.88	0.69	99.95
60.75	0.34	15.30	4.70	6.77	0.09	7.39	3.04	0.97	99.43
55.42	0.20	20.29	3.68	8.56	0.12	6.46	3.48	1.07	99.41
56.46	0.52	17.96	4.56	8.18	0.19	7.10	3.38	0.86	99.26
62.80	0.35	15.34	4.19	7.38	0.12	6.05	3.35	0.58	100.22
51.84	0.27	22.47	3.98	9.28	0.12	6.19	4.02	1.23	99.51

Table 3. Microprobe bulk analysis of sample 16.

SiO <sub>2</sub>	TiO <sub>2</sub>	Al <sub>2</sub> O <sub>3</sub>	MgO	CaO	MnO	FeO	Na <sub>2</sub> O	K <sub>2</sub> O	total
52.79	1.85	17.33	4.46	7.13	0.22	10.47	4.23	1.37	99.88
53.59	1.68	17.41	4.13	6.76	0.19	9.92	4.11	1.41	99.23
53.46	1.90	17.18	4.37	6.69	0.26	10.48	4.29	1.14	99.81
54.58	1.79	17.24	3.98	6.34	0.23	9.67	4.19	1.49	99.64
52.44	1.91	17.02	4.92	7.37	0.31	11.12	3.86	1.01	100.03
54.36	1.78	16.52	4.24	6.80	0.27	10.78	3.74	1.33	99.87
49.45	2.06	16.96	5.15	6.56	0.17	12.73	3.47	2.05	98.65
62.06	1.38	13.06	3.75	4.39	0.18	9.92	3.01	1.97	99.82
56.39	1.65	15.29	4.09	5.98	0.18	11.19	3.56	1.48	99.91
52.61	1.78	17.14	4.68	6.89	0.28	10.77	4.25	0.99	99.44
54.27	1.69	16.41	4.41	5.63	0.20	11.05	3.40	2.23	99.34
53.52	1.99	17.19	4.28	6.07	0.26	10.61	3.81	1.70	99.51
53.52	1.79	16.93	4.10	5.82	0.22	11.37	3.62	2.16	99.59
53.66	1.65	18.09	4.36	6.84	0.32	9.88	4.40	0.90	100.18
54.28	1.66	17.27	4.29	6.19	0.31	9.97	3.90	1.61	99.57
54.91	1.82	17.45	3.88	6.13	0.26	9.58	4.31	1.36	99.78
54.55	1.75	17.30	3.85	5.29	0.18	10.46	4.08	1.84	99.39
60.05	1.42	15.14	3.37	5.25	0.17	8.95	3.82	1.54	99.77
52.58	1.87	16.66	4.56	6.45	0.26	11.42	3.39	1.90	99.14
54.84	1.87	17.20	4.21	6.40	0.21	9.75	3.73	1.37	99.65
54.83	1.91	18.28	3.28	6.74	0.22	8.71	4.72	1.02	99.81
53.14	1.79	18.02	3.85	6.72	0.25	9.90	4.17	1.32	99.19
54.23	1.80	17.72	3.80	6.67	0.21	9.54	4.08	1.29	99.38
54.75	1.73	17.09	3.90	6.30	0.24	9.89	4.13	1.52	99.64
54.17	1.75	16.61	4.18	6.77	0.20	10.77	3.95	1.10	99.55
52.67	1.69	17.83	4.06	6.88	0.20	10.09	4.03	1.41	98.97
57.40	1.60	15.81	3.85	5.28	0.24	9.16	3.70	1.68	98.85
55.46	1.65	16.97	3.75	6.43	0.23	9.51	4.13	1.24	99.41
49.57	1.57	15.73	5.30	6.72	0.28	14.21	2.36	2.18	98.00
55.23	2.09	18.06	3.60	5.92	0.24	8.59	4.71	1.09	99.67

Table 4. Microprobe bulk analysis of sample J96-1.

SiO <sub>2</sub>	TiO <sub>2</sub>	Al <sub>2</sub> O <sub>3</sub>	MgO	CaO	MnO	FeO	Na <sub>2</sub> O	K <sub>2</sub> O	total
59.80	0.64	19.32	2.64	0.72	0.06	4.76	2.28	5.45	95.66
58.18	0.82	19.50	2.85	1.67	0.07	6.11	2.43	5.19	96.81
58.94	0.91	19.42	2.78	2.25	0.04	5.29	2.52	4.76	96.90
59.32	0.77	18.63	2.81	2.12	0.07	5.47	2.68	4.56	96.43
59.43	0.74	18.62	2.99	1.84	0.05	5.87	2.71	4.54	96.79
59.81	0.81	18.23	2.91	1.55	0.05	5.61	2.70	4.57	96.24
59.07	0.92	18.99	3.30	1.14	0.07	6.21	3.11	4.05	96.87
59.81	0.92	19.69	2.56	1.58	0.07	4.97	6.77	1.44	97.80
59.02	0.89	19.45	2.35	0.87	0.10	5.34	4.99	3.60	96.61
59.93	0.90	18.99	2.54	1.28	0.07	5.16	4.05	3.86	96.77
56.93	1.08	18.44	3.02	1.44	0.07	6.49	2.87	4.51	94.85
58.52	0.85	18.99	2.63	1.23	0.06	5.17	3.28	4.40	95.13
59.78	0.84	20.29	2.32	0.92	0.04	4.54	3.05	5.00	96.78
61.60	0.85	18.26	2.44	1.07	0.09	5.00	4.65	3.48	97.43
60.24	0.94	18.57	2.88	1.08	0.10	5.81	4.48	3.40	97.51
61.32	0.88	18.08	2.74	1.18	0.10	5.39	3.82	3.69	97.20
59.98	0.83	18.87	2.93	0.99	0.03	5.48	3.14	4.35	96.61
59.43	0.89	19.38	2.59	0.98	0.08	4.87	2.94	4.98	96.13
58.96	0.88	19.48	2.72	1.19	0.09	5.50	4.54	3.52	96.88
59.33	0.96	19.45	2.84	1.33	0.05	5.44	6.22	2.39	98.01
57.62	0.80	19.29	3.29	0.69	0.06	6.34	2.82	5.41	96.31
59.14	0.88	19.97	3.30	1.07	0.05	6.24	2.21	5.28	98.12
61.21	0.94	19.28	2.67	1.56	0.03	4.90	2.61	4.73	97.93
58.46	0.86	20.41	2.77	1.07	0.01	5.64	2.83	5.03	97.08
60.61	0.82	19.63	2.50	0.88	0.07	5.21	3.42	4.62	97.76
60.65	0.91	19.25	2.64	1.04	0.03	5.23	4.11	3.95	97.81
60.26	0.86	20.48	2.51	1.82	0.07	5.56	6.11	1.80	99.48
60.10	0.87	19.36	2.81	1.35	0.08	5.62	2.45	5.14	97.77
60.42	0.92	19.29	2.87	1.13	0.08	5.42	2.89	4.84	97.87
60.92	0.90	19.05	2.87	1.52	0.08	5.16	2.11	5.21	97.81
61.20	0.90	18.76	2.97	1.45	0.12	5.58	2.33	4.90	98.20
61.61	1.05	19.00	2.81	1.33	0.06	5.63	2.25	4.96	98.71
61.20	0.91	19.17	2.86	1.25	0.09	5.51	3.56	4.12	98.66
60.57	0.94	19.27	2.74	1.21	0.02	5.18	3.33	4.53	97.77
60.50	0.96	18.94	2.83	1.35	0.06	5.32	2.98	4.63	97.56
61.28	0.87	18.78	2.85	1.34	0.11	5.67	2.98	4.58	98.44
61.06	0.89	19.19	2.91	1.45	0.13	5.76	5.57	2.67	99.63
60.31	0.95	18.92	2.85	1.37	0.09	5.63	2.16	5.04	97.33
61.00	0.90	19.82	2.56	0.98	0.06	5.18	3.97	4.23	98.69
59.74	0.89	19.48	2.91	1.68	0.10	5.61	2.84	4.70	97.94
61.12	0.88	18.61	2.88	1.10	0.05	5.71	3.00	4.39	97.74
61.20	0.85	18.95	2.94	1.28	0.06	5.70	5.54	2.66	99.17
61.04	0.88	19.10	3.02	1.34	0.09	5.49	3.34	4.28	98.58
61.33	0.98	19.59	2.70	1.16	0.05	5.39	3.37	4.39	98.95
60.88	0.83	19.23	2.97	1.58	0.07	5.36	2.59	4.54	98.05
60.83	0.93	18.60	3.03	1.69	0.08	6.93	2.57	4.57	99.22
61.07	1.02	18.43	2.74	1.56	0.11	5.56	2.80	4.57	97.85
61.31	0.93	18.12	3.00	1.40	0.05	5.96	3.53	3.83	98.11
61.51	0.88	19.05	3.10	1.10	0.04	5.32	5.51	2.78	99.29

Table 5. Microprobe bulk analysis of sample J96-2.

SiO <sub>2</sub>	TiO <sub>2</sub>	Al <sub>2</sub> O <sub>3</sub>	MgO	CaO	MnO	FeO	Na <sub>2</sub> O	K <sub>2</sub> O	total
61.65	0.99	17.55	2.96	4.84	0.12	6.00	5.32	1.24	100.66
59.98	1.20	16.06	3.73	4.85	0.18	7.07	5.35	1.06	99.48
61.44	0.95	16.21	3.34	3.85	0.10	6.70	5.46	1.24	99.29
58.92	1.15	18.22	3.22	3.92	0.04	5.58	6.74	1.42	99.21
61.79	0.89	17.25	3.04	3.56	0.09	5.63	6.79	1.08	100.12
59.32	1.02	17.06	3.52	4.42	0.13	6.18	6.98	1.15	99.77
60.20	0.97	17.26	3.66	4.36	0.11	6.96	5.62	1.42	100.54
58.93	1.13	18.31	3.14	4.61	0.13	6.41	6.11	1.50	100.27
58.58	1.23	17.12	3.80	5.32	0.12	7.17	5.80	1.20	100.34
61.04	0.95	17.00	3.69	4.01	0.12	6.86	6.01	1.05	100.72
59.96	0.89	17.29	3.73	4.55	0.17	6.76	5.50	1.25	100.09
60.45	0.93	16.13	3.89	3.94	0.10	7.07	5.83	0.86	99.19
57.57	1.03	16.68	4.45	4.67	0.08	8.13	5.39	1.25	99.24
56.93	1.12	17.35	4.16	6.28	0.07	7.36	4.87	1.87	100.01
60.97	1.08	17.26	3.46	3.74	0.09	5.57	6.50	1.71	100.39
59.20	1.13	16.83	3.80	4.85	0.10	6.75	6.04	1.51	100.19
60.25	1.10	17.81	3.04	4.24	0.06	5.79	6.85	1.15	100.30
61.38	1.07	15.82	3.77	4.77	0.11	6.99	5.47	1.27	100.65
59.03	1.06	18.02	3.30	4.93	0.12	6.18	5.78	1.83	100.26
58.90	1.07	17.61	3.76	4.33	0.12	6.52	5.76	1.85	99.92
56.44	0.88	18.07	3.96	3.60	0.11	7.87	6.01	1.60	98.54
54.47	1.36	18.10	4.13	4.85	0.09	8.31	5.86	1.14	98.29
51.98	1.05	18.49	5.14	3.66	0.13	8.81	5.79	1.25	96.29
58.40	1.11	17.21	3.63	5.29	0.10	5.92	5.57	1.13	98.34
56.46	0.91	17.98	4.16	5.05	0.09	7.06	6.05	1.58	99.34
52.95	0.89	5.89	1.60	3.04	0.09	4.84	4.43	0.90	74.63
55.45	1.17	17.51	4.21	5.16	0.12	7.29	5.58	2.12	98.61
58.30	1.13	16.55	3.93	5.03	0.14	6.72	5.90	1.16	98.86
58.28	1.02	17.08	3.26	6.08	0.09	6.62	5.33	1.03	98.77
49.53	1.05	9.81	1.95	1.76	0.00	4.00	4.46	0.80	73.36
48.83	0.86	8.93	2.10	1.59	0.03	3.70	4.99	0.56	71.58
46.18	0.93	9.54	2.86	2.41	0.06	5.07	4.38	0.72	72.15
47.65	0.96	10.54	3.13	2.94	0.01	5.97	4.00	0.92	76.11
49.91	0.85	13.05	2.82	3.41	0.02	5.77	4.76	1.30	81.88
46.41	1.19	12.75	5.15	4.59	0.07	9.54	3.76	1.26	84.72
43.72	1.13	7.22	2.06	1.86	0.05	4.81	3.48	0.44	64.76
45.82	1.04	9.82	1.99	1.51	0.02	3.58	4.69	1.42	69.87
61.74	0.88	17.73	2.39	3.65	0.07	4.87	6.90	0.79	99.01
53.62	1.38	17.81	3.69	7.20	0.16	8.14	4.82	0.82	97.65
56.41	1.21	18.09	4.04	3.73	0.13	6.90	6.06	1.80	98.37
60.16	0.99	16.50	2.89	3.63	0.13	5.44	6.70	0.85	97.28

## Appendix B

$^{40}\text{Ar}/^{39}\text{Ar}$  analytical data

Table 1. Analytical data for sample 1b.

Laser output	$^{40}\text{Ar}/^{39}\text{Ar}$	$^{37}\text{Ar}/^{39}\text{Ar}$	$^{36}\text{Ar}/^{39}\text{Ar}$	K/Ca	$^{40}\text{Ar}^*$	$^{39}\text{Ar}_K$	$^{40}\text{Ar}^*/^{39}\text{Ar}_K$	Age( $\pm$ 1s)
			( $\times 10^{-3}$ )		(%)	fraction (%)		(Ma)
<b>1-b d2-A</b>	<i>C07221</i>	<i>GeNF</i>						
	J= 0.00205							
0.014	176.2347 $\pm$ 0.8948	0.254 $\pm$ 0.0539	559.706 $\pm$ 4.604	2.313	6.2	1.1	10.876 $\pm$ 1.075	39.78 $\pm$ 3.89
0.016	17.46 $\pm$ 0.04	0.249 $\pm$ 0.013	4.3 $\pm$ 0.2	2.358	92.9	5.5	16.23 $\pm$ 0.07	59.0 $\pm$ 0.3
0.018	23.64 $\pm$ 0.05	0.112 $\pm$ 0.004	1.73 $\pm$ 0.05	5.271	97.9	18.0	23.15 $\pm$ 0.05	83.6 $\pm$ 0.4
0.02	23.07 $\pm$ 0.05	0.138 $\pm$ 0.004	0.94 $\pm$ 0.05	4.276	98.9	23.0	22.82 $\pm$ 0.05	82.5 $\pm$ 0.4
0.022	22.75 $\pm$ 0.08	0.159 $\pm$ 0.006	1.19 $\pm$ 0.13	3.688	98.5	12.1	22.42 $\pm$ 0.09	81.1 $\pm$ 0.4
0.024	22.35 $\pm$ 0.05	0.158 $\pm$ 0.008	0.74 $\pm$ 0.07	3.722	99.1	10.3	22.15 $\pm$ 0.05	80.1 $\pm$ 0.4
0.026	21.80 $\pm$ 0.05	0.168 $\pm$ 0.008	0.50 $\pm$ 0.07	3.500	99.4	16.4	21.67 $\pm$ 0.05	78.4 $\pm$ 0.4
0.028	20.59 $\pm$ 0.03	0.226 $\pm$ 0.010	0.56 $\pm$ 0.10	2.600	99.3	11.3	20.46 $\pm$ 0.04	74.1 $\pm$ 0.3
0.042	21.39 $\pm$ 0.11	0.40 $\pm$ 0.04	5.2 $\pm$ 0.5	1.488	93.1	2.3	19.91 $\pm$ 0.17	72.2 $\pm$ 0.7

Table 2. Analytical data for sample 5 (2. analysis).

Laser output	$^{40}\text{Ar}/^{39}\text{Ar}$	$^{37}\text{Ar}/^{39}\text{Ar}$	$^{36}\text{Ar}/^{39}\text{Ar}$	K/Ca	$^{40}\text{Ar}^*$	$^{39}\text{Ar}_K$	$^{40}\text{Ar}^*/^{39}\text{Ar}_K$	Age( $\pm 1s$ )				
			( $\times 10^{-3}$ )		(%)	fraction (%)		(Ma)				
<b>5 (2) d11-13</b>	C07277	GeNF										
	J= 0.00205											
0.016	47.3166 $\pm$ 0.4107	1.875	$\pm$ 0.2989	121.626	$\pm$ 1.940	0.313	24.5	5.3	11.628	$\pm$ 0.548	42.48	$\pm$ 1.98
0.018	30.32 $\pm$ 0.16	1.8	$\pm$ 0.2	16.3	$\pm$ 0.8	0.327	84.8	10.4	25.8	$\pm$ 0.3	92.8	$\pm$ 1.0
0.02	33.10 $\pm$ 0.10	1.43	$\pm$ 0.11	7.4	$\pm$ 0.2	0.412	94.0	29.3	31.14	$\pm$ 0.12	111.6	$\pm$ 0.6
0.022	35.88 $\pm$ 0.12	3.4	$\pm$ 0.2	7.2	$\pm$ 0.4	0.172	95.3	17.5	34.28	$\pm$ 0.18	122.5	$\pm$ 0.8
0.024	30.9 $\pm$ 0.3	6.3	$\pm$ 0.7	8.8	$\pm$ 1.6	0.093	94.1	4.3	29.2	$\pm$ 0.5	104.9	$\pm$ 1.9
0.026	31.1 $\pm$ 0.5	2	$\pm$ 2	3	$\pm$ 4	0.264	97.9	1.5	30.5	$\pm$ 1.4	109	$\pm$ 5
0.028	31.18 $\pm$ 0.11	5.0	$\pm$ 0.4	8.1	$\pm$ 0.6	0.118	94.3	12.4	29.5	$\pm$ 0.2	106.0	$\pm$ 0.8
0.028	35.94 $\pm$ 0.14	6.6	$\pm$ 0.2	9.5	$\pm$ 0.5	0.088	94.5	19.2	34.2	$\pm$ 0.2	122.0	$\pm$ 0.9

Table 3. Summarized data for sample 16 (2. analysis).

Laser output	$^{40}\text{Ar}/^{39}\text{Ar}$	$^{37}\text{Ar}/^{39}\text{Ar}$	$^{36}\text{Ar}/^{39}\text{Ar}$	K/Ca	$^{40}\text{Ar}^*$ (%)	$^{39}\text{Ar}_K$ fraction (%)	$^{40}\text{Ar}^*/^{39}\text{Ar}_K$	Age( $\pm$ 1s) (Ma)
<b>16 (2) d1-12</b>	<i>C07278</i>		<i>GeNF</i>					
	J= 0.00205							
0.016	61.2576 $\pm$ 0.3245	2.155 $\pm$ 0.8153	154.865 $\pm$ 1.564	0.272	25.7	6.4	15.792 $\pm$ 0.448	57.45 $\pm$ 1.62
0.018	42.56 $\pm$ 0.16	1.6 $\pm$ 0.4	12.4 $\pm$ 0.8	0.373	91.9	11.2	39.2 $\pm$ 0.3	139.2 $\pm$ 1.1
0.02	50.29 $\pm$ 0.14	1.0 $\pm$ 0.3	5.9 $\pm$ 0.3	0.593	96.8	22.2	48.70 $\pm$ 0.17	171.6 $\pm$ 0.9
0.022	45.1 $\pm$ 0.2	2.2 $\pm$ 0.4	6.3 $\pm$ 0.3	0.266	96.5	19.8	43.6 $\pm$ 0.2	154.4 $\pm$ 1.0
0.024	41.2 $\pm$ 0.2	4.9 $\pm$ 0.8	6.4 $\pm$ 1.0	0.120	96.9	7.8	40.1 $\pm$ 0.4	142.5 $\pm$ 1.4
0.026	42.58 $\pm$ 0.18	5.3 $\pm$ 0.3	6.1 $\pm$ 0.4	0.111	97.3	18.5	41.6 $\pm$ 0.2	147.6 $\pm$ 0.9
0.03	61.1 $\pm$ 0.3	7.1 $\pm$ 0.4	9.3 $\pm$ 0.6	0.082	96.9	14.2	59.6 $\pm$ 0.4	208.0 $\pm$ 1.4

Table 4. Summarized data for sample J96-1.

Lasert output	$^{40}\text{Ar}/^{39}\text{Ar}$	$^{37}\text{Ar}/^{39}\text{Ar}$	$^{36}\text{Ar}/^{39}\text{Ar}$ ( $\times 10^{-3}$ )	K/Ca	$^{40}\text{Ar}^*$ (%)	$^{39}\text{Ar}_K$ fraction (%)	$^{40}\text{Ar}^*/^{39}\text{Ar}_K$	Age( $\pm$ 1s) (Ma)
<b>J96-1 d2-C</b>	<b>C07218</b>	<b>GeNF</b>						
	J= 0.00205							
0.012	843.1821 $\pm$ 62.7998	2.432 $\pm$ 0.3	2712.260 $\pm$ 5	0.241	5.0	0.0	42.105 $\pm$ 15.862	149.36 $\pm$ 54.01
0.014	47.4 $\pm$ 0.7	0.2	139 $\pm$ 0.03	2.942	13.7	0.2	6.5 $\pm$ 1.5	24 $\pm$ 6
0.018	17.767 $\pm$ 0.016	0.175 $\pm$ 0.002	3.09 $\pm$ 0.03	3.352	95.0	34.4	16.879 $\pm$ 0.017	61.4 $\pm$ 0.2
0.02	22.29 $\pm$ 0.03	0.114 $\pm$ 0.004	1.87 $\pm$ 0.09	5.161	97.6	15.5	21.75 $\pm$ 0.04	78.7 $\pm$ 0.3
0.022	21.07 $\pm$ 0.04	0.137 $\pm$ 0.010	1.95 $\pm$ 0.09	4.292	97.3	8.8	20.52 $\pm$ 0.05	74.3 $\pm$ 0.3
0.024	20.49 $\pm$ 0.03	0.136 $\pm$ 0.008	2.07 $\pm$ 0.18	4.337	97.1	9.4	19.89 $\pm$ 0.06	72.1 $\pm$ 0.4
0.026	20.124 $\pm$ 0.018	0.169 $\pm$ 0.006	1.61 $\pm$ 0.08	3.488	97.7	18.3	19.67 $\pm$ 0.03	71.3 $\pm$ 0.3
0.028	19.72 $\pm$ 0.03	0.189 $\pm$ 0.008	1.79 $\pm$ 0.14	3.114	97.4	9.2	19.22 $\pm$ 0.05	69.7 $\pm$ 0.3
0.036	19.79 $\pm$ 0.05	0.19 $\pm$ 0.02	2.7 $\pm$ 0.3	3.073	96.2	4.2	19.03 $\pm$ 0.09	69.0 $\pm$ 0.4

Table 5. Summarized data for sample J96-1 (2. analysis).

Laser output	$^{40}\text{Ar}/^{39}\text{Ar}$	$^{37}\text{Ar}/^{39}\text{Ar}$	$^{36}\text{Ar}/^{39}\text{Ar}$	K/Ca	$^{40}\text{Ar}^*$	$^{39}\text{Ar}_K$	$^{40}\text{Ar}^*/^{39}\text{Ar}_K$	Age( $\pm$ 1s)
			( $\times 10^{-3}$ )		(%)	fraction (%)		(Ma)
<b>J96-1_2 d2-C</b>	<b>C07223</b>	<b>GeNF</b>						
	J= 0.00205							
0.014	42.5188 $\pm$ 0.4148	0.120 $\pm$ 0.0971	122.930 $\pm$ 2.650	4.915	14.6	0.7	6.208 $\pm$ 0.717	22.82 $\pm$ 2.62
0.016	11.75 $\pm$ 0.03	0.272 $\pm$ 0.006	3.25 $\pm$ 0.09	2.166	92.1	13.3	10.82 $\pm$ 0.04	39.6 $\pm$ 0.2
0.018	21.87 $\pm$ 0.07	0.121 $\pm$ 0.007	1.96 $\pm$ 0.13	4.875	97.4	16.4	21.30 $\pm$ 0.08	77.1 $\pm$ 0.4
0.02	21.84 $\pm$ 0.04	0.132 $\pm$ 0.007	1.48 $\pm$ 0.08	4.441	98.1	20.5	21.42 $\pm$ 0.04	77.5 $\pm$ 0.3
0.022	21.25 $\pm$ 0.05	0.182 $\pm$ 0.012	1.47 $\pm$ 0.13	3.239	98.1	11.2	20.84 $\pm$ 0.06	75.5 $\pm$ 0.4
0.024	20.975 $\pm$ 0.018	0.227 $\pm$ 0.007	1.58 $\pm$ 0.09	2.586	97.9	20.2	20.54 $\pm$ 0.03	74.4 $\pm$ 0.3
0.026	20.00 $\pm$ 0.06	0.250 $\pm$ 0.011	1.76 $\pm$ 0.13	2.355	97.6	11.6	19.51 $\pm$ 0.07	70.8 $\pm$ 0.4
0.028	19.24 $\pm$ 0.05	0.27 $\pm$ 0.03	2.5 $\pm$ 0.3	2.165	96.4	3.9	18.54 $\pm$ 0.10	67.3 $\pm$ 0.4
0.04	19.15 $\pm$ 0.12	0.26 $\pm$ 0.05	3.5 $\pm$ 0.7	2.259	94.8	2.2	18.2 $\pm$ 0.2	65.9 $\pm$ 0.8

Table 6. Summarized data for sample J96-2.

Laser output	$^{40}\text{Ar}/^{39}\text{Ar}$	$^{37}\text{Ar}/^{39}\text{Ar}$	$^{36}\text{Ar}/^{39}\text{Ar}$	K/Ca	$^{40}\text{Ar}^*$	$^{39}\text{Ar}_K$	$^{40}\text{Ar}^*/^{39}\text{Ar}_K$	Age( $\pm 1\text{s}$ )
			( $\times 10^{-3}$ )		(%)	fraction (%)		(Ma)
<b>J96-2 d2-B</b>	C07222	GeNF						
	J= 0.00205							
0.014	51.2676 $\pm$ 2.1496	1.573 $\pm$ 0.9876	206.645 $\pm$ 23.085	0.374	1.0	0.3	0.504 $\pm$ 6.393	1.86 $\pm$ 23.62
0.016	12.04 $\pm$ 0.10	1.73 $\pm$ 0.05	11.3 $\pm$ 0.7	0.340	74.1	6.7	8.9 $\pm$ 0.2	32.8 $\pm$ 0.8
0.018	17.60 $\pm$ 0.08	0.53 $\pm$ 0.04	3.9 $\pm$ 0.6	1.119	93.8	7.4	16.52 $\pm$ 0.19	60.1 $\pm$ 0.7
0.02	17.48 $\pm$ 0.03	0.91 $\pm$ 0.02	2.2 $\pm$ 0.2	0.645	97.0	21.8	16.97 $\pm$ 0.08	61.7 $\pm$ 0.4
0.022	17.40 $\pm$ 0.11	1.78 $\pm$ 0.04	2.6 $\pm$ 0.4	0.330	96.9	9.4	16.89 $\pm$ 0.16	61.4 $\pm$ 0.6
0.024	17.37 $\pm$ 0.04	1.818 $\pm$ 0.020	2.28 $\pm$ 0.14	0.323	97.4	39.9	16.95 $\pm$ 0.05	61.6 $\pm$ 0.3
0.026	17.68 $\pm$ 0.08	1.55 $\pm$ 0.05	2.0 $\pm$ 0.6	0.380	97.8	10.1	17.3 $\pm$ 0.2	62.9 $\pm$ 0.8
0.026	18.73 $\pm$ 0.12	1.52 $\pm$ 0.09	3.8 $\pm$ 1.0	0.386	95.1	4.4	17.8 $\pm$ 0.3	64.8 $\pm$ 1.2



## **Appendix C**

### Sample locations

Table 1. Sample locations for the European Alps.

outcrop	sample	study area	location	easting	northing	profile
1	1 a	Alps	Engadine window	808060	194760	5
1	1 b	Alps	Engadine window	808060	194760	5
1	1 c	Alps	Engadine window	808060	194760	5
2	2 a	Alps	Engadine window	810360	196360	5
3	3 a	Alps	Partnun	783310	206970	1
3	3 b	Alps	Partnun	783310	206970	1
3	3 c	Alps	Partnun	783310	206970	1
4	4 a	Alps	Partnun	785310	206210	1
4	4 b	Alps	Partnun	785310	206210	1
4	4 c	Alps	Partnun	785310	206210	1
4	4 d	Alps	Partnun	785310	206210	1
5	5 a	Alps	Partnun	785280	206540	1
6	6 a	Alps	Partnun	785300	206590	1
7	7 a	Alps	Monbiel	788830	193700	2
8	8 a	Alps	Monbiel	789450	193620	2
8	8 b	Alps	Monbiel	789450	193620	2
9	9 a	Alps	Monbiel	789570	193670	2
10	10 a	Alps	Monbiel	789660	193660	2
10	10 b	Alps	Monbiel	789660	193660	2
10	10 c	Alps	Monbiel	789660	193660	2
11	11 a	Alps	Monbiel	789840	193700	2
12	12 a	Alps	Monbiel	790320	193370	2
12	12 b	Alps	Monbiel	790320	193370	2
13	13 a	Alps	Davos	782420	189070	3
14	14 a	Alps	Davos	781030	190120	3
14	14 b	Alps	Davos	781030	190120	3
14	14 c	Alps	Davos	781030	190120	3
14	14 d	Alps	Davos	781030	190120	3
14	14 e	Alps	Davos	781030	190120	3
15	15 a	Alps	Davos	780570	189180	3
15	15 b	Alps	Davos	780570	189180	3
15	15 c	Alps	Davos	780570	189180	3
15	15 d	Alps	Davos	780570	189780	3
16	16 a	Alps	Arosa	768710	180540	4
16	16 b	Alps	Arosa	768710	180540	4
16	16 c	Alps	Arosa	768710	180540	4
16	16 d	Alps	Arosa	768710	180540	4
16	16 e	Alps	Arosa	768710	180540	4
16	16 f	Alps	Arosa	768710	180540	4
16	16 g	Alps	Arosa	768710	180540	4
16	16 h	Alps	Arosa	768710	180540	4
17	17 a	Alps	Arosa	768670	181130	4
17	17 b	Alps	Arosa	768670	181130	4
18	18 a	Alps	Arosa	768670	181130	4
18	18 b	Alps	Arosa	768670	181130	4
19	19 a	Alps	Bivio	768030	152820	6
19	19 b	Alps	Bivio	768030	152820	6
19	19 c	Alps	Bivio	768030	152820	6
19	19 d	Alps	Bivio	768030	152820	6
19	19 e	Alps	Bivio	768030	152820	6
19	19 f	Alps	Bivio	768030	152820	6
19	19 g	Alps	Bivio	768030	152820	6

Table 1. continued.

<b>outcrop</b>	<b>sample</b>	<b>study area</b>	<b>location</b>	<b>easting</b>	<b>northing</b>	<b>profile</b>
19	19 h	Alps	Bivio	768030	152820	6
19	19 i	Alps	Bivio	768030	152820	6
20	20 a	Alps	Bivio	76983	149060	6
21	21 a	Alps	Bivio	773670	148410	6
22	22 a	Alps	Bivio	776060	149200	6
22	22 b	Alps	Bivio	776060	149200	6
22	22 c	Alps	Bivio	776060	149200	6
24	24 a	Alps	Piz Grialetsch	780800	142810	8
24	24 b	Alps	Piz Grialetsch	780800	142810	8
24	24 c	Alps	Piz Grialetsch	780800	142810	8
26	26 a	Alps	Piz Grialetsch	781280	142360	8
26	26 b	Alps	Piz Grialetsch	781280	142360	8
27	27 a	Alps	Piz Grialetsch	781280	142360	8
28	28 a	Alps	Piz Grialetsch	780100	142960	8
30	30 a	Alps	Bivio	777440	149370	6
31	31 a	Alps	Bivio	774780	147850	6
31	31 b	Alps	Bivio	774780	147850	6
31	31 c	Alps	Bivio	774780	147850	6
31	31 d	Alps	Bivio	774780	147850	6
31	31 e	Alps	Bivio	774780	147850	6
31	31 f	Alps	Bivio	774780	147850	6
32	32 a	Alps	Bivio	774950	148110	6
32	32 b	Alps	Bivio	774950	148110	6
33	33 a	Alps	Bivio	774870	148350	6
34	34 a	Alps	Guarda	807180	183640	
34	34 b	Alps	Guarda	807180	183640	
35	35 a	Alps	Scoul	818240	185950	
36	36 a	Alps	Scoul	818300	184990	
36	36 b	Alps	Scoul	818300	184990	
36	36 c	Alps	Scoul	818300	184990	
37	37 a	Alps	Scoul	818280	144910	
38	38 a	Alps	Plaun de Lei	774770	144490	7
38	38 b	Alps	Plaun de Lei	776100	144180	7
38	38 c	Alps	Plaun de Lei	776100	144180	7
38	38 d	Alps	Plaun de Lei	776100	144180	7
39	39 a	Alps	Plaun de Lei	775480	144160	7
39	39 b	Alps	Plaun de Lei	775480	144160	7
40	40 a	Alps	Engadine window	811250	194600	5
41	41 a	Alps	Engadine window	811640	194730	5
41	41 b	Alps	Engadine window	811640	194730	5
41	41 c	Alps	Engadine window	811640	194730	5
41	41 d	Alps	Engadine window	811640	194730	5
41	41 e	Alps	Engadine window	811640	194730	5
1-05	B-7	Alps	Piz Grialetsch	780780	142700	8
1-05	B-8	Alps	Piz Grialetsch	780780	142700	8
2-05	B-9	Alps	Piz Grialetsch	781170	142520	8
2-05	B-10	Alps	Piz Grialetsch	781170	142520	8
3-05	B-11	Alps	Piz Grialetsch	781750	140970	8
4-05	B-12	Alps	Piz Grialetsch	780320	142440	8
4-05	B-13	Alps	Piz Grialetsch	780320	142440	8
5-05	B-14	Alps	Piz Grialetsch	780160	142840	8

Table 1. continued.

<b>outcrop</b>	<b>sample</b>	<b>study area</b>	<b>location</b>	<b>easting</b>	<b>northing</b>	<b>profile</b>
6-05	B-15	Alps	Piz Grialetsch	783150	145130	8
7-05	B-16	Alps	Bivio	768030	152820	6
8-05	B-17	Alps	Partnun	785340	206780	1
8-05	B-18	Alps	Partnun	785340	206780	1
10-05	B-19	Alps	Monbiel	789570	193670	2
10-05	B-20	Alps	Monbiel	789570	193670	2
11-05	B-21	Alps	Monbiel	789670	193610	2
11-05	B-22	Alps	Monbiel	789670	193610	2
11-05	B-23	Alps	Monbiel	789670	193610	2
12-05	B-24	Alps	Monbiel	789690	193660	2
13-05	B-25	Alps	Partnun	786860	209640	1
14-05	B-26	Alps	Partnun	786320	209450	1
14-05	B-27	Alps	Partnun	786320	209450	1
14-05	B-28	Alps	Partnun	786320	209450	1
15-05	B-29	Alps	Arosa	768670	181130	4
15-05	B-30	Alps	Arosa	768670	181130	4
35	B-31	Alps	Scoul	818280	144910	
24	B-32	Alps	Piz Grialetsch	780780	142700	8
24	B-33	Alps	Piz Grialetsch	780780	142700	8
24	B-34	Alps	Piz Grialetsch	780780	142700	8
16-05	B-35	Alps	Engadine window	811180	195640	5
17-05	B-36	Alps	Engadine window	811560	194960	5
17a-05	B-37	Alps	Engadine window	808060	194760	5
17a-05	B-38	Alps	Engadine window	808060	194760	5
18-05	B-39	Alps	Engadine window	808730	195470	5
20-05	B-40	Alps	Davos	780500	189510	3
21-05	B-41	Alps	Davos	780780	189180	3
21-05	B-42	Alps	Davos	780780	189180	3
21-05	B-43	Alps	Davos	780780	189180	3
22-05	B-44	Alps	Engadine window	811230	195530	5
23-05	B-45	Alps	Engadine window	811620	195400	5
25-05	B-46	Alps	Engadine window	811380	194190	5
8 - 06	C-1	Alps	Bivio	770320	152710	6
10 - 06	C-2	Alps	Bivio	777470	149160	6
18 - 06	C-3	Alps	Monbiel	789650	192240	2
19 - 06	C-4	Alps	Arosa	765070	180390	4
24 - 06	C-5	Alps	Bivio	772630	151470	6
24 - 06	C-6	Alps	Bivio	772630	151470	6
26 - 06	C-7	Alps	Bivio	770490	148430	6
26 - 06	C-8	Alps	Bivio	770490	148430	6
28 - 06	C-9	Alps	Piz Grialetsch	780690	142770	8
29 - 06	C-10	Alps	Piz Grialetsch	781030	142710	8
34 - 06	C-11	Alps	Plaun de Lej	776040	144510	7
34 - 06	C-12	Alps	Plaun de Lej	776040	144510	7
34 - 06	C-13	Alps	Plaun de Lej	776040	144510	7
33 - 06	C-14	Alps	Plaun de Lej	775350	143840	7
36 - 06	C-15	Alps	Plaun de Lej	775380	143740	7
39 - 06	C-16	Alps	Bivio	775180	149000	6
39 - 06	C-17	Alps	Bivio	775180	149000	6

Table 2. Sample location for Southern Chile.

outcrop	sample	study area	Lokation	longitude	latitude
2	R 1	Chile	N' Niebla	73°24'11" W	39°49'31" S
2	R 2	Chile	N' Niebla	73°24'11" W	39°49'31" S
3	R 3	Chile	N' Niebla	73°24'12" W	39°42'51" S
3	R 4	Chile	N' Niebla	73°24'12" W	39°42'51" S
3	R 5	Chile	N' Niebla	73°24'12" W	39°42'51" S
4	R 6	Chile	N' Niebla	73°22'45" W	39°41'20" S
5	R 7	Chile	S' Corral	73°32'04" W	39°55'10" S
5	R 8	Chile	S' Corral	73°32'04" W	39°55'10" S
6	R 9	Chile	N' Parc Oncol	73°21'04" W	39°40'13" S
7	R 10	Chile	Punta Nihue	73°13'19" W	39°18'31" S
7	R 11	Chile	Punta Nihue	73°13'19" W	39°18'31" S
8	R 12	Chile	Ortiega	73°50'23" W	41°24'44" S
8	R 13	Chile	Ortiega	73°50'23" W	41°24'44" S
9	R 14	Chile	Lliefen	72°15'45" W	40°12'36" S
10	R 15	Chile	Tirua	73°30'12" W	38°20'21" S
13	R 16	Chile	S' Tirua	73°17'27" W	38°32'39" S
13	R 17	Chile	S' Tirua	73°17'27" W	38°32'39" S
13	R 18	Chile	S' Tirua	73°17'27" W	38°32'39" S
13	R 19	Chile	S' Tirua	73°17'27" W	38°32'39" S
13	R 20	Chile	S' Tirua	73°17'27" W	38°32'39" S
13	R 21	Chile	S' Tirua	73°17'27" W	38°32'39" S
14	R 22	Chile	S' Corral	73°27'56" W	39°51'37" S
14	R 23	Chile	S' Corral	73°27'56" W	39°51'37" S
14	R 24	Chile	S' Corral	73°27'56" W	39°51'37" S
15	R 25	Chile	N' Los Molinos	73°24'08" W	39°41'56" S
15	R 26	Chile	N' Los Molinos	73°24'08" W	39°41'56" S
16	R 27	Chile	La Union	73°05'53" W	40°04'02" S
17	R 28	Chile	Villarrica	72°18'26" W	39°18'47" S
18	R 29	Chile	Villarrica	72°18'59" W	39°19'07" S



An dieser Stelle möchte ich mich bei einigen Personen bedanken, ohne deren Hilfe und Unterstützung, sei es privat oder im wissenschaftlichen Bereich, diese hier vorliegende Dissertation wohl nicht das geworden wäre, was sie ist.

Zu Beginn möchte ich meinem Betreuer Onno Oncken ganz herzlich danken. Durch gemeinsame Diskussionen formte sich diese spannende und zugleich herausfordernde Arbeit, gemeinsame Diskussionen brachten sie auch immer wieder voran. Dafür und für seine Organisation finanzieller Unterstützung bin ich sehr dankbar, ebenso für die Freiheit, die er mir in wissenschaftlichen Fragen ließ.

Charlotte Krawczyk danke ich ganz herzlich für die Bereitschaft zur Übernahme des Zweitgutachtens und für gemeinsame Diskussionen! Bei Problemen jeglicher Art fand sie immer die passenden Worte.

Georg Dresen möchte ich vor allem für interessante Geländetage, sowie spannende und fordernde Diskussionen danken! Wenn mich nicht alles täuscht, wartet noch ein Caprese im Engadin auf uns ;-)

Besonders danke ich Tina Lohr, die nie den Glauben an mich verlor, als ich es oftmals schon längst getan hatte. Ihrer beständigen Unterstützung, sei es im Gelände, im Büro oder in unseren vier Wänden, verdanke ich am meisten. Sie war mein schlechtes Gewissen in den letzten Wochen der Fertigstellung. Die folgenden Worte drücken meine Gedanken vielleicht am besten aus: „*Du bist da, wenn ich reden will; Du bist da und die Welt steht still; Du weißt immer ganz genau was mir fehlt; Du bist da, gibst mir Leichtigkeit...*“

Viktoria Georgieva, Dir möchte ich für unsere schöne Zeit im Gelände danken und für die vielen interessanten und aufschlussreichen Diskussionen danach. Eine bessere Diplomandin hätte man sich nicht wünschen können!

Ganz besonderer Dank gilt Johannes Glodny! Er brachte mir mit unendlicher Geduld die faszinierende Welt der Isotopengeochronologie näher. Auch unsere fortwährenden Diskussionen bereicherten diese Arbeit immens!

Masafumo Sudo möchte ich danken, dass er mich die Geheimnisse der Ar/Ar Datierung lehrte. Und vor allem für sein Vertrauen, die Messungen alleine durchführen zu können. Dabei kann man am besten lernen!

Lothar Ratschbacher bin ich sehr dankbar, dass er mir immer wieder aufs Neue mit Rat und Tat zur Seite stand, sei es in Fragen zu Literatur, Geochronologie, Regionaler Geologie, und vieles vieles mehr. Ihm verdanke ich, dass ich diesen Weg gegangen bin!

Thomas Kenkmann, Rafael Ferreira Mählmann, Niko Froitzheim und Mark Handy möchte ich für die Diskussionen über die regionale Geologie der Alpen danken!

Monika Sobiesiak hat versucht, mich in die Mysterien der Seismologie einzuweihen. Unsere Diskussionen haben mir immer sehr viel Spaß gemacht!

Jens Nüchter, Dir danke ich für die unzähligen Gespräche über Gott und die Welt, oftmals auch die Geologische! Deine Hinweise bezüglich mineralisierter Risse haben mir sehr geholfen! Du bist einer der fernen Fremden, die zu Freunden worden ;-)

Bernhard Stöckhert, Paola Vannucchi, Francesca Remitti, Cesar Ranero, Taras Gerya, Andreas Rietbrock, Stephan Sobolev und Steve Miller danke ich für Ihre Teilnahme an meinem workshop! Dass Ihr meiner Einladung spontan gefolgt seid, hat mich sehr beeindruckt!

Familie Just möchte ich ganz besonders danken! Durch sie hatte ich immer eine trockene und vor allem warmherzige Unterkunft in Graubünden gefunden!

Rudi Wenk danke ich für unsere schönen und lehrreichen Geländetage, die unterhaltsamen Abende auf der urgemütlichen Berghütte, sowie für spätere Diskussionen und Anregungen.

Petra Paschke, Ihnen bin ich für all die Unterstützung in den vergangenen Jahren dankbar!

Maike Buddensiek möchte ich besonders für unsere gemeinsamen Diskussionen danken, in denen sie versuchte, mir die geophysikalische Weltsicht näher zu bringen. Ob dies gelungen ist? Aber auch privat werde ich mich immer an die Heiterkeit, die von innen kommende Heiterkeit erinnern, die die fröhliche Basis für das harmonische Miteinander darstellte. Maike, Du weißt, wie ich das meine?!

Gabi Arnold bin ich äußerst dankbar für die unkomplizierte, schnelle und „1-a“ Schliffherstellung, auch wenn Dein morgendliches „Hallo“ mich oftmals fast zu Tode erschreckte! Juliane Herwig danke ich für ihre Hilfe bei der Rasterelektronenmikroskopie und der Probenaufbereitung.

Helga Kemnitz möchte ich für Ihre Hilfe bei der Rasterelektronenmikroskopie, bei der Durchführung der Provenance-Analyse, sowie für unsere zahlreichen Diskussionen danken.

Knuth Hahne, Birgit Plessen und Volker Lüders möchte ich für Ihre Hilfe bei geochemischen und isotopengeochemischen Fragen, sowie bei der Analyse von Fluideinschlüssen danken. Knut, Dir möchte ich außerdem für die schöne Zeit in Chile danken! Diese Bootsfahrt werde ich nie vergessen!

Matthias Rosenau, Dir bin ich sehr dankbar für unsere vielen interessanten Diskussionen. Unsere gemeinsame Geländetour war spannend! Die Pizza am Abend konnte nicht einmal von „unserem“ Dortmunder Pizzabäcker in Perugia übertroffen werden ;-)

Ulrike Schönrock und Thomas Ziegenhagen, Euch danke ich für allerlei private Ablenkungen, das eine oder andere Bier und vieles weitere! Nina Kukowski und Silvan Hoth, danke für die Diskussionen!

Helmut Echtler, wo soll ich da anfangen und vor allem wieder aufhören??? Ok, zuerst danke ich Dir für Deine Unterweisungen in zielorientierter Kommunikation. Ich hoffe, irgendwann schaffe ich das auch! Ein Spruch von Dir war immer da, ob man ihn brauchte oder nicht! Ich fand's gut! Danke auch für die aufschlussreichen Geländetage in Chile. Dabei konnte ich endlich Deine Witze mal auf Englisch hören! Spaß beiseite, unsere Diskussionen habe ich

immer sehr genossen und sie haben mir sehr geholfen, sowie ständig neue Impulse für meine Arbeit geliefert!

Wolfgang Seifert, besten Dank für unsere Geländezeit, wo wir so manchen Karren aus dem Dreck gezogen haben, die zahlreichen Diskussionen und die Hilfe an der Mikrosonde!

Dietrich Lange, Dir danke ich für vielfache Diskussionen und vor allem für die Erdbebendaten für Südamerika.

Wolfgang Müller schulde ich Dank für viele Diskussion über die Grenzen der Ar/Ar Datierung!

Mein Dank gilt auch der Studienstiftung des Deutschen Volkes, sowie dem GFZ Potsdam, die durch finanzielle Unterstützung dieses Projekt ermöglichen!

Last but not least danke ich allen Murmeltieren, die mit selbstlosem Einsatz und unter Gefahr für Leib und Leben auch diejenigen Aufschlüsse zugänglich machten, die mir ansonsten für immer unter mächtigen quartären Bedeckungen verborgen geblieben wären.



# Curriculum vitae

# Raik Bachmann

## Personal Information

Name: Raik Bachmann  
Date of birth: 30/04/1978 in Zwickau, Germany  
Nationality: German

## School

09/1984 – 08/1992 secondary school “Sigmund Jähn“ Zwickau  
09/1992 – 07/1996 grammar school “Käthe-Kollwitz“ Zwickau, A-level (grade 1.8)

## Academic Formation

2004 – 2007 PhD student at the GFZ Potsdam (GeoResearchCentre, Potsdam, Germany), scholarship of the German National Merit Foundation  
2003 Diploma degree “Diplom-Geologe” (mark 1.3)  
2003 1-year Diploma thesis (mark 1.3)  
1999 intermediate exam (mark 1.1)  
1997 – 2003 5-year degree in Geology at the Freiberg University (scholarship of the German National Merit Foundation)

